



Rita Maria Mourão Salazar Branquinho

Licenciada em Química

Label-free detection of biomolecules with Ta₂O₅-based field effect devices

Dissertação para obtenção do Grau de Doutor
em Nanotecnologias e Nanociências

Orientador: Doutora Elvira Maria Correia Fortunato, Professora
Catedrática, Faculdade de Ciências e Tecnologia da
Universidade Nova de Lisboa

Co-orientador: Doutor Pedro Miguel Ribeiro Viana Baptista, Professor
Auxiliar com Agregação, Faculdade de Ciências e
Tecnologia da Universidade Nova de Lisboa

Júri:

Presidente: Professor Doutor Fernando José Pires Santana

Arguentes: Prof. Doutora Maria Goreti Ferreira Sales

Prof. Doutor Abel Martim González Oliva

Vogais: Professor Doutor José Higinio Gomes Correia

Prof. Doutor Guilherme Nuno de Passos Correia Matos Ferreira

Professor Doutor Rodrigo Ferrão de Paiva Martins

Prof. Doutor Hugo Manuel Brito Águas



FACULDADE DE
CIÊNCIAS E TECNOLOGIA
UNIVERSIDADE NOVA DE LISBOA

Dezembro de 2012

Rita Maria Mourão Salazar Branquinho

Licenciada em Química

Label-free detection of biomolecules with Ta₂O₅-based field effect devices

Dissertação para obtenção do Grau de Doutor
em Nanotecnologias e Nanociências

Orientador: Doutora Elvira Maria Correia Fortunato, Professora
Catedrática, Faculdade de Ciências e Tecnologia da
Universidade Nova de Lisboa

Co-orientador: Doutor Pedro Miguel Ribeiro Viana Baptista, Professor
Auxiliar com Agregação, Faculdade de Ciências e
Tecnologia da Universidade Nova de Lisboa

Júri:

Presidente: Professor Doutor Fernando José Pires Santana

Arguentes: Prof. Doutora Maria Goreti Ferreira Sales

Prof. Doutor Abel Martim González Oliva

Vogais: Professor Doutor José Higinio Gomes Correia

Prof. Doutor Guilherme Nuno de Passos Correia Matos Ferreira

Professor Doutor Rodrigo Ferrão de Paiva Martins

Prof. Doutor Hugo Manuel Brito Águas



Dezembro de 2012

Label-free detection of biomolecules with Ta₂O₅-based field effect devices

Copyright: Rita Maria Mourão Salazar Branquinho

FCT/UNL e UNL

A Faculdade de Ciências e Tecnologia e a Universidade Nova de Lisboa têm o direito, perpétuo e sem limites geográficos, de arquivar e publicar esta dissertação através de exemplares impressos reproduzidos em papel ou de forma digital, ou por qualquer outro meio conhecido ou que venha a ser inventado, e de a divulgar através de repositórios científicos e de admitir a sua cópia e distribuição com objectivos educacionais ou de investigação, não comerciais, desde que seja dado crédito ao autor e editor.

Acknowledgements

It is said that scientific research is a lonely line of work but as I think back and look around the lab there are many people that contributed to this work and to whom I wish to thank.

First I want to acknowledge my supervisors for their support, advice and guidance throughout this work. Their complementarity in scientific and teaching expertise and their shared enthusiasm for science largely contributed to both my professional and personal growth. Prof. Elvira Fortunato; for the opportunity to develop this new line of work within the group, for her relentless efforts to provide all the necessary means for the success of this research investing in lab facilities, international collaborations and my own academic formation. Thank you for the trust you deposited in me and my work. Prof. Pedro Baptista; for lively and fruitful discussions, for saying ‘you know this won’t work!’ it was always uplifting and for providing the ‘sexy’ DNA targets. Thank you for the confidence in me and my work.

To Prof. Rodrigo Martins, for allowing the development of this work in the research facilities of DCM/FCT-UNL and for all his support.

To Dr. Joana Vaz Pinto and future Dr. Bruno Veigas, friends and companions in endless lab work and whose contribution to this work was indispensable.

To former colleagues whose support and friendship surpassed distance; Ing. Nuno Correia, future Dr. Vitor Figueiredo, Dr. Gonalo Gonalves, Dr. Leonardo Silva and Msc. Lucia Gomes.

To all my colleagues in the MEO group that, direct or indirectly, contributed to this work: Msc. Alexandra Gonalves, Ing. Sonia Pereira, Msc. Diana Gaspar, Msc. Joana Neto, Ing. Ana Ramos, Msc. Raquel Barros, Msc. Andreia Araujo, future Dr. Iwona Wojcik, Dr. Pedro Barquinha, Dr. Lus Pereira, future Dr. Antnio Vicente, future Dr. Jonas Duermeier, Dr. Tito Busani, Msc. Tiago Mateus, future Dr. Pawel Wojcik, Dr. Janadeesh Chandra and everybody else I don’t have room to mention. Thank you all!

To Manuel Quintela, Joel Figueiredo, Ricardo Ferreira and Salomo Lopes for all the help in solving technical issues.

To Dr. Pedro Estrela, for sharing his knowledge on field effect sensors and lab facilities in Cambridge which was very helpful at the beginning of this project.

To Prof. Michael Schöning for welcoming me in his research lab in Jülich campus of Aachen University of Applied Sciences and Dr. Maryam Abouzar for her help in the lab and hospitality during my stay.

To the International Iberian Nanotechnology Laboratory (INL) for the fellowship and financial support for conferences attendance.

To all my friends for their comprehension and support. To Dr. Filipa Siopa, Dr. Sofia Miguel and future Dr. Lídia Santos (you're up next!); companions during Chemistry college and PhD. Most especially to Cláudia Campos; you are like a sister to me! Thank you!

To my family: to my brother Duarte for a lifetime of crazy; to my mother Juca for being my role model and believing in me always! To my grandmother Victoria whose joy for life was overwhelming and will long live within us all. I wouldn't be who I am today without all of you...

Finally, I want to thank my son Rodrigo whose patience and comprehension largely surpass his age. I dedicate this work to him.

Por último, que é sempre o mais importante, quero agradecer ao meu filho Rodrigo. Meu querido; 'dás-me' a melhor companhia, és a minha pessoa preferida, adoro-te sempre! Obrigada por seres o melhor filho do Mundo!

Resumo

Os dispositivos de efeito de campo estão a tornar-se na base estrutural de uma nova geração de micro-biossensores. Inúmeras vantagens tais como, tamanho reduzido, resposta directa e versatilidade, aliadas à possibilidade de integração e à perspectiva de produção em massa, tornam o seu desenvolvimento extremamente importante.

A presente tese foca o estudo e optimização de filmes finos de pentóxido de tântalo (Ta_2O_5) depositados por pulverização catódica assistida por magnetron à temperatura ambiente e a sua aplicação como camada sensível em biossensores baseados em dispositivos de efeito de campo (BioFEDs). Assim, estudou-se a influência de diversos parâmetros de deposição e de tratamentos pós-produção de temperatura e plasma nas propriedades dos filmes.

Sensores com estrutura electrólito-isolante-semicondutor (EIS) contendo a camada sensível de Ta_2O_5 optimizada foram utilizados no desenvolvimento de BioFEDs. Produziram-se sensores funcionalizados com uma camada enzimática (EnFEDs) para detecção de penicilina. Estes sensores foram também utilizados na detecção directa de DNA e na monitorização da sua amplificação por PCR, PCR em tempo real (RT-PCR) e amplificação isotérmica (LAMP). Foram também produzidos transístores sensíveis a iões (ISFETs) baseados em óxidos semicondutores, contendo a camada sensível de Ta_2O_5 optimizada.

Sensores EIS contendo a camada sensível de Ta_2O_5 optimizada possuem uma elevada sensibilidade ao pH, 58 ± 0.3 mV/pH. Estes foram aplicados com sucesso na detecção directa de penicilina e DNA. Sensores funcionalizados com penicilinase demonstraram sensibilidade à penicilina de 29 ± 7 mV/mM até uma concentração de 4 mM. Estes sensores revelaram sensibilidade ao DNA de 30 mV/ μM e a sua aplicação na monitorização da amplificação de DNA demonstrou resultados comparáveis com os métodos tradicionais baseados em fluorescência. ISFETs de óxidos semicondutores foram também produzidos com sucesso.

Por fim, a excelente qualidade e sensibilidade revelada pelos filmes de Ta_2O_5 produzidos por pulverização catódica à temperatura ambiente permite a sua aplicação como camada sensível em sensores de efeito de campo.

Termos chave: sensores de efeito de campo; pentóxido de tântalo; pulverização catódica; baixa temperatura; monitorização directa da amplificação de DNA; ISFETs baseados em óxidos semicondutores.

Abstract

Field-effect-based devices (FEDs) are becoming a basic structural element in a new generation of micro biosensors. Their numerous advantages such as small size, label-free response and versatility, together with the possibility of on-chip integration of biosensor arrays with a future prospect of low-cost mass production, make their development highly desirable.

The present thesis focuses on the study and optimization of tantalum pentoxide (Ta_2O_5) deposited by rf magnetron sputtering at room temperature, and their application as sensitive layer in biosensors based on field effect devices (BioFEDs). As such, the influence of several deposition parameters and post-processing annealing temperature and surface plasma treatment on the film's properties was investigated.

Electrolyte-insulator-semiconductor (EIS) field-effect-based sensors comprising the optimized Ta_2O_5 sensitive layer were applied to the development of BioFEDs. Enzyme functionalized sensors (EnFEDs) were produced for penicillin detection. These sensors were also applied to the label free detection of DNA and the monitoring of its amplification via polymerase chain reaction (PCR), real time PCR (RT-PCR) and loop mediated isothermal amplification (LAMP). Ion sensitive field effect transistors (ISFETs) based on semiconductor oxides comprising the optimized Ta_2O_5 sensitive layer were also fabricated.

EIS sensors comprising Ta_2O_5 films produced with optimized conditions demonstrated near Nernstian pH sensitivity, 58 ± 0.3 mV/pH. These sensors were successfully applied to the label-free detection of penicillin and DNA. Penicillinase functionalized sensors showed a 29 ± 7 mV/mM sensitivity towards penicillin detection up to 4 mM penicillin concentration. DNA detection was achieved with 30 mV/ μM sensitivity and DNA amplification monitoring with these sensors showed comparable results to those obtained with standard fluorescence based methods. Semiconductor oxides-based ISFETs with Ta_2O_5 sensitive layer were also produced.

Finally, the high quality and sensitivity demonstrated by Ta_2O_5 thin films produced at low temperature by rf magnetron sputtering allows for their application as sensitive layer in field effect sensors.

Keywords: *field-effect-based sensors; tantalum pentoxide; magnetron sputtering; low temperature; label-free DNA amplification monitoring; oxide-based ISFETs.*

Table of contents

Chapter 1. Motivation	1
1.1. Introduction	3
1.2. Scientific context	5
1.3. Objectives	6
1.4. Thesis outline	7
1.5. Publications and presentations	8
Chapter 2. Introduction	11
2.1. Biosensors	13
2.2. Field effect based sensors	15
2.2.1. Electrolyte-Insulator-Semiconductor (EIS) capacitors	15
2.2.2. Ion-Sensitive-Field-Effect-Transistors (ISFETs)	20
2.3. Oxide/Electrolyte interface	23
2.3.1. Electrochemical double layer	24
2.3.2. Site binding model	27
2.4. Sensitive layer	31
2.5. Field effect biosensors (BioFEDs)	34
2.5.1. Chemically-modified FEDs (ChemFEDs)	35
2.5.2. Immunologically modified FEDs (ImmunoFEDs)	36
2.5.3. Cell-based FEDs (CellFEDs)	37
2.5.4. Enzyme-modified FEDs (EnFEDs)	38
2.5.5. DNA modified FEDs (DNAFEDs)	41
Chapter 3. Device fabrication and characterization techniques	45
3.1. Fabrication of field effect devices (FEDs)	47
3.1.1. Electrolyte-insulator-semiconductor devices (EIS)	47

3.1.2. Ion sensitive field effect transistors (ISFET)	48
3.2. Device fabrication techniques	49
3.2.1. Thin film deposition	49
3.2.2. Photolithographic patterning	53
3.3. Post-deposition processes	55
3.3.1. Influence of annealing temperature	55
3.3.2. Influence of plasma surface treatments	56
3.4. Thin film characterization techniques	56
3.4.1. Structural, morphological and compositional characterization	57
3.4.2. Optical characterization	60
3.4.3. Contact angle measurements	63
3.5. Characterization of field effect devices (FEDs)	64
3.5.1. Impedance Spectroscopy (IS)	64
3.5.2. Static current-voltage characteristics	68
Chapter 4. Ta₂O₅ based field effect devices	71
4.1. Electrolyte-insulator-semiconductor (EIS) sensors development	73
4.1.1. Sensor characteristics	73
4.1.2. Sensor behaviour	75
4.1.3. Sensor structure	78
4.2. Influence of deposition conditions	79
4.2.1. Influence of deposition rate	80
4.2.2. Influence of rf power	81
4.2.3. Influence of deposition pressure and Ar:O ₂ ratio	87
4.3. Influence of post-production treatments	91
4.3.1. Influence of annealing temperature	91
4.3.2. Influence of surface plasma treatments	98
4.3.2.1. Influence of argon plasma	98

4.3.2.2. Influence of oxygen plasma	101
Chapter 5. Label-free detection of biomolecules	105
5.1. Penicillinase-modified field effect devices (PenFEDs)	107
5.1.1. Penicillin detection with Ta ₂ O ₅ based PenFEDs	109
5.1.2. Penicillin detection with O ₂ plasma treated Ta ₂ O ₅ based PenFEDs	112
5.2. Label-free detection of DNA with field effect devices	114
5.2.1. DNA structure	115
5.2.2. Intrinsic charge based detection of DNA	117
5.2.3. Non-specific DNA concentration detection	122
5.3. DNA amplification monitoring	123
5.3.1. DNA amplification via polymerase chain reaction (PCR)	123
5.3.2. Field effect detection of PCR amplification of DNA	125
5.3.3. Loop-mediated isothermal DNA amplification (LAMP)	133
5.3.4. Field effect real-time monitoring of LAMP DNA amplification	133
Chapter 6. Semiconductor oxides based ISFETs	139
6.1. Introduction	141
6.2. Extended gate oxide semiconductor-based ISFETs	142
6.2.1. Sensor structure	142
6.2.2. Sensor fabrication	143
6.2.3. Structural and compositional characterization	144
6.2.4. Electrical characterization	146
6.3. pH sensitivity of oxide ISFETs	148
Chapter 7. Conclusions and future perspectives	155
7.1. Conclusions	157
7.1.1. Optimization of sputtered Ta ₂ O ₅ thin films for sensing applications	157
7.1.2. Enzyme-functionalized FEDs for penicillin detection	160

7.1.3. Label-free detection of DNA	161
7.1.4. Oxide semiconductor–based ISFETs	163
7.2. Future perspectives	164
References	171

List of Figures

Figure 1.1. The total biosensors market, showing the percent of revenues predicted by vertical markets (world) for 2016, based on 2009 market values (Web01).....	3
Figure 1.2. Ion sensitive chips: a) 8'' wafer containing ~200 ion sensor die; b) unpackaged die and c) die in ceramic package with moulded fluidic lid to allow addition of sequencing reagents (Rothberg 2011).	4
Figure 2.1. Generalized schematics of a biosensor system.....	14
Figure 2.2. Professor Piet Bergveld (from http://www.knaw.nl/)	16
Figure 2.3. Schematic illustration of MIS and EIS structures.....	17
Figure 2.4. Capacitance-voltage characteristics of an ideal p-type MIS structure. Adapted from (Schroder 2006).....	18
Figure 2.5. Energy-band diagram of an ideal p-type MIS capacitor in flat-band condition; accumulation; depletion and inversion regimes. Adapted from (Sze 2007).....	18
Figure 2.6. Band-diagram with $V_{FB} \neq 0$ at $V_G = 0$ V (left) and new flat-band voltage; $V_G = V_{FB}$ (right).....	20
Figure 2.7. Schematic structure of FET and ISFET.....	21
Figure 2.8. Energy band diagrams of an ideal gate electrode/dielectric/n-type semiconductor capacitor for different bias conditions: (a) equilibrium ($V_G = 0$ V); (b) depletion ($V_G < 0$ V); (c) accumulation ($V_G > 0$ V).....	22
Figure 2.9. Typical output (left) and transfer (right) characteristics of a TFT (Barquinha 2010a).....	23
Figure 2.10. The Helmholtz model of the double layer (Brett 1993).....	25
Figure 2.11. The Gouy-Chapman model of the double layer (Shinwari 2007).....	25
Figure 2.12. The Stern model of the double layer including the ion adsorption effect that defines the IHP introduced by Grahame in 1947 (Shinwari 2007).....	28
Figure 2.13. Oxide/Electrolyte interface showing the oxide's surface sites and possible reactions (Shinwari 2007).....	29
Figure 2.14. Schematic representation of potential drops along the ISFED structure (Shinwari 2007).....	32
Figure 2.15. Schematic representation of an immunologically modified sensor (ImmunoFED).....	38
Figure 2.16. SEM image of cells on an ISFET sensor (Baumann 1999).	38

Figure 2.17. Schematic representation of an enzyme functionalized sensor (EnFED).....	40
Figure 2.18. Schematic representation of a DNA functionalized sensor (DNAFED).....	43
Figure 2.19. IonTorrent™ ISFET-based DNA sequencing equipment: schematic representation of the pH-based sensing mechanism.....	44
Figure 3.1. Schematic representation of the EIS sensors production steps.....	49
Figure 3.2. Schematic representation of ISFET sensors deposition steps sequence...	49
Figure 3.3. Schematic representation of the magnetron sputtering deposition process (Web02).....	52
Figure 3.4. AJA ATC-1300F sputtering system used for the deposition of dielectrics (left) and detail of the main chamber (right), showing the magnetrons' configuration.....	52
Figure 3.5. Image of the yellow room where photolithographic processes are performed.....	54
Figure 3.6. Process flows showing the main steps of lift-off photolithographic process.....	55
Figure 3.7. Image of the combination of the photomasks of all the layers of an ISFET device.	56
Figure 3.8. Schematic representation of Bragg's law (left) and Panalytical X'Pert PRO diffractometer (right).....	58
Figure 3.9. SEM-FIB Cross-Beam Auriga system existent in CENIMAT.....	59
Figure 3.10. Asylum MFP3D atomic force microscope system existent in CENIMAT.....	60
Figure 3.11. Schematic representation of optical band gap (E_{opt}) determination from a Tauc's plot.....	62
Figure 3.12. Jobin Yvon Uvisel ellipsometer system existent in CENIMAT (left) and schematic representation of an ellipsometry setup (right).....	63
Figure 3.13. Schematic representation of contact angle measurement (left) and Dataphysics OCA15plus system existent in CENIMAT (right).....	65
Figure 3.14. Graphical representation of the time (t) dependent sinusoidal current response (I) to a small ac voltage (E), in a linear system.....	66
Figure 3.15. Gamry Reference 600 Potentiostat (left) and experimental setup (right) used for impedance measurements of EIS sensors.....	68
Figure 3.16. Agilent 4155C semiconductor parameter analyser (left) and Cascade M150 microprobe station (right) used in I(V) measurements of ISFET sensors.....	70

Figure 4.1. Electrochemical impedance spectroscopy measurement cell: real image (left) and schematic assembly representation (right).....	76
Figure 4.2. Geometric capacitance variation with sensitive area diameter for a double layered insulator of SiO_2 and Ta_2O_5 (100 nm each) and considering $\epsilon_{\text{SiO}_2}=3.9$ and $\epsilon_{\text{Ta}_2\text{O}_5}=25$	76
Figure 4.3. Schematic representation of the measurement setup (left) and typical C(V) response of a EIS sensor to different pH electrolytes (right).....	77
Figure 4.4. Simplified equivalent circuit of an EIS sensor. Adopted from (Bousse 1983).....	78
Figure 4.5. Potentiostatic impedance curves of an EIS sensor in pH 7 buffer solution. Open symbols refer to Z_{modulus} , solid symbols to Z_{phase} and lines to data fitting results.....	78
Figure 4.6. Frequency dependence of C(V) characteristics (left) and leakage current - I(V) (right) of an EIS sensor in pH 7 buffer solution.....	79
Figure 4.7. Capacitance-voltage and leakage current characteristics of Al/Si/ Ta_2O_5 (left) and Al/Si/ SiO_2 / Ta_2O_5 (right) sensors exposed to electrolytes of pH 4, 7 and 10.....	80
Figure 4.8 Capacitance-voltage and leakage current characteristics of Al/Si/ SiO_2 / Ta_2O_5 sensor exposed to electrolytes of pH 4, 7 and 10.....	81
Figure 4.9. Influence of deposition parameters on the deposition rate; power (left); oxygen content and deposition pressure (right).....	82
Figure 4.10. XRD diffractogram (left) and RBS spectra (right) of Ta_2O_5 EIS sensors produced with different rf power.....	83
Figure 4.11. SEM and AFM images of the Ta_2O_5 films deposited with 200 W rf power, Ar: O_2 =14:1 sccm and 0.3 Pa.....	84
Figure 4.12. Optical transmittance spectra of Ta_2O_5 films deposited with varied rf power.....	85
Figure 4.13. Model used in spectroscopic ellipsometry analysis of Ta_2O_5 thin films...	86
Figure 4.14. Refraction index (n) and extinction coefficient (k) of Ta_2O_5 deposited with different rf power, obtained by modulation of SE results.....	86
Figure 4.15. Parameters obtained by modulation with Tauc-Lorentz dispersion of SE data of Ta_2O_5 deposited with different rf power.....	87
Figure 4.16. C(V) curves (top) and pH sensitivity (bottom) determination for a Ta_2O_5 EIS sensor produced with P=100 W, p=0.3 Pa and Ar: O_2 =14/1.....	88
Figure 4.17. Variation of pH sensitivity of Ta_2O_5 EIS sensors produced with different rf power. The dashed line represents Nernst sensitivity of 59.2 mV/pH.....	89

Figure 4.18. XRD diffractograms of Ta ₂ O ₅ EIS sensors produced at different deposition pressures (left) and oxygen content (right).....	90
Figure 4.19. RBS spectra of Ta ₂ O ₅ EIS sensors produced at different deposition pressures (left) and oxygen content (right).....	90
Figure 4.20. SEM (left) and AFM (right) images of the Ta ₂ O ₅ films deposited with a 0.2 Pa pressure, Ar:O ₂ =12:3 sccm and 150 W rf power.....	91
Figure 4.21. Parameters obtained by modulation with Tauc-Lorentz dispersion of SE data of Ta ₂ O ₅ deposited with different deposition pressure and Ar:O ₂ ratio.....	92
Figure 4.22. Variation of pH sensitivity of Ta ₂ O ₅ EIS sensors produced with different deposition pressure and Ar:O ₂ ratio.....	92
Figure 4.23. X-ray diffractogram of Ta ₂ O ₅ film before and after post deposition annealing (vertical lines represent diffraction planes of orthorhombic Ta ₂ O ₅).....	94
Figure 4.24. RBS spectra of samples annealed at 200 °C and 800 °C with respective fit curves.....	94
Figure 4.25. Morphological characterization of Ta ₂ O ₅ sensors: SEM micrograph and AFM deflection images (R_{rms} calculated using height profile) of Ta ₂ O ₅ surface of sensors a) as deposited; b) annealed at 700 °C and c) 800 °C.....	95
Figure 4.26. Spectroscopic ellipsometry simulation results of the interfacial layer thickness and band-gap energy of the Ta ₂ O ₅ sensors annealed at various temperatures.....	96
Figure 4.27. Imaginary component of the dielectric function of Ta ₂ O ₅ sensors annealed at various temperatures; obtained from spectroscopic ellipsometry data modulation.....	97
Figure 4.28. Variation of pH sensitivity of Ta ₂ O ₅ EIS sensors with post-deposition annealing temperature.....	97
Figure 4.29. Variation of the reference voltage obtained at 60% of maximum capacitance with annealing temperature for solution and aluminium-gated Ta ₂ O ₅ EIS sensors.....	98
Figure 4.30. AFM image of Ta ₂ O ₅ sensor after argon plasma treatment at 30 W for 10 minutes.....	100
Figure 4.31. Ta ₂ O ₅ pH sensitivity variation with argon plasma surface treatments...	101
Figure 4.32. Variation of reference voltage at pH 7 with argon plasma surface treatments.....	102
Figure 4.33. Ta ₂ O ₅ pH sensitivity variation with oxygen plasma surface treatments.....	104
Figure 4.34. Variation of reference voltage at pH 7 with oxygen plasma surface treatments.....	104

Figure 5.1. SEM micrograph of enzyme functionalized Ta ₂ O ₅ EIS sensor.....	110
Figure 5.2. Variation of C(V) characteristics of a penicillinase functionalized sensor when exposed to penicillin solutions of increasing concentration.....	111
Figure 5.3. Sensitivity of a penicillinase functionalized sensor to penicillin and its correlation with pH variation.....	112
Figure 5.4. Variation of C(V) characteristics of a oxygen plasma treated sensor functionalized with penicillinase when exposed to penicillin solutions of increasing concentration.....	114
Figure 5.5. Sensitivity to penicillin of an oxygen plasma treated sensor functionalized with penicillinase and its correlation with pH variation.....	115
Figure 5.6. Schematic structure of DNA molecule illustrating the chemical structure of the nucleotides, the anti-parallel nature of the two strands and the base pair hydrogen bonds that binds them together. (Becker 2009).....	117
Figure 5.7. Schematic illustration of fraction of DNA molecule contained within the Debye length (λ_D) and its variation with the ionic strength of the electrolyte (I).....	120
Figure 5.8. Semi-quantitative response of EIS sensor to the presence of ssDNA and dsDNA oligonucleotides (Oligo A, Oligo B, Oligo A+B) used at different concentrations (1 and 2 μ M).....	124
Figure 5.9. Schematic representation of DNA amplification via PCR (Web03).....	127
Figure 5.10. Conventional fluorescence-based detection with SYBR-green intercalating agent of DNA accumulation during PCR amplification. •) c-MYC gene sequence amplification, ■) PCR negative control.....	129
Figure 5.11. Capacitance-voltage curves obtained for a positive sample of DNA amplification at PCR cycle n ($n=0, 3, 6, 9, 12, 15, 18, 21, 24, 27$).....	130
Figure 5.12. Field effect-based detection with optimized Ta ₂ O ₅ sensitive layer of DNA accumulation during PCR amplification. •) c-MYC gene sequence amplification, ■) PCR negative control.....	131
Figure 5.13. EIS sensor drift analysis: C(V) measurements performed on PCR cycle 0 following the same procedure as for the amplified DNA samples.....	132
Figure 5.14. Corrected data of field effect-based detection with optimized Ta ₂ O ₅ sensitive layer of DNA accumulation during PCR amplification. •) c-MYC gene sequence amplification, ■) PCR negative control.....	132
Figure 5.15. Monitoring DNA amplification in real-time. Comparison between A) corrected Ta ₂ O ₅ EIS sensor amplification curve and B) standard RT-PCR: •) c-MYC gene sequence amplification, ■) RT-PCR negative control.....	134
Figure 5.16. Melting temperature profile of the amplified products.....	134

Figure 5.17. LAMP DNA amplification measurement cell: real image (left) and schematic assembly representation (right).....	136
Figure 5.18. Field effect-based detection with optimized Ta ₂ O ₅ sensitive layer of DNA accumulation during LAMP DNA amplification. •) c-MYC gene sequence amplification, ■) LAMP negative control.....	138
Figure 5.19. EIS sensor drift analysis: C(V) measurements performed on a LAMP buffer solution following the same procedure as for the amplified DNA samples.....	139
Figure 6.1. Schematic representation of an extended gate amorphous oxide based ISFET.....	143
Figure 6.2. Amorphous oxides based extended gate ISFET sensors and detail of a TFT device.....	144
Figure 6.3. XRD diffractograms of semiconductor (GIZO) and multicomponent dielectric (Ta ₂ O ₅ :SiO ₂) thin films.....	145
Figure 6.4. RBS spectra of GIZO semiconductor (top) and multicomponent Ta ₂ O ₅ :SiO ₂ dielectric (bottom) thin films and corresponding fit lines.....	146
Figure 6.5. Transfer (left) and output (right) characteristics of an amorphous oxides based TFT.....	147
Figure 6.6. Influence of passivation on device stability and measurement reproducibility (GIZO TFT on glass/ITO/ATO substrate).....	148
Figure 6.7. ISFET sensors measurement cell: real image (left) and schematic assembly representation (right).....	149
Figure 6.8. Transfer characteristics obtained with $V_D = 0.1$ V for two pH cycles (top) and pH sensitivity expressed as variation of the reference voltages with buffer solution pH (bottom).....	150
Figure 6.9. Temporal response variation of the reference voltages obtained at $0.3 \mu\text{A}$ for both cycles of pH measurements.....	151
Figure 6.10. ISFET output characteristics at fixed gate voltage ($V_G = 0, 0.5, 1.0, 1.5$ V) with different pH solutions.....	152
Figure 6.11. Device response to varied buffer solutions in a pH range between pH 2 and pH 12: (top) transfer characteristics obtained at $V_D = 0.1$ V and (bottom) pH sensitivity expressed as variation of the reference voltages with buffer solution pH.....	153
Figure 6.12. Variation of the transfer characteristics of a GIZO based ITO/ATO ISFET device with buffer solution's pH ($V_D = 0.1$ V).....	154
Figure 7.1. Image of a transparent EIS based sensor depicting peeling of the layers.....	165
Figure 7.2. Schematic representation of both paper device structures.....	166

List of Tables

Table 2.1. Classification of electrochemical biosensors according to type of measurement. Adapted from (Thevenot 1999).....	15
Table 2.2. Overview of materials applied as sensitive layer in field effect based pH sensors.....	33
Table 2.3. Relevant historical milestones in the development of BioFEDs. (adapted from Schoning 2002)	36
Table 2.4. Overview of developed EnFEDs including the enzyme used and the analyte detected. Adapted from (Dzyadevych 2006; Schoning 2002).....	40
Table 3.1. Production details of each of the ISFET sensors layers.	49
Table 4.1. Equivalent circuit parameters obtained from fitting of IS characteristics of an EIS sensor in different operation regimes.....	77
Table 4.2. Sputtering deposition parameters for the production of Ta ₂ O ₅ EIS sensors.....	80
Table 4.3. Optical band gap energy of Ta ₂ O ₅ films deposited with varied rf power....	84
Table 4.4. Optical band gap of Ta ₂ O ₅ films deposited with varied deposition pressure and Ar:O ₂	90
Table 4.5. Sensitivity and contact angle variation with annealing temperature.	98
Table 4.6. Parameters obtained by modulation with Tauc-Lorentz dispersion of SE data of Ta ₂ O ₅ films exposed to argon plasma under different conditions.....	100
Table 4.7. Parameters obtained by modulation with Tauc-Lorentz dispersion of SE data of Ta ₂ O ₅ films exposed to oxygen plasma under different conditions.....	102
Table 5.1. Overview of penicillinase modified field effect devices for penicillin detection.....	108
Table 5.2. Relevant differences in Ta ₂ O ₅ penicillinase FEDs produced in this work ^a and by Siqueira et al (2009) ^b	112
Table 6.1. Elemental composition of the deposited oxides obtained from RBS data fitting.....	146

Abbreviations

a.c. – alternate current

AFM – atomic force microscopy

ALD – atomic layer deposition

APTES – 3-amino-propyltriethoxysilane

ATO – aluminium oxide / titanium oxide multi-layer dielectric

AVT – average transmittance in the visible range

BioFED – biologically modified field effect device

CellFED – cell-based field effect device

CEMOP – Centre of Excellence in Microelectronics Optoelectronics and Processes

CENIMAT – Centro de Investigação de Materiais

ChemFED – chemically modified field effect device

c-Si – crystalline Si

C(V) – capacitance-voltage

CVD – chemical vapour deposition

d.c. – direct current

DNA – deoxyribonucleic acid

DNAFED – DNA field effect device

dsDNA – double stranded DNA

EG-ISFET – extended gate ion sensitive field effect transistor

EIS – electrolyte-insulator-semiconductor

EnFED – enzyme modified field effect device

FED – field effect device

FET – field effect transistor

FTO – fluorine doped tin oxide

GIZO – gallium indium zinc oxide

IHP – inner Helmholtz plane

IL – interfacial layer

ImmunoFED – immunologically modified field effect device

IPA – isopropyl alcohol

IS – impedance spectroscopy

ISFED – ion sensitive field effect device

ISFET – ion sensitive field effect transistor

ITO – indium tin oxide

IUPAC – International Union of Pure and Applied Chemistry

I(V) – current-voltage

IZO – indium zinc oxide

LAMP – loop-mediated isothermal DNA amplification

MIS – metal-insulator-semiconductor

MISFET – metal-insulator-semiconductor field-effect transistor

MOSFET – metal-oxide-semiconductor field-effect transistor

MOCVD – metal-organic chemical vapour deposition

MPCVD – microwave plasma-assisted chemical vapour deposition

nc-Diamond – nanocrystalline diamond

NIR – near infrared

NPs – nanoparticles

OHP – outer Helmholtz plane

PAMAM – polyamidoamine dendrimers

PBS – phosphate buffer solution

PCR – polymerase chain reaction

PDMS - polydimethylsiloxane

PECVD – plasma enhanced chemical vapour deposition

PenFED – penicillinase modified field effect device

PenG – penicillin G; benzylpenicillin

poly-Si – poly-crystalline Si

PVD – physical vapour deposition
RBS – Rutherford backscattering spectrometry
rf – radio-frequency
RT-PCR – real-time polymerase chain reaction
SAM - self-assembled monolayer
sccm – standard cubic centimeters per minute
SE – spectroscopic ellipsometry
SEM – scanning electron microscopy
SNP – single nucleotide polymorphism
SPA – semiconductor parameter analyzer
ssDNA – single stranded DNA
swCNT – single-walled carbon nanotube
TCO – transparent conductive oxide
TEOS – tetraethylorthosilicate
TFT – thin-film transistor
TSO – transparent semiconductive oxide
UV – ultra-violet
Vis. – visible
W/O – without
XRD – x-ray diffraction
ZTO – zinc-tin oxide

Symbols

A – optical absorption

c – speed of light

c_o – electrolyte concentration

c_i – ionic concentration

C – capacitance

C_{dif} – differential capacitance

C_{dl} – double layer capacitance

C_{GC} – Gouy-Chapman capacitance

$C_{\text{Helmholtz}}$ – Helmholtz capacitance

C_i – insulator capacitance

C_{SC} – semiconductor capacitance

C_{Stern} – Stern capacitance

C_t – total capacitance

d – film thickness

d_{ip} –inter planar distance

E – energy of electromagnetic wave

E_c – conduction band

E_F – Fermi level

E_g - bandgap

E_i – intrinsic energy level

E_{opt} – optical bandgap

E_{Ref} – reference electrode potential

f – frequency

F – Faraday constant

h – Planck's constant (4.135×10^{-15} eV.s)

I – current

I_D – drain-to-source current
 $I_{D\text{ sat}}$ – drain-to-source current in saturation regime
 I_G – gate leakage current
 I_{on} – on current
 I_{off} – off current
 I^s – ionic strength
 j – imaginary number
 k – extinction coefficient
 k_B – Boltzmann constant
 K_a – acid equilibrium constant
 K_b – basic equilibrium constant
 L – channel length
 N – free carrier concentration
 N_A – Avogadro constant
 n – refractive index
 p – deposition pressure
 P – rf power density
 q – elementary charge of a particle (1.6×10^{-19} C)
 Q_{DNA} – DNA molecule charge
 Q_f – fixed oxide charge
 Q_i – insulator charge
 Q_{it} – interface trapped oxide charge
 Q_m – mobile oxide charge
 Q_{ot} –oxide trapped charge
 Q_{ox} –oxide charge
 R – reflectivity
 R_{rms} – root-mean-square roughness
 R_{SC} – semiconductor resistance
 R_t – combined resistance

r_{ionic} – ionic radius
 r_p – parallel reflection coefficient
 r_s – perpendicular reflection coefficient
 S – subthreshold swing
 T – transmittance
 T_A – annealing temperature
 V – voltage
 V_D – drain voltage
 V_{FB} – flat band voltage
 V_G – gate voltage
 V_{Ref} – reference voltage
 V_T – threshold voltage
 W – channel width
 z_i – ionic valency
 Z – impedance
 $Z' \equiv Z_{\text{real}}$ – real component of impedance
 $Z'' \equiv Z_{\text{imag}}$ – imaginary component of impedance
 α – absorption coefficient
 β_{int} – intrinsic buffer capacity
 γ_{LG} – surface tensions of liquid–gas interface
 γ_{SG} – surface tensions of solid– gas interface
 γ_{SL} – surface tensions of solid–liquid interface
 Δ – differential phase angle
 ϵ_0 – vacuum permittivity
 ϵ_2 – imaginary component of the dielectric function
 ϵ_{el} – electrolyte permittivity
 ϵ_i – insulator permittivity
 θ – Bragg angle

κ – dielectric constant
 λ – wavelength of electromagnetic wave
 λ_D – Debye length
 μ – mobility
 ν – frequency of electromagnetic wave
 ρ – electrical resistivity
 ρ_F – Fresnel coefficient
 σ – electrical conductivity
 σ_o – accumulated oxide surface charge density
 σ_d – surface charge density
 χ^2 – error function
 χ_{sol} – surface-dipole potential of the solution
 ψ – differential amplitude angle
 ψ_o – oxide/electrolyte surface potential
 ψ_s – semiconductor potential
 ψ_{ox} – oxide potential
 ϕ – phase shift
 ϕ_M – metal work function
 ϕ_{SC} – semiconductor work function
 ω – radial frequency

Chapter 1. Motivation

- 1.1. Introduction 3
- 1.2. Scientific context5
- 1.3. Objectives..... 6
- 1.4. Thesis outline.....7
- 1.5. Publications and presentations 8

Chapter 1. Motivation

1.1. Introduction

Biosensors represent a well established market involving high investments in research and industry. The variety of sensors and sensor applications is overwhelming and still it is expected to continue to grow. Perhaps the most recognized and successful example is the glucose biosensor. It represents about 70 % of the biosensors market and has become a household device for diabetes monitoring. A similar development can be envisioned for other sensors, including DNA diagnostics. DNA detection based diagnostics have applications in various fields such as pathogen identification, drug screening and diagnosis of genetic diseases. The development of sensors that allow for fast, simple and cost-effective detection of DNA, especially for point-of-care applications, is thus highly desirable; as demonstrated in Figure 1.1 (Drummond 2003; McKinnon 2009; Shinwari 2007).

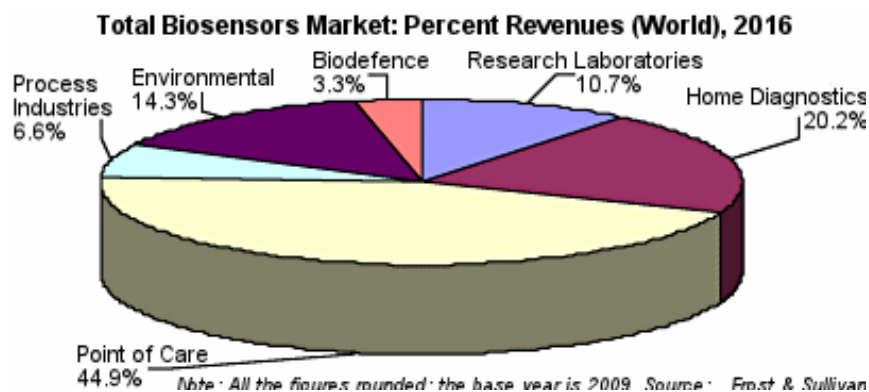


Figure 1.1. The total biosensors market, showing the percent of revenues predicted by vertical markets (world) for 2016, based on 2009 market values (Web01).

Field effect devices are a promising alternative in the label free detection of DNA and consequently considerable research efforts have been invested towards their development. These devices provide several advantages: small dimensions, fast response, possibility of integration into biosensor arrays and the possibility of low-cost mass production. As such, the simultaneous analysis of various DNA targets in miniaturised analytical systems, as lab-on-chip sensors, could become a reality (Shinwari 2007; Schoning 2002). In fact, last year, it became a reality with the publication ‘An integrated semiconductor device enabling non-optical genome sequencing’ in *Nature* (Rothberg 2011) and subsequent application of this technology to a commercially available DNA sequencing equipment – IonTorrent™ (<http://www.iontorrent.com/>).

The incorporation of a nucleotide into strand of DNA by a polymerase releases a hydrogen ion as a by-product; resulting in a local pH variation that can be detected by the underlying ISFET sensor and converted to a measurable signal. The IonTorrent is similar to standard fluorescence-based DNA sequencing equipments that uses a high-density array of wells, each holding a different DNA template, to perform this biochemical process in a massively parallel way. The difference is that beneath the wells lies an array of ion-sensitive field effect sensors, fabricated by standard CMOS technology Figure 1.2. The ISFET directly detects the sequencing event thus eliminating the need for fluorescent labels and complex optical detection methods and equipments.

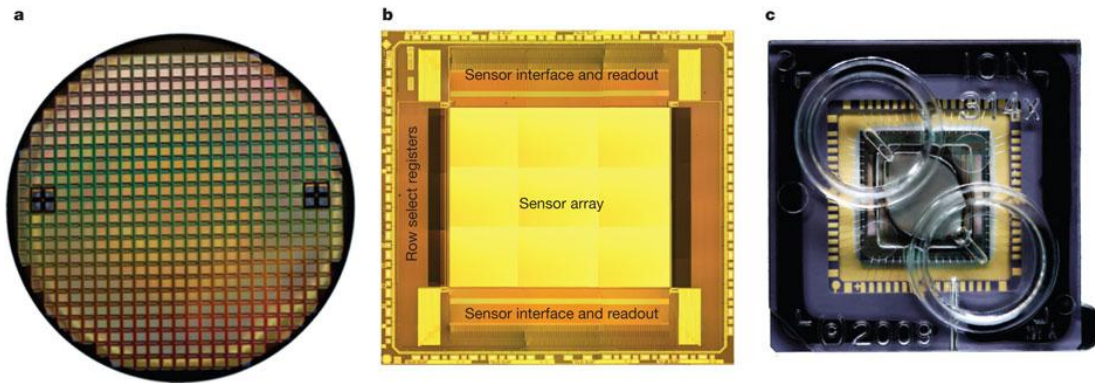


Figure 1.2. Ion sensitive chips: a) 8'' wafer containing ~200 ion sensor die; b) unpackaged die and c) die in ceramic package with moulded fluidic lid to allow addition of sequencing reagents (Rothberg 2011).

1.2. Scientific context

Since the introduction of the ion sensitive field-effect transistor (ISFET) in the 1970's by Bergveld the development of these devices and their applications has significantly grown. However, it took almost 30 years for the first pH sensitive ISFET to be commercially available and despite the intensive research and the breakthrough of IonTorrent TM, that testifies to the enormous possibilities of field effect based biosensors (BioFEDs), no other BioFED device has been made commercially available.

The reality is that, together with all their advantages, FEDs also possess some drawbacks related to device stability, reproducibility and drift issues. Low-cost disposable sensors, which for some applications are preferred, would resolve most of these drawbacks while presenting new challenges. The use of plastic or even paper substrates for field effect sensor's production would require low temperature fabrication process. This is not possible for silicon-based technology nor with the commonly used fabrication techniques for Si based FEDs. Consequently alternative fabrication methods and materials should be pursuit.

Field effect devices based on oxide semiconductors and materials produced by radio frequency (rf) magnetron sputtering have demonstrated excellent properties and are compatible with low-cost substrates due to the low process temperature (Barquinha 2010 and 2010a; Fortunato 2008 and 2008a; Pereira 2008). The remarkable development of oxide semiconductors based devices and their application in display technology has established these as a new generation of electronic devices, providing an attractive alternative for BioFEDs sensors. (Barquinha 2012; Fortunato 2012)

The development of the sensitive layer for field effect based sensors will be the main focus of this work as most of the currently reported sensitive materials are either produced via high temperature techniques, such as thermal oxidation, or require post-deposition annealing at high temperatures. To overcome these drawbacks and produce a sensitive layer under conditions compatible with low-cost and/or flexible substrates, rf magnetron sputtering was chosen as the deposition technique for it allows the deposition of materials at low temperature.

In this context the aim of this work is the production, study and optimization of the sensitive layer by rf magnetron sputtering and its application in field effect based biosensors.

1.3. Objectives

The development of field effect based biosensors within the microelectronic and optoelectronic research group was initiated by this work. As such, one of the initial objectives was to establish the necessary conditions for the development of biosensors research. For that the remodelling and refurbishing of a new dedicated laboratory as well as the acquisition of specific equipments and adaptation of existing equipment, to allow measurements with solutions, was initially performed.

The main goals of this work are:

- ◆ The production and study of low temperature sputtered Ta_2O_5 thin films for application as a sensitive layer in field effect based sensors.
- ◆ The optimization of the Ta_2O_5 sensitive layer production and post-production parameters, towards maximum pH sensitivity.
- ◆ Production of enzyme functionalized field effect devices (EnFED) for penicillin detection.
- ◆ The field effect detection of DNA and real-time label-free monitoring of DNA amplification via polymerase chain reaction (PCR) and loop-mediated isothermal amplification (LAMP).
- ◆ The low temperature production of oxide semiconductor based ISFETs comprising the optimized Ta_2O_5 sensitive layer and their application as field effect based sensors.

1.4. Thesis outline

- ◆ **Chapter 1** presents the aim and motivation of this study.
- ◆ **Chapter 2** provides some fundamental background regarding the functioning principle of field effect based devices and the electric potential of the electrolyte/oxide interface. A brief overview of materials applied as sensitive layer in FEDs and of BioFEDs developments is also described.
- ◆ **Chapter 3** describes the production and characterization techniques used during the research work of this dissertation, mostly highlighting rf magnetron sputtering and electrochemical characterization of the devices.
- ◆ **Chapter 4** focuses on the presentation and discussion of the main results obtained on tantalum pentoxide thin films produced by rf magnetron sputtering and their application as pH sensitive layer in FEDs. The influence of several processing and post-processing parameters on the films properties and pH sensitivity is analyzed. A section of this chapter is devoted to the establishment of the measurement protocol as it proved to be crucial to obtain reliable data.
- ◆ **Chapter 5** describes the main results obtained for the detection of biomolecules. The production of enzyme functionalized field effect devices (EnFEDs) and results for penicillin detection are presented and discussed. Also, results of the field effect detection of DNA and real-time label-free monitoring of DNA amplification via polymerase chain reaction (PCR) and loop-mediated isothermal amplification (LAMP) are presented and the detection mechanism is discussed.
- ◆ **Chapter 6** is devoted to the presentation and discussion of the production of oxide semiconductor-based ISFETs comprising the optimized Ta₂O₅ sensitive layer and their application as field effect based sensors.
- ◆ **Chapter 7** presents the main conclusions of this dissertation and provides possible further applications of the results and concepts developed.

1.5. Publications and presentations

The main results obtained during this dissertation were presented in several international conferences and published in peer-reviewed publications.

Publications

- ◆ R. Branquinho, B. Veigas, J. V. Pinto, R. Martins, E. Fortunato and P. V. Baptista, 'Real-time monitoring of PCR amplification of proto-oncogene c-MYC using a Ta₂O₅ electrolyte–insulator–semiconductor sensor', *Biosensors and Bioelectronics*, 2011, 28, p. 44-49.
- ◆ R. Branquinho, J.V. Pinto, T. Busani, P. Barquinha, L. Pereira, P.V. Baptista, R. Martins, E. Fortunato, 'Biosensors based on Sputtered Ta₂O₅ with Low Thermal Annealing', *IEEE/OSA Journal of Display Technology Special Issue in association with the 8th International Thin Film Transistor Conference (ITC 2012)*, in press.
- ◆ J.V. Pinto, R. Branquinho, P. Barquinha, E. Alves, R. Martins, E. Fortunato, 'Extended-gate ISFETs based on Sputtered Amorphous Oxides', *IEEE/OSA Journal of Display Technology Special Issue in association with the 8th International Thin Film Transistor Conference (ITC 2012)*, in press.

Oral presentations in international conferences

- ◆ R. Branquinho*, B. Veigas, J. V. Pinto, P. Baptista, R. Martins, E. Fortunato, '*Sputtered Ta₂O₅ Field Effect Based Biosensors*', *EMRS 2011 Fall Meeting*, Warsaw, Poland, 19-23 September 2011.
- ◆ J.V. Pinto*, R. Branquinho, P. Barquinha, R. Martins, E. Fortunato, '*ISFETs based on amorphous oxides and produced at room temperature*', *EMRS 2011 Fall Meeting*, Warsaw, Poland, 19-23 September 2011.
- ◆ R. Branquinho, J.V. Pinto, L. Pereira, P. Barquinha, P. Estrela, P. Baptista, R. Martins, E. Fortunato* '*New Amorphous Oxide-based ISFETs for Biosensor Applications*' *MRS2010 Spring Meeting*, San Francisco USA 5-9 April 2010.
- ◆ R. Branquinho*, J. V. Pinto, P. Barquinha, L. Pereira, P. Estrela, P. Baptista, R. Martins, E. Fortunato '*Room Temperature Sputtered Ta₂O₅ for Solid State Biosensors*' *TNT2010*, Braga PT 6-10 September 2010

Poster presentations in international conferences

- ◆ R. Branquinho*, J. V. Pinto, T. Busani, P. Barquinha, L. Pereira, P. V. Baptista, R. Martins, E. Fortunato, '*Biosensors based on Sputtered Ta₂O₅ with Low Thermal Annealing*', ITC 2012, Lisbon PT, 30-31 January 2012
- ◆ J. V. Pinto*, R. Branquinho, P. Barquinha, E. Alves, R. Martins, E. Fortunato, '*Extended-gate ISFETs based on Sputtered Amorphous Oxides*', ITC 2012, Lisbon PT, 30-31 January 2012
- ◆ R. Branquinho*, B. Veigas, J. V. Pinto, R. Martins, P.V. Baptista, E. Fortunato, '*Ta₂O₅ electrolyte-insulator-semiconductor sensor for Real Time PCR*', Bio-Sensing Technology 2011, Amsterdam, The Netherlands, 10-12 October 2011
- ◆ J.V. Pinto, R. Branquinho*, P. Barquinha, P. Estrela, R. Martins, E. Fortunato, '*Room Temperature Processed ISFETs Based on Amorphous Oxides*', Bio-Sensing Technology 2011, Amsterdam, The Netherlands, 10-12 October 2011
- ◆ R. Branquinho*, J. V. Pinto, P. Barquinha, L. Pereira, P. Estrela, P. Baptista, R. Martins, E. Fortunato '*Room Temperature Sputtered Ta₂O₅ for Solid State Biosensors*' TNT2010, Braga PT 6-10 September 2010 – **Best Poster Award**
- ◆ R. Branquinho*, J. V. Pinto, P. Barquinha, L. Pereira, P. Baptista, R. Martins, E. Fortunato '*Room temperature sputtered high-k dielectrics for biosensing applications*' Biosensors2010, Glasgow UK 26-28 May 2010

Chapter 2. Introduction

2.1. Biosensors.....	13
2.2. Field effect based sensors.....	15
2.2.1. Electrolyte-Insulator-Semiconductor (EIS) capacitors	15
2.2.2. Ion-Sensitive-Field-Effect-Transistors (ISFETs)	20
2.3. Oxide/Electrolyte interface	23
2.3.1. Electrochemical double layer	24
2.3.2. Site binding model	27
2.4. Sensitive layer	31
2.5. Field effect biosensors (BioFEDs)	34
2.5.1. Chemically-modified FEDs (ChemFEDs)	35
2.5.2. Immunologically modified FEDs (ImmunoFEDs)	36
2.5.3. Cell-based FEDs (CellFEDs)	37
2.5.4. Enzyme-modified FEDs (EnFEDs)	38
2.5.5. DNA modified FEDs (DNAFEDs)	41

Chapter 2. Introduction

In this chapter a fundamental background regarding the functioning principle of biosensors, field effect based devices and the electric potential of the electrolyte/oxide surfaces interface is provided. A brief overview of the materials applied as sensitive layer in FEDs and of BioFEDs developments is also described.

2.1. Biosensors

As defined by IUPAC (International Union of Pure and Applied Chemistry) a chemical sensor is a device that transforms chemical information, ranging from the concentration of a specific sample component to total composition analysis, into an analytically useful signal. Chemical sensors usually contain two basic components connected in series: a chemical (molecular) recognition system (receptor) and a physicochemical transducer. Biosensors are chemical sensors in which the recognition system utilizes a biochemical mechanism (Thevenot 1999; Turner 1987).

The recognition system can be based on organic or inorganic materials and biologically active substances can be proteins, enzymes, antibodies or antigens, nucleotides, whole cells or even an insect's sensory organ (Schoning 2002). The specificity and selectivity is thus provided by the sensitive layer that upon interaction with a substance of interest (analyte) generates a physical-chemical change. This change is detected and translated by the transducer into a measurable signal that is directly correlated to the analyte concentration. A schematic representation of a biosensor system is shown in Figure 2.1.

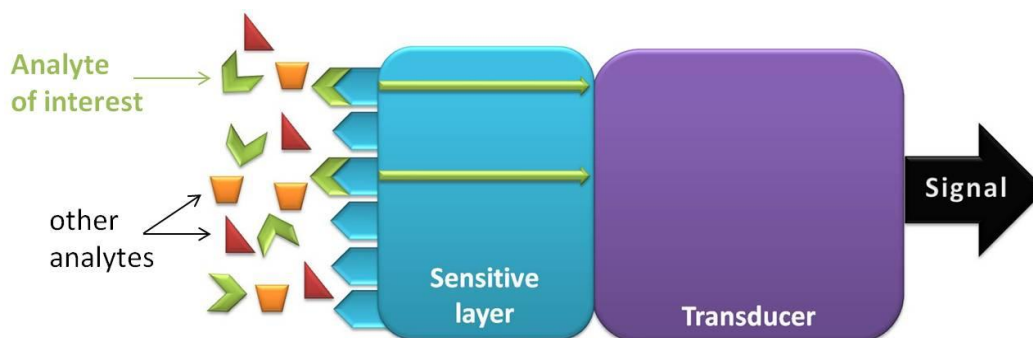


Figure 2.1. Generalized schematics of a biosensor system.

Biosensors should ideally demonstrate stability during operation and overtime, reversibility of the recognition event; a linear range of operation; defined detection limit and reproducibility of sensor response (Kissinger 2005).

Biosensors can be classified according to the nature of the variation that occurs from the physical-chemical interaction between the analyte and the sensitive layer. These can be optic, thermal, acoustic, magnetic, piezoelectric or electrochemical, to name just a few. Electrochemical sensors, in their turn, can be divided into potentiometric, amperometric, conductometric and field effect-based according to the measurement type. Table 2.1 shows some examples of transducers and respective analytes from each class of electrochemical sensors.

Table 2.1. Classification of electrochemical biosensors according to type of measurement. Adapted from (Thevenot 1999).

Measurement	Transducer	Analyte
Amperometric	Metal or carbon electrodes; Chemically modified electrodes	O ₂ , sugars, alcohols...; Sugars, alcohols, phenols, oligonucleotides...
Conductometric	Interdigitated electrodes; Metal electrode	Charged species, oligonucleotides...
Potentiometric	Glass electrode; Ion-selective electrode (ISE); Gas electrode; Metal electrode	H ⁺ , Na ⁺ ; K ⁺ , Ca ²⁺ , Cl ⁻ , F ⁻ ... CO ₂ , NH ₃ ; redox species
Field effect	Ion-sensitive field effect device (ISFED); Enzyme FED (EnFED); DNA-based FED	H ⁺ , Na ⁺ , K ⁺ , Ca ²⁺ , Cl ⁻ , F ⁻ , charged species... Penicillin, glucose, urea... DNA, oligonucleotides...

Historically the first biosensor was reported in 1962 (Clark and Lyons, 1962). It was an electrochemical biosensor where an enzyme (glucose-oxidase) membrane was combined with an oxygen electrode to yield the well known glucose sensor. The interest and development of biosensors has been growing ever since due to the uncountable possibilities of applications of such devices. The demands in process control and monitoring of complex biochemical reactions both *in-vitro* and *in-vivo* and the constant progress in biotechnology (genomics, proteomics and pharmaceuticals) have been some of the driving forces behind the increased development of this new generation of analytical devices.

2.2. Field effect based sensors

In field effect based biosensors the transducer is usually a metal-insulator-semiconductor (MIS) capacitor or metal-oxide-semiconductor field effect transistor (MOSFET) that are slightly modified. Initially classified as potentiometric sensors, since the detection mechanism is based on an electrical potential variation at the transducer when placed in contact with an electrolyte, these were separated into a new class of electrochemical biosensors after 30 years of their discovery; which demonstrates their importance (Dzyadevych 2006; Thevenot 1999).

The first ion sensitive field effect transistor (ISFET) was invented by Bergveld (Figure 2.2) in the 1970's (Bergveld 1970 and 1972) where it was applied for electrophysiological measurements of the composition of the area surrounding nerve tissues. It was shown that with this device not only electrical potentials but also ion concentrations could be measured hence the name ion sensitive field effect transistor (Bergveld 2003). The electrolyte-insulator-semiconductor (EIS) capacitor has also been widely studied for biosensing applications.



Figure 2.2. Professor Piet Bergveld (from <http://www.knaw.nl/>)

The structure and operation principles of electrolyte-insulator-semiconductor (EIS) capacitors and ion sensitive field effect transistors (ISFET) are presented in the next sections.

2.2.1. *Electrolyte-Insulator-Semiconductor (EIS) capacitors*

The EIS structure, as depicted in Figure 2.3, is identical to that of a metal-insulator-semiconductor (MIS) capacitor where the gate electrode is replaced by an electrolyte and a reference electrode (E_{Ref}); usually Ag/AgCl. The insulator, commonly an oxide, is thus directly exposed to the electrolyte so changes in the solution can affect the oxide surface potential and modulate the device's response.

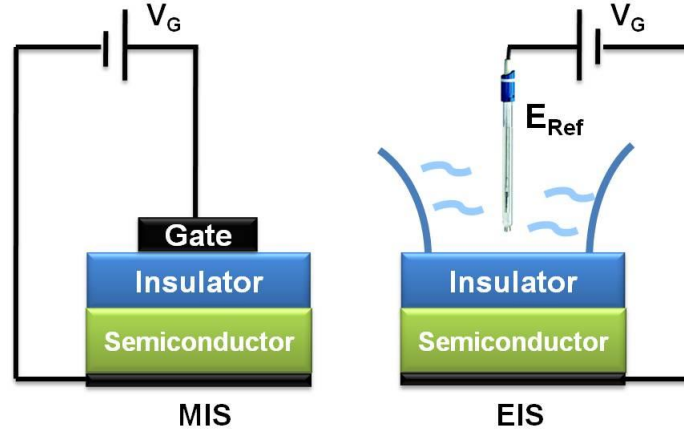


Figure 2.3. Schematic illustration of MIS and EIS structures.
 E_{Ref} : reference electrode; V_G : gate voltage.

The operation principles of EIS sensors are thus similar to those of the MIS capacitor with additional parameters arising from the additional components (electrolyte and reference electrode).

The MIS capacitor is one of the most simple and useful devices in the study of electronic circuits. The Si-SiO₂ MIS structure was first reported in 1960 by Ligenza et al and it is still looked upon as the most ideal semiconductor-insulator interface to serve as a model for understanding surface physics in electronic devices. (Sze 2007)

The MIS capacitor is a two electrode device where a semiconductor is separated from the gate electrode by an insulator layer. It is similar to a parallel plate capacitor with an additional semiconductor layer that has a variable capacitance. By applying a voltage to the gate electrode the space-charge distribution in the semiconductor can be modulated. The total capacitance of the device (C) is a series combination of the insulator capacitance (C_i) and the voltage dependent semiconductor capacitance (C_{sc}).

$$\frac{1}{C} = \frac{1}{C_i} + \frac{1}{C_{sc}} \equiv C = \frac{C_i C_{sc}}{C_i + C_{sc}} \quad (2.1)$$

For an insulator of a given thickness (d) C_i is constant, corresponding to the maximum capacitance of the system, and depends only on the material's properties and device geometry ($C_i = \epsilon_0 \epsilon_i A / d$; where ϵ_0 and ϵ_i are the air and insulator permittivity respectively and A is the surface area). The semiconductor's capacitance is variable and is determined by the space-charge region thickness which is dependent on the voltage applied to the gate electrode. The capacitance-voltage characteristics of the MIS device show three different regions depending on the applied gate voltage (V_G): accumulation, depletion and inversion.

The capacitance-voltage characteristics of a MIS device can be obtained by applying a dc gate voltage with a superimposed small ac signal of known frequency. A typical C-V curve of an ideal p-type Si/SiO₂ MIS capacitor is depicted in Figure 2.4.

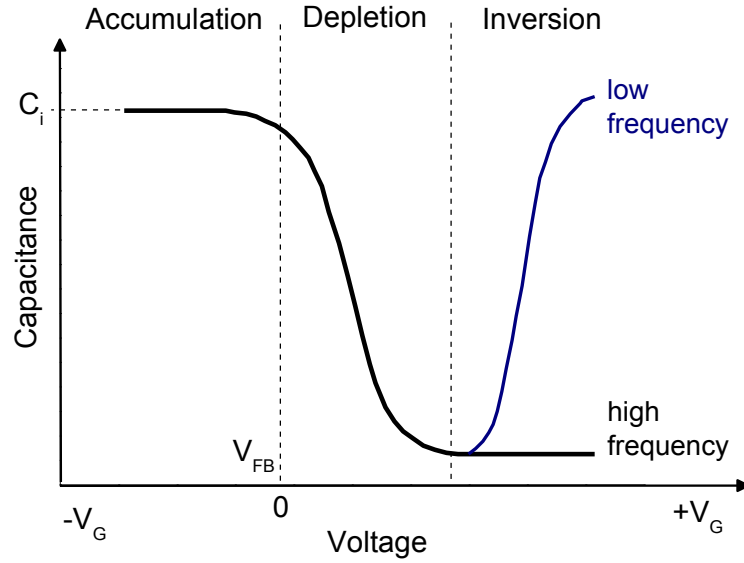


Figure 2.4. Capacitance-voltage characteristics of an ideal p-type MIS structure. Adapted from (Schroder 2006)

The different regimes can be explained with the energy-band diagram of an ideal MIS structure (Figure 2.5), where it is assumed that under the biasing conditions no current flows through the insulator and the only charges that exist are those in the gate electrode which are mirrored in the semiconductor (equal but of opposite sign).

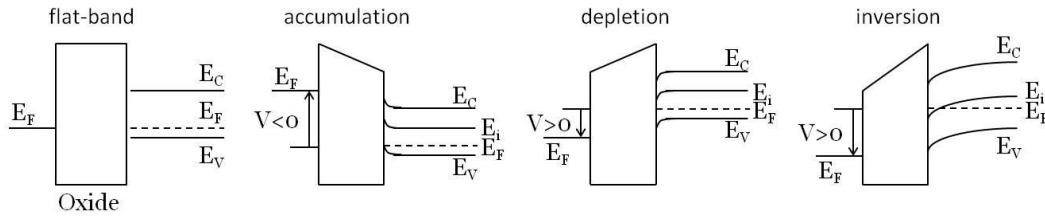


Figure 2.5. Energy-band diagram of an ideal p-type MIS capacitor in flat-band condition; accumulation; depletion and inversion regimes. Adapted from (Sze 2007)

The system is in equilibrium when no voltage is applied ($V_G=0$ V) to the device and assuming that there is no difference between the metal gate and semiconductor work functions, the Fermi level of the semiconductor is flat (flat-band condition) and aligned with the metal's Fermi level.

The device is in accumulation when a negative voltage is applied to the gate electrode ($V_G < 0$ V). Under negative bias the silicon energy bands bend upwards and positive

charges (holes); which are the majority charge carriers in p-type Si; accumulate at the semiconductor-insulator interface creating a thin charged layer. In this accumulation regime the device is similar to a parallel plate capacitor and the total capacitance is defined by the insulator capacitance ($C=C_i$) corresponding to the maximum capacitance of the system.

When the gate electrode is positively biased ($V_G > 0$ V) the energy band bend downwards and the electric field pushes the positive charge carriers away from the interface, thus forming a depletion region, that acts as an insulator, at the semiconductor-insulator interface. The thickness of the depletion region (w_d) increases with applied potential hence the depletion layer capacitance decreases, consequently the total capacitance will also decrease (equation (2.1)).

Further increase in applied voltage ($V_G \gg 0$ V) causes the intrinsic level to cross over the semiconductor Fermi level which leads to the accumulation of electrons; the minority charge carriers in p-type Si; at the Si/SiO₂ interface. When the electron concentration exceeds the hole concentration at the interface a thin n-type layer forms within the p-type Si, hence the designation inversion. This region of the curve can assume two forms depending on the measuring frequency. For low frequency the electron concentration can follow the ac signal applied so total capacitance increases reaching maximum value close to C_i in a similar way as in accumulation. At high frequency the electron concentration cannot follow the signal variation because it is faster than the recombination-generation rates of these minority charge carriers. In this case the capacitance curve reaches a plateau of minimum capacitance (Sze 2007; Schroder 2006).

The ideal MIS structure is useful for describing and understanding the capacitance-voltage characteristics of this type of devices however in a non-ideal capacitor other parameters must be taken into account. In a non-ideal capacitor the flat-band voltage (V_{FB}) is not usually zero and its value is affected by the existence of oxide charges (such as interface trapped charges – Q_{it} ; fixed oxide charge – Q_f ; mobile ionic charge – Q_m ; and oxide trapped charge – Q_{ot}) and also by the work function difference between the semiconductor (ϕ_{sc}) and the gate metal (ϕ_M).

$$V_{FB} = \phi_M - \phi_{sc} - \frac{Q_{it} + Q_f + Q_m + Q_{ot}}{C_i} \quad (2.2)$$

In this case the system is not in equilibrium when $V_G = 0$ V and it is necessary to apply a certain voltage to attain the flat-band condition (Figure 2.6). The experimental C-V curve is thus shifted from the theoretical curve by this amount.

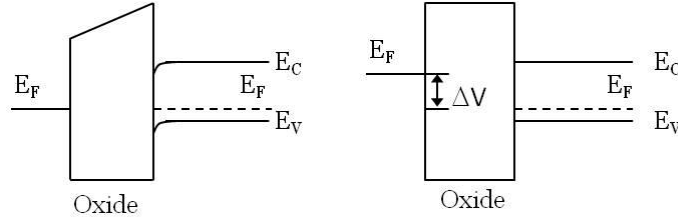


Figure 2.6. Band-diagram with $V_{FB} \neq 0$ at $V_G = 0$ V (left) and new flat-band voltage; $V_G = V_{FB}$ (right).

The flat-band voltage (V_{FB}) is the most relevant parameter when considering these devices for sensing applications because its value will be affected by the changes in solution.

The EIS sensor is basically a MIS capacitor where the metal gate electrode is substituted by an electrolyte and a reference electrode (Figure 2.3). The capacitance-voltage characteristics of an EIS device can be obtained in a similar way by applying a dc voltage though the reference electrode with a superimposed small ac signal of known frequency.

The expressions obtained for the MIS device can be modified to account for the additional potential contributions from the reference electrode and electrolyte.

The flat-band voltage of an EIS sensor can thus be expressed as:

$$V_{FB} = E_{Ref} + \chi_{sol} - \psi_0 - \phi_{SC} - \frac{Q_{it} + Q_f + Q_m + Q_{ot}}{C_i} \quad (2.3)$$

where E_{Ref} is the reference electrode potential, χ_{sol} is the surface-dipole potential of the solution, which are constant for a given solution; and ψ_0 is the electrolyte/insulator interface potential, which is determined by the interaction of ions in solution with insulator active surface sites (Barabash 1987; Bergveld 2003). Depending on the ion concentration the insulator surface potential will change so the space-charge capacitance, and consequently the total capacitance, is thus modulated by the electrolyte composition.

Similarly to the MIS device and for controlled electrolyte concentration and measurement frequency, the capacitance-voltage characteristics of the EIS sensor can be described by a series combination of the insulator capacitance and the space-charge capacitance. However the space-charge capacitance can be modulated by electrolyte composition through variations in the electrolyte/insulator surface potential (Bousse 1982 and 1983; Diot 1985; Barabash 1987; Madou 1989; Shinwari 2007).

The electrochemical potential of ionic species in solution and the electrolyte/insulator surface potential (ψ_o) will be discussed in more detail in section 2.3.

2.2.2. Ion-Sensitive-Field-Effect-Transistors (ISFETs)

As described in the previous section for the EIS sensor, the ISFET sensor structure and operation can be related to its electronic counterpart; the field effect transistor (FET). Again by replacing the gate electrode with an electrolyte and a reference electrode the gate dielectric, typically an oxide, is directly exposed to the electrolyte so changes in the solution can affect the oxide surface potential and modulate the device's response. A schematic representation of a FET and an ISFET structure is depicted in Figure 2.7.

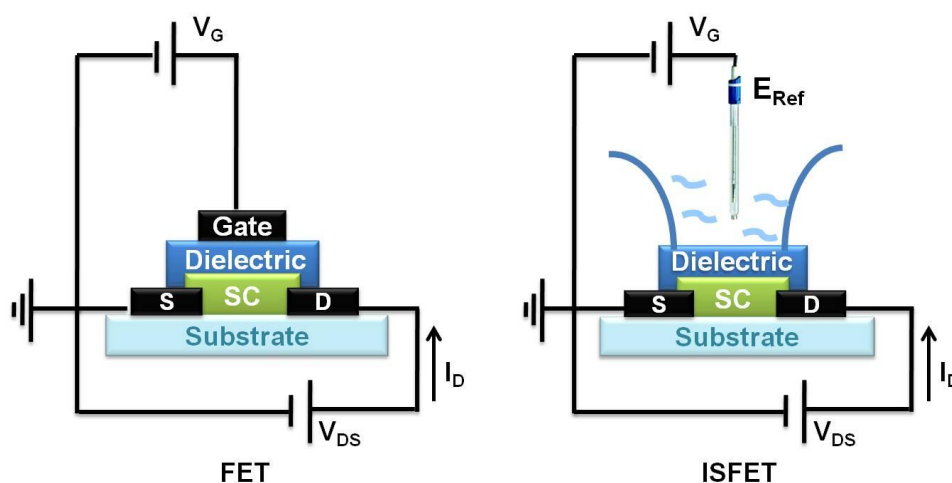


Figure 2.7. Schematic structure of FET and ISFET.

The field effect transistor is one of the most important electronic devices in integrated circuits such as microprocessors and memories. Its invention was patented in the 1930s by Lilienfeld but due to the lack of adequate materials and technological facilities its successful fabrication was only reported 23 years later by Shockley. In the 1960s the production of the Si-SiO₂ based MOSFET and the thin film transistor (TFT) led to the increased interest and development of these devices. Although MOSFETs and TFTs differ in some aspects (mainly in the materials properties, modes of conduction, fabrication process and device substrate) the operation principle is the same (Sze 2006; Tickle 1969).

The field effect transistor can be generically described as a three electrode device where the current flow between the source and drain electrodes (I_D) can be modulated by varying the potential applied to the gate and source electrodes (V_G). The semiconductor

layer is separated from the gate electrode by an insulator layer that prevents current flow between them. In this way the FET gate structure is similar to a MIS capacitor so the field effect modulation of charge carrier's concentration at the semiconductor-insulator interface can be explained by the energy band diagram variation of this capacitor with applied V_G . Figure 2.8 depicts the energy bands diagram of an ideal capacitor comprising an n-type semiconductor.

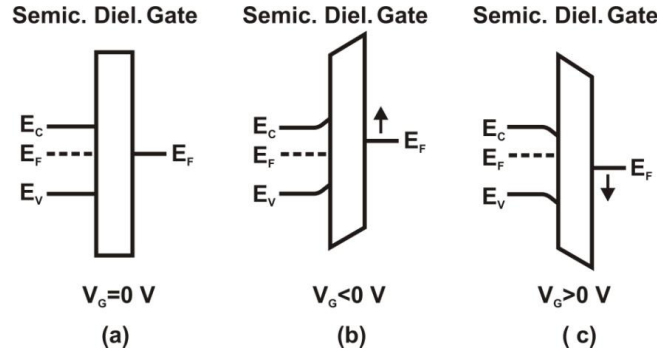


Figure 2.8. Energy band diagrams of an ideal gate electrode/dielectric/n-type semiconductor capacitor for different bias conditions: (a) equilibrium ($V_G = 0$ V); (b) depletion ($V_G < 0$ V); (c) accumulation ($V_G > 0$ V).

As explained in the previous section for p-type Si, band bending occurs when a voltage is applied to the gate electrode however for n-type semiconductors the polarity is reversed because in this case the majority charge carriers are electrons. When the gate electrode is negatively biased ($V_G < 0$ V) electrons are repelled from the semiconductor-insulator interface creating a depletion layer that acts as an insulator, consequently negligible current flows between source and drain (I_D) even at high drain-source voltage (V_D). Accumulation occurs when a positive bias, which attracts electrons to the semiconductor surface, is applied to the gate ($V_G > 0$ V). A conductive channel forms at the semiconductor-insulator interface when a sufficiently high concentration of electrons is accumulated in this region and current can flow between source and drain ($I_D > 0$ A). The conduction mechanism differs from silicon because in this case no inversion layer is formed. (Sze 2006, Tickle 1969)

The voltage required to generate the conductive channel is the threshold voltage (V_T). At voltages higher than the threshold, the accumulation charges increases which leads to an increase in the channel conductance and in drain-source current flow (I_D). The gate voltage thus modulates the channel conductance and, as it is increased, the TFT can be switched from the OFF ($V_G < 0$ V) to the ON ($V_G > V_T$) state.

In the ON state the drain-to-source current varies with both the gate voltage and the drain voltage. Depending on the drain voltage value two regimes of operation can be distinguished: linear and saturation.

The linear regime occurs when $V_D < (V_G - V_T)$, and I_D is described by:

$$I_D = C_i \mu \frac{W}{L} \left[(V_G - V_T) V_D - \frac{V_D^2}{2} \right] \quad (2.4)$$

where W and L are the channel's width and length, respectively; C_i is the insulator capacitance and μ is the carrier mobility. For low V_D the quadratic term can be neglected so I_D varies linearly with V_D .

For $V_D > (V_G - V_T)$, I_D saturates and becomes independent of V_D , depending only on V_G , which is described by:

$$I_{D\text{ sat}} = C_i \mu \frac{W}{2L} (V_G - V_T)^2 \quad (2.5)$$

The TFTs characteristics can be assessed by graphical representation of the I_D dependence on V_D with fixed V_G - output characteristics; and the I_D dependence on V_G with fixed V_D - transfer characteristics (Figure 2.9).

In the output characteristics the linear and saturation regimes are clearly identified. As described by equation (2.4), initially I_D increases linearly with V_D until the onset of I_D saturation is reached ($V_D = V_G - V_T$). For higher V_D values this equation is no longer valid and $I_{D\text{ sat}}$ is described by equation (2.5) (Tickle 1969).

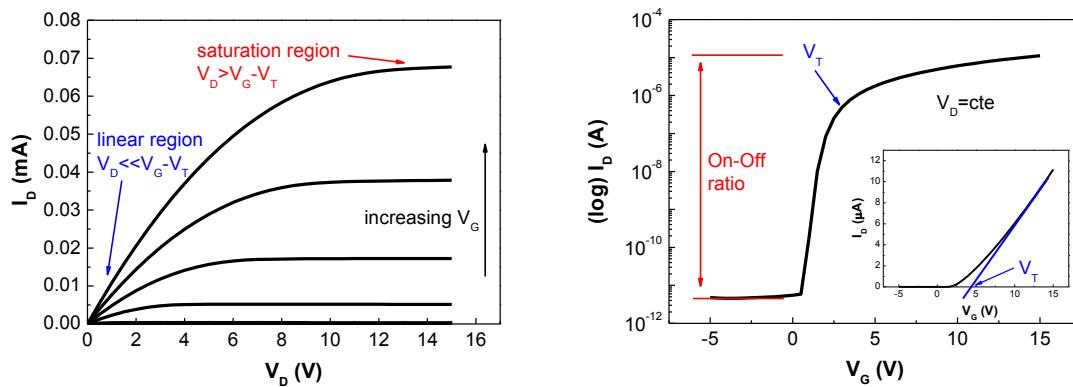


Figure 2.9. Typical output (left) and transfer (right) characteristics of a TFT (Barquinha 2010a).

The transfer characteristics, represented in both linear and logarithmic I_D scale, allow the determination of several electrical parameters that characterize the TFTs performance: threshold voltage; carriers mobility (both in linear and saturation

regimes); ON/OFF current ratio (I_D ON/ I_D OFF) and subthreshold swing, which is the necessary V_G to increase I_D by one decade and is strongly correlated to the semiconductor/dielectric interface.

Concerning ISFETs the most important of the TFTs parameter is the threshold voltage as it is influenced by the flat-band voltage of the gate/semiconductor/insulator capacitor structure (equation (2.3)). The ISFET's sensitivity towards changes in the electrolyte composition can be defined similarly to that of an EIS capacitive sensor. As explained in the previous section, in a non-ideal device the flat-band voltage is not usually zero and its value is affected by the existence of oxide charges (Q_{ox}), the work function difference between the semiconductor and the solution (ϕ_{sc}), the reference electrode potential (E_{Ref}), the surface-dipole potential of the solution (χ_{sol}) and the electrolyte/insulator interface potential (ψ_o), which is dependent on the ion concentration in the solution; according to equation (2.6): (Madou 1989; Dzyadevych 2006)

$$V_T = E_{Ref} + \chi_{sol} - \psi_o - \phi_{sc} - \frac{Q_{ox}}{C_i} \quad (2.6)$$

The electrolyte/insulator surface potential (ψ_o) is a key parameter in the devices sensitivity and will be discussed in more detail in the following section.

2.3. Oxide/Electrolyte interface

The interface potential that arises when an oxide is exposed to an electrolyte and its dependence on solution composition is the most important parameter in the application of field effect devices as biosensors so understanding the oxide/electrolyte interface is crucial.

The relationship between the potential applied to an EIS capacitor and the accumulated charge at the surface of electrochemical interfaces can be divided into two components; the electrostatic potential of ions in solution, as defined by the electrochemical double layer, and charge formation due to chemical reactions that occur at the oxide's surface, as described by the site binding model.

2.3.1. Electrochemical double layer

Under applied bias charges accumulate on both sides of the electrode/electrolyte interface. The model for the potential distribution at the electrolyte side of the interface is complex and has been evolving since the first double layer model developed by Helmholtz in 1879. This model stated that an ionic layer of opposite charge would accumulate at the surface of the biased electrode in a rigid manner (Figure 2.10). The double layer would thus be similar to a parallel plate capacitor where the distance of closest approach was defined by the ionic radius ($C_{\text{Helmholtz}} = \epsilon_{\text{el}} \epsilon_0 / r_{\text{ionic}}$). However this model neglected interactions further into solution and did not account for electrolyte composition and concentration (Brett 1993).

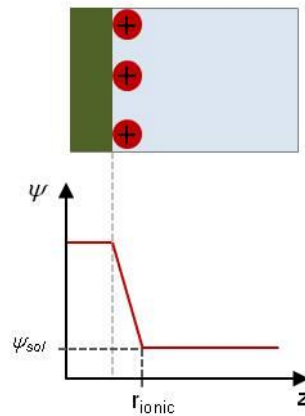


Figure 2.10. The Helmholtz model of the double layer. (Brett 1993)

A model of a diffuse double layer, of variable thickness and where ions are free to move, was later proposed by Gouy and Chapman in the 1910's. This model considered that the applied potential and the electrolyte concentration would both influence the double layer capacity since the ion distribution at the surface differs from that of the solution bulk (Figure 2.11). (Brett 1993, Shinwari 2007)

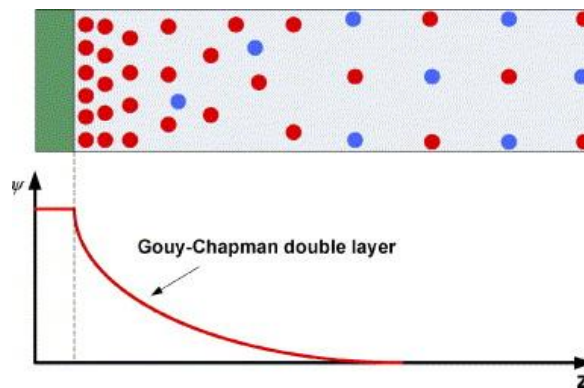


Figure 2.11. The Gouy-Chapman model of the double layer. (Shinwari 2007)

The potential drop within this layer can be described by the Poisson-Boltzmann's equation, where charge distribution from the electrode follows Boltzmann's law and the potential is related with the charge distribution by the Poisson equation. Assuming a planar electrode and for low surface potentials ($\psi_o < 80$ mV) the one dimensional linearized Poisson-Boltzmann equation (2.7) describes the potential distribution (ψ) in the diffuse double layer.

$$\psi = \psi_o e^{-kx} \quad (2.7)$$

with

$$k = \sqrt{\frac{N_A c_o q^2}{\epsilon_{el} \epsilon_0 k_B T}} = \lambda_D^{-1} \quad (2.8)$$

where N_A is the Avogadro constant, c_o is the electrolyte concentration in mol.m^{-3} , q is the elementary charge, ϵ_{el} the dielectric constant of the electrolyte, ϵ_0 the permittivity of vacuum, k_B is the Boltzmann constant and T the absolute temperature (Brett 1993, Shinwari 2007).

The potential decreases exponentially with the distance from the electrode (x) and the decay length, also called the Debye length, is $\lambda_D = k^{-1}$. At distances greater than λ_D charges in solution are balanced by counter-ions, resulting in a zero net charge. For biosensing purposes, λ_D is very important because only events that occur at the sensor's surface or close to λ_D should be detected. For an aqueous solution ($\epsilon_{\text{water}} = 78.4$) of a monovalent salt of concentration c'_0 (in mol.dm^{-3}) at 25 °C the Debye length is $\lambda_D = 30.4/\sqrt{c'_0}$ (in nm). However for more complex electrolytes, which are generally used, the concentration (c_i) and valency (z_i) of all ions present must be taken into account, so in equation (2.8) c_o is substituted by the ionic strength of the solution (I^s) as defined by:

$$I^s = \frac{1}{2} \sum_{i=1}^n c_i z_i^2 \quad (2.9)$$

So that λ_D becomes

$$\lambda_D = \sqrt{\frac{\epsilon_{el} \epsilon_0 k_B T}{2 N_A I^s q^2}} \quad (2.10)$$

The low potential approximation of the one dimensional Poisson-Boltzmann's equation (equation (2.7)) is quite useful however, for higher surface potential ($\psi_o > 80$ mV) the

diffuse layer potential is overestimated. In this case the full one-dimensional equation should be used (Butt 2003).

The surface charge density (σ_d) can be related to the surface potential (ψ_0) through the Grahame equation (2.11), based on the Gouy-Chapman model. Using the linearized one-dimensional Poisson-Boltzmann's equation and the electroneutrality condition (i.e. the total charge, which is the sum of the surface charge density and the double layer charge, must be zero).

$$\sigma_d = \sqrt{8c_0\varepsilon_{el}\varepsilon_0k_BT} \sinh\left(\frac{q\psi_0}{2k_BT}\right) \quad (2.11)$$

which for low potentials ($\sinh x \approx x$) simplifies to

$$\sigma_d = \sqrt{8c_0\varepsilon_{el}\varepsilon_0k_BT} \left(\frac{q\psi_0}{2k_BT}\right) \Leftrightarrow \psi_0 = \frac{2k_BT}{q} \left(\frac{\sigma_d}{\sqrt{8c_0\varepsilon_{el}\varepsilon_0k_BT}}\right) \quad (2.12)$$

$$\sigma_d = \frac{\varepsilon_{el}\varepsilon_0\psi_0}{\lambda_D} \Leftrightarrow \psi_0 = \frac{\sigma_d\lambda_D}{\varepsilon_{el}\varepsilon_0} \quad (2.13)$$

The diffuse double layer capacitance per unit area can thus be defined by the following equation:

$$C_{GC} = \frac{\delta\sigma_d}{\delta\psi_0} = \frac{\varepsilon_{el}\varepsilon_0}{\lambda_D} \quad (2.14)$$

It is similar to a parallel plate capacitor with plate separation equal to the Debye length.

A combination of the previous models was proposed by Stern in 1924. The electrochemical double layer would thus be composed of a compact ionic layer closer to the electrode surface followed by a diffuse layer extended to the bulk of the solution (Figure 2.12). The separation plane between these two regions is called the outer Helmholtz plane (OHP). This distance of closest approach includes the solvation shell that typically forms around ions in aqueous solution and is thus larger than the ionic radius. The region within the OHP is depleted of ionic charges so the charge separation yields a constant capacitance known as the Stern capacitance, which typically has a value around 20 $\mu\text{F}/\text{cm}^2$ (Bousse 1983). Outside the OHP the potential drop will follow the Poisson-Boltzmann's equation. This is equivalent to two capacitors in series, with C_{Stern} representing the compact layer capacitance and C_{GC} representing the Gouy-Chapman diffuse layer capacitance. The total double layer capacitance per unit area (C_{dl}) can be defined by: (Brett 1993, Butt 2003, Shinwari 2007)

$$\frac{1}{C_{dl}} = \frac{1}{C_{Stern}} + \frac{1}{C_{GC}} \quad (2.15)$$

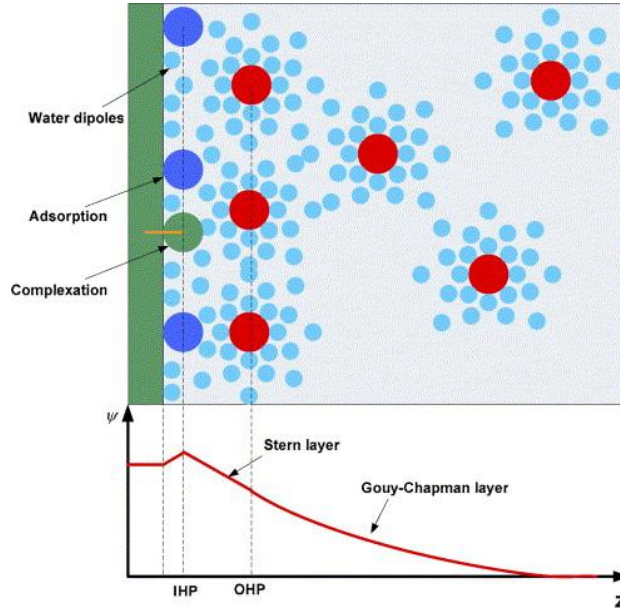


Figure 2.12. The Stern model of the double layer including the ion adsorption effect that defines the IHP introduced by Grahame in 1947. (Shinwari 2007)

Other contributions to the overall electrostatic potential drop can arise from polarization of the solvent, complexation, non-specific and specific adsorption of ions onto the surface; which consists of ions approaching the surface closer than the OHP due to liberation of their solvation shell thus defining the inner Helmholtz plane (IHP). Nonetheless these effects are generally small and can usually be neglected (Shinwari 2007).

2.3.2. Site binding model

The site binding model describes the component of the potential drop that arises from chemical processes at the surface of the insulator. These chemical reactions occur within the OHP because chemical phenomena are limited to molecular distances. The only ionic species that can penetrate the OHP and are present herein are hydrogen and hydroxyl ions, due to their small sizes and lack of solvation shell. (Shinwari 2007; Yates 1974)

Insulator materials that are used as sensitive layers for field-effect sensors are typically oxides; common examples are SiO_2 ; Al_2O_3 ; Ta_2O_5 . The surface of these oxides contains unsatisfied bonds which create a large amount of active sites. These surface sites are

amphoteric, meaning that they can act as proton donors or acceptors. The oxide surface contains sites in three possible forms: neutral (MOH), positively charged (MOH_2^+) or negatively charged (MO^-) as depicted in Figure 2.13.

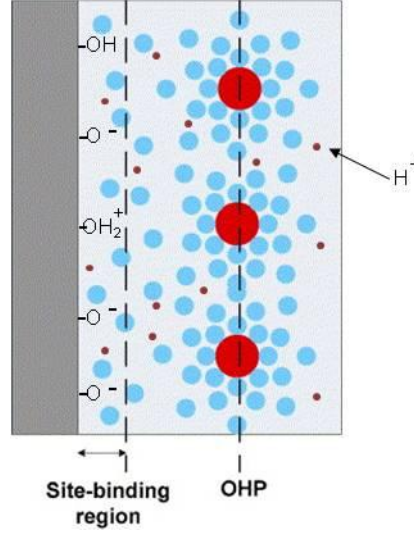
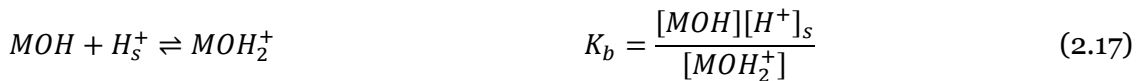
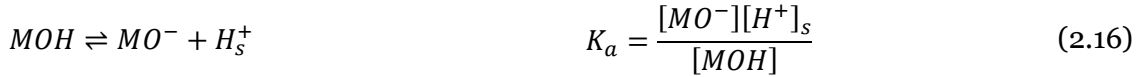


Figure 2.13. Oxide/Electrolyte interface showing the oxide's surface sites and possible reactions. (Shinwari 2007)

The acidic and basic nature of the active surface sites can be described according to the following reactions, with equilibrium constants K_a and K_b .



These reactions are dependent of the surface concentration of protons ($[\text{H}^+]_s$) which can be related to the bulk concentration ($[\text{H}^+]_b$), and hence the pH of the solution, by Boltzmann statistics.

$$[\text{H}^+]_s = [\text{H}^+]_b e^{\frac{-q\psi_0}{k_B T}} \quad (2.18)$$

The total number of surface sites (N_s) is given by

$$N_s = [\text{MOH}_2^+] + [\text{MOH}] + [\text{MO}^-] \quad (2.19)$$

and the total surface charge per unit area (σ_o) is given by

$$\sigma_0 = q([MOH_2^+] - [MO^-]) \quad (2.20)$$

The combination of equations (2.16) to (2.20) provides a relation between the surface potential of the electrolyte (ψ_0), the charge density accumulated on the oxide surface (σ_0) and pH. (Bousse 1983; Shinwari 2007; vanHal 1995 and 1996)

The change in the number of surface charged groups as a result of a small change in proton concentration at the surface is directly related to the oxide's intrinsic buffer capacity, β_{int} .

$$\frac{\delta\sigma_0}{\delta pH_s} = -q \frac{\delta[B]}{\delta pH_s} = -q\beta_{int} \quad (2.21)$$

where $[B]$ is the number of charged groups, defined as $[B] = [MO^-] - [MOH_2^+]$, per unit area.

In the electrolyte side of the double layer an equal but opposite charge ($\sigma_d = -\sigma_0$) is built up, as defined by the Gouy-Chapman-Stern model (equations (2.12)–(2.15)). The ability of the electrolyte solution to adjust the amount of charge stored as a result of a small change in the electrostatic potential is the differential capacitance, C_{dif} .

$$\frac{\delta\sigma_d}{\delta\psi_0} = -\frac{\delta\sigma_0}{\delta\psi_0} = -C_{dif} \quad (2.22)$$

The sensitivity of the electrostatic potential to changes in the pH at the surface is

$$\frac{\delta\psi_0}{\delta pH_s} = \frac{\delta\psi_0}{\delta\sigma_0} \frac{\delta\sigma_0}{\delta pH_s} = -q \frac{\beta_{int}}{C_{dif}} \quad (2.23)$$

which can be related to the bulk pH by the Nernst equation.

$$pH_s = pH_B + \frac{q\psi_0}{2.3k_B T} \quad (2.24)$$

Combining the previous equations leads to a general expression for the sensitivity of the electrostatic potential to changes in the bulk pH.

$$\frac{\delta\psi_0}{\delta pH_B} = -2.3 \frac{k_B T}{q} \alpha \quad (2.25)$$

with

$$\alpha = \left(\frac{2.3k_B T C_{dif}}{q^2 \beta_{int}} + 1 \right)^{-1} \quad (2.26)$$

where α is a dimensionless sensitivity parameter ($0 < \alpha \leq 1$) that depends on the intrinsic buffer capacity of the oxide and the differential double layer capacitance. The differential capacitance value is mainly determined by the ionic concentration of the electrolyte via the Debye length. The intrinsic buffer capacity depends on the number of surface sites (N_s) and on the dissociation constants (K_a and K_b) which are a characteristic of the oxide material. Sensitivity close to the theoretical maximum ($\alpha \cong 1$) can be obtained for a low value of C_{dif} and oxides with high β_{int} (Bergveld 2003; Bousse 1983; vanHal 1995 and 1996)

Another important parameter to characterize the oxide is the pH at which the number of positively and negatively charged surface groups is equal and consequently the net charge on the surface is zero; i.e. the pH at the point of zero charge; pH_{pzc} . An alternative expression to equation (2.25) relating the surface potential to the pH and pH_{pzc} can also be used. (Bergveld 2003; Landheer 2005)

The theoretical maximum sensitivity can be calculated from the Nernst-like equation (equation (2.25)) and corresponds to the potential variation induced by a pH change of one unit ($\Delta pH=1$).

$$\Delta\psi = \frac{2.3k_B T}{q} \Delta pH \quad (2.27)$$

For an ideal sensitive oxide ($\alpha = 1$) at 25 °C, $\Delta\psi = 59.2$ mV/pH which is known as the Nernstian sensitivity.

Summarising; ion sensitive field effect devices, such as EIS and ISFETs, are electronic devices with the possibility of the threshold voltage modulation by means of the oxide/electrolyte interface potential. The difference in applied potential is distributed among various components: the electrolyte/oxide interface potential due to the electrochemical double layer (Gouy-Chapman-Stern model) together with the oxide surface potential (site-binding model); the potential drop through the dielectric; the depletion charge potential drop in the semiconductor and the potential drops due to the electron affinities between the electrolyte and the semiconductor (Figure 2.14).

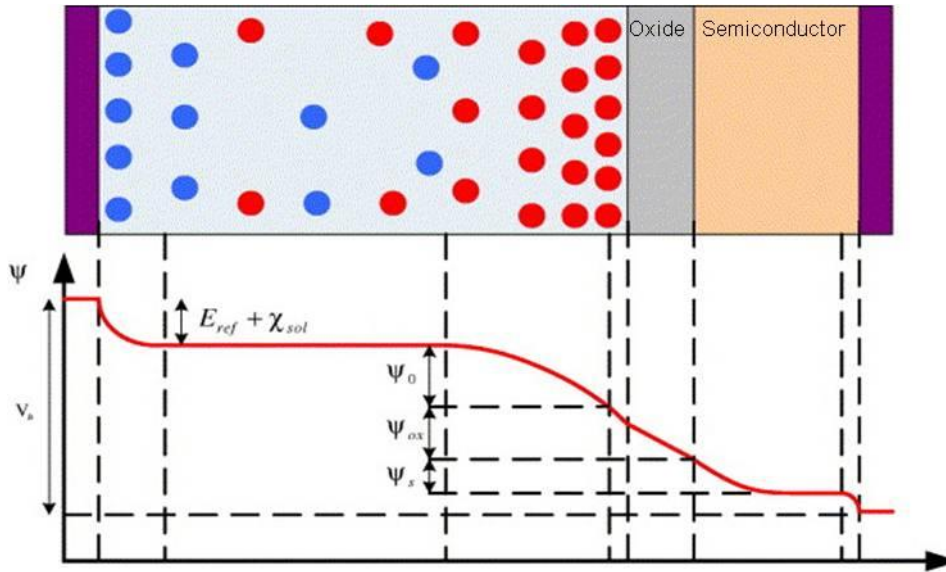


Figure 2.14. Schematic representation of potential drops along the ISFET structure. (Shinwari 2007)

Chemical processes that occur at the electrolyte/oxide interface give rise to a change in ψ_0 which will affect the semiconductor surface potential and thus modulate the devices response. The relation between this interface potential and the pH, hence the pH sensitivity, is mainly determined by the intrinsic buffer capacity of the oxide surface.

2.4. Sensitive layer

The sensitive layer material is a crucial component of the sensor device. As explained by the site-binding model, theoretically, any material with surface amphoteric groups, mainly oxides but also other materials, can act as a sensitive layer for hydrogen ions in solution, hence as pH sensors. However material's properties such as the number of active surface sites, their dissociation constants and the pH of point of zero charge will influence the materials intrinsic buffer capacity and, consequently, the sensitivity.

Historically the first materials studied as pH sensitive surfaces were commonly used field effect transistor gate dielectrics; SiO_2 , Si_3N_4 , Al_2O_3 and Ta_2O_5 (Bergveld 2003). Since then, not only several other oxides but also new materials and material combinations have been pursued as sensitive layers towards pH. An overview of materials applied as pH sensitive layers and their characteristics is given in Table 2.2.

Table 2.2. Overview of materials applied as sensitive layer in field effect based pH sensors.

Material	Production method	Maximum temperature	Device	pH sens.	References
Ta₂O₅	rf sputtering	200 °C	EIS	58 mV/pH	This work
Ta₂O₅	Thermal oxidation	510 °C	EIS	57 mV/pH	Siqueira 2009
SiO₂	Thermal evaporation	300 °C	ISFET	46 mV/pH	Gotoh 1989
SiO₂	Thermal oxidation	1000 °C	EIS	37 mV/pH 32 mV/pH	Abouzar 2011 This work
Si₃N₄	PECVD	unknown	ISFET	54 mV/pH	Estrela 2005
Al₂O₃	ALD	450 °C	EIS	54.9 mV/pH	Oh 2012
HfO₂	rf sputtering	unknown	EIS	51.2 mV/pH	Lu 2010
SnO₂	rf sputtering	unknown	SEGFET	56 mV/pH	Chi 2000a
TiO₂	rf sputtering	500 °C	ISFET	56.2 mV/pH	Chou 2005
WO₃	rf sputtering	unknown	ISFET	45 mV/pH	Chiang 2001
ZnO	Sol-gel	150 °C	SEGFET	38 mV/pH	Batista 2005
Y₂O₃	rf sputtering	800 °C	EIS	56 mV/pH	Pan 2007
Er₂O₃	rf sputtering	700 °C	EIS	57.6 mV/pH	Pan 2009a
Sm₂O₃	rf sputtering	700 °C	EIS	56.2 mV/pH	Wu 2009
Pr₂O₃	rf sputtering	900 °C	EIS	53 mV/pH	Pan 2008
PrTiO₃	rf sputtering	800 °C	EIS	56.8 mV/pH	Pan 2008
HoTiO₃	rf sputtering	900 °C	EIS	59.5 mV/pH	Pan 2009b
NdTiO₅	rf sputtering	800 °C	EIS	57 mV/pH	Pan 2009c
Eu₂Ti₂O₇	rf sputtering	900 °C	EIS	59 mV/pH	Pan 2011
nc-Diamond	MPCVD	840 °C	SEGFET	45 mV/pH	Song 2006
nc-Diamond	PECVD	490 °C	EIS	40-45 mV/pH	Abouzar 2008

nc-Diamond: nanocrystalline diamond; SEGFET: separated extended gate field effect transistor; PECVD: plasma enhanced chemical vapour deposition; ALD: atomic layer deposition; MPCVD: microwave plasma-assisted chemical vapour deposition.

Amongst the commonly used dielectric oxides, Ta_2O_5 has the largest buffer capacity due to the large number of active surface sites. Theoretical calculations predict a value of the sensitivity parameter above 0.98 over a broad pH range and for varied electrolyte concentration; consequently near-Nernstian sensitivity is expected and has been demonstrated (vanHal 1995; Bergveld 2003).

The development of tantalum pentoxide films for application in electronic devices was motivated by the pursuit of high permittivity (high-k) dielectrics that allowed the scaling down of silicon integrated circuits. In single crystalline silicon technology the mainly used dielectric is thermal SiO_2 which forms the almost perfect interface; Si/ SiO_2 . However the demand for miniaturization requires the reduction of dielectric thickness beyond the physical limit for SiO_2 . High-k dielectrics provide an alternative as, since these possess a higher dielectric constant than SiO_2 , thicker films can be used while maintaining the capacitance per unit area (Chaneliere 1998; Sze 2007). This is also relevant in the geometrical scaling of BioFEDs (Shinwari 2007).

Several deposition methods, both chemical and physical, can be used to produce thin films of high-k materials, including Ta_2O_5 . Chemical based deposition methods include metal-organic chemical vapor deposition (MOCVD); atomic layer deposition (ALD) and solution based methods. MOCVD is widely used in microelectronics fabrication and requires the use of gaseous metal-organic precursors that are thermally decomposed to yield dense and good quality films of the material; however the precursors can be toxic and dangerous and decomposition temperatures above 400 °C are usually needed (Porporati 2003; Briand 2005). ALD is dominantly influenced by the surface chemistry as evaporated precursors are carried into the reactor by an inert gas and allowed to adsorb to the substrate surface. The solid film grows layer-by-layer via successive surface reaction cycles resulting in controlled thickness and good quality films; however the process depends on the use of fairly high substrate temperature (>300 °C) (Kim 2009; Kukli 2000 and 2002). Solution based methods, such as sol-gel, have the advantage of being simple and not requiring complex equipment however reproducibility and quality films are difficult to obtain and high temperature annealing is needed to remove the organic precursors (Cappellani 1999; Ozer 1997; Yildirim 2005).

Physical methods include: thermal evaporation and sputtering. Thermal evaporation of a metal layer followed by thermal oxidation can lead to good quality films but a high production temperature is needed (Lee 2005; Poghosian 2007). Sputtering techniques such as radio frequency (rf) magnetron sputtering is perfectly suited for low temperature fabrication however dielectric materials are hard to sputter requiring high

power density that might damage the growing film and interfaces. Nevertheless this deposition technique allows for quality films of a variety of materials to be obtained at room temperature being compatible with low-cost and disposable substrates (Atanassova 2010; Dimitrova 1998; Jagadeesh 2010; Pai 2008; Paskaleva 2000; Pereira 2008). For these reasons rf magnetron sputtering was chosen as the deposition technique for semiconductor oxide based ion sensitive field effect transistors (ISFETs) and for Ta₂O₅ thin films applied as a sensitive layer in field effect based sensor devices; EIS and ISFETs.

The production process and processing conditions influence the film's properties (Pai 2008), so understanding how pH sensitivity and sensor performance is dependent on these factors is of great importance.

2.5. Field effect biosensors (BioFEDs)

The combination of a biological layer with a field effect-based electronic device leads to bio-selectivity and specificity; yielding a powerful tool – a BioFED.

The development of microelectronics technology has stimulated the fabrication of miniaturised analytical systems such as lab-on-chip sensors and micro total analysis systems. The application of field effect devices as transducers is very attractive as these provide numerous advantages: small dimensions, fast response, possibility of integration into biosensor arrays and the possibility of low-cost mass production. Moreover, the versatility of these devices to biological functionalization allows the possibility to fabricate a sensor array for simultaneous multi-parameter analysis and thus a portable device for medical and environmental monitoring can be envisioned.

In the 40 years since the introduction of the ISFET (Bergveld 1970) research on these devices and their applications has significantly grown. A diversity of BioFEDs with variations in the device structure and operation conditions, sensitive layer composition, biological functionalization methods and biological target of detection, have been developed (Bergveld 2003; Lee 2009; Schoning 2002 and 2006).

A summarised view of some of the most relevant historical milestones in the development of BioFEDs is given in Table 2.3.

Table 2.3. Relevant historical milestones in the development of BioFEDs. (adapted from Schoning 2002)

Year	BioFEDs development milestone
1970	Concept of an ISFET, first ISFET-based neurophysiological measurements
1976	Concept of the first BioFED (EnFED)
1980	First realised EnFED
1980	Concept of an ImmunoFED
1981	Coupling cells with a MOSFET
1981	First neuron-transistor (CellFED)
1989	First a-Si:H-based ISFET (Gotoh, Oda et al.)
1992	First commercial ISFET pH sensor (DuraFET, Honeywell)
1997	'Beetle/chip' BioFED
1997	First experimental attempt of direct DNA-hybridization detection
2005	First polySi-based EG-ISFET (Yan, Estrela et al.)
2011	Label-free DNA amplification monitoring with EIS sensor (Branquinho et al.)
2011	Label-free DNA genome sequencing detection with ISFETs (Rothberg et al.)
2012	First oxide semiconductor-based EG-ISFET (Pinto, Branquinho et al.)

EG-ISFET: extended gate ISFET.

Over 25 years of research were needed for the successful detection of a DNA hybridization event and another 15 years for its development into technology applied in label-free DNA sequencing of genomes (Rothberg 2011).

BioFEDs can be classified according to the biorecognition element that is used for detection: chemically-modified FEDs (ChemFEDs); immunologically modified FEDs (ImmunoFEDs); cell-based FEDs (CellFEDs); enzyme-modified FEDs (EnFEDs); DNA modified FEDs (DNAFEDs).

2.5.1. Chemically-modified FEDs (ChemFEDs)

The most simple ion sensitive field effect device is applied to hydrogen ion detection, hence pH, as typical gate insulator materials possess active surface sites that can react with protons. However field effect devices that are selectively sensitive to other ions can be obtained by additional modification of the insulator surface. These sensors are referred to as chemically-sensitive field effect devices; ChemFEDs.

ChemFEDs can be obtained by modifying the gate material or depositing an ion selective membrane onto the gate, in a similar way to the development of ion-selective electrodes (ISE) from the glass pH electrode. The small size, fast response, robustness, easiness of storage and cleaning and the possibility of mass production are the main advantages of ChemFEDs over conventional ISEs (Jimenez-Jorquera 2010; Shoning 2002)

Initially heterogeneous membranes of silver halides and membranes based on polyvinyl chloride (PVC) were used in the development of ChemFEDs, exploiting the same technology developed for ISEs. New materials such as photo-cured polymers (polysiloxanes, polyurethanes and other methacrylate derived polymers), which are compatible with photolithographic techniques, were later explored and demonstrated higher performances regarding reproducibility and long-term stability compared with PVC membranes (Abramova 2009; Jimenez-Jorquera 2010).

ChemFEDs have been reported for the determination of several ions of biological interest such as Na^+ , K^+ , Ca^{2+} , Cl^- , F^- and NO_3^- (Beging 2010; Bratov 2000 and 2004; Jimenez-Jorquera 2010; Mourzina 2003; Shoning 2002) and recently ‘electronic tongues’; a multi-sensor array based on ChemFEDs with polymeric photo-curable membranes deposited onto their gates was developed for mineral water monitoring by the simultaneous detection of K^+ , Na^+ , Ca^{2+} and Cl^- (Moreno 2006) and K^+ , Na^+ and Cl^- (Abramova 2009a; Ipatov 2008). The majority of these ionic based FEDs are applied to environmental and clinical analysis.

2.5.2. Immunologically modified FEDs (ImmunoFEDs)

An immunologically modified field effect device (ImmunoFED) can be obtained by the functionalization of the gate insulator with an antibody layer (Figure 2.15). In the presence of the specific antigen an antibody-antigen complex would be formed causing charge variations that could, in principle, be detected by the FED. The antibody-antigen interaction can be useful for monitoring the human immune system and therefore these sensors are of great interest as clinical diagnostic tools (Colapicchioni 1991, Schoning 2002).

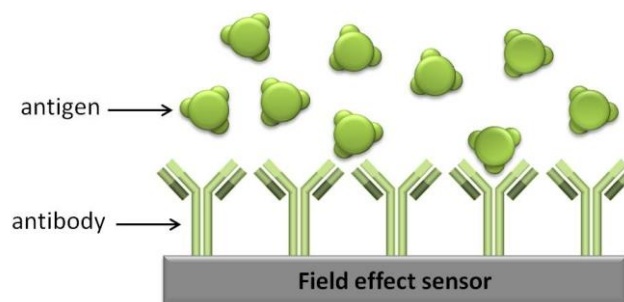


Figure 2.15. Schematic representation of an immunologically modified sensor (ImmunoFED).

However the practical realization of such ImmunoFEDs has proven difficult so their development has suffered some drawbacks. Mainly two factors have contributed to this; i) these are very large molecules thus the majority of its structure, including the specific binding antigen site, would lie too far from the sensor surface to allow charge variation detection; ii) the immobilization of 'vertically' aligned antibodies is highly unlikely and in the antibody layer conformational constraints are bound to occur. As the specificity of antibody-antigen interaction also relies on their conformational structure, obtaining a reliable measurable signal would be very difficult (Bergveld 1991; Schoning 2002).

Nevertheless recent efforts towards the improvement of the antibody layer functionalization onto the sensing surface and the device itself have led to signal increase and possibly to a renewed interest in these BioFEDs (Casal 2012; Eteshola 2008; Tlili 2005).

2.5.3. Cell-based FEDs (CellFEDs)

The combination of field effect devices, usually ISFETs, with whole cells that act as the recognition element has led to cell-based BioFEDs or CellFEDs (Figure 2.16). These devices have been used for both cell metabolism detection and extracellular potential measurement (Baumann 1999; Lee 2009; Schoning 2002 and 2006).

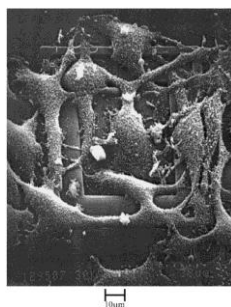


Figure 2.16. SEM image of cells on an ISFET sensor (Baumann 1999).

The monitorization of cell metabolism can involve several parameters such as extracellular pH, concentration of ions, oxygen consumption, CO₂ production and redox potentials. As cells are living microstructures they are capable of providing a direct response to external physical or chemical stimulus. A direct measurement of the cell's response to these stimuli can be extremely important in cell biology, drug screening, toxicology and clinical diagnostics. ISFET arrays have been applied to the monitoring of cell metabolism by measuring cellular acidification and respiration through pH and CO₂ based sensors. (Baumann 1999; Fanigliulo 1996; Gustavsson 2008; Lehmann 2000; Lorenzelli 2003; Mohri 2006). A solid-state multi-parameter sensor system for cell-culture monitoring comprising a Ta₂O₅-based EIS pH sensor that can be sterilised has been reported (Backer 2009). Also, following in the steps of the initial application of ISFETs the real time, non-invasive in-vitro monitoring of the physiological state of a cell population and study of the electrical activity of neurons and their response to electrical stimuli has been reported (Martinoia 2001 and 2004; Poghosian 2009).

2.5.4. Enzyme-modified FEDs (EnFEDs)

The concept of combining the specific biocatalytic capabilities of enzymes with field effect devices was first proposed by Janata and Moss in 1976 (Janata 1976). Only after four years the first results on the application of an enzyme-modified ISFET (EnFET) for the detection of penicillin were presented by Caras and Janata (Caras 1980). Since then many research and development has been done and a wide range of EnFEDs differing in sensor design and/or gate material have been constructed with a large variety of enzymes that allow the detection of numerous analytes.

EnFEDs have applications in several areas of interest: environmental monitoring of wastewater and pollutants (Jimenez-Jorquera 2010; Flores 2003; Turek 2008); food quality control (Gaudin 2001; Liu 1998) and monitoring of clinical relevant parameters such as urea and glucose (Chen 2003; Schoning 2002).

Generally, EnFEDs are based on the principle of pH sensitive FEDs so that theoretically these can be constructed with any enzyme that upon reaction with the analyte induces a local change of pH. When the enzymatic reaction takes place the underlying pH sensitive transducer measures the local change of pH (Figure 2.17), which can be directly correlated with the concentration of analyte in solution (Dzyadevych 2007; Estrela 2007a; Lee 2009; Schoning 2002 and 2006).

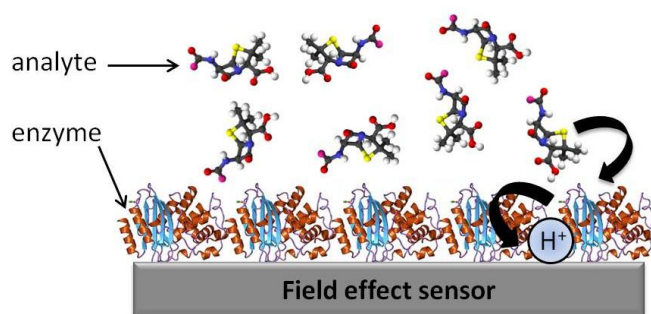


Figure 2.17. Schematic representation of an enzyme functionalized sensor (EnFED).

The most preferred enzymes for EnFEDs construction are penicillinase, urease and glucose oxidase due to their suitability as model systems for EnFED studies and to the importance of detecting penicillin, urea and glucose in many fields of application. However several other enzymes/analytes have been reported (Schoning 2002). An overview of developed EnFEDs, regarding both the enzyme and the analyte detected, is given in Table 2.4.

Table 2.4. Overview of developed EnFEDs including the enzyme used and the analyte detected. Adapted from (Dzyadevych 2006; Schoning 2002)

Analyte tested	Enzyme	References
Penicillin	Penicillinase	Abouzar 2008; Caras 1980; Estrela 2007b; Liu 1998; Poghossian 2000 and 2001; Siqueira 2009; Turek 2008
Urea	Urease	Chen 2003; Hamlaoui 2002; Lue 2011; Melo 2003; Pan 2009; Sant 2011
Glucose	Glucose oxidase	Khanna 2006; Luo 2004; Pan 2009b; Park 2002;
Acetylcholine	Acetylcholinesterase	Chi 2000; Kharitonov 2000
Hypochlorite		Dzyadevych 2001
Organophosphorous Pesticides		Flores 2003
Organophosphorous Pesticides	Organophosphorous hydrolise	Schoning 2003; Turek 2008
Cyanide	Cyanidase	Turek 2007
Lactic acid	Lactate dehydrogenase	Kharitonov 2001; Zayats 2000

An important part of the EnFED construction relies on the attachment of the enzyme layer to the device's sensitive surface. Different immobilization methods can be employed for EnFEDs fabrication, the most common being physical adsorption, covalent immobilization and entrapment. Each method has advantages and drawbacks and usually the choice of immobilization method depends of the final application of the sensor. Covalent immobilization and entrapment methods provide higher reproducibility and stability as the enzymes are attached to the surface however they are cumbersome and costly. The most frequently used is physical adsorption as it is simple (no additional reagents are required) and provides an enzyme layer directly on the sensitive surface (favoring pH detection) with diminute enzyme activity loss (no tridimensional constrains) (Schoning 2002; Subramanian 1999).

The practical application of EnFEDs suffers from some limitations related not only to the semiconductor device itself but mainly to the dependence of the sensor's response on the samples characteristics such as, buffer capacity, ionic strength and pH of the medium; which can affect the enzyme kinetics and possibly to enzyme inhibition due to significant pH changes (Dzyadevych 2006). The relatively slow response and recovery times, the operation and storage stability, the dependence on the enzyme immobilization methods and reproducibility, are other factors that contribute to the slow commercial development and limit their practical use (Lee 2009; Schoning 2006).

In order to improve the working characteristics of EnFEDs and overcome these drawbacks some solutions have been proposed, such as the application of polymeric membranes for enzyme immobilization and to control the analyte and product diffusion (Flores 2003; Jimenez-Jorquera 2010; Turek 2007); the use of magnetic nanoparticles to improve enzyme immobilization (Vijayalakshmi 2008) and the use of thin enzyme layers that lowers the diffusion barrier for analyte penetration to the active sites thus reducing the sensor's response time (Kharitonov 2000). Besides this a differential pH FED/EnFED can be very advantageous. The pH FED is identical to the EnFED without the enzymatic layer and in this way it can act as a reference system. This allows minimization of some disturbing effects that can arise; such as pH and temperature variations and sensor signal drift (Dzyadevych 2006; Poghosian 2001a; Sant 2011; Schoning 2006; Turek 2007).

The many efforts towards EnFEDs development and improvement have not yet led to a commercial version of such a device; however the fact that ISFEDs for pH detection are already commercially available, it is fairly predictable that EnFEDs will eventually be to (Dzyadevych 2006; Schoning 2002).

2.5.5. DNA modified FEDs (DNAFEDs)

Molecular diagnostics based on DNA detection have applications in various fields such as pathogen identification, drug screening and diagnosis of genetic diseases. Moreover DNA diagnostics allow access to genetic information that distinguishes one individual's genome from another's, which can provide individual oriented insights on pre-disposition or susceptibility for particular diseases or even the most effective drug regimen for each individual (Fritz 2002; Ghosh 2006).

Conventionally used optical methods for DNA detection are generally based on the determination of fluorescent labels. Although being well established and demonstrating high sensitivity and low detection limits, these methods are expensive, cumbersome, and complex to implement. The development of sensors and new methodologies that provide a fast, simple and cost-effective detection of DNA are thus highly desirable (Drummond 2003; McKinnon 2009; Shinwari 2007).

Field effect based devices can be used in the label free detection of biomolecules, such as DNA and proteins, by their intrinsic molecular charge; consequently considerable research efforts have been invested towards the development of such sensors (Abouzar 2012; Shinwari 2007; Schoning 2006).

The majority of DNA detection techniques, including field effect detection, are based on a DNA hybridization process. Hybridization allows the specific recognition of DNA molecules due to the property of single stranded DNA (ssDNA) to specifically bind to a complementary molecule (target) to form double-stranded DNA (dsDNA). The unique complementary nature of the base pairing, *i.e.* adenosine-thymine (A-T) and cytosine-guanine (C-G) as determined by Watson and Crick (1953), is the basis for the extremely high specificity of the biorecognition process (Ghosh 2006; Schoning 2002).

DNAFEDs for hybridization detection can be constructed by immobilizing specific single stranded DNA molecules (probes) onto the sensor's surface (Figure 2.18). When the sensor is exposed to a solution containing a complementary target DNA the hybridization event can be converted to a measurable signal. The detection mechanism is based on the fact that DNA is an intrinsically charged molecule and when hybridization occurs, the charge density increase near the sensor's surface can modulate the devices response.

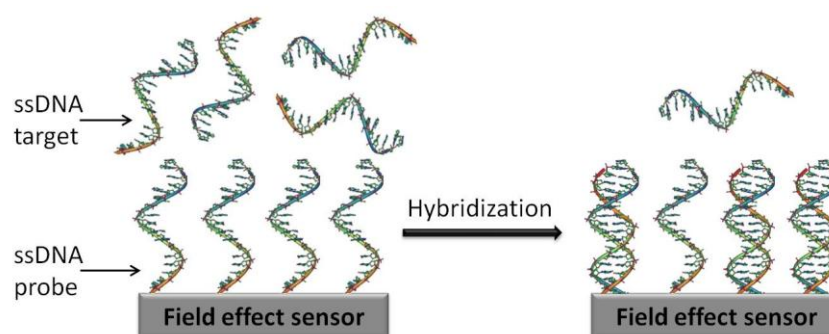


Figure 2.18. Schematic representation of a DNA functionalized sensor (DNAFED).

As for EnFEDs the immobilization of the biolayer; in this case ssDNA probes; onto the sensor's surface is an important factor in sensor fabrication (Shinwari 2007). Direct functionalization by covalent attachment of a self-assembled monolayer (SAM) of DNA probes to the sensor surface (either gold or oxide based) appears to be the preferred method. For oxide based sensitive layers silanization is usually performed with APTES (3-amino-propyltriethoxysilane) followed by DNA probe immobilization via the APTES amino groups (Gonçalves 2008; Han 2006; Lillis 2007; Souteyrand 1997). For gold based sensitive layers thiol-modified DNA probes are used and SAM formation occurs via Au-S bond (Estrela 2005). The DNA probe density on the sensitive area is also a relevant factor. Although in principle a higher probe density would result in a higher amount of hybridized charge and enhanced sensor signal; a decrease in hybridization efficiency can occur due to electrostatic repulsions if the probe density is too high (Keighley 2008).

The electrostatic immobilization of probe DNA on a layer of positively charged molecules, such as poly-L-lysine, for the detection of DNA hybridization has also been described (Bandiera 2007; Fritz 2002 ; Lin 2010). Actually the field effect detection of other charged molecules and of the layer-by-layer deposition of polyelectrolytes positive and negatively charged has been applied as a model system for the study and understanding of the complex intrinsic charge based detection mechanism (Abouzar 2011; Poghossian 2007; Uslu 2004).

Reported results on the field effect detection of DNA, although very exciting, are very diverse which leads to the conclusion that the detection mechanism cannot be solely attributed to a direct electrostatic detection of charged biomolecules by their intrinsic molecular charge (Poghossian 2005; Schoning 2006). Recently published theoretical models propose that other factors also contribute to the experimentally observed signal generation: i) the redistribution of ionic concentration in the intermolecular spaces induced upon hybridization and/or ii) the alteration of the ion sensitivity of the

transducer caused by the hybridization (Abouzar 2012; Landheer 2005 and 2008; McKinnon 2009; Poghosian 2005 and 2007; Wunderlich 2007).

Interesting recent achievements in hybridization based DNAFEDs include the detection of single nucleotide polymorphisms (SNP). Ingebrandt et al (2007) reported SPN detection in 20 base pair DNA samples using p-Si FET microarrays with SiO₂ sensitive layer in a differential ac readout concept that minimizes drift issues. Also Purushothaman et al (2006) reported on the pH based detection of single nucleotide insertion reaction with a commercial ISFET (Sentron Europe BV). More recently DNAFEDs have been applied in the label-free DNA sequencing of genomes (Rothberg 2011) and subsequent application of this technology to a commercially available DNA sequencing equipment – IonTorrent™ (<http://www.iontorrent.com/>).

The sequencing detection mechanism is based on the fact that the incorporation of a nucleotide into a strand of DNA by a polymerase releases a hydrogen ion as a by-product; resulting in a local pH variation that can be detected by the underlying ISFET sensor and converted to a measurable signal. The IonTorrent is similar to standard high-density array fluorescence-based DNA sequencing equipments; however, in the IonTorrent, the ISFET directly detects the sequencing event thus eliminating the need for fluorescent labels and complex optical detection methods and equipments.

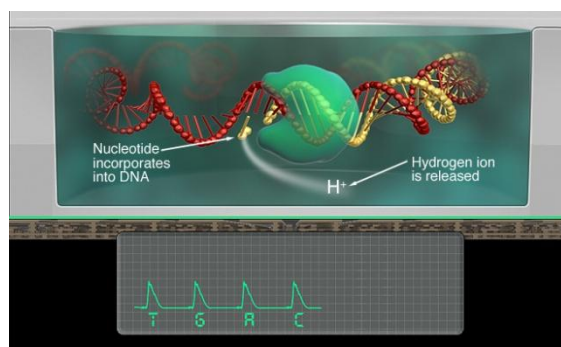


Figure 2.19. IonTorrent™ ISFET-based DNA sequencing equipment: schematic representation of the pH-based sensing mechanism. From (<http://www.iontorrent.com/>)

Chapter 3. Device fabrication and characterization techniques

3.1. Fabrication of field effect devices (FEDs).....	47
3.1.1. Electrolyte-insulator-semiconductor devices (EIS)	47
3.1.2. Ion sensitive field effect transistors (ISFET)	48
3.2. Device fabrication techniques	49
3.2.1. Thin film deposition	49
3.2.2. Photolithographic patterning	53
3.3. Post-deposition processes	55
3.3.1. Influence of annealing temperature.....	55
3.3.2. Influence of plasma surface treatments.....	56
3.4. Thin film characterization techniques	56
3.4.1. Structural, morphological and compositional characterization	57
3.4.2. Optical characterization.....	60
3.4.3. Contact angle measurements.....	63
3.5. Characterization of field effect devices (FEDs)	64
3.5.1. Impedance Spectroscopy (IS).....	64
3.5.2. Static current-voltage characteristics	68

Chapter 3. Device fabrication and characterization

The research work summarized in this dissertation involved the production and characterization of thin films and devices. The fabrication of the devices was performed in the clean room facilities of CEMOP and characterization was performed in the CENIMAT and CEMOP laboratory resources. This chapter describes relevant techniques used for that end. Regarding thin film deposition techniques, the main focus is given to sputtering, as it was selected to produce all the tantalum pentoxide sensitive layers for EIS and ISFET sensors and also semiconductors and high- κ dielectric layers of ISFETs. Conventional patterning techniques are also briefly discussed, as they were required for the production of ISFETs. Characterization techniques aiming the analysis of a broad range of materials and devices' properties are also covered in this chapter, with special relevance being given to electrochemical characterization.

3.1. Fabrication of field effect devices (FEDs)

The fabrication of field effect devices relies on a series of steps depending on the device's structure. A brief description of the production process and techniques used is provided in the following sections.

3.1.1. *Electrolyte-insulator-semiconductor devices (EIS)*

As described in Chapter 2, the structure of EIS devices is similar to a metal-insulator-semiconductor (MIS) capacitor where the metal gate electrode is replaced by an electrolyte solution. The fabrication of EIS sensors is quite simple, only requiring the deposition of a metal back-contact and the insulator sensitive layer as these were fabricated on p-type crystalline Si substrates (commercial wafers from HP, with 100 nm of thermally grown SiO_2 on both sides). A schematic representation of the EIS sensors production steps is depicted in Figure 3.1.

First, the aluminium back-contact (200 nm) was deposited by e-beam evaporation after etching of the SiO_2 on the wafer's rear side with buffered HF solution. Afterwards, the Ta_2O_5 sensitive layer (100 nm) was deposited by rf sputtering onto the thermal SiO_2 *.

* The importance of the SiO_2 insulator layer is discussed in the next chapter, *Section 4.1.3*.

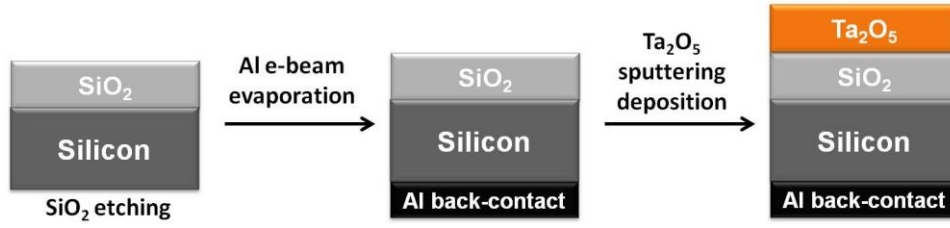


Figure 3.1. Schematic representation of the EIS sensors production steps.

The rf sputtering deposition parameters (rf power, pressure and $\text{Ar}:\text{O}_2$ gases ratio) were varied to study their influence on pH sensitivity of Ta_2O_5 . The thin film's thickness was verified either with spectroscopic ellipsometry or profilometry measurements.

3.1.2. Ion sensitive field effect transistors (ISFET)

The fabrication process of ISFET sensors is more complex than that of EIS sensors, as these require the deposition and patterning of several layers. The ISFET devices production followed the experience of the microelectronics and optoelectronics research group on the development of semiconductor oxides based TFTs (Barquinha 2010a). The devices were produced on glass substrates in a bottom gate configuration, as such the layer's production steps sequence is: metal gate electrode; multi-layered dielectric; semiconductor oxide; source and drain metal electrodes; Ta_2O_5 sensitive layer; passivation. Prior to each thin film deposition, patterning of each layer was performed by photolithography and lift-off techniques. A schematic representation of ISFET sensors deposition steps sequence is depicted in Figure 3.2.

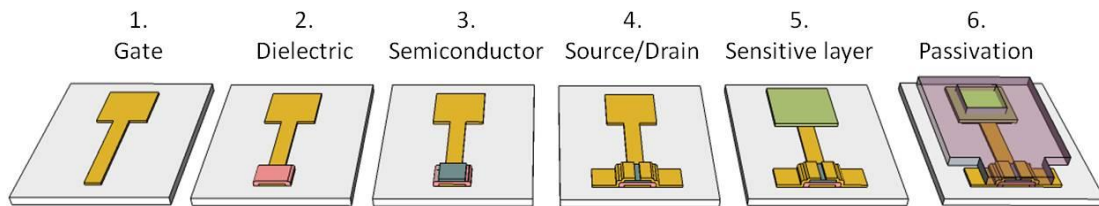


Figure 3.2. Schematic representation of ISFET sensors deposition steps sequence.

Generally, metal electrodes were deposited by e-beam evaporation, all other layers were produced by rf sputtering and passivation layer was either SU-8 deposited by spin-coating or PDMS. Details on each layer are given in Table 3.1.

Table 3.1. Production details of each of the ISFET sensors layers.

Layer	Composition	rf power (W)	Thickness (nm)
Gate, source and drain electrodes	Ti/Au	–	10/70
Semiconductor	GIZO (GIZO 1:2:1 target)	100	25-30
Dielectric	Ta ₂ O ₅ :SiO ₂ (co-sputtering)	100:150	350
Sensitive layer	Ta ₂ O ₅	150	100

* rf sputtered layers were deposited with 14:1 sccm Ar:O₂ ratio and 0.3 Pa deposition pressure.

ISFET devices were also fabricated on commercial glass/ITO/ATO substrates (Planar Systems Inc.), where indium tin oxide (ITO), being conductive, serves as a common gate electrode and ATO, aluminium oxide-titanium oxide multi-layer, is the dielectric; and commercial Si/SiO₂ substrates (HP, Dublin), where the highly doped silicon acts as a common gate electrode and SiO₂ as the dielectric layer. The remaining layers were produced with the previously described conditions (Table 3.1).

3.2. Device fabrication techniques

3.2.1. Thin film deposition

A variety of deposition techniques can be used to fabricate thin films. In this research work sputtering was used as the main technique. Additional techniques, such as electron-beam evaporation and spin coating, were used to deposit electrodes and passivation layers, being also briefly described herein.

3.2.1.1. Magnetron sputtering

Sputtering is a physical vapour deposition (PVD) technique where atoms or molecules are physically removed from a source material (target) and transported through vacuum to a substrate, forming a thin film. It is a well established and versatile deposition technique for a wide range of applications providing several advantages, such as low substrate temperatures, good film thickness and composition control, high film density, possibility to deposit a broad range of materials (either by using different

target compositions, a reactive gas or simultaneous sputtering from two or more target sources; co-sputtering) and scalability to large areas (Hartnagel 1995; Madou 2002).

Essentially, sputtering consists on ejecting atoms from the surface of the target as a result of collisions and momentum transfer from highly energetic ions that are created due to ionization of gaseous species. The sputtered species are directed through vacuum to a substrate by an electric field (Barquinha 2010a; Wasa 2004). To generate the electric field, the target is placed on the cathode and connected to an external excitation source, which in this case is a rf generator. The anode is generally grounded and consists of the whole vacuum chamber and the substrate. Since the target area is much smaller than the grounded anode, and given the lower mass of electrons relatively to ions, a self-biased dc voltage emerges in the target; creating the conditions for sputtering to occur (Wasa 2004). The highly energetic species needed for target bombardment are obtained by ionization of an inert gas, typically argon due to its low cost and high impact section.

In magnetron sputtering (Figure 3.3) the plasma is confined to a region close the target surface by a magnetic field, which is created due to strong magnets placed behind the target. This simultaneously reduces the substrate bombardment by electrons and increases the probability of ionization of neutral gaseous molecules, which is traduced in higher sputtering and growth rates (Wasa 2004). A disadvantage of magnetron sputtering systems is the poor target utilization, since material from the path defined by the magnetic field is preferentially sputtered.

Thin films can also be deposited by using a reactive gas inside the system, in addition to the inert gas. This process is known as reactive sputtering and is widely used to produce different materials, such as oxides or nitrides by using oxygen or nitrogen, respectively (Wasa 2004). Even if the deposition is performed from ceramic targets that already possess the desired thin film composition, reactive sputtering is useful to control film's stoichiometry. However, high concentrations of reactive gases can induce re-sputtering effects on the substrate due to the incidence of negative ions, which is particularly relevant for oxygen given its high electronegativity (Barquinha 2010a; Song 2009).

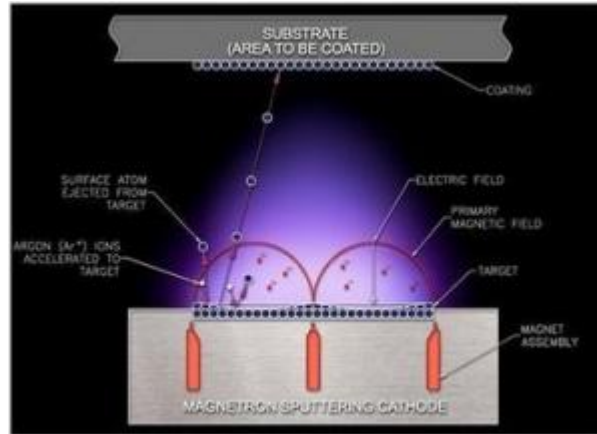


Figure 3.3. Schematic representation of the magnetron sputtering deposition process (Web02).

The rf magnetron sputtering system used in this work is an AJA ATC-1300F (Figure 3.4-left). It can be almost totally computer-controlled and provides the possibility of biasing the substrate with a rf signal; which was applied for post-deposition surface plasma treatments (Ar or O₂) of EIS sensors (described in *Section 3.3.2* and discussed in the next chapter *Section 4.3.2*). The AJA system is equipped with a load-lock chamber for sample introduction/removal, so very low base pressures are achieved in the main chamber ($p \leq 0.05$ mPa). Target-to-substrate distance was fixed at 10 cm and, during the deposition the substrate is kept rotating to allow for uniformity enhanced on the resulting thin film and no intentional substrate heating was applied. The system has three magnetrons (Figure 3.4-right) allowing co-sputtering and subsequent production of multicomponent materials; such as the dielectric layer of ISFET devices.

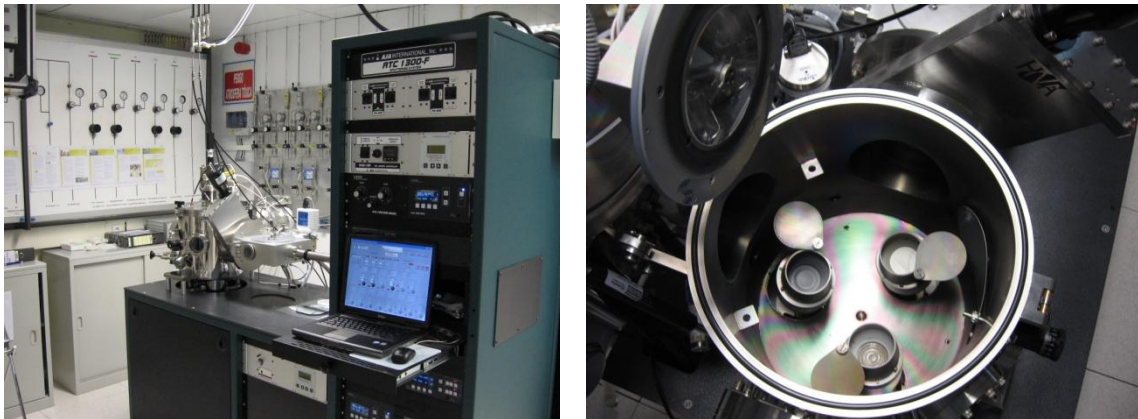


Figure 3.4. AJA ATC-1300F sputtering system used for the deposition of dielectrics (left) and detail of the main chamber (right), showing the magnetrons' configuration.

The studied tantalum oxide thin films were produced from a 2 inch (5.08 cm) Ta₂O₅ ceramic target (99.99% purity from SCM) and deposited on silicon wafers with thickness around 100 nm. Prior to deposition, pre-sputtering (sputtering with the shutter closed to prevent deposition) was performed for 10 min to assure thin film reproducibility. The rf sputtering deposition parameters were varied to study their influence on pH sensitivity of Ta₂O₅. For that deposition pressure between 0.2 and 1 Pa, deposition gases ratio (Ar:O₂) between 14.5:0.5 and 12:3, and rf power density between 100 and 200 W were used.

Deposition of the Ta₂O₅ thin film directly on Si (after etching both sides of the wafer) or glass substrates was also performed for characterization purposes.

3.2.1.2. Electron-beam evaporation

Physical evaporation is one of the most widely used methods to deposit metal thin films. This deposition technique consists essentially on heating a material up to its vaporization point, allowing the deposition of the evaporated molecules onto a substrate placed close to the source material. The heating process is performed under high vacuum in order to increase the mean free path of vaporized molecules and reduce contamination of the deposited thin films. Electron-beam evaporation uses a highly energetic electron beam as a heating source. As such, only the specific region of the material being evaporated is heated, allowing the deposition of materials with higher melting points. The source material is placed in a water-cooled crucible and the electron beam is deflected towards the surface of the source material by a magnetic field (Madou 2002).

Electron-beam evaporation was used in this research work to deposit aluminium back-contact (200 nm) in EIS devices and Ti/Au (10/70 nm) metal electrodes in ISFETs. The depositions were performed with a base pressure below 0.7 mPa. The depositions were performed using a home-made system existent in the clean room facilities of CENIMAT/CEMOP:I3N.

3.2.1.3. Spin-coating

Spin-coating can be used for to produce thin films and unlike sputtering or electron-beam evaporation it is a non-vacuum process; requiring a very simple equipment. The process is typically initiated by dropping an excess amount of a liquid precursor onto a substrate. The substrate is vacuum held to a chuck, which is then rotated at high speed (typically above 1000 rpm) to spread the liquid precursor over the entire substrate, forming a thin film which thickness is determined not only by the deposition parameters such as rotation speed and acceleration but also by the properties of the liquid precursor itself (viscosity, drying rate, surface tension). Afterwards the substrate is heated on a hot-plate or oven to remove the solvent (Madou 2002).

In this work spin-coating was used to deposit positive photoresist layers for photolithographic processes (Section 3.2.2) and also to deposit the SU-8 epoxy based negative resist used as a passivation layer in ISFETs. Positive photoresist was deposited using an initial rotation speed of 3000 rpm (10 s) that is increased to 4000 rpm (20 s), with a Headway Research PWM32 system existent in CENIMAT/CEMOP:I3N. A different spinner, KarlSuss CT62, was used to deposit SU-8, with a rotation speed of 1340 rpm for 40 s, to prevent contaminations.

3.2.2. Photolithographic patterning

Photolithography is an adaptation of lithographic processes to microelectronics fabrication, comprising all the steps involved in transferring a pattern from a mask to the surface of a substrate (Madou 2002). The overall process relies essentially on the light sensitivity of a material called photoresist; as such a yellow light ambient is required to prevent photoresist degradation (Figure 3.5).

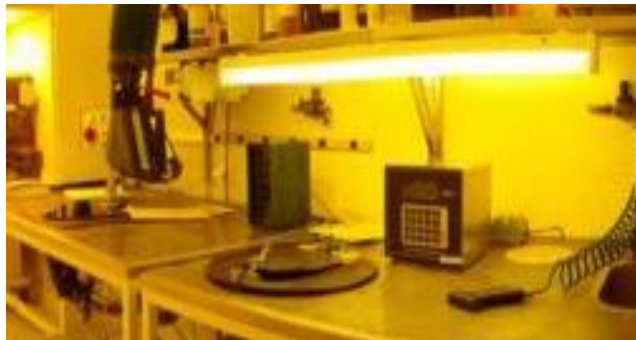


Figure 3.5. Image of the yellow room where photolithographic processes are performed.

A typical photolithography process flow used in the production of ISFETS is represented in Figure 3.6. After substrate cleaning with acetone, isopropyl alcohol (IPA) and ultra-pure water, and drying under a nitrogen flow, the photoresist (AZ6612) is spin-coated prior to thin film deposition. After spin-coating, the photoresist is subjected to a soft-bake by placing the coated substrates on a hot-plate at $\sim 115^\circ\text{C}$ for ~ 1 min. This reduces the photoresist's solvent content and improves adhesion to the substrate.

The photoresist coated substrate is then aligned with the mask and exposed to UV light, which was performed in a Karl-Suss MA6 mask-aligner. The exposed photoresist regions are weakened and can be removed with a suitable developer (AZ726 MIF, which is mainly composed of tetramethylammonium hydroxide). The unexposed regions are not removed with the developer so the desired pattern is thus transferred to the photoresist (Madou 2002). The substrate is then ready for thin film deposition. The photoresist pattern is the negative of the desired thin film layer, meaning that the desired thin film pattern is defined by the area that is without photoresist film.

After thin film deposition, the substrate goes directly to the resist stripping step; consisting of dipping the substrate in a liquid that dissolves the photoresist or causes it to swell and lose adhesion to the substrate. In this work, this was accomplished using acetone and a subsequent cleaning in IPA to avoid striations on the substrate. This removes both the photoresist and the thin film deposited on top of it; this process is known as lift-off. Lift-off has the great advantage of allowing selective patterning of a low-temperature deposited material without affecting others beneath it, but it generally results in poorer definition and/or increased contamination.

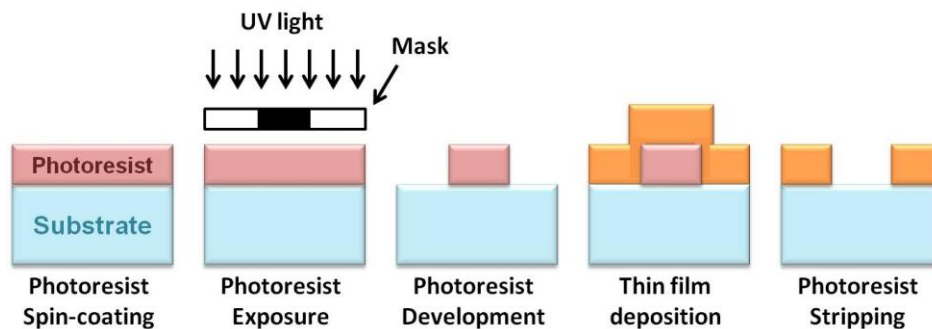


Figure 3.6. Process flows showing the main steps of lift-off photolithographic process.

These processes of photoresist spin-coating and soft-bake; mask alignment followed by UV exposure and photoresist development are repeated prior to the deposition of each layer of the device; ending with photoresist stripping and lift-off.

Photolithography patterning and lift-off processes were used for the fabrication all the layers of ISFET devices. For that, dark field photomasks, where only the desired pattern is left transparent, were developed for each layer. Figure 3.7 depicts a combination of the masks of all layers, showing an image of the complete device's structure. The coloured lines delimit the transparent patterns and each colour represents a layer: red – extended gate electrode; yellow – dielectric; green – semiconductor; dark blue – source and drain electrodes; light blue – sensitive area and pink – passivation layer.

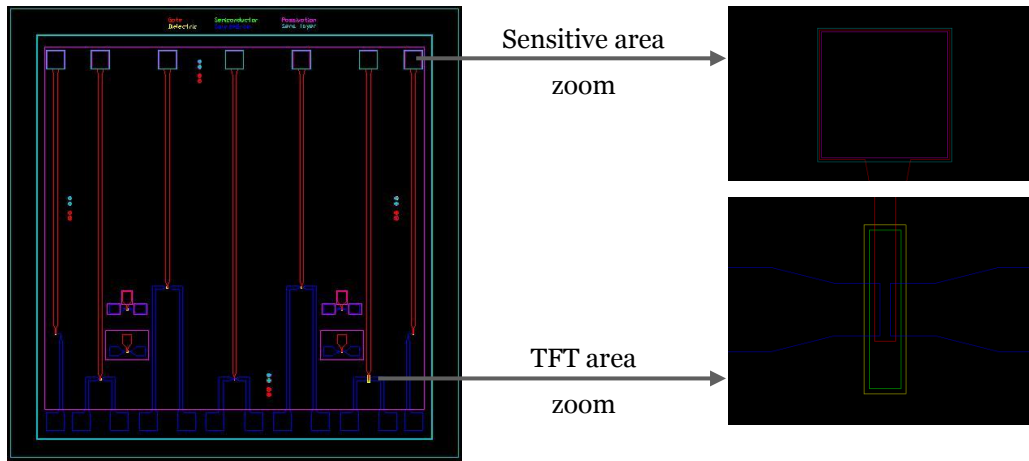


Figure 3.7. Image of the combination of the photomasks of all the layers of an ISFET device.

3.3. Post-deposition processes

The properties of thin films can be severely modified by different post-deposition processes, such as thermal or plasma treatments. The conditions under which the post-deposition annealing and plasma treatments were performed are described herein.

3.3.1. Influence of annealing temperature

Increased temperatures can influence the properties of thin films and devices by modifying interfaces, due to minimization of surface states, or promoting the crystallization of amorphous structures.

The influence of post-deposition annealing temperature was studied for Si/SiO₂/Ta₂O₅ samples produced with a rf power of 150 W, a deposition pressure of 0.3 Pa and an Ar:O₂ ratio of 14:1 sccm. In order to estimate the crystallization temperature of Ta₂O₅ thermal annealing was performed with temperatures ranging from 200 to 800 °C in an air atmosphere with a heating rate of 10 °C/min, maintaining the annealing temperature for 1 h and removing the samples only after cooling down below 50 °C. The annealing treatments were performed using a Barnstead Thermolyne F21130 tubular furnace existent in CENIMAT.

3.3.2. Influence of plasma surface treatments

The use of post-deposition room temperature plasma processes can influence the surface properties of thin films. In this work the influence of argon or oxygen plasma treatments on the sensing characteristics of Ta₂O₅ thin films was studied.

The argon and oxygen plasma treatments were performed in the AJA rf sputtering system used for film deposition by exposing the sensors to pure Ar (15 sccm) or O₂ (15 sccm) plasma at a 0.4 Pa pressure and varying the rf power applied to the substrate (10, 20 and 30 W) and process time (2, 5 and 10 minutes). Annealing of the sensors at 200 °C for 1 h in air was performed after the plasma treatment for Ar plasma and prior to plasma treatment, for O₂ plasma.

3.4. Thin film characterization techniques

The oxide thin films were characterized using a broad range of techniques to study their structural, morphological, compositional, optical and electrical properties. Relevant details about the characterization techniques used throughout the research work developed are given below.

3.4.1. Structural, morphological and compositional characterization

3.4.1.1. x-ray diffraction (XRD)

XRD is a non-destructive powerful characterization technique to determine a material's structure; whether it is amorphous or polycrystalline, which phases are present and if any preferential crystallographic orientations exist. When a monochromatic x-ray beam is directed at a material its photons can be either absorbed or dispersed by the atoms. For certain directions the dispersed waves are in phase, that is these interfere constructively, resulting in a diffracted beam with a direction that is dependent on the structural properties of the material. For a given x-ray radiation of wavelength (λ), with a value close to the inter-planar spacing (d_{ip}), that reaches the material with a certain incident angle (θ); constructive interferences occur when the phase difference between the waves dispersed by the distinct atomic planes are multiples (n) of the wavelength (λ). This phenomenon can be described by Bragg's law (Figure 3.8 - left):

$$n\lambda = 2d_{ip} \cdot \sin \theta \quad (3.1)$$

By varying 2θ (the diffraction angle) and measuring the diffracted beam intensity, which depends on the number of atomic planes equally spaced, a diffractogram is obtained and it can be compared with a database to identify the sample's structure (Atkins 1998).

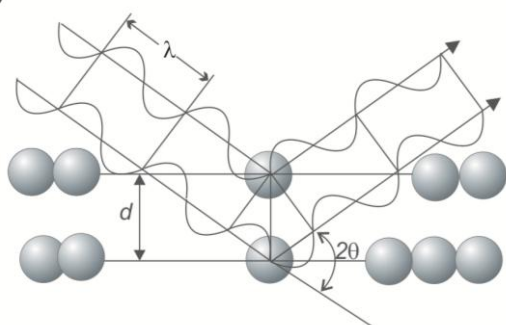


Figure 3.8. Schematic representation of Bragg's law (left) and Panalytical X'Pert PRO diffractometer (right).

In this work XRD was used to analyze oxide thin films produced on silicon substrates. The measurements were performed using a Panalytical X'Pert PRO (Figure 3.8 - right) diffractometer existent in CENIMAT, in Bragg-Brentano ($\theta/2\theta$ coupled) geometry with Cu K α line radiation ($\lambda=1.5406 \text{ \AA}$) and varying 2θ between 20 and 60° . An offset of 1° in 2θ was applied to the obtained diffractograms to minimize the highly intense c-Si diffraction.

3.4.1.2. Scanning electron microscopy (SEM)

Scanning electron microscopy (SEM) can provide high resolution images of the surface of a sample at the nanometer scale. To obtain an image by SEM a highly energetic electron beam is directed at the sample and several interactions can occur, such as absorption of electrons by the sample, reflection of primary (backscattered) electrons, emission of secondary electrons and emission of electromagnetic radiation (Schroder 2006). The conventional SEM image is formed by the detection of the secondary electrons emitted by the sample. However different detectors can be used to analyze, for example, backscattered electrons which can provide information about chemical composition of the sample as contrast is achieved due to the different atomic numbers of elements.

SEM images of samples produced in this work were performed using a SEM-FIB Cross-Beam Auriga system from Zeiss existent in CENIMAT (Figure 3.9).



Figure 3.9. SEM-FIB Cross-Beam Auriga system existent in CENIMAT.

3.4.1.3. Atomic force microscopy (AFM)

Atomic force microscopy (AFM) provides very high resolution three dimensional surface profiles, where atomic scale features can be detected, with the advantage that it does not require any sample preparation and measurements can be performed in air or liquid ambient. Given the low sample requirements and large imaging possibilities, AFM is used in several research fields, such as materials science, chemistry, biology and physics. Contact mode AFM is one of the most widely used scanning probe modes, and operates by scanning a sharp tip, which is attached to a cantilever, across the sample at an extremely low force. Either the repulsive force between the tip and sample or the

actual tip deflection is recorded relatively to spatial variation and then converted into an image of the sample's surface. The small cantilever deflection can be measured by using a laser beam reflected from the top surface of the cantilever into a photodiode. Other imaging modes are available, such as the tapping mode, which is particularly useful to analyze soft samples that can be damaged when using contact mode. (Blanchard 1996; Meyer 1992).

AFM analysis of surface morphology and calculation of root-mean-square roughness (R_{rms}) was performed on Ta₂O₅ thin films deposited on silicon substrates, using an Asylum MFP3D AFM system existent in CENIMAT (Figure 3.10).



Figure 3.10. Asylum MFP3D atomic force microscope system existent in CENIMAT.

3.4.1.4. Rutherford Backscattering Spectrometry (RBS)

Rutherford Backscattering Spectrometry (RBS) is a widely used method that allows the quantitative determination of the composition of a material and depth profiling of individual elements in a sample. The sample is bombarded with high energy ions, usually H⁺ or He⁺, and the energy of the backscattered projectiles is recorded with an energy sensitive detector, typically a solid state detector. The backscattered energy profile is a function of not only the type of atom (atomic mass of the nucleus) but also the depth at which the atom is inside the sample. The analyzed depth is typically about 2 μm for incident He-ions and about 20 μm for incident protons. RBS is quantitative without the need for reference samples, nondestructive, has a good depth resolution of the order of several nm, and a very good sensitivity for heavy elements of the order of parts-per-million (ppm); the drawback being its low sensitivity for light elements, such as oxygen (Mayer 2003).

RBS experiments were carried out at 3.1 MV van de Graaff accelerator from High Voltage B.V. (Netherlands) at ITN (Portugal) with a 2 MeV 4He^+ beam to study the film's composition. The depth profile of the samples constituents was extracted from spectra collected at distinct incident angles. The backscattered particles were detected at 140° with a silicon solid state detector of 13 keV energy resolution. The obtained spectra were fitted and analyzed with the IBA DataFurnace NDF software (Barradas 1997). Analysis of RBS data of Ta_2O_5 thin films provided information about the films stoichiometry.

3.4.2. Optical characterization

The interaction of photons with a material can generate a multitude of effects. The incident photons can be emitted, reflected, absorbed or transmitted and each one of these phenomena can be explored by different techniques (Schroder 2006). The energy (E) of the incident photons (equation (3.2)) and the material itself will determine which interactions occur.

$$E = h\nu = \frac{hc}{\lambda} \quad (3.2)$$

where h is the Planck's constant, ν is the photon frequency, c is the speed of light and λ is the photon wavelength. In this work two optical characterization techniques are explored; UV-Vis-Near-infrared (NIR) transmittance spectroscopy and spectroscopic ellipsometry.

3.4.2.1. UV-Visible-NIR transmittance spectroscopy

This technique can be used to extract important optical parameters of transparent materials, such as the absorption coefficient (α), the refractive index (n), the optical band gap energy (E_{opt}) and transition type, the thin film's thickness (d) and naturally, the degree of transparency for a given wavelength. To determine these parameters, the optical transmittance (T) is first measured across the λ range of interest, by using a spectrophotometer. From this data α can be determined by:

$$\alpha = -\frac{1}{d} \ln(1 - A) \quad (3.3)$$

where A is the optical absorption of the thin film; $A = 1 - T - R$. Neglecting R leads to $A \approx 1 - T$ and, although slightly inaccurate α values are obtained, the evolution of α with E is not severely affected, thus no significant errors in optical band gap determination are introduced. E_{opt} corresponds to the fundamental absorption process, i.e., to the excitation of a valence electron to a higher energy state. The optical band gap can be calculated by plotting $(\alpha h\nu)^x$ versus $(h\nu)$; known as Tauc's plot, near the absorption edge and the straight line portion of the curve extrapolated to the abscissa intercept whose value is taken as E_{opt} (Figure 3.11). The value of x is dependent on the transition type; assuming values of 2, 2/3, 1/2 or 1/3, depending if the transition is allowed direct, forbidden direct, allowed indirect or forbidden indirect, respectively (Buchholz 2009).

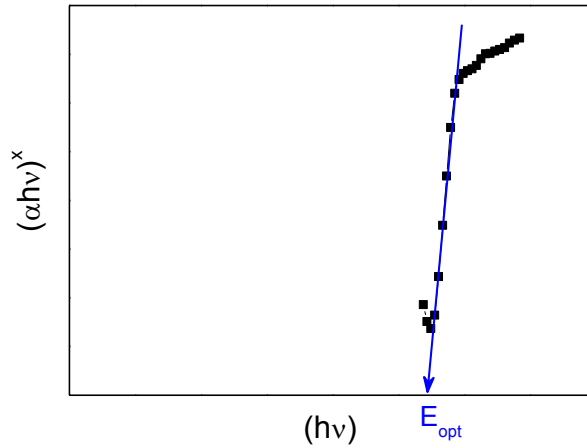


Figure 3.11. Schematic representation of optical band gap (E_{opt}) determination from a Tauc's plot.

The transmittance measurements of the Ta_2O_5 thin films deposited on glass substrates were performed with a double beam Shimadzu UV-3101 spectrophotometer system existent in CENIMAT/CEMOP:I3N, by varying λ between 250 and 2500 nm. This technique was mainly used to obtain the optical band gap energy of rf sputtered Ta_2O_5 thin films, and also to assess their transparency by averaging transmittance data between 400 and 700 nm (average visible transmittance, AVT).

3.4.2.2. Spectroscopic ellipsometry (SE)

Ellipsometry is a contactless and non-invasive optical technique that allows the determination of the dielectric function of a given material. Through experimental data modulation relevant information about the materials properties (film thickness, surface roughness, optical band gap energy, composition, and microstructure) can be obtained. Ellipsometry relies on the measurement of amplitude and phase variation between the parallel and perpendicular components of a polarized light beam, after being reflected by the sample. The experimental data are obtained by measuring the post reflection polarization, known as the Fresnel coefficient (ρ_F); which is a function of the parallel and perpendicular reflection coefficients (r_p and r_s , respectively) and of the ellipsometric angles ψ and Δ , that represent the differential changes in amplitude and phase, respectively: (Franke 2001; Pereira 2008a)

$$\rho_F = \frac{r_p}{r_s} = \tan \psi \cdot e^{i\Delta} \quad (3.4)$$

Single-wavelength ellipsometry employs a monochromatic light source; hence for a given sample the measurements provide a set of ψ and Δ angles. This data can be used to analyze various properties of the materials as the ellipsometric amplitude and phase angles are sensitive to film thickness, composition, microstructure, surface roughness, among other properties.

Measurements were performed over an energy range of 1.5-6.0 eV, with a 70° incident angle, with a Jobin Yvon Uvisel system existent in CENIMAT/CEMOP:I3N (Figure 3.12). The acquired data was modulated with DELTAPSI software using a Tauc-Lorentz dispersion formula model and pursuing the minimization of the error (χ^2).

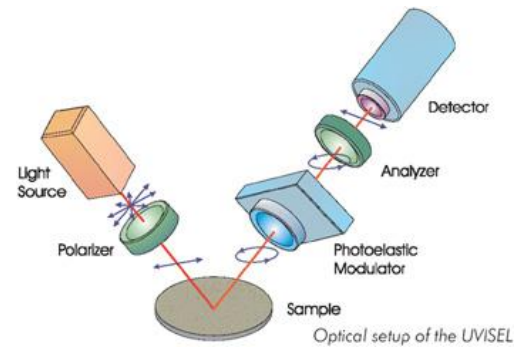


Figure 3.12. Jobin Yvon Uvisel ellipsometer system existent in CENIMAT/CEMOP:I3N (left) and schematic representation of an ellipsometry setup (right).

The analysis of the experimental data was done using the Tauc–Lorentz dispersion function which can be applied to describe the dielectric response of several materials such as high k dielectrics. The model combines the Tauc band edge with the classical Lorentz broadening function. This provides a parameterized form for the imaginary part of the dielectric function (ε_2), where:

$$\varepsilon_2(E) = \begin{cases} \left[\frac{1}{E} \frac{A \cdot E_0 \cdot C (E - E_g)^2}{(E^2 - E_0^2)^2 + C^2 \cdot E^2} \right], & E > E_g \\ 0, & E \leq E_g \end{cases} \quad (3.5)$$

The imaginary part of the dielectric function is a function of the photon energy (E) and it is defined by four parameters, where A is the transition matrix element, normally related with the density of the material; E_0 the peak transition energy; E_g the band gap energy and C the broadening parameter that it is inversely related to the short range order. The real part of the dielectric constant is obtained by performing a Kramers–Kronig transformation of ε_2 . (Aguas 2003; Pereira 2006 and 2008a)

In this work, spectroscopic ellipsometry was used for the determination of relevant parameters; extinction coefficient (k) and refractive index (n), thickness (d), surface roughness and energy band gap (E_g) for the studied Ta_2O_5 thin films. These parameters were used to assess and compare the properties of Ta_2O_5 films produced with different deposition parameters and relate these properties to pH sensitivity variation of Ta_2O_5 –based EIS sensors.

3.4.3. Contact angle measurements

Contact angle measurements are widely used for the characterization of the interfacial phenomenon, including wetting/dewetting of solid surfaces, capillary penetration into porous media, coating, and painting. Considering the thermodynamic equilibrium between the liquid (L), solid (S), and vapour (V) phases; the contact angle can be expressed by Young’s equation, which is valid for an ideal solid surface, namely, a perfectly smooth, chemically homogeneous, rigid, insoluble, and nonreactive surface (Barhoumi 2010):

$$\gamma_{LG} \cos \theta + \gamma_{SL} - \gamma_{SG} = 0 \quad (3.6)$$

where θ is the Young contact angle and γ_{LG} , γ_{SG} , and γ_{SL} are the surface tensions of the liquid–gas, solid– gas, and solid–liquid interfaces, respectively (Figure 3.13 - left).

In general, solid surface reactivity is measured by the nature and the number of active surface sites. The presence of these sites may influence the surface energy and hence the contact angle. As such, contact angle measurements on Ta_2O_5 thin films were used to infer on surface charge variation with annealing temperature (Barhoumi 2010).

Contact angle measurements were performed on 2 μL deionized water drops according to the sessile drop method in a Dataphysics OCA15plus system existent in CENIMAT (Figure 3.13 - right).

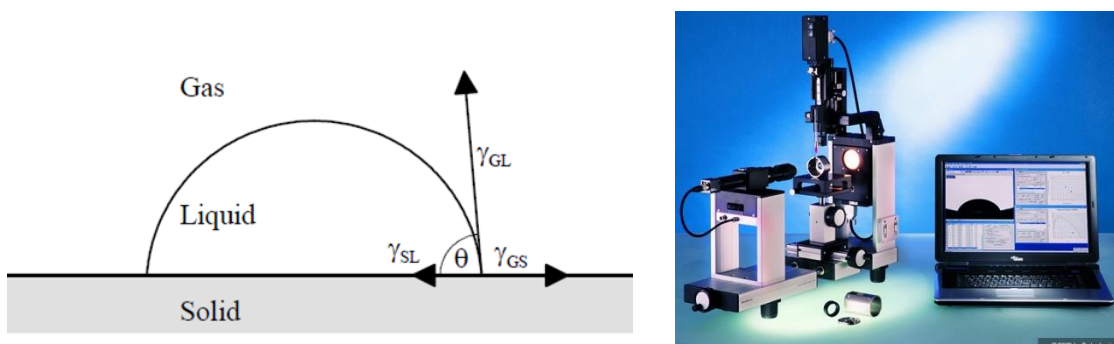


Figure 3.13. Schematic representation of contact angle measurement (left) and Dataphysics OCA15plus system existent in CENIMAT (right).

3.5. Characterization of field effect devices (FEDs)

The assessment of EIS devices sensitivity towards pH, penicillin and DNA was mainly performed by impedance spectroscopy, whilst ISFET sensors assessment was obtained by the devices static current-voltage characteristics. A brief description of these methods is given herein.

3.5.1. Impedance Spectroscopy (IS)

Impedance spectroscopy is a powerful method of characterizing many of the electrical properties of materials. It can be used to investigate the dynamics of charge in the bulk or interfacial regions of any kind of solid or liquid material; ionic, semiconducting and even insulators (dielectric). IS has been applied to the study of EIS devices allowing the

determination of electrical characteristics of the semiconductor, the insulator's capacitance and the effect of the electrolyte's pH on the devices (Barsoukov 2005).

Impedance is usually measured by applying an ac voltage to the sample and measuring the phase shift and amplitude, or real and imaginary parts, of the resulting current. Normally, a small sinusoidal excitation signal is used so that the response obtained is pseudo-linear. As long as the applied potential difference amplitude is smaller than the thermal voltage, $V_{thermal}=RT/F=kT/q$, about 25 mV at 25 °C, the system becomes linear to an excellent approximation (Barsoukov 2005). In a linear (or pseudo-linear) system the current response to a sinusoidal potential will be a sinusoid at the same frequency but shifted in phase (Figure 3.14).

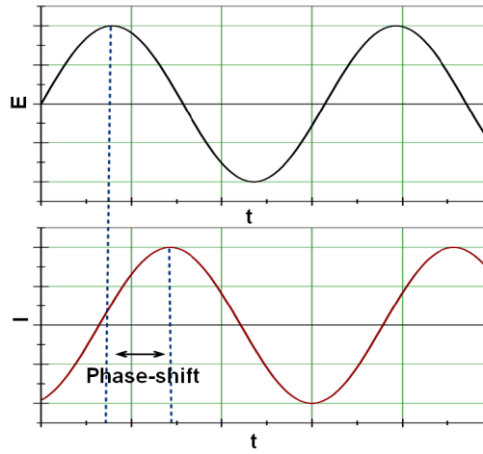


Figure 3.14. Graphical representation of the time (t) dependent sinusoidal current response (I) to a small ac voltage (E), in a linear system.

The excitation signal, expressed as a function of time, has the form

$$E_t = E_0 \sin(\omega t) \quad (3.7)$$

where E_t is the potential at time t, E_0 is the amplitude of the signal, and ω is the radial frequency ($\omega = 2\pi f$).

In a linear system the response signal, I_t , is shifted in phase (ϕ) and has a different amplitude, I_0 .

$$I_t = I_0 \sin (\omega t + \phi) \quad (3.8)$$

The impedance of the system can be calculated with an expression analogous to the Ohm's law (Barsoukov 2005; Gamry 2010).

$$Z = \frac{E_t}{I_t} = \frac{E_0 \sin (\omega t)}{I_0 \sin (\omega t + \phi)} = Z_0 \frac{\sin (\omega t)}{\sin (\omega t + \phi)} \quad (3.9)$$

The impedance is therefore expressed in terms of a magnitude (Z_0) and a phase shift (ϕ). The relation between system properties and the response to a periodic voltage excitation is very complex in the time domain, so in order to simplify the system Fourier transformations are used. Impedance can then be represented as a complex number (Barsoukov 2005; Gamry 2010).

$$Z = Z_0 e^{j\phi} = Z_0 (\cos \phi + j \sin \phi) \quad (3.10)$$

where $j \equiv \sqrt{-1}$ is the imaginary number.

To display the impedance characteristics, either a Bode plot of both the absolute magnitude of the impedance ($|Z|=Z_0$) and the phase-shift (ϕ) versus frequency, or the well-known Nyquist plot or an impedance plane plot of $Z_{imag} \equiv Z'' = |Z| \sin (\phi)$ (the imaginary or capacitive component of the impedance) versus $Z_{real} \equiv Z' = |Z| \cos (\phi)$ (the real or resistive component of the impedance) are typically used. Each point in the Nyquist plot is the impedance at one frequency (Barsoukov 2005).

Electrochemical impedance data is commonly analysed by fitting to an equivalent electrical circuit model where most of the circuit elements are common electrical elements such as resistors, capacitors and inductors.

For resistors $E=IR$ and $Z=R$, thus the impedance of a resistor is independent of frequency, having only a real impedance component since the current through a resistor stays in phase with the voltage across it.

For capacitors $I=C dE/dt$ and $Z=(j\omega C)^{-1}$, thus the impedance of a capacitor decreases as the frequency increases, having only an imaginary impedance component. The current through a capacitor is phase-shifted 90° with respect to the voltage (Gamry 2010).

Impedance measurements were performed using a Gamry Reference 600 Potentiostat/Galvanostat/ZRA with built in electronics for electrochemical impedance measurements (Figure 3.15), acquired specifically for the development of this work. This equipment has a frequency range of 10 μ Hz to 1 MHz, a current range of 0.6 A to 60 pA and a measurement voltage range of -8 V to 8 V. Cable connections include an earth lead, reference electrode, counter-electrode and working electrode.



Figure 3.15. Gamry Reference 600 Potentiostat (left) and experimental setup (right) used for impedance measurements of EIS sensors.

Electrochemical impedance measurements were performed in an electrochemical cell in a two electrode setup, which is usually used for high impedance materials measurements (Barsoukov 2005). For that both the counter-electrode and the reference electrode leads were connected to a Ag/AgCl (3 M KCl) reference electrode (Gamry) and the working electrode lead was connected to the back-contact of EIS capacitor sensors. This configuration leads to typical n-Si C(V) curves to be obtained with a p-Si device however, although switching the connections corrects this issue slight degradation of the reference electrode was noted when it was connected to the working electrode lead. All measurements were performed in a dark Faraday cage connected to the earth lead, to minimize electrical noise.

Potentiostatic impedance spectroscopy (IS) measurements were performed to assess the EIS devices behaviour as a function of frequency. The Bode plots of EIS devices exposed to a pH 7 buffer solution were obtained in a frequency range from 1 Hz to 1 MHz and data was fitted using the Gamry Echem Analyst software and a simplified equivalent circuit of the EIS device (Figure 4.4).

Electrochemical impedance measurements at a fixed frequency were used to obtain the capacitance-voltage curves ($C(V)$) of EIS sensors exposed to electrolyte solutions by applying a variable dc potential, with a superimposed ac signal of fixed amplitude (10 mV) and 500 Hz frequency, between the reference electrode (Ag/AgCl 3 M KCl) in solution and the EIS sensors back-contact. At least two sensor measurements were performed and five consecutive measurements were made at each solution and reference voltage values were obtained at 60% of the maximum capacity for each electrolyte solution. These measurements were performed to assess of Ta₂O₅ EIS sensors behaviour in terms of: pH sensitivity, penicillin sensitivity, DNA detection and monitoring of DNA amplification via PCR and LAMP.

3.5.2. Static current-voltage characteristics

The fundamental characterization of an ISFET encompasses the measurement of output and transfer characteristics of the device in a similar way as for a TFT (see *Section 2.2.2*). However, most of the characterization is focused on transfer characteristics and their variation due to electrolyte solutions of different pH.

The pH sensitivity of ISFET sensors was evaluated from the transfer characteristics curves in the linear regime. For that a constant source to drain voltage (V_D) was applied and a gate potential (V_G) was swept between -2 V and 3 V through a commercial Ag/AgCl reference microelectrode (Unisense). The devices pH sensing performance was evaluated by exposing the sensitive area to constant ionic strength buffer solutions of different pH. Three consecutive measurements were performed at each pH solution; upon changing solutions the sensitive surface was thoroughly rinsed with the next solution and it was allowed to stabilize for 15 min prior to the first $I(V)$ measurement. The reference voltages were obtained at a specific I_D , typically 0.3 μ A, from linear transfer curves and plotted against electrolyte pH to determine the devices pH sensitivity. Output characteristics were measured by sweeping V_D from 0 V to 3 V, with 4 steps of V_G , from 0 to 1.5 V.

The same measurement protocol was used to measure all the devices. This was essential to avoid erroneous analysis and comparisons between devices, as verified in samples initially assessed during this research work. The established protocol varies slightly, regarding V_G and V_D values, depending on the ISFET devices structure and if it is being analyzed with or without electrolyte.

All static current-voltage measurements were performed using an Agilent 4155C semiconductor parameter analyser and Cascade M150 microprobe station existent CENIMAT/CEMOP:I₃N (Figure 3.16). The measurements were made in a dark Faraday cage to minimize electrical noise. The protocol defined above is configured in the controller computer. For all the transfer and output characteristics, hold and delay times are fixed at 1 s and voltage step is fixed at 100 mV, to assure a 100 mV/s measurement speed.

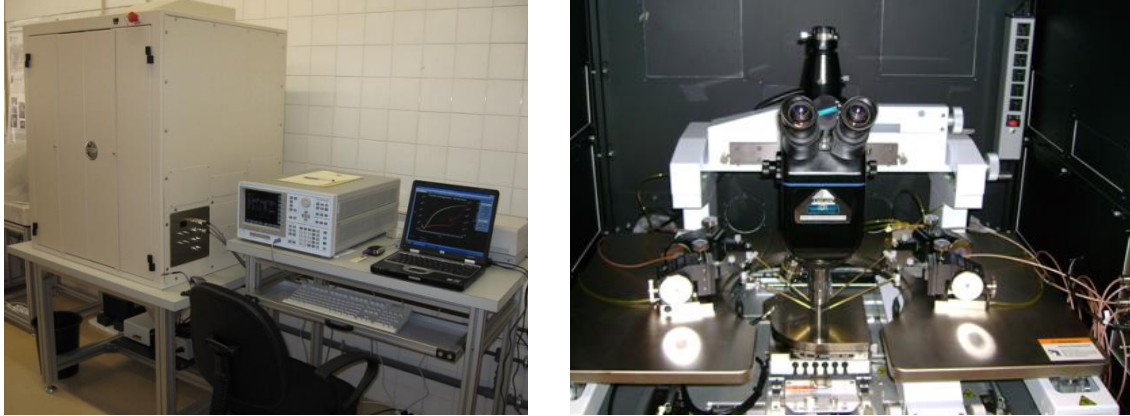


Figure 3.16. Agilent 4155C semiconductor parameter analyser (left) and Cascade M150 microprobe station (right) used I(V) measurements of ISFET sensors.

Chapter 4. Ta₂O₅ based field effect devices

4.1. Electrolyte-insulator-semiconductor (EIS) sensors development.....	73
4.1.1. Sensor characteristics	73
4.1.2. Sensor behaviour.....	75
4.1.3. Sensor structure	78
4.2. Influence of deposition conditions.....	79
4.2.1. Influence of deposition rate	80
4.2.2. Influence of rf power.....	81
4.2.3. Influence of deposition pressure and Ar:O ₂ ratio.....	87
4.3. Influence of post-production treatments.....	91
4.3.1. Influence of annealing temperature.....	91
4.3.2. Influence of surface plasma treatments	98
4.3.2.1. Influence of argon plasma	98
4.3.2.2. Influence of oxygen plasma.....	101

Some of the results presented in this chapter are currently in press in R. Branquinho, J.V. Pinto, T. Busani, P. Barquinha, L. Pereira, P.V. Baptista, R. Martins, E. Fortunato, *'Biosensors based on Sputtered Ta₂O₅ with Low Thermal Annealing'*, IEEE/OSA Journal of Display.

Chapter 4. Ta₂O₅ based field effect devices

In this chapter the results of the optimization of the pH sensitivity of tantalum pentoxide produced by rf magnetron sputtering are presented and discussed.

First, an insight of relevant practical parameters for the development of EIS sensors is given as it proved to be of great importance to achieve reliable data; especially considering that the electrochemical impedance spectroscopy technique was introduced in the scope of this work. Then, the influence of the deposition parameters on pH sensitivity was studied by varying deposition pressure, deposition gases ratio (Ar:O₂) and rf power density. The effect of post-production annealing temperature and surface plasma treatments with pure argon and pure oxygen atmosphere, were also studied for the optimized sensor.

4.1. Electrolyte-insulator-semiconductor (EIS) sensors development

The development of EIS sensors required the establishment of a specific measurement protocol to assess pH sensitivity of produced sensors. This was of great importance to allow for comparison between sensors and assure that differences in the sensors properties could be directly related to the fabrication process.

4.1.1. Sensor characteristics

The combination of electronic devices and aqueous solutions is a challenging task as the sensitive material needs to be exposed to the electrolyte while the remaining device has to be protected from it. A well defined sensitive area is also important as capacitance is directly related to exposed area and inversely proportional to dielectric film thickness.

$$C = \frac{\epsilon_i \epsilon_0 A}{d} \quad (4.1)$$

The geometric capacitance can be a relevant parameter in biosensing as the adsorption of biomolecules onto the insulators surface might affect its thickness and hence the total capacitance.

A specific measurement cell (Figure 4.1) was designed and fabricated with the purpose of protecting the device and prevent capacitance variations due to electrolyte leakage,

as observed in initial encapsulation experiments. The sensitive area is defined by an o-ring with the advantage that the sensor is not dipped in the electrolyte.

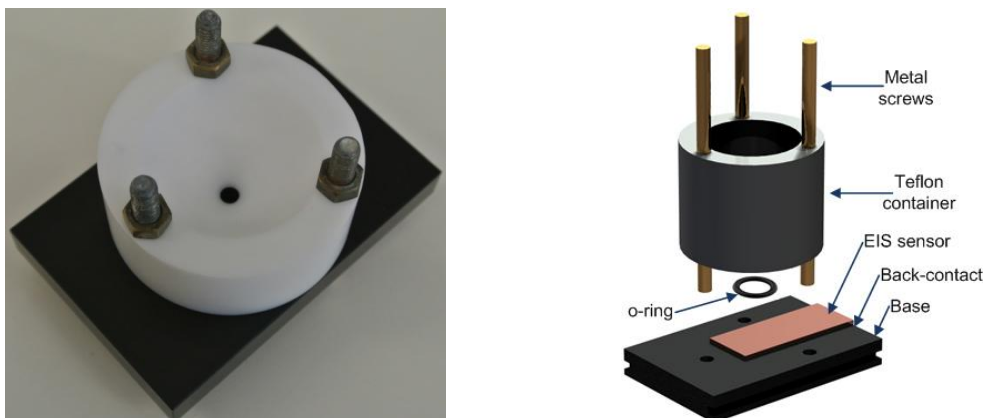


Figure 4.1. Electrochemical impedance spectroscopy measurement cell: real image (left) and schematic assembly representation (right).

However, the manual assembly of the measurement cell can lead to sensitive area variation due to o-ring compression. For a sensor comprising a double insulator layer of SiO₂ and Ta₂O₅, of 100 nm each, a 1 mm variation in the sensitive area diameter will lead to a significant geometric capacitance variation (Figure 4.2). This must be taken into consideration when comparing different sets of sensors especially in the study of biomolecules adsorption (Poghossian 2006; Turek 2007).

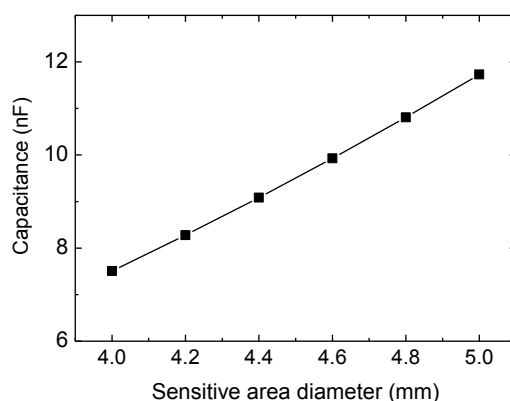


Figure 4.2. Geometric capacitance variation with sensitive area diameter for a double layered insulator of SiO₂ and Ta₂O₅ (100 nm each) and considering $\epsilon_{\text{SiO}_2}=3.9$ and $\epsilon_{\text{Ta}_2\text{O}_5}=25$.

The pH sensitivity of tantalum pentoxide was evaluated by means of electrochemical impedance spectroscopy measurements with a Gamry Reference 600 potentiostat. The capacitance-voltage curves (C(V)) of EIS sensors exposed to buffer solutions of different pH were obtained by applying a variable dc potential, with a superimposed ac

signal of fixed amplitude and frequency, between the reference electrode (Ag/AgCl 3 M KCl) in solution and the EIS sensor back-contact (Figure 4.3). Measurements were performed in a dark Faraday cage to minimize external noise.

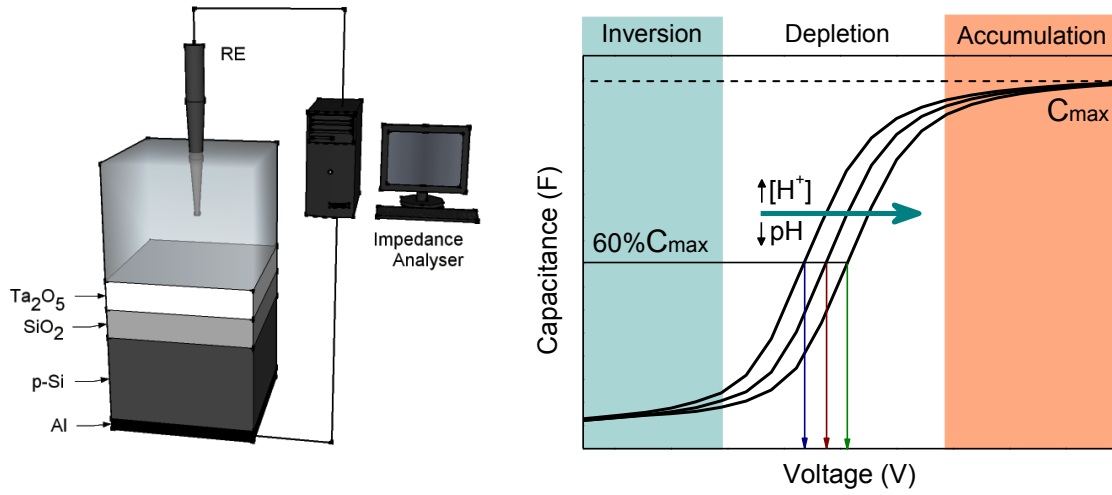


Figure 4.3. Schematic representation of the measurement setup (left) and typical C(V) response of a EIS sensor to different pH electrolytes (right).

The C(V) curves show three different regimes: accumulation, depletion and inversion. In the accumulation regime the insulator capacitance is substantially smaller than the space charge capacitance, hence the EIS device's capacitance is mainly determined by the geometrical capacitance of the insulator. The most useful range for capacitive field-effect sensors is the depletion region as changes in the solution will cause the curves to shift along the voltage axis due to oxide surface potential changes (vanHal 1996; Yates 1974). For each electrolyte solution the reference voltage was obtained within this region, at 60% of the maximum capacity. In order to infer on measurement stability at least three consecutive curves were registered for each solution. Sensitivity is defined as the potential variation induced by a unitary pH change.

4.1.2. Sensor behaviour

The complete equivalent circuit of an EIS device is complex however, for typical values of insulator thickness (100 nm) and electrolyte concentration ($>10^{-4}$ M), it can be simplified to a series combination of insulator and semiconductor capacitances (C_i and C_{sc}) and a resistance element that combines the reference electrode, electrolyte, contact resistances (R_t) and the semiconductor resistance (R_{sc}).

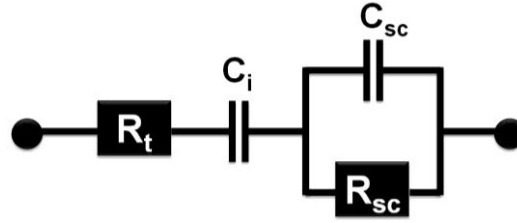


Figure 4.4. Simplified equivalent circuit of an EIS sensor. Adopted from (Bousse 1983).

The existence of any series resistance can lead to a frequency dependent behaviour of the $C(V)$ curves of EIS devices; as a result the measured capacitance can be smaller than the real capacitance of the system. (Demos 1995, Fabry 1990, Mourzina 2003)

Potentiostatic impedance spectroscopy (IS) measurements allow the assessment of the EIS device behaviour in accumulation ($V_{dc}=2$ V), depletion ($V_{dc}=-0.2$ V) and inversion ($V_{dc}=-2$ V) regimes (defined from $C(V)$ curves) as a function of frequency. The Bode plots of an EIS device exposed to a pH 7 buffer solution are represented in Figure 4.5 for the different regimes. These data can be fitted using the EIS device simplified equivalent circuit (Figure 4.4) and relevant parameters can thus be obtained.

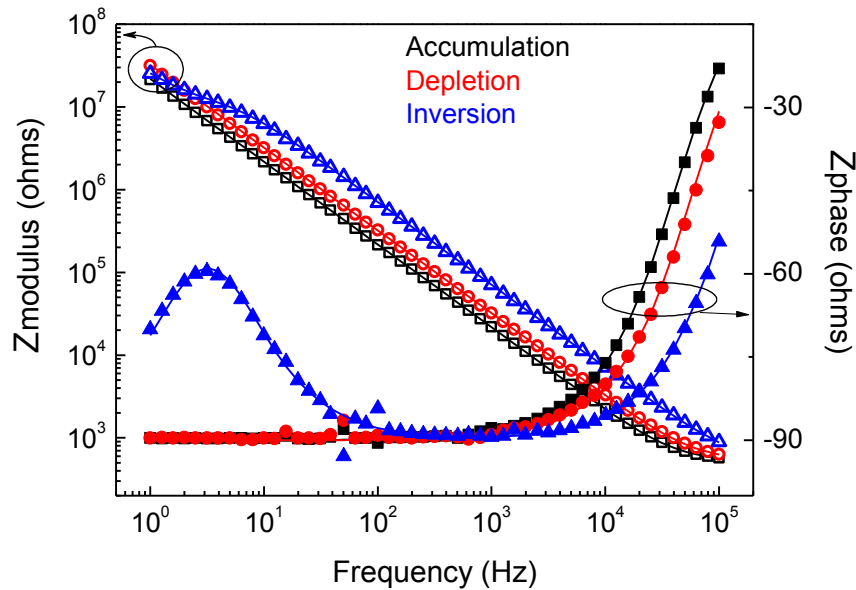


Figure 4.5. Potentiostatic impedance curves of an EIS sensor in pH 7 buffer solution. Open symbols refer to $Z_{modulus}$, solid symbols to Z_{phase} and lines to data fitting results.

In accumulation $C_i \ll C_{sc}$ and $C_t \cong C_i$ so the EIS device can be seen as a parallel plate capacitor and be modelled by a series combination of a resistance (R_t) and a capacitor ($C_t \cong C_i$). In depletion and inversion this is no longer valid. However, for highly doped silicon substrates, as in this case, R_{sc} is very low and can be neglected which explains the similar device behaviour in both depletion and accumulation regimes. The

equivalent circuit can thus be simplified as before however $C_t = C_i + C_{sc}$ as the contribution of C_{sc} can no longer be neglected. The fitting results for each equivalent circuit element are represented in Table 4.1.

Table 4.1. Equivalent circuit parameters obtained from fitting of IS characteristics of an EIS sensor in different operation regimes.

	R_t (Ω)	C_t (nF)	C_i (nF)	C_{sc} (nF)	R_{sc} (M Ω)
Accumulation	530 \pm 5	7.32 \pm 0.02	7.32 \pm 0.02	–	–
Depletion	541 \pm 7	4.95 \pm 0.2	7.32	15.25 \pm 0.2	–
Inversion	527 \pm 14	2.4 \pm 0.2	7.32	3.25 \pm 0.02	8.52 \pm 0.2

Parameters for depletion and inversion were obtained by using constant $C_i = 7.32$ nF.

The results of the fitting data are in good agreement with that of experimentally measured capacitance values (C_t and C_i) from C(V) device characteristics (Figure 4.6).

From Figure 4.5 it can also be seen that the devices show capacitive behaviour ($Z_{phase} \cong 90^\circ$) for a broad range of frequency: $f \leq 2$ kHz in accumulation and depletion regimes and $60 \text{ Hz} \leq f \leq 5 \text{ kHz}$, so in principle any frequency in the range $60 \text{ Hz} \leq f \leq 2 \text{ kHz}$ can be applied for C(V) characterization (Berney 1997).

The definition of the measurement frequency is relevant for EIS sensor electrochemical characterization. The C(V) and I(V) curves of an EIS sensor exposed to a pH 7 electrolyte solution recorded at several frequencies are depicted in Figure 4.6.

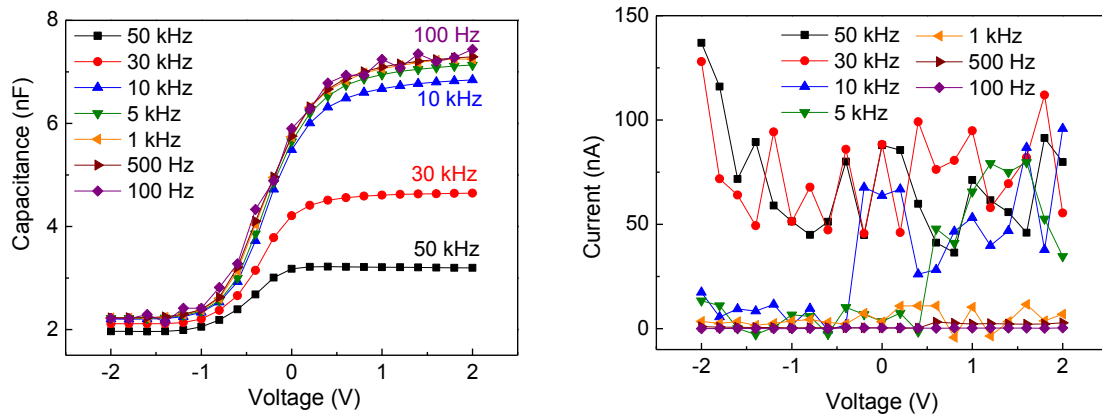


Figure 4.6. Frequency dependence of C(V) characteristics (left) and leakage current - I(V) (right) of an EIS sensor in pH 7 buffer solution.

The frequency dependence of capacitance is more significant for higher frequencies. Above 5 kHz maximum capacitance decreases significantly with increasing frequency and also high leakage currents are obtained, which for EIS sensors should be ≤ 10 nA

(Bergveld 2003). The C(V) curve obtained with 100 Hz shows high noise, probably because it is double the frequency at which electrical current is supplied (50 Hz).

Several measurement frequencies have been reported and are generally accepted for this type of sensors (Berney 1997; Pan 2009; Schoning 2002a and 2003). The frequency chosen for this study was 500 Hz as it combined the best compromise in leakage current (lower for low f), measurement time (longer for lower f ; which can cause device stress) and curve stability.

4.1.3. Sensor structure

The general structure of EIS sensor requires only a sensitive oxide layer and a semiconductor with variable capacitance so initially the Ta₂O₅ films were deposited directly on silicon substrates. However capacitance–voltage characteristics of these sensors showed high measurement variability which did not allow pH sensitivity assessment of the tantalum pentoxide films (Figure 4.7-left). As expected for a high- k material high capacitance was obtained. However, a variation above 190 mV was observed for consecutive measurements of pH 7 buffer solution when the maximum expected sensitivity is ~59 mV/pH. Also a leakage current above 100 nA was obtained for potential values below -2.2 V.

The deposition of a thin SiO₂ passivation layer (15 nm) prior to Ta₂O₅ film deposition was performed to improve the Si/insulator interfacial properties and measurement variability. As expected the maximum capacity decreases due to the presence of an additional layer of a lower permittivity material ($\epsilon_{\text{SiO}_2}=3.9$). However stability was not significantly improved as a variability of 80 mV was obtained (Figure 4.7-right).

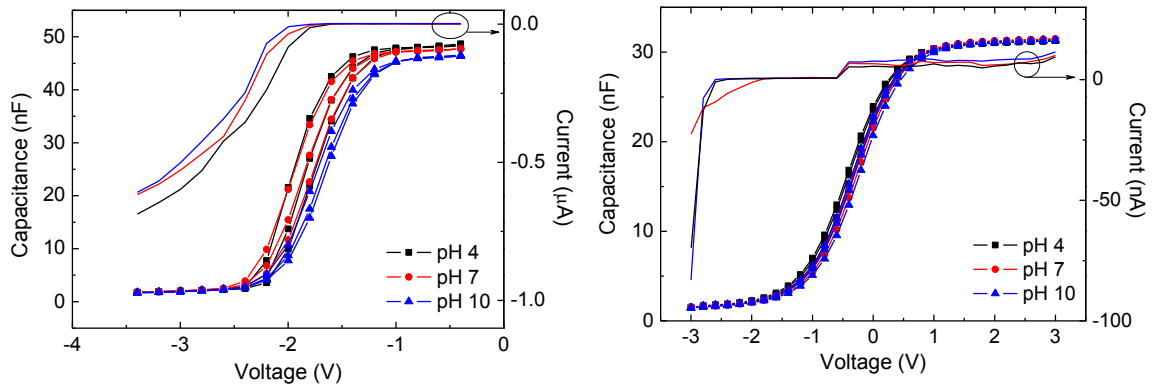


Figure 4.7. Capacitance-voltage and leakage current characteristics of Al/Si/Ta₂O₅ (left) and Al/Si/SiO₂/Ta₂O₅ (right) sensors exposed to electrolytes of pH 4, 7 and 10.

The Si-SiO₂ interface is considered the closest to an ideal interface as the oxide is grown from the thermal oxidation of the silicon itself. Thus a lower number of interfacial defects and a lower leakage current are expected (Sze 2007; Schroder 2006). Since the goal is to characterize the sensitivity of the EIS system it is essential to maintain the conditions at the insulator/semiconductor interface constant so that the measured changes can be mainly attributed to the reactions at the insulator/electrolyte interface.

For these reasons the EIS sensors were constructed by depositing tantalum pentoxide films on Si substrates with a thermally grown SiO₂ layer (100 nm). Although maximum capacity decreased significantly the measurement stability gain largely compensates, as variations of only a few mV (maximum 6 mV) and also leakage current below 12 nA were obtained in this configuration (Figure 4.8).

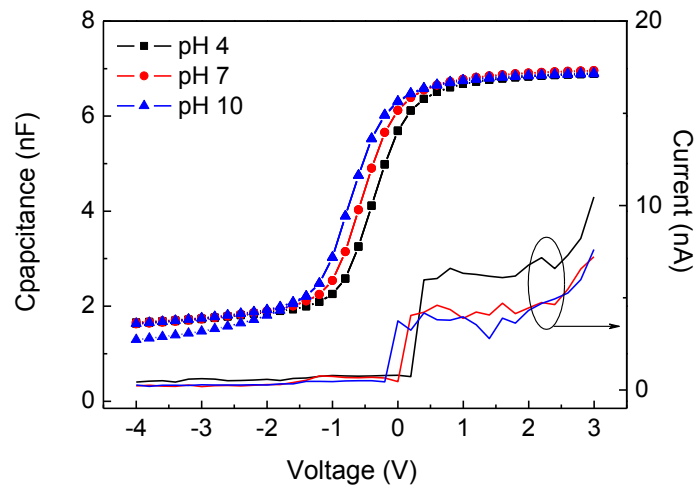


Figure 4.8 Capacitance-voltage and leakage current characteristics of Al/Si/SiO₂/Ta₂O₅ sensor exposed to electrolytes of pH 4, 7 and 10.

4.2. Influence of deposition conditions

The influence of the deposition parameters on pH sensitivity was studied, to determine the best set of conditions that allow enhanced pH sensitivity and sensor performance, by varying deposition pressure, deposition gases ratio (Ar:O₂) and rf power density (Table 4.2). The films were produced from a 2 inch (5.08 cm) Ta₂O₅ ceramic target (99.99% purity) in an AJA ATC-1300F sputtering system with a base pressure below 0.05 mPa, target to substrate distance of 10 cm and no intentional substrate heating. As defined in the previous section the tantalum pentoxide films (100 nm) were deposited on p-type silicon substrates (2.5×2.5 cm) with a 100 nm layer of thermally grown SiO₂ (commercial wafers). The aluminium back-contact (200 nm) was deposited by e-beam

assisted evaporation after etching of the silicon dioxide with a buffered HF solution. To allow structural, morphological and optical characterization simultaneous production of films on silicon and glass substrates was performed. The EIS sensors were all subjected to a post-deposition annealing at 200 °C (with a heating rate of 10⁰/min) for one hour in an air atmosphere (the effect of post-deposition annealing temperature is discussed in *Section 4.3.1*).

Table 4.2. Sputtering deposition parameters for the production of Ta₂O₅ EIS sensors.

rf power (W)	Ar:O ₂ ratio (sccm)	Pressure (Pa)
100 < P < 200	14.5:0.5 < Ar:O ₂ < 12:3	0.2 < p < 1

The influence of rf power was studied for samples produced with a deposition pressure of 0.3 Pa and an Ar:O₂ ratio of 14:1 sccm. A rf power of 150 W (9.4 W/cm²) was used for the study of the influence of both Ar:O₂ ratio and deposition pressure. Samples of varied Ar:O₂ were produced at each deposition pressure.

4.2.1. Influence of deposition rate

The deposition rate of thin films produced by sputtering varies with the deposition parameters. As such, the deposition rate was assessed at different process conditions to allow the production of Ta₂O₅ films with a thickness of ~100 nm. The results are depicted in Figure 4.9.

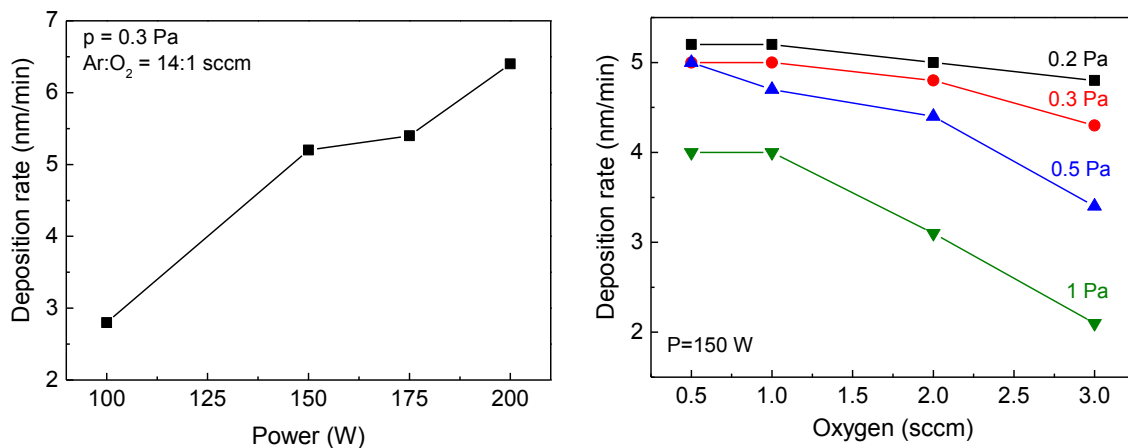


Figure 4.9. Influence of deposition parameters on the deposition rate; power (left); oxygen content and deposition pressure (right).

The deposition rate of sputtered oxides increases with increasing rf power as more energy is supplied to the system, resulting in a higher sputtering efficiency. Increasing oxygen content causes a decrease in the deposition rate regardless of deposition pressure however; this effect is more significant at higher pressures. The ionic radius of oxygen is smaller than that of argon; this reduces the transversal impact area and thus the deposition rate. Regardless of oxygen content, the deposition rate decreases with increasing deposition pressure which can be related to the increased number of collisions due to shorter mean free path between species inside the chamber. (Assuncao 2003; Ellmer 2000; Hartnagel 1995).

4.2.2. Influence of rf power

The influence of rf power was studied for samples produced with a deposition pressure of 0.3 Pa and an Ar:O₂ ratio of 14:1 sccm. The applied power was varied between 100 and 200 W corresponding to a 6.3 to 12.5 W/cm² power density.

Structural analysis of Al/Si/SiO₂/Ta₂O₅ sensors was performed by XRD. A one degree offset in 2θ was applied to eliminate the intense diffraction peaks of crystalline silicon. The diffractograms of samples produced with different rf power are presented in Figure 4.10 (left). The absence of diffraction peaks indicates that amorphous Ta₂O₅ was obtained regardless of applied rf power. This is in agreement with published results where Ta₂O₅ is usually amorphous requiring temperatures of at least 400 °C (Jagadeesh 2010) but generally above 600 °C to induce crystallization (Chaneliere 1998; Pereira 2006; Pignolet 1995).

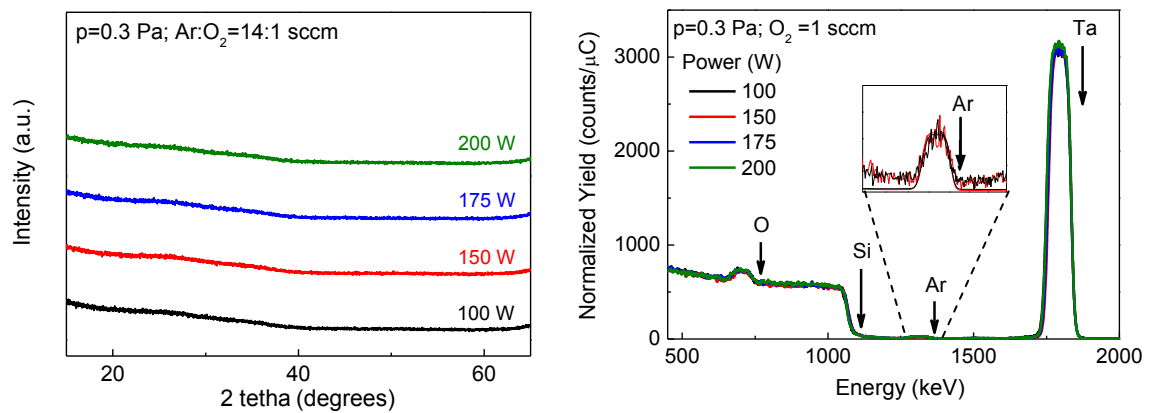


Figure 4.10. XRD diffractogram (left) and RBS spectra (right) of Ta₂O₅ EIS sensors produced with different rf power.

Compositional characterization was performed by RBS analysis of Ta₂O₅ thin films deposited on silicon substrates (Si/Ta₂O₅). The spectra are presented in Figure 4.10 (right) where the arrows indicate the energy barrier for each element. As can be seen there is no significant difference induced by power variation and the curves are well fitted to a simulated spectra of stoichiometric Ta₂O₅. Thus, stoichiometric Ta₂O₅ films were obtained regardless of rf power. This was expected as the thin films were produced from a Ta₂O₅ ceramic target. Although the sputtering deposition process might induce a small oxygen deficiency (Chaneliere 1998), even in films produced from targets of the same composition, the introduction of 1 sccm of oxygen in the reactive atmosphere seems to be sufficient to compensate this effect under the applied deposition conditions. It is interesting to point out that a small amount of argon is incorporated into the thin films as a consequence of the reactive deposition process. The low percentage of argon (~3%) does not vary significantly with deposition power and does not seem to influence the films stoichiometry.

Morphological characterization of the films was performed by SEM and AFM analysis (Figure 4.11).

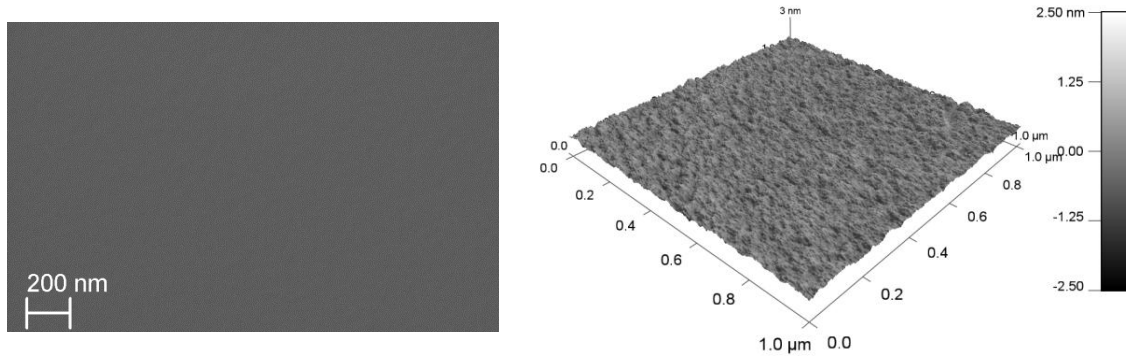


Figure 4.11. SEM and AFM images of the Ta₂O₅ films deposited with 200 W rf power, Ar:O₂=14:1 sccm and 0.3 Pa.

Regardless of deposition rf power the obtained films are uniform with a smooth surface, revealing a surface roughness below 0.5 nm; as typically observed for amorphous films.

Optical characterization of the films was performed by UV-Vis-NIR spectroscopy and spectroscopic ellipsometry. The transmittance spectra of Ta₂O₅ thin films deposited on glass substrates (glass/Ta₂O₅) shows that all samples are highly transparent in the measuring range (Figure 4.12). The average visible transparency was calculated by averaging the films transmittance in the visible range of the spectra (300-700 nm range); values of ~90% were obtained for all samples.

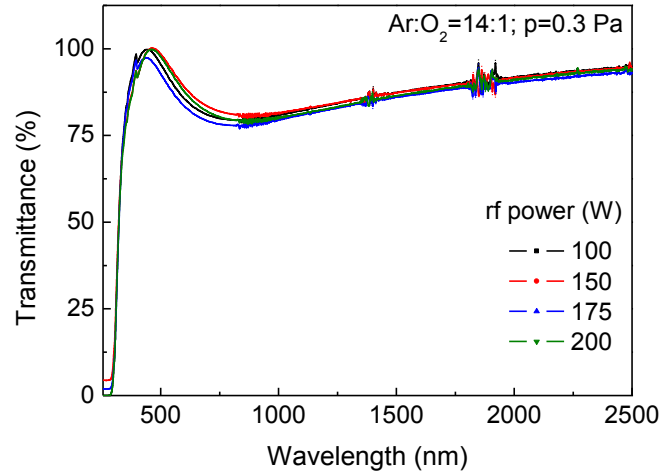


Figure 4.12. Optical transmittance spectra of Ta₂O₅ films deposited with varied rf power.

The optical band gap energy for the different films was calculated from the Tauc's plot; $(\alpha h\nu)^{1/2}$ vs $(h\nu)$, for amorphous oxides where non-direct optical transitions are allowed as observed for Ta₂O₅ (Franke 2001). The results are shown in Table 4.3.

Table 4.3. Optical band gap energy of Ta₂O₅ films deposited with varied rf power.

Power (W)	E _{opt} (eV)
100	3.96
150	4.16
175	3.97
200	3.75

The values are within reported values for amorphous Ta₂O₅; 4 – 4.3 eV (Franke 2001; Ngaruiya 2003). A slight band gap increase is observed for deposition power of 150 W.

The spectroscopic ellipsometry (SE) analysis of the samples was performed by means of a Tauc-Lorentz dispersion to fit the data obtained for Ta₂O₅ films. A four layer model (Figure 4.13) comprising a standard reference for Si and SiO₂, a double Tauc-Lorentz dispersion formula to simulate the dielectric response of Ta₂O₅ and a mixture of 50% of the Tauc-Lorentz dispersion and 50% of void reference simulated the surface roughness, was used as it is commonly reported for amorphous materials with good fitting results (Pereira 2006).

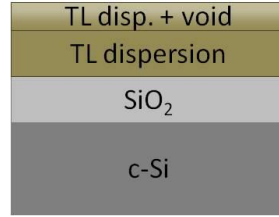


Figure 4.13. Model used in the spectroscopic ellipsometry analysis of Ta₂O₅ thin films.

Modulation of SE data allows the determination of relevant parameters; not only the dielectric function and from it the refraction index and extinction coefficient but also film thickness and surface roughness.

The refraction index (n) and extinction coefficient (k) of Ta₂O₅ do not vary significantly regardless of deposition power as can be seen in Figure 4.14, however other modulation parameters such as the band gap (E_g), the transition matrix element A which is normally related to the material density and the broadening parameter C that is inversely proportional to the short range order, allow further insight of the films properties (Pereira 2006; Aguas 2003). These are represented in Figure 4.15.

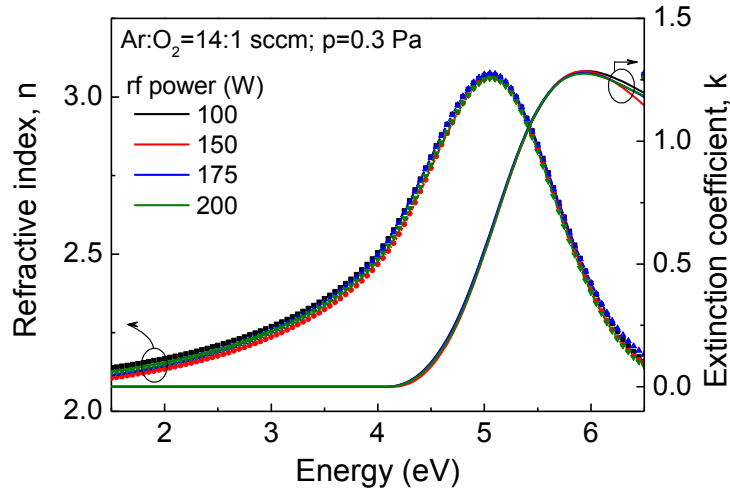


Figure 4.14. Refraction index (n) and extinction coefficient (k) of Ta₂O₅ deposited with different rf power, obtained by modulation of SE results.

The films are approximately 100 nm thick, as intended, and show very low surface roughness, as confirmed by AFM measurements. The band gap values obtained are in agreement with the E_{opt} values in Table 4.3. As can be seen, at a deposition power of 150 W higher band gap energy and film density improvement are attained.

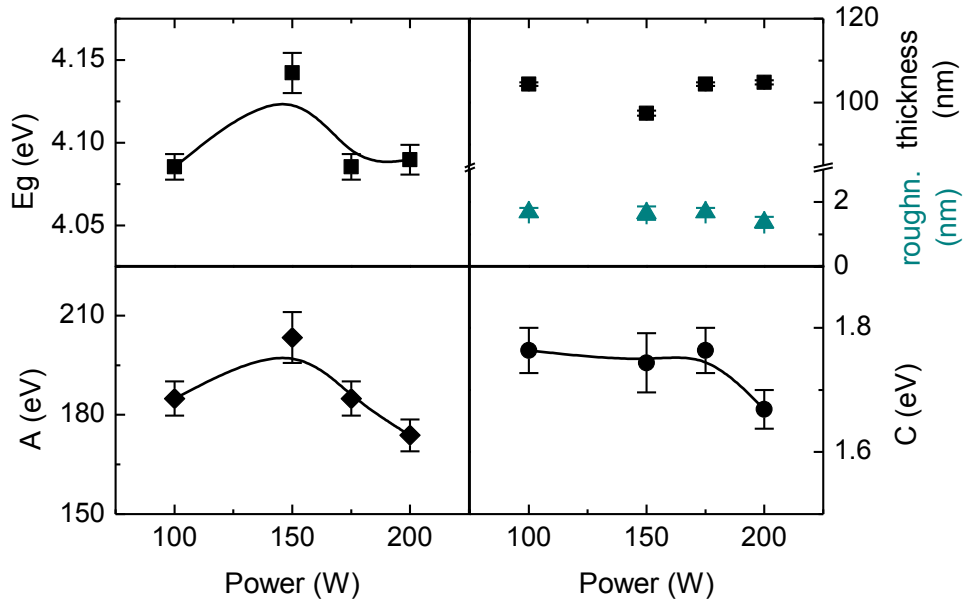


Figure 4.15. Parameters obtained by modulation with Tauc-Lorentz dispersion of SE data of Ta₂O₅ deposited with different rf power.

The pH sensitivity of EIS sensors with a Ta₂O₅ sensitive layer produced with different rf power was evaluated by means of electrochemical impedance spectroscopy measurements. The capacitance-voltage curves ($C(V)$) of EIS sensors exposed to buffer solutions of different pH were obtained by applying a variable dc potential to the sensor back-contact with respect to the reference electrode (Ag/AgCl) at a 500 Hz frequency, as described in *Section 4.1*. At least two sensor measurements were performed and five consecutive measurements were made at each buffer solution. Freshly prepared buffer solutions of pH 4, 7 and 10 with constant ionic strength (0.9) and 50 mM concentration were used to assess pH sensitivity. When changing measurement solution the sensors were thoroughly rinsed with the following solution to be measured.

Figure 4.16 represents the pH sensitivity determination for a EIS sensor with a Ta₂O₅ film produced with 100 W rf power, 0.3 Pa deposition pressure and an Ar:O₂ ratio of 14:1 sccm.

The pH variation leads to a shift in the $C(V)$ characteristics that arises from the surface potential variation due to the ionization of the active surface sites which is dependent on proton concentration (vanHal 1996; Yates 1974). Higher hydrogen ion concentration (lower pH) leads to an increase of positive charge at the surface causing a shift in $C(V)$ curves towards positive potentials, according to the used experimental setup.

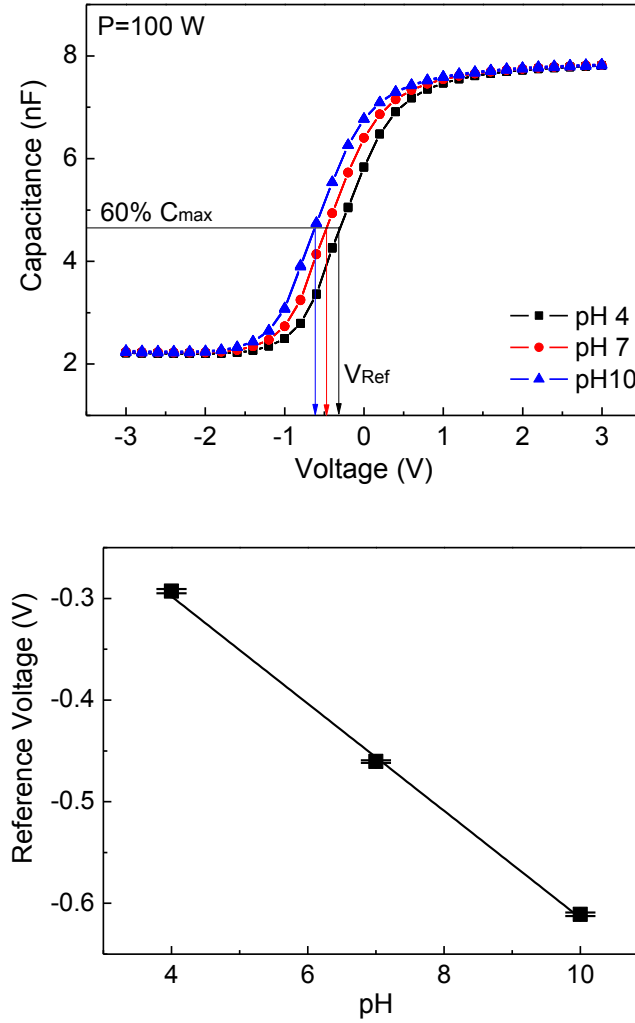


Figure 4.16. C(V) curves (top) and pH sensitivity (bottom) determination for a Ta₂O₅ EIS sensor produced with P=100 W, p=0.3 Pa and Ar:O₂=14/1.

The reference voltages are registered at 60% of the maximum capacitance and pH sensitivity of EIS sensors was obtained by linear fitting of V_{Ref} variation with pH, as depicted in Figure 4.16 (bottom). This procedure was followed for all sensors.

Maximum capacitance of the different sensors did not vary significantly (~7.7 nF) and values are in agreement with a calculated geometrical capacitance (4.1 mm diameter) and considering $\epsilon_{\text{SiO}_2}=3.9$ and $\epsilon_{\text{Ta}_2\text{O}_5}=25$ (Figure 4.2). Low leakage currents (< 8 nA) were obtained for all sensors as expected from the sensor structure.

The influence of the deposition rf power on Ta₂O₅ pH sensitivity is represented in Figure 4.17.

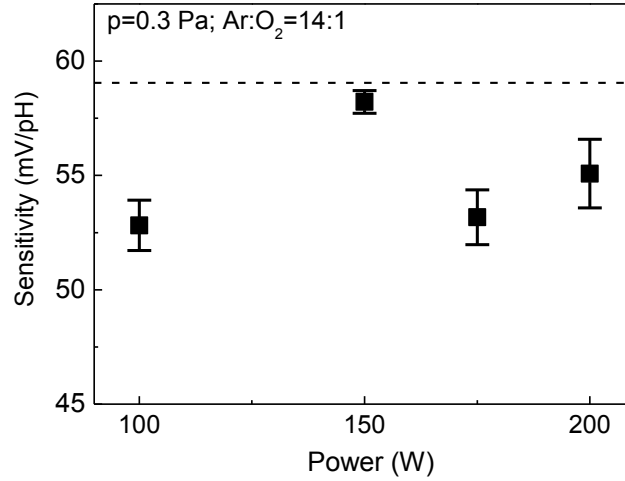


Figure 4.17. Variation of pH sensitivity of Ta₂O₅ EIS sensors produced with different rf power. The dashed line represents maximum Nernst sensitivity of 59.2 mV/pH.

As can be seen all sensors demonstrate high pH sensitivity; above 52 mV/pH. However, at 150 W power a maximum sensitivity of 58.2 ± 0.3 mV/pH was obtained. This can be related to the slightly improved film properties achieved at this deposition conditions.

As sputtering with 150 W rf power appears to slightly improve the films properties and EIS sensors produced with these deposition conditions revealed higher pH sensitivity, this condition was chosen to study the effect of both deposition pressure and Ar:O₂ ratio.

4.2.3. Influence of deposition pressure and Ar:O₂ ratio

The influence of the deposition pressure was studied for samples produced with a rf power of 150 W and various Ar:O₂ ratio. The oxygen content was varied between 0.5 and 3 sccm and maintaining the total gases volume constant at 15 sccm by adjusting the argon content (14.5:0.5; 14:1; 13:2; 12:3 sccm). As these parameters are interconnected the results are presented jointly.

Structural and compositional analysis revealed that amorphous and stoichiometric Ta₂O₅ was obtained regardless of deposition conditions. The results of selected samples are shown in Figure 4.18 (XRD) and Figure 4.19 (RBS).

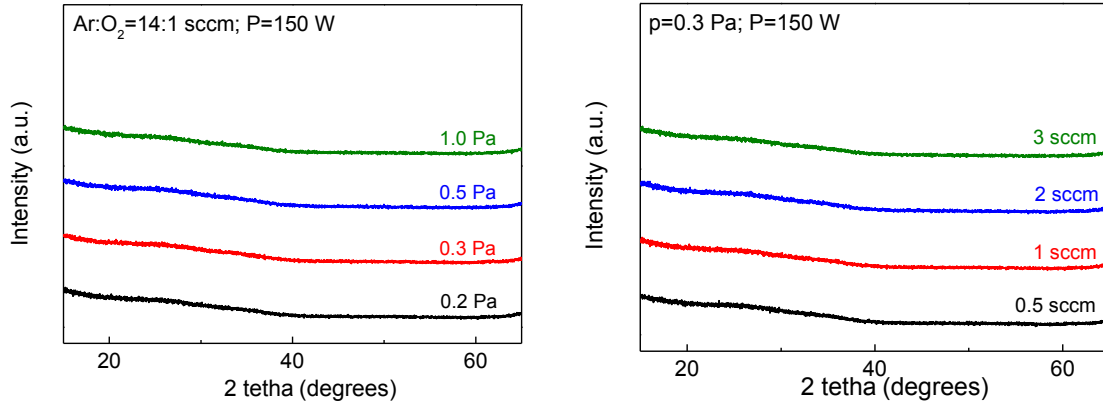


Figure 4.18. XRD diffractograms of Ta₂O₅ EIS sensors produced at different deposition pressures (left) and oxygen content (right).

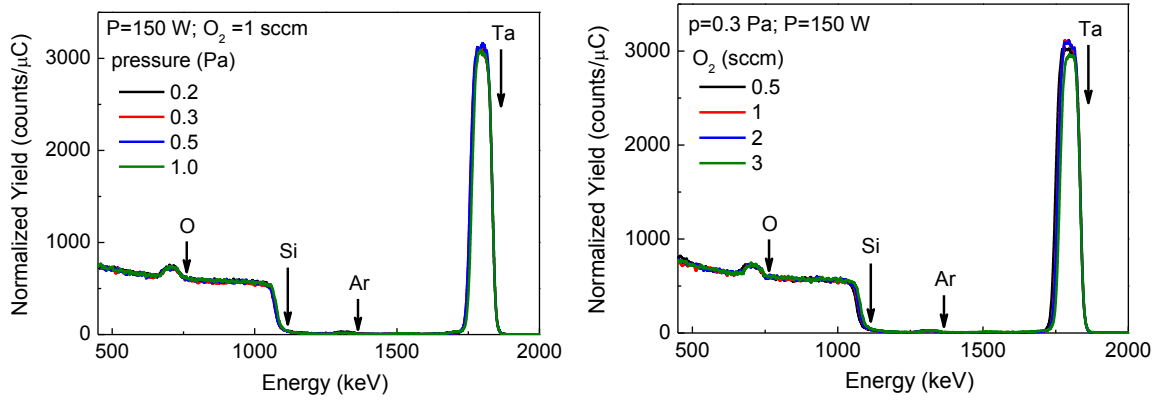


Figure 4.19. RBS spectra of Ta₂O₅ EIS sensors produced at different deposition pressures (left) and oxygen content (right).

A small variation in O/Ta ratio (between 2.2 and 2.8) was observed for films deposited with higher oxygen content however these can be due to the highest error (up to 10%) in the determination of oxygen with RBS technique, as it is more accurate for the analysis of heavier atoms. Nonetheless the data can be well fitted to a simulated RBS spectrum of stoichiometric Ta₂O₅.

SEM and AFM analysis revealed smooth and uniform films with surface roughness below 0.5 nm even at high deposition pressure and oxygen content (Figure 4.20).

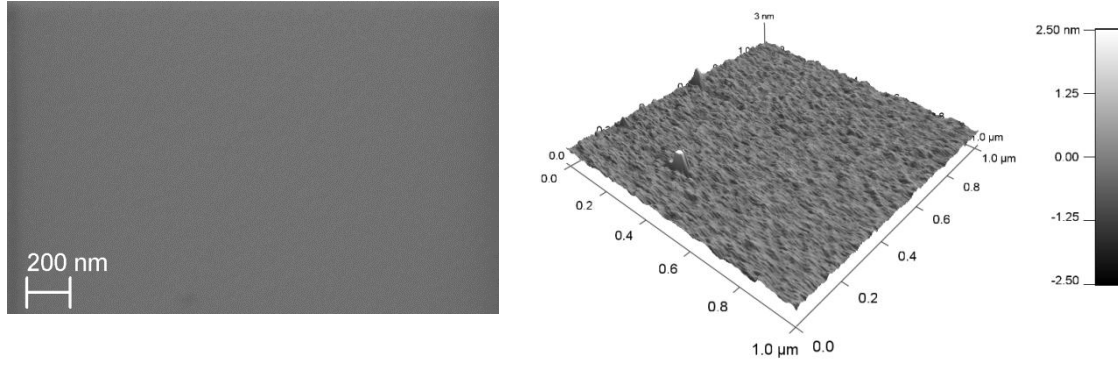


Figure 4.20. SEM (left) and AFM (right) images of the Ta₂O₅ films deposited with a 0.2 Pa pressure, Ar:O₂=12:3 sccm and 150 W rf power.

Optical characterization reveals highly transparent films in the measuring range with an average visible transparency above 84% for all deposition conditions. The calculated optical band gap energies from transmittance data are presented in Table 4.4.

Table 4.4. Optical band gap of Ta₂O₅ films deposited with varied deposition pressure and Ar:O₂.

		Ar:O ₂ (sccm)			
		14.5:0.5	14:1	13:2	12:3
Deposition pressure	0.2 Pa	3.75 eV	4.01 eV	3.91 eV	4.06 eV
	0.3 Pa	4.23 eV	4.16 eV	3.76 eV	4.12 eV
	0.5 Pa	4.17 eV	3.75 eV	3.86 eV	3.74 eV
	1.0 Pa	4.19 eV	3.96 eV	4.01 eV	4.14 eV

Generally, E_{opt} values are in agreement with E_g obtained from SE modulation and reported band gap energy for amorphous Ta₂O₅. (Franke 2000; Pereira 2006)

Parameters obtained by modulation of spectroscopic ellipsometry data for the variation of pressure and Ar:O₂ deposition conditions, namely E_g and A (related to film density) are represented in Figure 4.21.

As can be seen, by increasing oxygen content from 0.5 sccm to 1 sccm there is a slight increase in band gap energy and densification of the films is improved, demonstrated by an increase in the parameter A . The lower band gap and density observed at low oxygen content can be due to a small oxygen deficiency; however this could not be confirmed by RBS as previously explained. Further increase in the oxygen content did not lead to significant properties variation as E_g and A values stabilize. The same tendency is observed for every deposition pressure studied.

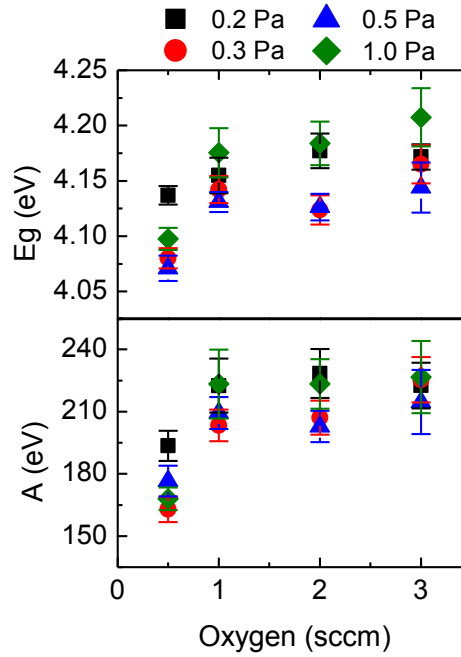


Figure 4.21. Parameters obtained by modulation with Tauc-Lorentz dispersion of SE data of Ta₂O₅ deposited with different deposition pressure and Ar:O₂ ratio.

The pH sensitivity of EIS sensors was assessed by capacitance-voltage characteristics (C(V)) of EIS sensors exposed to buffer solutions of different pH (Figure 4.22).

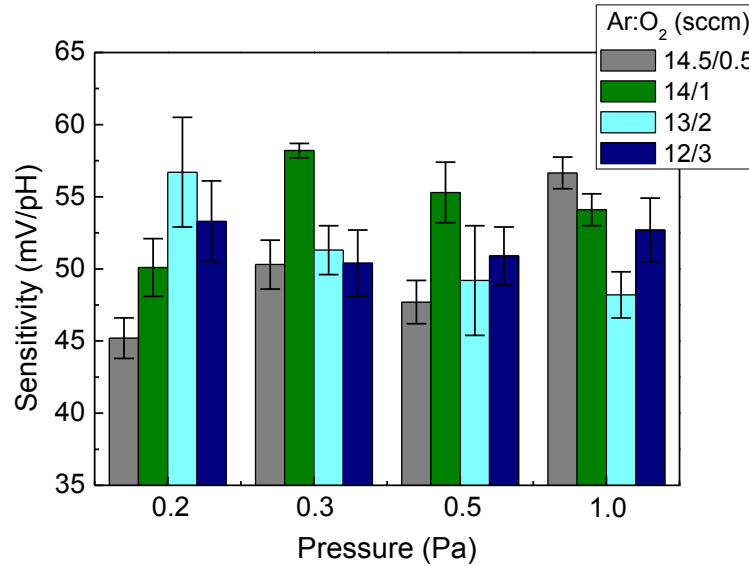


Figure 4.22. Variation of pH sensitivity of Ta₂O₅ EIS sensors produced with different deposition pressure and Ar:O₂ ratio.

A pH sensitivity higher than that of SiO₂, 40 mV/pH (Poghossian 2007a) was obtained for all produced sensors. Typically high sensitivity, expected for Ta₂O₅ (above 55 mV/pH), was attained with selected deposition conditions and some relations between production parameters and pH sensitivity can be drawn.

Intermediate deposition pressures; 0.3 and 0.5 Pa, show the same tendency of pH sensitivity variation with increasing oxygen content. An improvement in pH sensitivity is achieved at 1 sccm O₂. Lower O₂ content might result in moderately sub-stoichiometric films; similarly to what occurs upon rf power variation. Higher oxygen content might lead to the creation of defects within the film (Tomaszewski 2002). Low deposition pressure shows a similar tendency however maximum pH sensitivity is obtained with an oxygen content of 2 sccm. For high deposition pressure (1 Pa) maximum pH sensitivity is obtained at 0.5 sccm O₂; however this oxygen content led to lower density and bad gap energy of the films, as demonstrated by ellipsometry modulation data.

Considering Ta₂O₅ EIS sensors with high pH sensitivity and low variability, produced under moderate deposition conditions that yield high quality films at reasonably high deposition rates; the optimal Ta₂O₅ sensing layer was obtained with the following deposition conditions: 150 W rf power; 0.3 Pa pressure and 14:1 Ar:O₂ ratio.

4.3. Influence of post-production treatments

4.3.1. Influence of annealing temperature

The influence of post-deposition annealing temperature was studied for Si/SiO₂/Ta₂O₅ samples produced with a rf power of 150 W, a deposition pressure of 0.3 Pa and an Ar:O₂ ratio of 14:1 sccm; as defined as in the previous section. In order to estimate the crystallization temperature of Ta₂O₅ thermal annealing was performed up to 800 °C in an air atmosphere with a heating rate of 10 °C/min (Branquinho 2012).

Structural analysis of the samples was performed by XRD (Figure 4.23). Results show an absence of diffraction peaks that indicate the existence of an amorphous phase, which is maintained after post-deposition annealing up to 600 °C. At 700 °C the Ta₂O₅ film starts to crystallize in an orthorhombic phase as identified by comparison of diffraction peaks with reference crystallographic data file 98-004-8854 (vertical lines) and at 800 °C the diffraction peaks are better defined consistent with improved crystallinity as confirmed by SEM and AFM analyses.

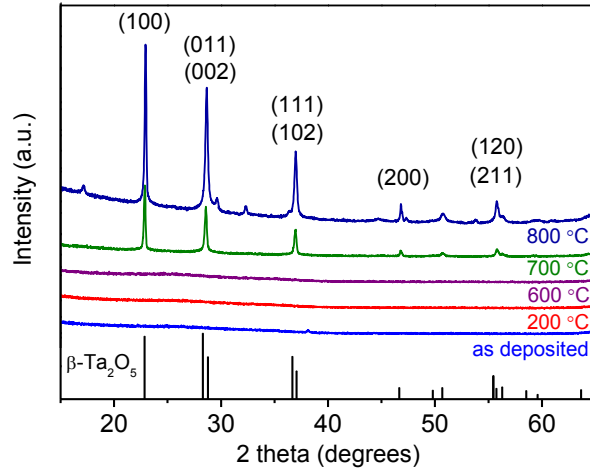


Figure 4.23. X-ray diffractogram of Ta₂O₅ film before and after post deposition annealing (vertical lines represent diffraction planes of orthorhombic Ta₂O₅).

Compositional analysis was performed on Al/Si/SiO₂/Ta₂O₅ samples so in the RBS spectra two distinct contributions of silicon (SiO₂ and c-Si) and of oxygen (SiO₂ and Ta₂O₅) can be identified; as represented in Figure 4.24. Results show that stoichiometric Ta₂O₅ films were obtained regardless of annealing temperature, as RBS spectra of samples annealed at different temperature do not reveal significant variation and are well fitted to the simulated spectra of a stoichiometric Ta₂O₅ film.

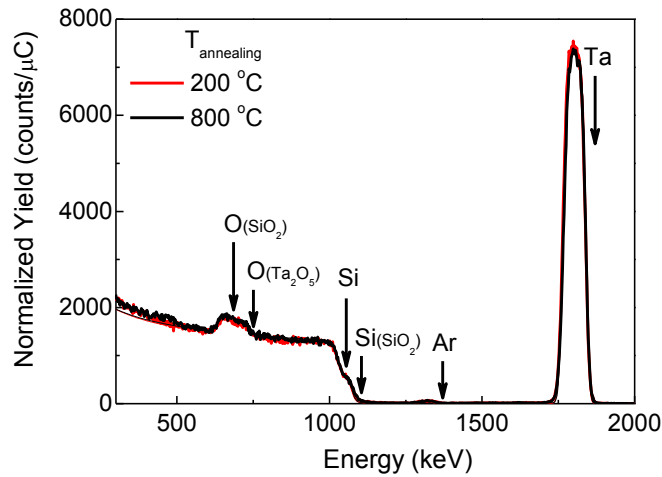


Figure 4.24. RBS spectra of samples annealed at 200 °C and 800 °C with respective fit curves.

Surface morphology was studied by SEM and AFM (Figure 4.25). For temperature up to 600 °C, results show a very homogeneous and smooth surface, with a root mean square roughness (R_{rms}) of less than 0.25 nm. At 700 °C, the Ta₂O₅ film starts to crystallize and surface morphology changes, depicting two distinct areas corresponding

to amorphous and crystalline phases. At 800 °C, crystallinity is improved and a maximum peak-to-valley height of 10 nm was observed.

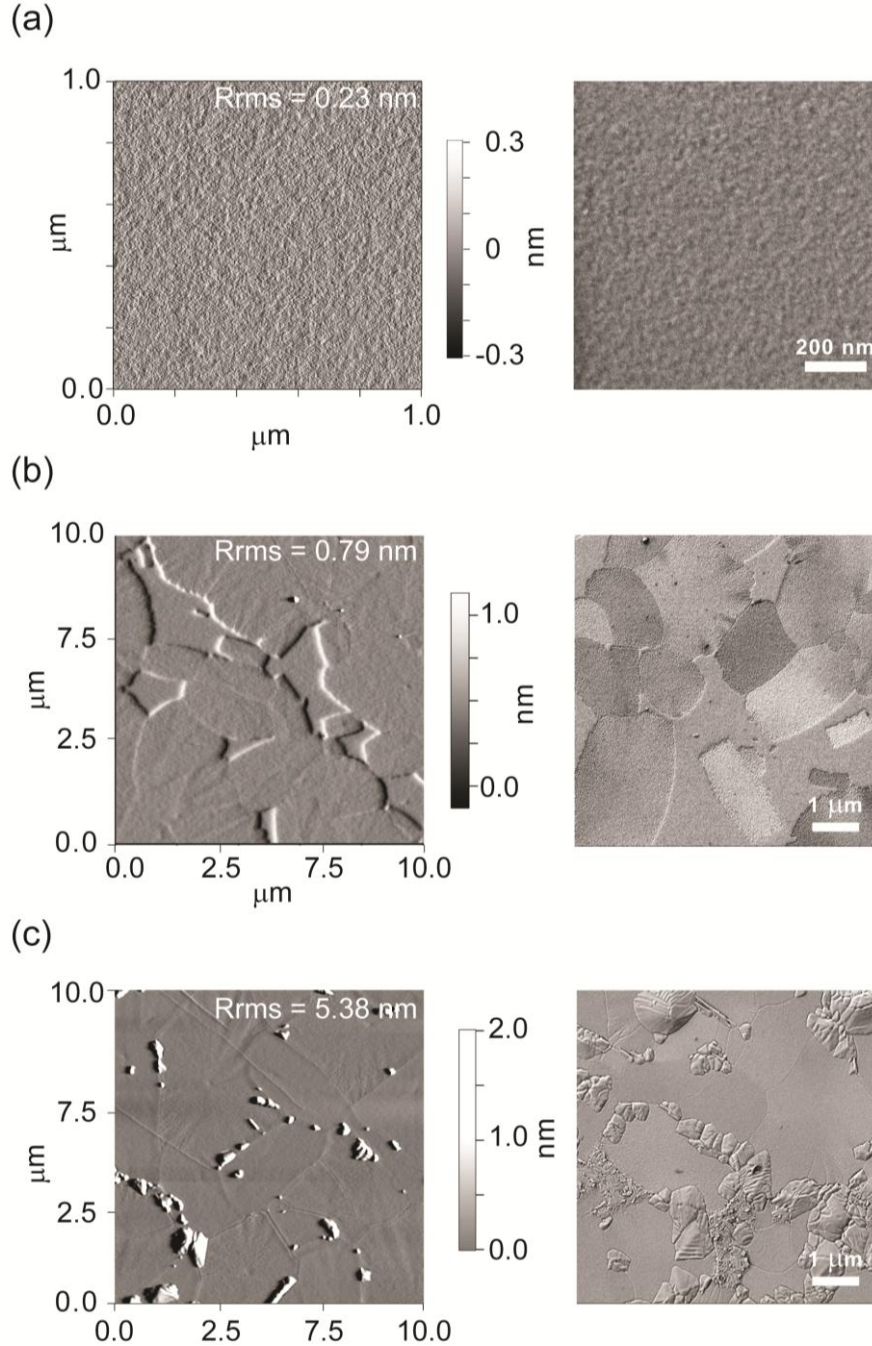


Figure 4.25. Morphological characterization of Ta₂O₅ sensors: SEM micrograph and AFM deflection images (R_{rms} calculated using height profile) of Ta₂O₅ surface of sensors a) as deposited; b) annealed at 700 °C and c) 800 °C.

The spectroscopic ellipsometry (SE) analysis of the samples was performed by means of a Tauc-Lorentz dispersion to fit the data obtained for Ta₂O₅ films, as in the previous sections. However with the four layer model (Figure 4.13) used previously the fitting

results were not satisfactory for crystalline Ta₂O₅ films (high values of goodness of fit; $\chi^2 > 30$), so an additional interfacial layer (IL) between SiO₂ and Ta₂O₅ was introduced to simulate any modification that may occur at this interface during crystallization (or even prior to this). This layer is based on a classical oscillator used to describe SiO₂ but was allowed to vary under fitting procedure. This five layer model (Figure 4.26 inset) was applied to all samples to guarantee data comparability. The simulation results for the interfacial layer thickness and band gap energy are depicted in Figure 4.26.

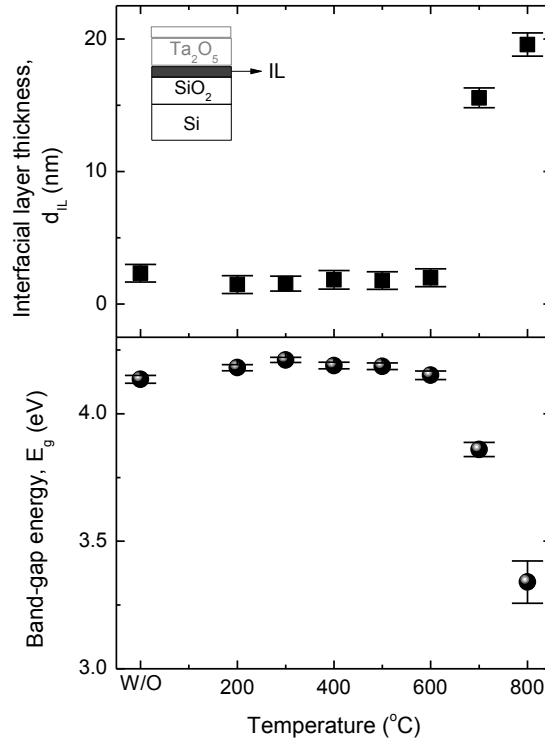


Figure 4.26. Spectroscopic ellipsometry simulation results of the interfacial layer thickness and band-gap energy of the Ta₂O₅ sensors annealed at various temperatures.

Up to Ta₂O₅ crystallization, no significant change in film thickness or roughness occurred and values are in agreement with morphological analysis. The interfacial layer's thickness is below 2.5 nm for amorphous films. Upon crystallization at 700 °C, the interfacial layer thickness increases, which can be explained by the formation of an intermixed layer that may act as incubation layer. The band gap energy decreases upon crystallization and data are in agreement with reported values for both amorphous and poly-crystalline Ta₂O₅ (Franke 2001; Pereira 2006).

The imaginary component of the dielectric function obtained from spectroscopic ellipsometry data modulation is depicted in Figure 4.27. There is an increase of the dielectric function's maximum with annealing temperature which indicates a

densification of the films and at 700 °C the peak becomes less broad indicating a short range order increase, coherent with crystallization.

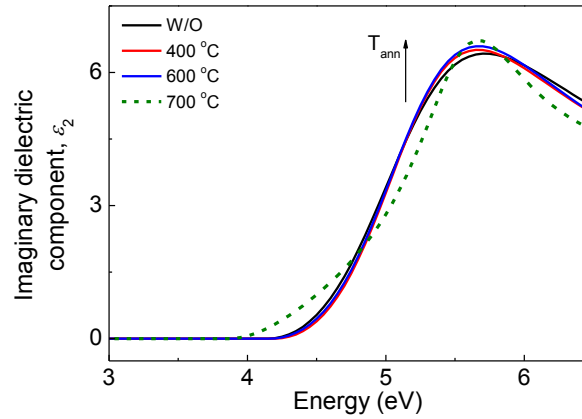


Figure 4.27. Imaginary component of the dielectric function of Ta₂O₅ sensors annealed at various temperatures; obtained from spectroscopic ellipsometry data modulation.

The pH sensitivity of produced Ta₂O₅ thin films was assessed by electrochemical impedance measurements of EIS sensors by exposing the Ta₂O₅ sensitive membranes annealed at different temperatures to solutions of varied pH.

The pH sensitivity dependence of Ta₂O₅ sensing layers on annealing temperature is shown in Figure 4.28.

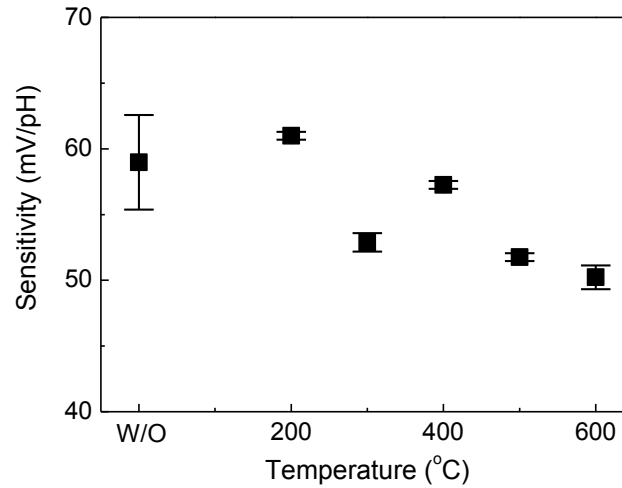


Figure 4.28. Variation of pH sensitivity of Ta₂O₅ EIS sensors with post-deposition annealing temperature.

All sensors with an amorphous Ta₂O₅ sensing layer (up to 600 °C) show pH sensitivity above 50 mV/pH as expected for Ta₂O₅, nevertheless maximum sensitivity was obtained for an annealing temperature of 200 °C. Although the as deposited samples have high pH sensitivity, significant improvement of sensor stability is achieved with

the post-deposition annealing treatment as translated by a considerable reduction of the standard deviation of each measurement.

With increasing annealing temperature, the C(V) curves were shifted towards positive potentials with the exception for the sensor annealed at 200 °C. For EIS sensors with a crystalline Ta₂O₅ film, the curves were shifted beyond the equipments voltage range ([−8; 8] V) thus for these samples pH sensitivity could not be assessed. To discard the possibility of a solution induced effect, C(V) measurements were performed in identical manner to EIS sensors on aluminum gated devices where the gate voltage was applied by means of an electrical probe. Results reveal a similar tendency in both solution and metal-gated devices as can be seen in Figure 4.29.

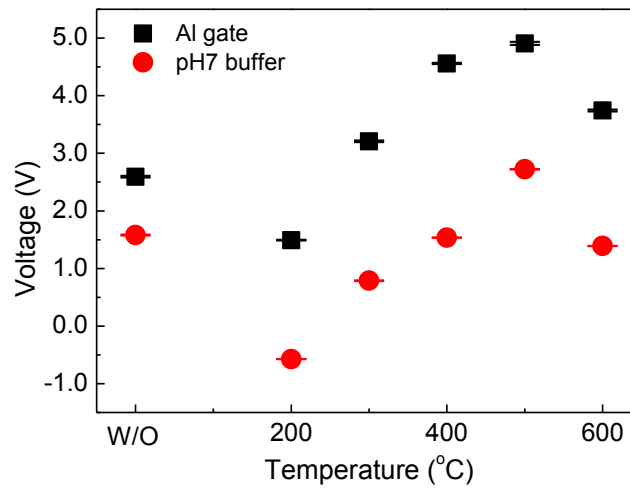


Figure 4.29. Variation of the reference voltage obtained at 60% of maximum capacitance with annealing temperature for solution and aluminum- gated Ta₂O₅ EIS sensors.

A shift in the C(V) characteristics of metal-semiconductor-insulator (MIS) devices can be a consequence of semiconductor/oxide interfacial effects or a work function difference that arises from charge accumulation on the Ta₂O₅ surface.

The formation of an interfacial layer upon deposition of oxide films on silicon substrates, its growth with annealing temperature and its influence on C(V) characteristics of devices is well known (Chaneliere 1998; Ono 1999; Pan 2009). In order to minimize interfacial effects and maintain the semiconductor/oxide interface constant, Ta₂O₅ films were deposited on Si/SiO₂ substrates; as explained in *Section 4.1.3*. Also, spectroscopic ellipsometry analysis of the sensors indicates an interfacial layer formation between SiO₂ and Ta₂O₅ but it is only relevant for samples annealed at 700 °C and 800 °C which may be consistent with the presence of an incubation layer.

In order to infer on surface charge variation with annealing temperature contact angle measurements of all samples were performed (Table 4.5).

Table 4.5. Sensitivity and contact angle variation with annealing temperature.

Annealing T (°C)	Sensitivity (mV/pH)	Contact angle (degrees)
W/O	58.9±3.6	94.9
200 °C	60.9±0.3	74.6
300 °C	52.9±0.7	86.1
400 °C	57.2±0.3	88.8
500 °C	51.7±0.3	83.7
600 °C	50.2±0.9	89.0
700 °C	–	84.8
800 °C	–	83.3

A contact angle decrease occurred for the sample annealed at 200 °C consistent with an increase of hydroxyl surface active sites (Barhoumi 2010) which can explain the sensitivity improvement obtained for this sample. However the observed contact angle changes are small and cannot justify the observed C(V) curves shift. A possible explanation could be that the post-deposition annealing was performed in an air atmosphere. Nevertheless high pH sensitivity was obtained for a low post-deposition annealing temperature; 200 °C (Branquinho 2012).

4.3.2. Influence of surface plasma treatments

The use of room temperature plasma processes has been reported to increase pH sensitivity of insulator layers either by promoting an increase in film roughness, thus increasing sensitive area, or in the number of active surface sites (Kim 1998; Lai 2008; Li-Te 2001).

The influence of post-production room temperature surface plasma treatments on the Ta₂O₅ sensing characteristics was assessed by exposing the samples to either argon or oxygen plasma.

4.3.2.1. Influence of argon plasma

The effect of surface treatment with argon plasma was performed after film deposition by exposing the sensors to Ar (15 sccm) plasma at a 0.4 Pa pressure and varying the rf power applied to the substrate (10, 20 and 30 W) and process time (2, 5 and 10 minutes). Annealing at 200 °C for 1 h in air was performed after the plasma treatment.

It was expected that the bombardment of the Ta₂O₅ film with high energy argon ions induced a surface roughness increase yielding a higher sensitive surface area and hence a higher pH sensitivity. However this was not confirmed by AFM or spectroscopic ellipsometry measurements. In fact a surface roughness ($R_{rms} < 0.25$ nm) identical to that of the untreated film was obtained even after the harshest argon plasma treatment (Figure 4.30).

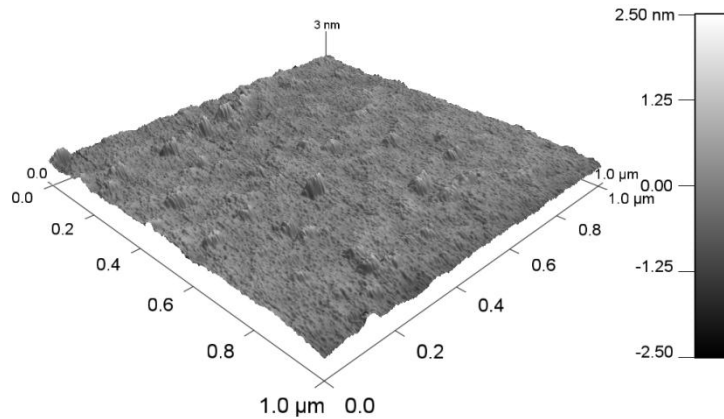


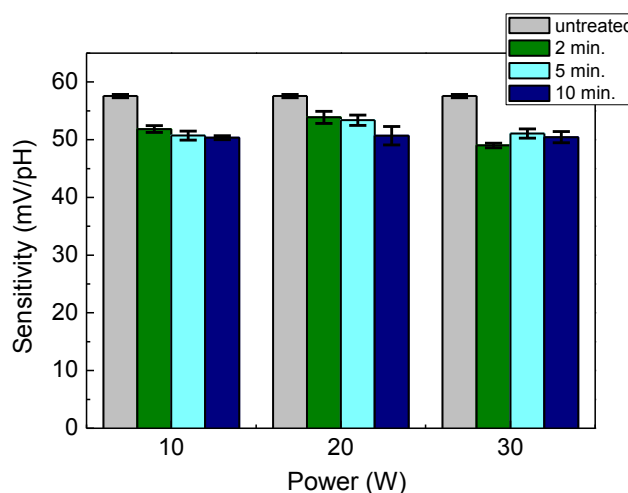
Figure 4.30. AFM image of Ta₂O₅ sensor after argon plasma treatment at 30 W for 10 minutes.

Surface roughness obtained by SE data modulation (Table 4.6) are slightly higher but still no significant variation is observed and values are similar to that of the untreated film; 1.6 nm.

Table 4.6. Parameters obtained by modulation with Tauc-Lorentz dispersion of SE data of Ta₂O₅ films exposed to argon plasma under different conditions.

Power (W)	Time (min)	Thickness (nm)	Roughness (nm)	E _g (eV)	χ ²
10	2	91.5	1.5	4.26	2.84
	5	93.8	1.2	4.16	3.29
	10	96.0	1.3	4.18	2.81
20	2	95.0	1.0	4.15	3.33
	5	94.1	1.5	4.15	3.73
	10	94.5	1.1	4.16	3.36
30	2	95.0	1.0	4.15	3.38
	5	93.0	1.4	4.17	2.65
	10	95.4	2.1	4.16	3.06

The influence of argon plasma treatment on Ta₂O₅ pH sensitivity is depicted in Figure 4.31. Argon plasma treated EIS sensors revealed a sensitivity ranging from 49±0.5 to 54±1 mV/pH, which is lower than for untreated samples (58±0.3 mV/pH).

Figure 4.31. Ta₂O₅ pH sensitivity variation with argon plasma surface treatments.

In general, the argon plasma treatment has a negative influence on the pH sensitivity of Ta₂O₅. The bombardment of the Ta₂O₅ sensitive layer with high energy argon ions appears to damage the oxide's surface as pH sensitivity significantly decreases even with the mildest process conditions (10 W; 2 minutes). Also an increase in measurement variability was noted for most samples, as represented by the increased measurement error.

The increase of rf power applied during the plasma treatment leads to a significant decrease in pH sensitivity of the Ta₂O₅ layer as the poorer results were obtained with 30 W rf power. Although sensitivity also decreases with treatment time increase (except for 30 W) variations are smaller and, for most cases, are within measurement error.

The C(V) curves of argon plasma treated samples were shifted towards more positive potentials when compared to untreated samples. The reference voltages of selected samples exposed to a pH 7 buffer solution are represented in Figure 4.32.

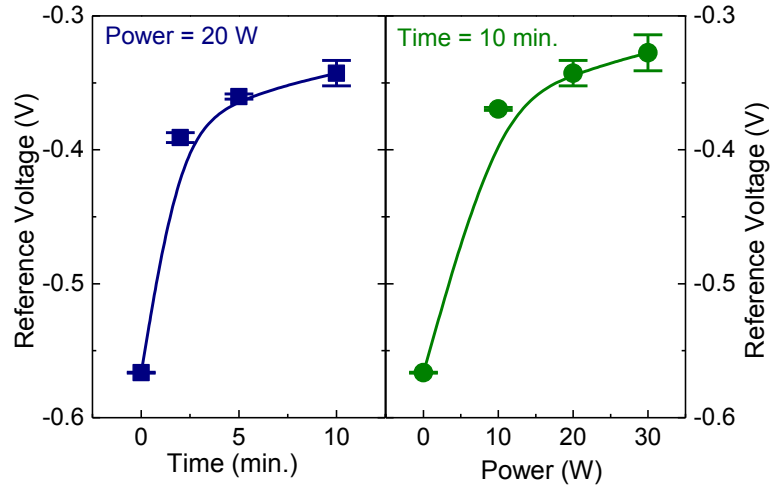


Figure 4.32. Variation of reference voltage at pH 7 with argon plasma surface treatments.

A shift towards more positive potentials can be explained by an increase of positive charges at the oxide surface; such as argon ions. As can be seen in Figure 4.32, a higher reference voltage shift towards positive potentials is obtained for increasing time and rf power process conditions, which is in agreement with an increase of argon ions accumulation at the oxide surface.

The decrease in sensitivity with increase time and power of argon plasma treatment might be a consequence of the blocking of surface active sites by argon ions.

Considering that the sputtering of dielectric materials, such as Ta₂O₅, requires high rf power due to their inert nature, the low rf power applied during the argon plasma treatment might not be sufficient to promote the removal of material; as demonstrated by the lack of surface roughness increase confirmed by AFM and spectroscopic ellipsometry data. However the process conditions may instead lead to the accumulation of positive argon ions at the oxides surface resulting in a positive shift of C(V) curves and a decrease in pH sensitivity due to the blocking of surface active sites.

4.3.2.2. Influence of oxygen plasma

The effect of surface treatment with oxygen plasma was performed after film deposition by exposing the sensors to O₂ (15 sccm) plasma at a 0.4 Pa pressure and varying the rf power applied to the substrate (10, 20 and 30W) and process time (2, 5 and 10 minutes). Annealing at 200 °C for 1 h in air was performed prior to plasma treatment.

The exposure to pure O₂ plasma was intended to increase the number of active surface sites and thus improve pH sensitivity of the Ta₂O₅ EIS sensors as reported by Yin et al (2001) for a silicon nitride sensing layer.

Spectroscopic analysis of the sensors after oxygen plasma treatment revealed that band gap energy and surface roughness obtained by data modulation (Table 4.7) did not vary significantly upon bombardment of the films with oxygen ions; similarly to the argon plasma treatment.

Table 4.7. Parameters obtained by modulation with Tauc-Lorentz dispersion of SE data of Ta₂O₅ films exposed to oxygen plasma under different conditions.

Power (W)	Time (min)	Thickness (nm)	Roughness (nm)	E _g (eV)	χ ²
10	2	92.1	1.4	4.17	2.91
	5	92.1	1.7	4.24	3.81
	10	92.0	1.6	4.23	3.26
20	2	95.7	1.6	4.15	2.43
	5	91.9	1.6	4.17	3.47
	10	93.4	1.7	4.21	3.19
30	2	94.9	1.8	4.15	3.25
	5	93.7	1.4	4.19	3.53
	10	97.0	1.8	4.16	3.74

The influence of oxygen plasma treatment on Ta₂O₅ pH sensitivity is depicted in Figure 4.33. Oxygen plasma treated EIS sensors revealed a high sensitivity increase, ranging from 1.5 up to 3.5 times the untreated sample depending on process conditions, however measurement variability also increases.

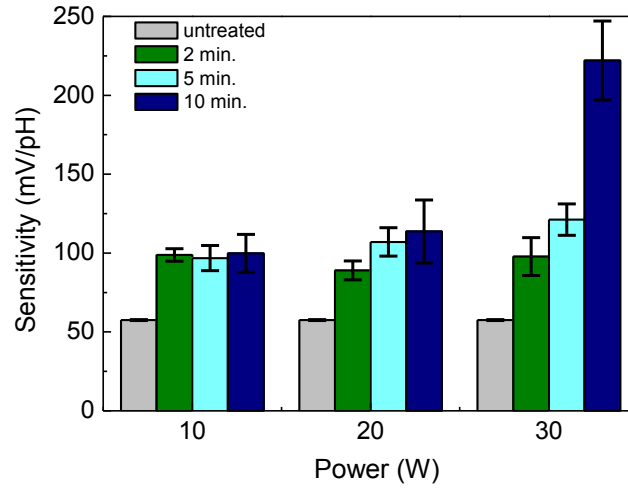


Figure 4.33. Ta₂O₅ pH sensitivity variation with oxygen plasma surface treatments.

Generally, pH sensitivity increases with both power and duration of plasma treatment. Although at 10 W sensitivity appears to be independent of process time; at 20 W and 30 W sensitivity increases with treatment time however for 30 W it is more pronounced and a process time dependency is clear.

As noted for the argon plasma treatment, the sensors C(V) curves are also shifted from the untreated sensor characteristics. However, after O₂ surface plasma treatment, C(V) curves shift towards more negative potentials which can be explained by an increase of negative charge at the oxide's surface induced by the oxygen ions.

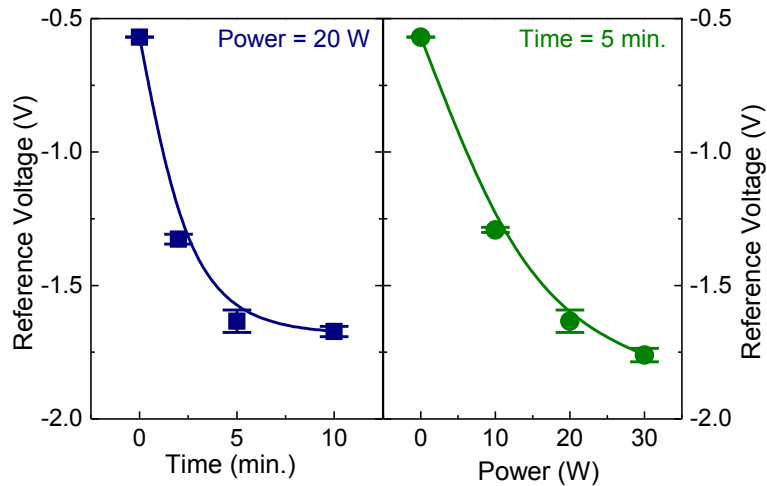


Figure 4.34. Variation of reference voltage at pH 7 with oxygen plasma surface treatments.

The higher concentration of oxygen ions at the oxide surface can justify the pH sensitivity increase; however obtained values are much higher than the maximum theoretically predicted by the Nernst equation (2.27). This clearly indicates that additional mechanisms that are not being accounted for must exist.

The oxygen plasma enhanced pH sensitivity effect is temporary as it decreases to original values ($\sim 57 \pm 5$ mV/pH) after one day and results suffer from poor reproducibility. Nevertheless, the most effective oxygen surface plasma treatment appears to be the one obtained for a 5 min. exposure with 30 W applied rf power since it yielded the best compromise between sensitivity enhancement and measurement variability; 121 ± 10 mV/pH (a ~ 2 times increase) and this sample was used to successfully fabricate an enzyme-based penicillin sensor (see *Section 5.1.3.*)

Summarising; the effect of deposition and post-deposition conditions on the pH sensitivity of room temperature rf sputtered Ta₂O₅ was investigated. Structural, morphological and optical features of these films vary slightly with deposition conditions but generally amorphous, stoichiometric, smooth Ta₂O₅ films were obtained. Crystallization of Ta₂O₅ in an orthorhombic phase occurs at 700 °C and surface morphology reveals increased surface roughness.

High pH sensitivity, above 50 mV/pH, was obtained for the majority of produced sensors. Near Nernstian pH sensitivity of 58 ± 0.3 mV/pH was achieved for the optimal Ta₂O₅ sensing layer produced with the following deposition conditions: 150 W rf power; 0.3 Pa pressure and 14:1 Ar:O₂ ratio and low temperature annealing at 200 °C for one hour.

Post-production surface treatments with argon plasma decreased pH sensitivity due to the blocking of Ta₂O₅ active surface sites by argon ions. Oxygen plasma treatment effectively increased pH sensitivity a maximum of 3.5 times the untreated sensor; however treated sensors suffered from instability and reproducibility issues. The obtained sensitivity values were above the theoretical maximum indicating the existence of additional sensing mechanisms.

Chapter 5. Label-free detection of biomolecules

5.1. Penicillinase-modified field effect devices (PenFEDs).....	107
5.1.1. Penicillin detection with Ta ₂ O ₅ based PenFEDs.....	109
5.1.2. Penicillin detection with O ₂ plasma treated Ta ₂ O ₅ based PenFEDs	112
5.2. Label-free detection of DNA with field effect devices	114
5.2.1. DNA structure	115
5.2.2. Intrinsic charge based detection of DNA.....	117
5.2.3. Non-specific DNA concentration detection	122
5.3. DNA amplification monitoring	123
5.3.1. DNA amplification via polymerase chain reaction (PCR).....	123
5.3.2. Field effect detection of PCR amplification of DNA	125
5.3.3. Loop-mediated isothermal DNA amplification (LAMP)	133
5.3.4. Field effect real-time monitoring of LAMP DNA amplification	133

The results presented in this chapter were partially published in R. Branquinho, B. Veigas, J. V. Pinto, R. Martins, E. Fortunato and P. V. Baptista, '*Real-time monitoring of PCR amplification of proto-oncogene c-MYC using a Ta₂O₅ electrolyte–insulator–semiconductor sensor*', Biosensors and Bioelectronics, 2011, 28, p. 44-49 doi:10.1016/j.bios.2011.06.039.

Chapter 5. Label-free detection of biomolecules

Field effect devices have been proven to be sensitive to electrical interactions at or nearby the sensitive layer/electrolyte interface so, in principle, nearly any chemical or biochemical reaction leading to chemical or electrical changes at this interface can be measured by coupling of the FED with a specific biological agent. The label-free detection of biomolecules is thus possible as the detection mechanism is solely based on these interactions; meaning that conventional labelling of biomolecules is avoided. Functionalization of the sensitive layer is possible for a variety of biological molecules to yield bio-specific sensors. Field effect devices are thus sensitive, label-free and versatile biosensors.

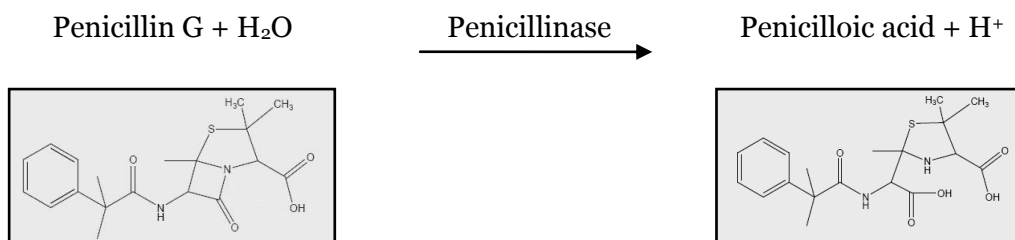
In this chapter the detection of penicillin with penicillinase functionalized EIS sensors comprising the optimized Ta₂O₅ sensitive layer is presented and discussed. These sensors were also applied to the label free detection of DNA amplification via polymerase chain reaction (PCR) and loop-mediated isothermal amplification (LAMP) and the obtained results were compared to conventional fluorescence based DNA detection methods.

5.1. Penicillinase-modified field effect devices (PenFEDs)

The discovery of penicillin revolutionized the pharmaceutical industry as it is an effective drug in the treatment of various diseases and infections such as syphilis, pneumonia, arthritis, meningitis, and endocarditis. Penicillin, PenG, is a β -lactam antibiotic (PenG 2011) which antibacterial properties are related with the very labile lactam ring comprised in its molecular structure. The mechanism of action of these antibiotics is the irreversible binding of PenG molecule to a specific protein at the bacterial cell wall, inhibiting its growth and thus causing cell lyses (Fenollar-Ferrer 2002; Kadurina 2004). Penicillins are still widely used antibiotics, consequently the determination of different kinds of penicillin is very important in drug control-analysis, (bio)chemical process control, pharmaceutical production, environmental monitoring and for food control (Gaudin 2001; Poghosian 2001; Schneider 2010).

The sensing principle of PenG with penicillinase-modified FEDs is based on the detection of a pH variation that arises from the penicillinase–penicillin reaction. In the functionalized sensor the enzyme penicillinase acts as the biocatalyst, it hydrolyzes

penicillin dissolved in aqueous solution to penicilloic acid liberating a hydrogen ion, as represented by the simplified reaction.



As a result, the local hydrogen ion concentration increases and the consequent pH change can be detected by the underlying pH-sensitive transducer (Dzyadevych 2006; Poghossian 2001; Schoning 2006).

A variety of penicillinase-modified FEDs differing in sensor design, sensitive gate material and enzyme concentration and immobilization method, and other practical conditions, have been developed for penicillin detection. An overview of penicillinase EnFEDs, emphasizing these parameters is given in Table 5.1.

Table 5.1. Overview of penicillinase modified field effect devices for penicillin detection.

Device	c-Si pHFET/ PenFET	poly-Si ISFET	c-Si pHFET/ PenFET	c-Si/SiO ₂ EIS	c-Si/SiO ₂ EIS	
Sensitive surface	Si ₃ N ₄	Si ₃ N ₄	Ta ₂ O ₅	nc-Diamond	Ta ₂ O ₅	
Immobilization conditions	Cross-linking	Physical adsorption	Physical adsorption	Physical adsorption (P. A.)	P. A.	P. A. to PAMAM /swCNT film
Buffer solution	5 mM Phosphate pH 7.2	5 mM Phosphate pH 7	0.2 mM Polymix pH 8	0.5 mM Polymix pH 8	0.2 mM Polymix pH 8	
[PenG] range	0.2-6 mM	1-7 mM	0.05-1 mM	0.005-2.5 mM	0.25-25 mM	
Sensor response	16 mV/mM	11 mV/mM	120±10 mV/mM	60-70 mV /decade	100 mV /decade	116 mV /decade
Reference	Caras 1980	Estrela 2005	Poghossian 2001	Abouzar 2008	Siqueira 2009	

c-Si: crystalline Si; poly-Si: poly-crystalline Si; nc-Diamond: nanocrystalline diamond; swCNT: single-walled carbon nanotube; PAMAM: polyamidoamine dendrimers; [PenG]: penicillin concentration. Ag/AgCl reference electrode was used in all cases.

5.1.1. Penicillin detection with Ta_2O_5 based PenFEDs

Penicillinase-modified sensors were constructed by coating the sensitive membrane with a penicillinase layer. Penicillinase (*Bacillus cereus* 1650 units/mg protein; Sigma-Aldrich) was adsorptively immobilized directly onto the pH sensitive Ta_2O_5 film. A uniform textured porous enzyme layer was obtained as confirmed by SEM morphological analysis (Figure 5.1).

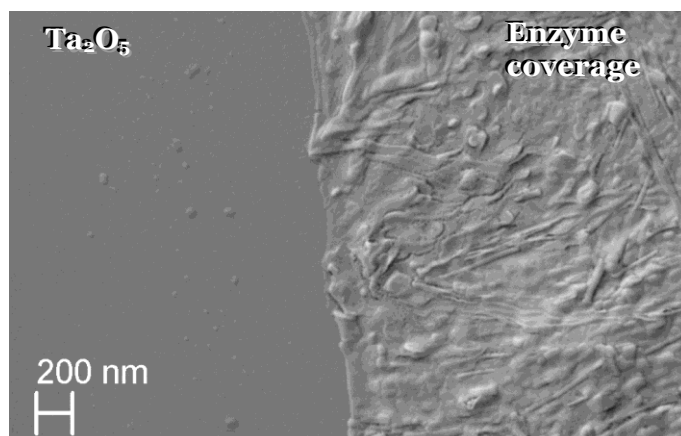


Figure 5.1. SEM micrograph of enzyme functionalized Ta_2O_5 EIS sensor.

The enzyme solution (3 mg/mL penicillinase in 50 mM phosphate buffer pH 7.5) was pipetted onto the sample (40 μ L) and incubated at room temperature in a humid chamber for 1 hour. The sensors were then rinsed with buffer solution to remove any unadsorbed penicillinase. Penicillinase functionalized sensors were then tested by assessing C(V) characteristics variation from exposure to penicillin solutions with increasing concentration; 1 mM to 10 mM penicillin in 5 mM phosphate buffer pH 7 (working buffer). Three sensors were tested and three consecutive C(V) curves were measured for each concentration; upon solutions change the sensor was rinsed with the working buffer. Measurements were performed in an identical manner as for the pH sensors.

The working buffer (5 mM phosphate buffer pH 7) was measured prior to enzyme immobilization and after as a reference solution for 0 mM penicillin. Variations observed in both reference voltage (2 mV) and accumulation capacitance (0.03 nF) were within measurement variability indicating that the enzyme adsorption did not significantly affect the sensors characteristics. The C(V) characteristics of penicillinase functionalized sensors are depicted in Figure 5.2.

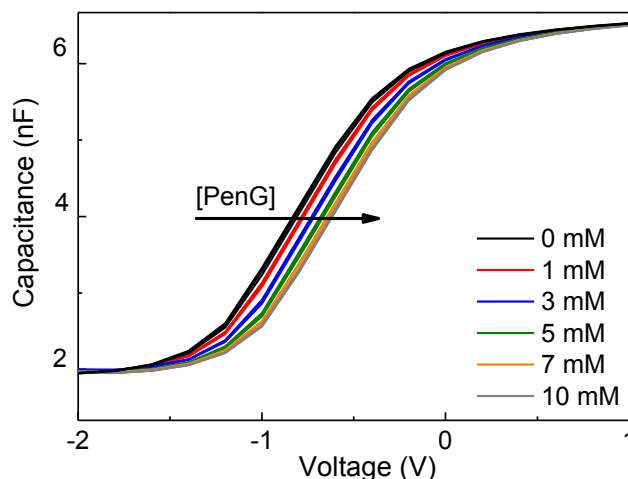


Figure 5.2. Variation of $C(V)$ characteristics of a penicillinase functionalized sensor when exposed to penicillin solutions of increasing concentration.

The curves shift to higher potentials upon penicillin concentration increase which is in agreement with a pH decrease that arises from proton production due to penicillin hydrolysis. The sensitivity to penicillin can be directly correlated to the local pH change induced by the enzymatic reaction, as depicted in Figure 5.3.

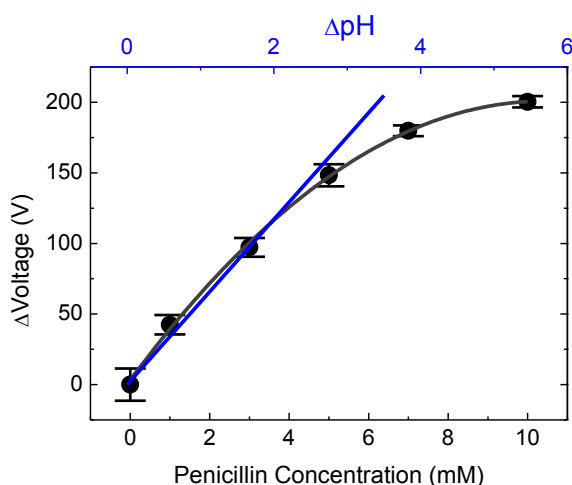


Figure 5.3. Sensitivity of a penicillinase functionalized sensor to penicillin and its correlation with pH variation.

The results show that a typical enzymatic reaction curve was obtained where the sensor signal variation with analyte concentration is linear until saturation is reached. Generically a sensitivity of 139 ± 11 mV/decade was obtained, as this was the signal variation induced by a tenfold increase in penicillin concentration. Sensitivity is higher for low penicillin concentrations with a tendency to decrease for more concentrated

solutions. A linear variation of reference voltage was found for penicillin concentrations below 4 mM and a sensitivity of 29 ± 7 mV/mM penicillin was obtained in this range. Considering that the sensor has a pH sensitivity of 58.2 ± 0.3 mV/pH, the hydrolysis of a 4 mM penG solution generates a local pH variation of two pH units meaning that at the sensor surface the local pH is ~ 5 . The decrease in sensitivity above 4 mM penicillin might be a consequence of the local pH decrease to pH 5 which is far from the optimum pH for penicillinase (pH 6.5-7.5) which could cause enzyme inhibition (Dzyadevych 2006; Waley 1975).

Sensors were stable for three days if stored in working buffer at 4 °C. However sensitivity decreased with storage time and was lost after one week, which might be a consequence of enzyme activity loss and/or enzyme desorption upon usage.

The direct comparison of FEDs sensor performance and even sensitivity is quite difficult due to the numerous differences not only in the sensor itself (device structure; sensitive material and its production method; sensitive surface area) but also in the experimental details (measurement setup; buffer solutions; biological molecules concentration). Nevertheless the results obtained in this work are in agreement with published sensitivity values of EIS based penicillinase FEDs (Table 5.1).

Moreover, the device structure (p-Si/SiO₂/sensitive layer) and experimental conditions are similar enough to allow a realistic comparison between the obtained results and those reported by Abouzar *et al* (2008) and Siqueira *et al* (2009). Penicillinase FEDs with a sensitive layer of Ta₂O₅ show better results than of nanocrystalline diamond, which can possibly be mainly attributed to the lower pH sensitivity of this material 40-45 mV/pH (Abouzar 2008) when compared to that of Ta₂O₅; 58 mV/pH (this work) and 57 mV/pH (Siqueira 2009). The major difference between this work and that of Siqueira *et al* is the production method of the Ta₂O₅ sensitive layer; room temperature rf sputtering from Ta₂O₅ ceramic target and thermal oxidation (515 °C) of electron-beam evaporated Ta, respectively. Despite other differences, described in Table 5.2, it can be concluded that room temperature sputtered Ta₂O₅ provides a high quality alternative to high temperature methods.

Table 5.2. Relevant differences in Ta₂O₅ penicillinase FEDs produced in this work^a and by Siqueira et al (2009)^b.

Production method	Film thickness	Sensitive area	Enzyme conc./volume	[PenG] range	PenG sensitivity
^a rf sputtering	100 nm	0.25 cm ²	3 mg.mL ⁻¹ / 40 µL	1-10 mM	139±11 mV/decade
^b Thermal oxidation	55 nm	0.5 cm ²	Unknown / 80 µL	0.25-25 mM	100 mV/decade

The slightly higher penicillin sensitivity obtained for sputtered Ta₂O₅ cannot be directly attributed to the fabrication method as there are other variables that must be considered.

5.1.2. Penicillin detection with O₂ plasma treated Ta₂O₅ based PenFEDs

The oxygen plasma surface treatment of 5 minutes at 30 W revealed a high pH sensitivity increase (see *Section 4.3.2*), consequently enzyme functionalized sensors were produced as previously described. The working buffer (5 mM phosphate buffer pH 7) was measured prior to enzyme immobilization and after as a reference solution for 0 mM. Accumulation capacitance did not vary significantly (0.02 nF) indicating that the enzyme layer does not affect the total insulator thickness which is probably due to its porous structure. However a ~0.8 V reference voltage variation towards positive potentials was observed after enzyme immobilization. A positive voltage shift is related to a positive charge increase at or near the surface. Penicillinase has an isoelectric point of 8.1 – 8.6 (Connolly 1983; Felici 1993), meaning that when dissolved in solutions of pH within this range its net charge is zero. In solutions of pH lower than the isoelectric point, such as the working buffer (pH 7), it possesses a positive net charge which might explain the C(V) characteristics shift upon penicillinase immobilization.

The C(V) characteristics of oxygen plasma treated sensors functionalized with penicillinase are depicted in Figure 5.4.

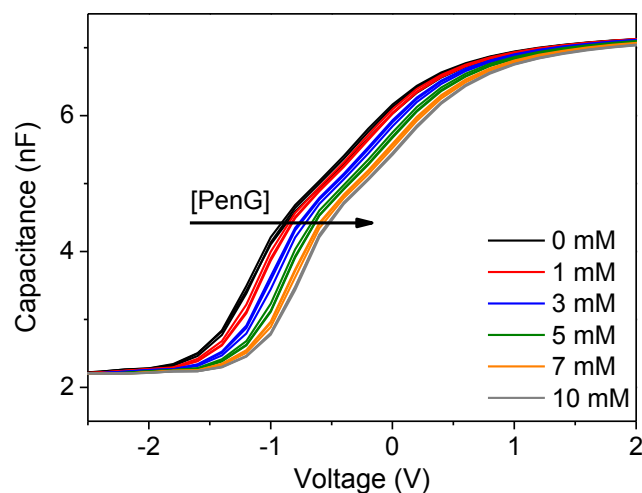


Figure 5.4. Variation of $C(V)$ characteristics of an oxygen plasma treated sensor functionalized with penicillinase when exposed to penicillin solutions of increasing concentration.

Similarly to what was observed for pH sensitivity measurements, the $C(V)$ curves are shifted to more negative potentials due to the excess surface negative charge induced by the oxygen ions and measurement variability increases accordingly. Figure 5.5 depicts the reference voltage variation as a consequence of increasing penicillin concentration.

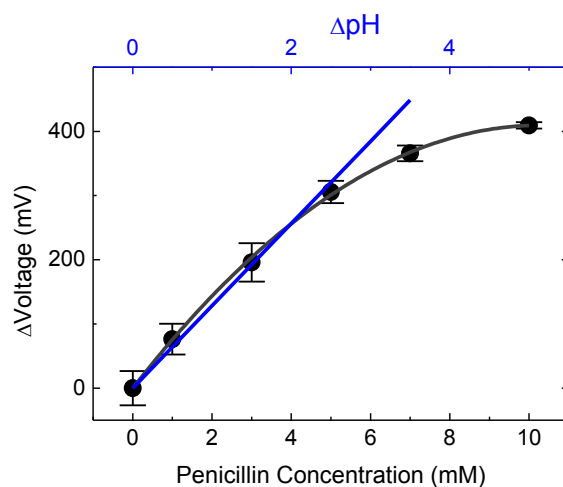


Figure 5.5. Sensitivity to penicillin of an oxygen plasma treated sensor functionalized with penicillinase and its correlation with pH variation.

As can be seen, results also show a typical enzymatic reaction curve. However a higher signal variation was obtained as a tenfold increase in penicillin concentration yields a 333 ± 29 mV/decade sensitivity. As for the untreated sensor a linear variation of reference voltage was found for penicillin concentrations below 4 mM. Considering that the oxygen plasma treated sensor has a pH sensitivity of 121 ± 10 mV/pH, a local pH

variation of two pH units (pH ~5 near sensor surface) is induced by a 4 mM penicillin solution. This is in agreement with the untreated sensor results as the generation of protons due to the enzymatic reaction is independent of sensor sensitivity; however a sensitivity twice as high, 62 ± 18 mV/mM penicillin was obtained. Similarly to the untreated sensor a decrease in sensitivity above 4 mM penicillin is also observed thus indicating possible enzyme inhibition as a consequence of the local pH decrease to ~5 (Dzyadevych 2006; Waley 1975).

Although a significant sensor signal increase was obtained with the oxygen plasma treated sensor, the associated measurement variability and reproducibility issues must be taken into consideration when weighing the viability of this method for FEDs sensitivity increase.

5.2. Label-free detection of DNA with field effect devices

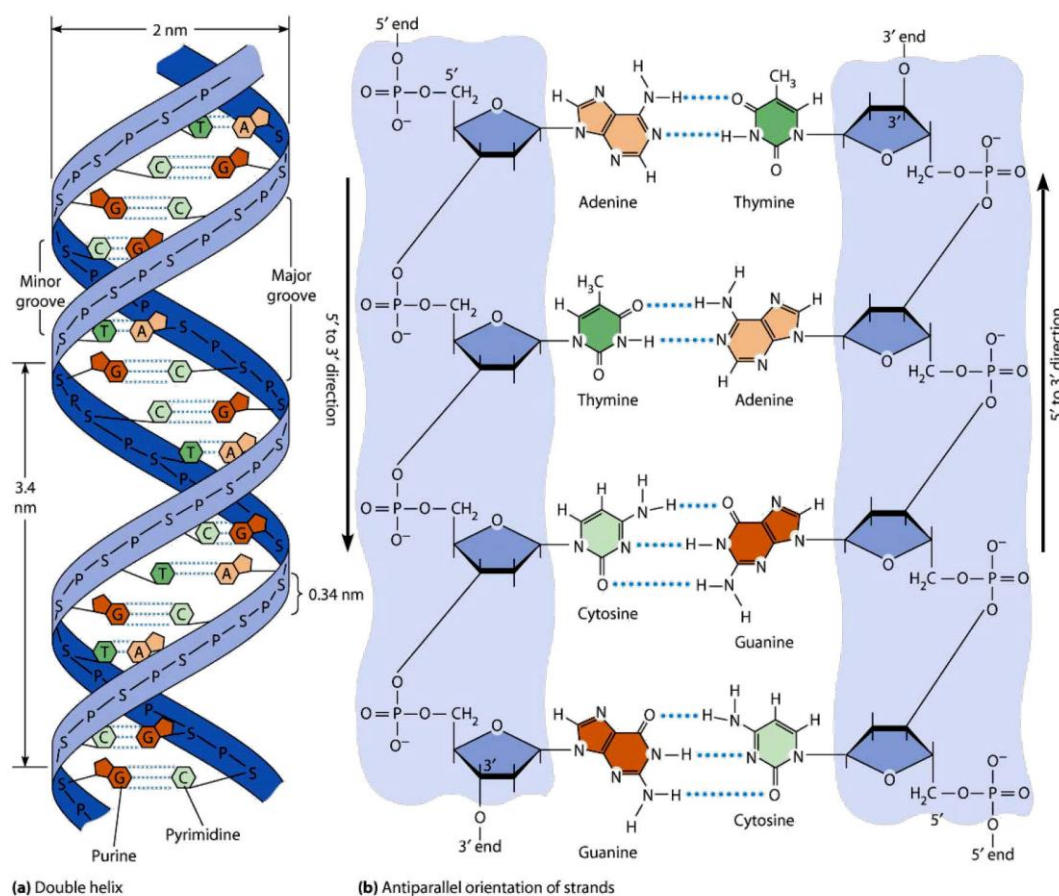
The unravelling of the human genome has revolutionized the understanding of many aspects of human disease at the molecular level and provided opportunities to identify new disease markers and individual genetic variability associated to several diseases, such as cancer, diabetes, and to the individual response to therapeutics (Bell 2004; ENCODE 2004; Venter 2001). Consequently DNA detection and its implementation in rapid, cost-effective and reliable assays is currently one of the great challenges in biosensors development.

The intrinsic molecular charge that arises from the DNA phosphate backbone allows for its direct and label-free detection with FEDs devices. Currently, research on DNAFEDs has focused on the detection of a target DNA molecule via hybridization to ssDNA probes functionalized on the sensors' surface, which requires an intermediate layer for the chemical bonding of the probes, usually through silanization (Han 2006; Lillis 2006; Poghosian 2007), or adsorption of the ssDNA to a previously immobilized charged molecule (e.g. protein, poly-L-lysine residues, etc.) (Bandiera 2007; Fritz 2002; Lin 2010). However the non-specific detection of DNA concentration, specifically the direct detection of dsDNA, is of great interest in DNA diagnostics namely in the monitoring of DNA amplification by polymerase chain reaction (PCR), real-time PCR and loop mediated DNA amplification (LAMP) (Ghosh 2006).

5.2.1. DNA structure

Deoxyribonucleic acid, DNA, is a macromolecule composed by the repetition of building blocks called nucleotides. It can be seen as a polymer composed of many monomers – nucleotides, so DNA is considered a polynucleotide. Nucleotides are composed of three types of molecules: 5-carbon-atom pentose sugars – deoxyribose, cyclic nitrogenous organic bases – purines and pyrimidines, and an inorganic phosphate group. The phosphate group is bonded to the 5' carbon of the deoxyribose sugar whilst the nitrogenous base is bonded to the 1' carbon (Figure 5.6).

There are four different nitrogenous bases: adenine (A) and guanine (G) which are purines due to their double ring structure; thymine (T) and cytosine (C) which are pyrimidines and possess only one ring (Becker 2009; Bryce 1998).



Copyright © 2009 Pearson Education, Inc.

Figure 5.6. Schematic structure of DNA molecule illustrating the chemical structure of the nucleotides, the anti-parallel nature of the two strands and the base pair hydrogen bonds that binds them together. (Becker 2009).

A DNA strand is formed by the combination of nucleotide molecules through sugar-phosphate bonds. These phosphodiester linkages bond the 5' carbon of one sugar molecule to the 3' carbon of the next, thus creating an alternating sugar-phosphate sequence commonly referred to as the backbone of DNA. The DNA strand has a direction or polarity meaning that it starts from the top with a phosphate-carbon 5' and ends with 3' carbon-OH at the bottom (Becker 2009; Bryce 1998). In living organisms DNA does not usually exist as a single molecule, but instead as a double stranded molecule composed of two strands that are linked together in the shape of a double helix; as depicted in Figure 5.6. The double helix model of DNA structure was first proposed by Watson and Crick in 1953 and is considered a landmark in biology research (Becker 2009; Watson 1953).

In the double helix structure the negatively charged phosphate groups are directed outwards whilst the bases are directed inwards and lay perpendicular to the sugar-phosphate backbone. The two strands are "antiparallel"; meaning that one strand runs from 5' to 3' while the other runs from 3' to 5'. The two strands are bound together via hydrogen bonds between the bases, creating base pairs. The base pairing is specific where a purine binds to a pyrimidine, with A bonding only to T via two hydrogen bonds, and G bonding only to C via three hydrogen bonds; these base pairs are the same length and therefore the DNA helix has a uniform diameter of about 2 nm. Generally a complete turn of the double helix, composed of a minor and a major groove, requires 10 nucleotide pairs, measuring around 3.4 nm as shown in Figure 5.6 (Becker 2009; Bryce 1998).

The non-covalent nature of the bonds between DNA strands allows for the dissociation of the double stranded DNA (dsDNA) to single stranded DNA (ssDNA) by breaking of the hydrogen bonds via temperature increase; this process is called denaturation. Usually denaturation temperature is in the 95 to 100 °C range depending on the nucleotides composition of the DNA fragment. Lowering the temperature favors the recombination of the ssDNA to dsDNA; this process is called hybridization. The base pairing restrictions dictate that a ssDNA chain will only hybridize to a complementary ssDNA and this is the basis of DNA replication and detection.

Conventional DNA detection methods rely on the specific hybridization of an unknown target ssDNA to a known probe ssDNA. Generally these methods are based on the labeling of the target ssDNA molecules with a label (metallic nanoparticles, radiochemical, enzymatic or fluorescent) followed by detection with adequate equipment. Fluorescence-based methods, such as DNA microarrays, are the most commonly used being well established and sensitive (Gosh 2006; Heller 2002).

However the labelling step is cumbersome and the need for specialized detector equipment and personnel makes these methods expensive and complex to implement, consequently direct and label-free detection of DNA methods are highly desirable.

5.2.2. Intrinsic charge based detection of DNA

The intrinsic molecular charge that arises from the DNA phosphate backbone allows for its direct and label-free detection with FEDs devices. The detection mechanism in field effect-based sensors is based on the fact that charge variation in the electrolyte solution modulates the devices response. As described in Chapter 2, the modulation of the space-charge capacitance by ionic species in solution is mainly a consequence of the electrochemical double layer, which is a characteristic of the electrolyte solution, and the oxide surface potential, which depends on the oxide's active sites according to the site binding theory. The electrolyte composition determines the Debye length (λ_D); which is the maximum distance, from the sensor surface, at which a charge variation that occurs in solution can affect the surface potential.

In pH sensing, either pH sensors or pH-based enzyme functionalized sensors, the Debye length is of small importance since the diminute size of hydrogen ions allows these to easily reach the sensor surface and chemically react with amphoteric sites at the oxide's surface thus changing the surface potential. Consequently the contribution of the electrochemical double layer is constant and the generally accepted detection mechanism for field effect pH sensing is mainly described by the site-binding theory. However the field effect detection of charged biomolecules cannot be treated as adsorbed charge in the site-binding model because of their large volume, so many additional factors need to be considered. Actually the detection mechanism is not yet completely clear and due to the complexity of variables involved a complete model for the field effect detection of biomolecules based on their intrinsic charge is still lacking. (Landheer 2005; Poghosian 2005; Shinwari 2007)

Intrinsically charged molecules, such as DNA, can in principle directly modulate the capacitance of an EIS device due to the charge density variation that arises from their proximity to the sensor surface. However, only charge density changes that occur within the Debye length can be detected.

The Debye length (equation 2.10, repeated bellow) is inversely proportional to the ionic strength of the electrolyte solution, meaning that higher electrolyte concentration will

lead to a smaller λ_D , consequently only a fraction of the biomolecules structure lies within this region and a smaller percentage of charge will be detected.

$$\lambda_D = \sqrt{\frac{\epsilon_{el}\epsilon_0 k_B T}{2N_A I^s q^2}} \quad (2.10)$$

where ϵ_{el} is the dielectric constant of the electrolyte, ϵ_0 the permittivity of vacuum, k_B is the Boltzmann constant, T the absolute temperature, N_A the Avogadro constant, I^s the ionic strength of the electrolyte (in mol/m³) and q the elementary charge.

In physiological conditions the ionic strength of the electrolyte (I^s) is in the order of 150 mM which yields $\lambda_D=0.8$ nm (Butt 2003). A dsDNA molecule with 10 base pairs can be approximately modelled by a 2 nm diameter and 3.4 nm length cylinder; as such most of its charge will be outside the Debye length even if the molecules are arranged horizontally to the surface. Figure 5.7 schematically illustrates this situation also demonstrating that in electrolytes with lower ionic strength the fraction of the DNA molecules that remains in the double layer and is thus mirrored in the sensor would be larger. However the lowering of the ionic content of the electrolyte diminishes the charge compensation effect thus compromising the solutions stability which could lead to lower hybridization efficiency, aggregation or even precipitation.

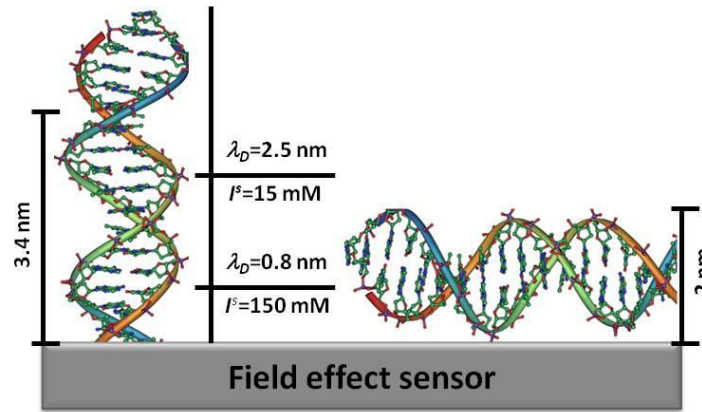


Figure 5.7. Schematic illustration of fraction of DNA molecule contained within the Debye length (λ_D) and its variation with the ionic strength of the electrolyte (I^s).

Furthermore, most of the intrinsic charge can be screened by counter ions in solution; in fact the use of divalent cation salts in DNA solutions is common practice as these tend to stabilize the DNA molecules dispersion due to the more efficient charge compensation. This charge neutralization due to counter ion condensation can reduce the expected signal.

Poghossian et al (2005) estimated that only a 1.7% of the charge induced by a hybridization event would be mirrored in a field effect device (with $C_i=0.35 \mu\text{F}/\text{cm}^2$), and that the remaining charge would be compensated by counter ions in solution. The resulting expected sensor signal for hybridization would be only a few mV (~ 3 mV and ~ 6 mV for hybridization efficiency of 50 and 100 %, respectively). The calculations are based on the assumption that a charge density increase such as the hybridization of target ssDNA to probe molecules immobilized to the sensor surface can be modelled as a charge transfer from the solution to the sensitive layer's surface. Considering that electroneutrality must be maintained an equal amount of opposite charge must be observed in the space-charge region of the FED or the electrochemical double layer.

The hybridization event, considering a hybridization efficiency of 100 %, is similar to a doubling of the DNA concentration in solution so this calculation can also be applied to non-specific DNA concentration detection.

The charge transfer due to DNA molecules, Q_{DNA} , can induce a charge change, Q_i , on the insulator sensitive layer's capacitance, C_i , which is mirrored in the space-charge region of the FED.

$$Q_i = \frac{Q_{DNA}C_i}{C_i + C_{dl}} \quad (5.1)$$

were C_{dl} is the capacitance of the electrochemical double layer. Considering $C_i=32 \text{ nF}/\text{cm}^2$ for the developed Ta_2O_5 sensor and typical value for $C_{dl}=20 \mu\text{F}/\text{cm}^2$ (Bousse 1983); $Q_i/Q_{DNA} \sim 0.1\%$. The expected fraction of charge detected with this sensor is even lower since, due to the smaller insulator capacitance of the device, a higher amount of charge will enter the double layer.

The charge change induced upon DNA concentration increase can be described as:

$$Q_{DNA} = mN(1 - \theta) \quad (5.2)$$

were $m=q\lambda_D/b$ is the fraction of DNA charge in the double layer (DNA molecules are considered arranged horizontally to the surface and with one negative charge per base pair), q is the elementary charge, $\lambda_D=0.8 \text{ nm}$ for physiological conditions, b is the distance between the nearest unit charges along the DNA ($b=0.34 \text{ nm}$). The density of molecules at the sensors surface, N , can be estimated by considering dsDNA molecules as a 2 nm diameter, 3.4 nm length rod with an interspatial distance of 2 nm between them; $N \sim 7 \times 10^{11} \text{ molecules}/\text{cm}^2$. The fraction of DNA charge screened by condensed

cations, θ , depends on electrolyte composition ($\theta=0.76$ and 0.88 for mono and divalent cations respectively).

The corresponding interface potential change, φ , which is the expected sensor signal, can be defined as:

$$\varphi = \frac{Q_i}{C_i} = mN \frac{1 - \theta}{C_i + C_{dl}} \quad (5.3)$$

The sensor signal can be estimated using the aforementioned values. A variation of only ~ 3 mV is expected. In reality this value is an optimistic estimation as DNA molecules do not actually behave like rigid charged rods, being usually coiled to some extent and that surface coverage is probably lower due to electrostatic repulsions (Poghossian 2005).

All these factors lead to the conclusion that field effect detection of pure electrostatic charges associated with DNA hybridization or increased concentration in physiological conditions is highly unlikely. Therefore an alternative detection mechanism that justifies the observed sensors response must exist.

In a more realistic approach the DNA molecules do not form closely packed and perfectly homogeneous layers. In fact due to conformational structure variations and electrostatic repulsions the biological layer has enough interstitial space to allow electrolyte penetration and the low surface coverage permits electrolyte and other ions to reach the device's sensitive surface. In this way and considering that a DNA induced charge variation, either by hybridization or concentration increase, causes ionic rearrangement in the molecules vicinity which will influence charge distribution and the double layer capacitance, the observed sensors response might be explained by a mechanism based on the detection of this redistribution of the ionic concentration in the intermolecular spaces that arises from DNA induced charge variation (Mckinnon 2009; Poghossian 2005).

As DNA molecules are negatively charged due to the phosphate groups in their structure, these will attract positively charged ions (counter-ions) that will effectively screen the DNA's charge. Also the vicinity of the DNA molecules will be depleted of anions as these will be repelled. The redistribution of ionic species in solution due to the DNA intrinsic charge may result in a local ion concentration variation within the intermolecular spaces that can substantially differ from the concentration in the bulk electrolyte.

A change in DNA content, either due to hybridization or simply to a concentration increase, will lead to a rearrangement of ionic species within the intermolecular spaces and consequently to a redistribution of electrostatic potential.

Actually, calculations of the distribution of cations and anions in the intermolecular spaces before and after a hybridization event using electrostatic potential equations (Poghossian 2005 and 2007) show that not only the ionic concentration in the intermolecular spaces is significantly different from that of the bulk electrolyte, for both cations and anions, but also that upon hybridization a substantial ionic concentration redistribution occurs.

A difference in the average ion concentration within the intermolecular spaces in the DNA layer after hybridization was found to be three to four times higher for cations than that prior to the hybridization event. This difference would be enough to obtain a measurable signal even in high ionic strength electrolytes, required to allow high hybridization efficiency. The effect is dependent on the electrolyte's ionic strength being smaller for high ionic strength electrolytes that are typically used. However, in typical physiological conditions of ionic strength (150 mM) and vertically immobilized ssDNA probe density (2×10^{13} molecules/cm²) such a ionic concentration variation can be expected to induce a sensor signal change of about 28-35 mV for a field effect device that demonstrates a typical Nernstian sensitivity. Similar ion redistribution effects induced by a hybridization event could also occur when DNA molecules are in other orientations such as lying flat on the surface which is typical for DNA adsorption (Poghossian 2005).

Considering that in a hybridization event, with a hybridization efficiency of 100 %, the quantity of DNA molecules and consequently the net intrinsic charge is nearly doubled; similar results can be expected for a doubling of the DNA concentration. The aforementioned assumptions and conclusions can in principle be applied for the detection of a DNA concentration increase. Whether the concentration variation is due to the addition of identical ssDNA or non-complementary ssDNA, complementary ssDNA or dsDNA, should not dramatically influence the results as the increase in net charge density would result in the ionic concentration redistribution in either case. As such this model might also be valid for non-specific DNA concentration detection.

5.2.3. Non-specific DNA concentration detection

The monitoring of DNA amplification requires that the sensor responds to increasing DNA concentration in a non-specific way; the goal is to detect a variation in the dsDNA content of biological samples. For that the optimized Ta₂O₅ EIS sensor response to increasing concentrations of DNA was initially assessed through the use of two complementary 40 base pairs synthetic oligonucleotides:

Oligo A: 5'-TGG ATT TAA GCA GAG TTC AAA AGC CCT TCA GCG GCC AGT A-3'

Oligo B: 5'-T ACT GGC CGC TGA AGG GCT TTT GAA CTC TGC TTA AAT CCA-3'

at different concentrations. DNA solutions of 1 and 2 μ M of each nucleotide in PCR buffer solution (20 mM Tris-HCl pH 8.4; 50 mM KCl; 20 mM MgCl₂; with $I^s=0.12$ mM and $\lambda_D \approx 0.9$ nm) were measured. These two oligonucleotides were also hybridized to each other and used in similar measurements maintaining the total DNA concentration, i.e. in a 1:1 ratio. The DNA samples were prepared in buffered solution so as to minimize the contribution of pH variations to the interfacial potential, and thus the sensor's response can be directly related solely to the charge variation induced by the increasing DNA concentration. The PCR buffer was measured prior to the DNA solutions as a reference solution for 0 μ M DNA. Three consecutive C(V) curves were measured for each concentration; upon solutions change the sensor was thoroughly rinsed with the working buffer. Measurements were performed in an identical manner as for the pH sensors. The reference voltage variation induced by the different DNA sample solutions is depicted in Figure 5.8.

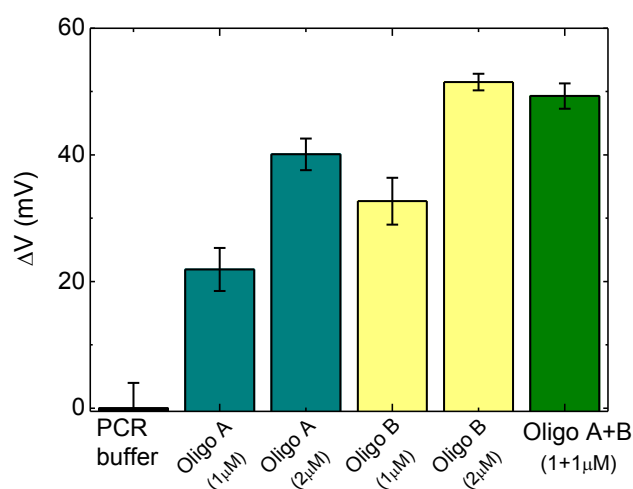


Figure 5.8. Semi-quantitative response of EIS sensor to the presence of ssDNA and dsDNA oligonucleotides (Oligo A, Oligo B, Oligo A+B) used at different concentrations (1 and 2 μ M).

The differential calculation of the potential variation diminishes the contribution of the buffer solution composition to the overall sensor signal and thus the obtained variation can be attributed solely to charge density variations that arise from the presence of DNA molecules.

A two times increase of the voltage shift occurred upon increasing the DNA concentration from 1 to 2 μM . As expected, for hybridized DNA (2 μM total concentration) the shift is similar to 2 μM samples.

The detection of DNA concentration variations with 30 mV/ μM maximum sensitivity was achieved with the optimized Ta_2O_5 EIS sensor. The obtained average value of potential variation due to hybridization of oligonucleotides A and B was ~ 25 mV. This is in good agreement with estimated sensor signal of 28-35 mV, with a device that exhibits Nernstian sensitivity (Poghossian 2005), which can also be applied to a two times increase in DNA concentration. The observed potential shifts occur towards more positive potentials which is consistent with an increase of positive charge (counter ions) near the sensor's surface upon DNA concentration increase. The obtained results suggest that the detection mechanism is in fact based on the redistribution of ionic concentration near the sensor's surface as explained in the previous section.

The sensor successfully detected concentration variations of ssDNA and dsDNA in a direct and label-free manner being thus suitable for the monitoring of DNA amplification.

5.3. DNA amplification monitoring

DNA amplification is an indispensable molecular biology process as it allows the replication of a particular DNA fragment into millions of copies. It is used in molecular diagnostics for a variety of applications such as, hereditary diseases diagnosis and infectious diseases detection and diagnosis.

5.3.1. DNA amplification via polymerase chain reaction (PCR)

Polymerase chain reaction (PCR) has become the most predominant technology in DNA amplification. It is an enzymatic reaction used to amplify a specific region of a DNA strand (the DNA target) and requires several reagents: a DNA template that contains the target region to be amplified; two primers complementary to each end of the strand of DNA target; a DNA polymerase; nucleotides, which are the building-

blocks from which the DNA polymerase synthesizes a new DNA strand; and a suitable buffer solution, generally containing Mg^{2+} and K^+ ions, for optimal enzyme activity and stability.

PCR amplification is schematically depicted in Figure 5.9 and consists of a sequence of three steps of different temperature: denaturation at $\sim 95^\circ C$ (to melt target DNA into single stranded DNA); annealing at $50 - 65^\circ C$ (to promote binding of the primers to ssDNA target and enzymatic DNA formation) and elongation at $\sim 75^\circ C$ (for new DNA formation via DNA polymerase mediated enzymatic synthesis). Each sequence of steps comprises a PCR cycle and usually 20 to 40 cycles are needed for amplification (Sambrook 2001).

The PCR reaction can be divided into three distinct stages: exponential, when PCR reaction components are in large excess and there is an exact doubling of product on each cycle (assuming 100% reaction efficiency) yielding an exponential increase of the amount of DNA (2^n); linear, that results from the consumption of the components with consequent slowing of the reaction; and plateau, the final stage of PCR amplification when most components have been consumed and no more products are generated (Sambrook 2001). The monitoring of the amplification process requires that aliquots are withdrawn during the PCR reaction. Afterwards the amplified DNA samples are labelled (with fluorophores) and analyzed, usually by gel electrophoresis or spectroscopic fluorimetry, to confirm that the amplification was successfully achieved and quantify the amplification products.

The recent development of Real-time PCR allows target DNA template quantification in real-time by detection and quantitation of a fluorescent label which signal increases in direct proportion to the amount of DNA product being amplified; simultaneously with the amplification process (Arya 2005; Mackay 2007). By recording the amount of fluorescence emission at each cycle it is possible to monitor the PCR reaction during exponential phase, where the first significant increase in the amount of PCR product correlates to the initial amount of target template, which in turn allows for comparison between samples and/or comparative quantitation (Wong 2005). The fluorescent signal can be generated via three main approaches: i) DNA-binding agents (e.g. SYBR Green); ii) hydrolysis probes (e.g. TaqMan probes); and iii) hybridization probes (e.g. molecular beacons) (Espy 2006). The advantage of RT-PCR is that the target DNA sequences are amplified and detected simultaneously so there is no need to collect samples during the reaction or to further process them (Bustin 2005; Sambrook 2001).

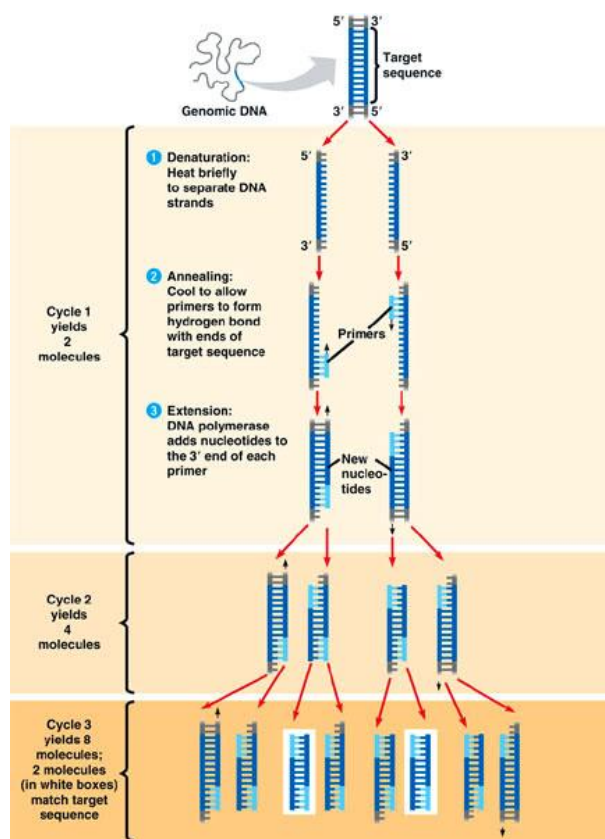


Figure 5.9. Schematic representation of DNA amplification via PCR. (Web03)

5.3.2. Field effect detection of PCR amplification of DNA

The optimized Ta₂O₅ EIS sensor was used to monitor DNA amplification via PCR amplification of a specific nucleic acid sequence of cMYC proto-oncogene.

The importance of this gene in the cause of human cancers is relevant as it was found that altered expression of human cMYC is frequently displayed in human cancers. In contrast to the tightly regulated cMYC gene in normal cells, cancer cells may express the gene in an uncontrolled fashion as the result of genetic aberrations. This deregulated expression of cMYC plays a significant role in human cancer development.

The cMYC gene is overexpressed in a wide variety of human cancers; breast cancers, colon cancer, gynecological cancers, carcinomas, among others. The fact that cMYC proto-oncogene is estimated to be involved in 20% of all human cancers has made it an attractive target for cancer detection and therapeutic purposes (Dang 2006; Hermeking 2003; Web04).

The applicability of the optimized Ta₂O₅ EIS sensor to monitor DNA amplification via PCR was assessed by measuring its response to aliquots collected during the PCR amplification process of a specific nucleic acid sequence of cMYC proto-oncogene.

For that PCR amplification of a 229 base pair (bp) fragment of the human MYC proto-oncogene (GenBank accession no. NM_002467) was performed in 100 µl of buffer solution (20 mM Tris-HCl pH 8.4; 50 mM KCl; 20 mM MgCl₂; with $I^s=120$ mM and $\lambda_D\approx 0.9$ nm) using 2.5 mM dNTPs with 1 U Taq DNA Polymerase (GE Healthcare Europe, Germany) and 1 µM of the specific primers;

MYCforward: 5'-GCTCATTCTGAAGAGGACTTGT-3'

MYCreverse: 5'-AGGCAGTTTACATTATGGCTAAATC-3'

PCR amplification was performed in triplicate on a Bio-Rad MyCycler Thermocycler (BioRad, CA, USA) with the following thermal cycling conditions: initial 5 min denaturation at 95 °C, 27 amplification cycles of denaturation at 95 °C for 30 s, annealing at 60 °C for 30 s, elongation at 72 °C for 30 s, and a final elongation at 72 °C for 5 min. As a control, a sample solution submitted to the same cycling program without any template DNA was used, i.e. negative control where no amplification is expected.

The fluorescence based quantification of PCR products was performed by DNA labeling with a SYBR Green intercalation agent, commonly used in standard real-time PCR applications, and analyzing DNA amplification samples (positive and negative) after n PCR cycles ($n=0, 3, 6, 9, 12, 15, 18, 21, 24, 27$) by spectroscopic fluorimetry. For that, the PCR products were incubated with an 1:100000 dilution of SYBR Green in TE buffer (10 mM Tris-Cl, pH 7.5, 1 mM EDTA) for 30 minutes and analyzed using a SYBR Green Quantitation Kit® (Invitrogen, Carlsbad, CA, USA) according to the manufacturer's guidelines on a VARIAN Cary Eclipse Fluorescence Spectrophotometer (Agilent Technologies Inc., Santa Clara, CA, USA) using a 3 mm optical path quartz cuvette (HELLMA, Germany).

The variation of relative fluorescence due to DNA content variation at each PCR attained via the use of SYBR-green intercalating agent, is presented in Figure 5.10.

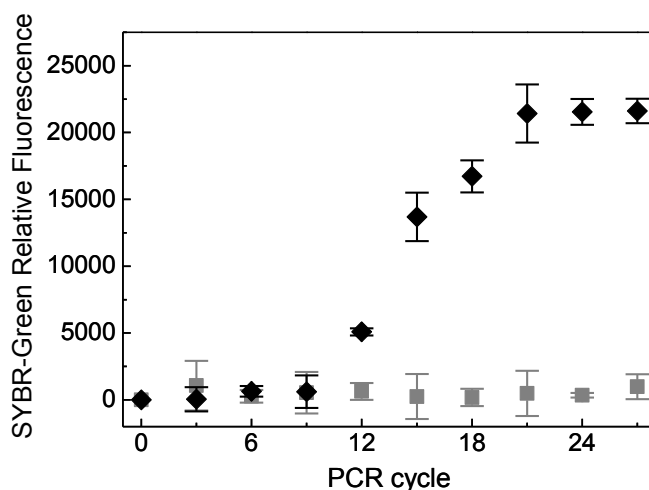


Figure 5.10. Conventional fluorescence-based detection with SYBR-green intercalating agent of DNA accumulation during PCR amplification. ♦) c-MYC gene sequence amplification, ■) PCR negative control.

As can be seen, the typical DNA amplification curve was obtained for the positive samples as the increase in DNA double-helices results in increased fluorescence. A clear distinction between positive and negative amplification samples was obtained after 12 cycles and the plateau stage was reached after 21 cycles. In the absence of template DNA (negative samples) no amplification occurred as demonstrated by the lack of fluorescence.

The sensing performance of the Ta_2O_5 films was investigated by capacitance-voltage measurements of DNA amplification samples (positive and negative) after n PCR cycles ($n=0, 3, 6, 9, 12, 15, 18, 21, 24, 27$). Sensor drifting assessment was made by collecting C(V) data for PCR buffer and PCR control sample solutions in an identical manner as for the samples. The mean average of three independent measures was taken together with standard deviation.

The capacitance-voltage curves measured at PCR cycles 0, 3, 6, 9, 12, 15, 18, 21, 24 and 27 obtained for a positive sample of DNA amplification, are presented in Figure 5.11.

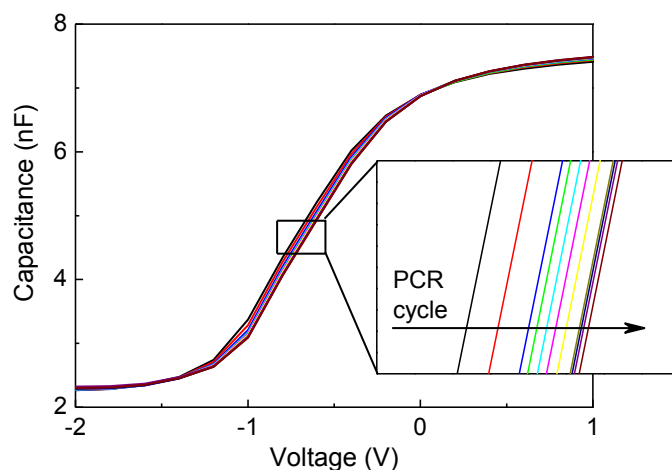


Figure 5.11. Capacitance-voltage curves obtained for a positive sample of DNA amplification at PCR cycle n ($n=0, 3, 6, 9, 12, 15, 18, 21, 24, 27$).

The PCR amplification process leads to a DNA concentration increase with each cycle. As the PCR process proceeds the $C(V)$ curves shift towards more positive potentials due to the DNA concentration increase, which is consistent with an increase of positive charge (counter ions) near the sensor's surface. This is in agreement with the previously described detection mechanism based on the redistribution of ionic concentration near the sensor's surface induced by a DNA concentration variation.

The quantification of amplified DNA is expected to be less precise when compared to the former attained value ($30 \text{ mV}/\mu\text{M}$) for the synthetic oligonucleotides since in PCR amplification samples there are other components, which can contribute to the overall solution net charge. The quantity and composition of the samples change during the PCR process so in order to minimize the interference of these components a differential method of calculating voltage variation was applied and presented values are corrected to the PCR cycle zero that contains the initial reagents prior to the amplification process. The results of the potential variation due to DNA content variation at each PCR cycle are depicted in Figure 5.12.

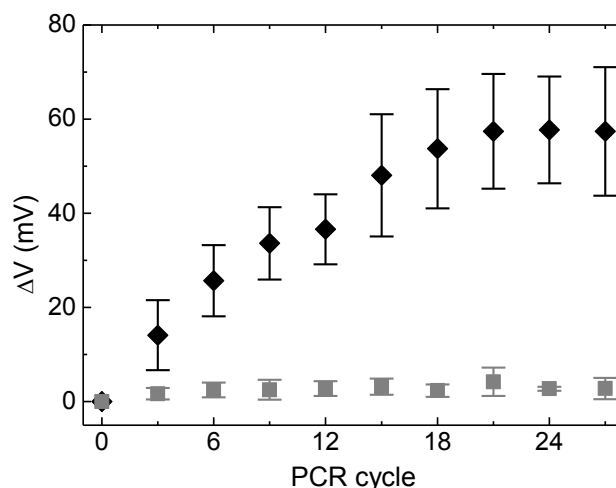


Figure 5.12. Field effect-based detection with optimized Ta_2O_5 sensitive layer of DNA accumulation during PCR amplification. \blacklozenge) c-MYC gene sequence amplification, \blacksquare) PCR negative control.

The EIS curve profile is easily compared to that of a typical PCR amplification. Nevertheless, though following a similar trend, a slight deviation from the typical profile is noted. Because the goal of real-time DNA amplification monitoring is to avoid unnecessary PCR cycles, thus saving precious time, usually only the beginning of the curve is used for amplification analysis. With the EIS sensor, it is clearly visible the increase in DNA content after each cycle and a clear distinction between positive and negative samples is attained after only six PCR cycles with the plateau stage also being reached at cycle 21.

The deviation between the amplification profile attained by the EIS sensor and that of traditional PCR could be due to drift effects that may arise not only from the device itself but also from incompatibility of electronics and liquid solutions (Jamasp 1998; Pan 2008). Although no significant variation was observable in consecutive measurements, variations of sensor response were noticeable in measurement sets recorded on different days. This may not be a crucial issue as each PCR amplification can be followed in real-time. Nonetheless, if comparison between sets of results from different experiments is required, it becomes relevant.

In control samples that lacked template DNA (negative) no significant drift effect was observed. Considering that the only difference between positive and negative samples is the presence of template DNA this can indicate that the template DNA might undergo changes during the PCR process that influence the obtained sensor signal. Consequently, in order to assess the contribution of template DNA to this effect, a

statistical analysis was performed by collecting C(V) data of PCR cycle zero, that contains all reagents but were no amplification has yet occurred, in an identical manner as for the samples (Figure 5.13).

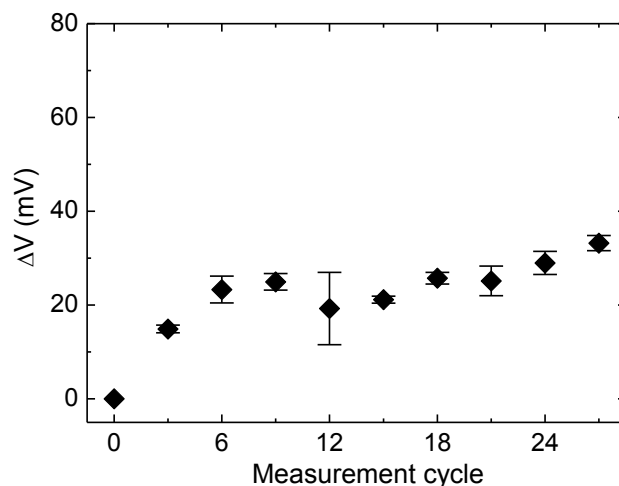


Figure 5.13. EIS sensor drift analysis: C(V) measurements performed on a PCR *cycle 0* following the same procedure as for the amplified DNA samples.

The results show that there is a higher initial variation followed by stabilization of the system. The obtained data was used to correct PCR amplification samples data to minimize drift influence on the sensitivity assessment.

The potential variation curve of corrected data is presented in Figure 5.14.

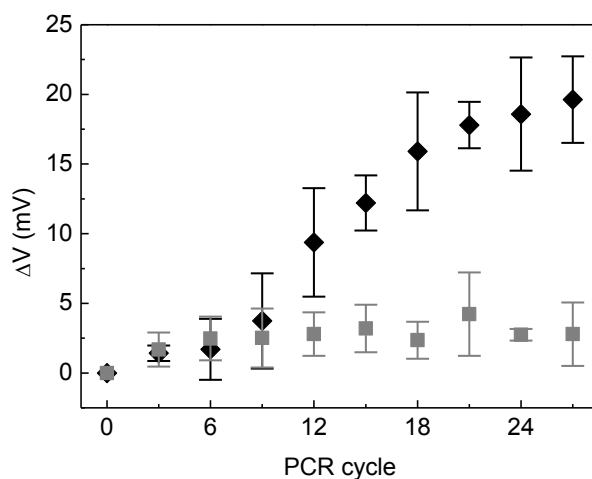


Figure 5.14. Corrected data of field effect-based detection with optimized Ta₂O₅ sensitive layer of DNA accumulation during PCR amplification. ♦) c-MYC gene sequence amplification, ■) PCR negative control.

Results show that, by removing the drift effect, the typical PCR exponential curve is revealed. The discrimination between positive and negative samples occurs at cycle 12 and the plateau stage is achieved at cycle 21, in agreement with fluorescence-based analysis. This permits a clear discrimination of the exponential stage where the first significant increase in the amount of PCR product correlates to the initial amount of target template, therefore allowing for the application of the EIS sensor to quantification of PCR amplified product generation.

The applicability of the optimized Ta₂O₅ EIS sensor to follow the real time PCR amplification (RT-PCR) of cMYC gene sequence from genomic DNA was also assessed.

As such RT-PCR was performed in a Corbett Research Rotor-Gene RG3000 using SYBR GreenER Real-Time PCR Kit (Invitrogen, Carlsbad, CA, USA) according to manufacturer's specifications in 50 µl reactions containing DNA from cMYC amplicon, 1× SYBR Green SuperMix and 200 nM of MYCforward and MYCREVreverse. The amplification conditions consisted of 50 °C for 2 min hold, 95 °C during 10 min hold, followed by 27 cycles consisting of denaturation at 95 °C for 30 s, annealing at 60 °C for 30 s, extension at 72 °C for 30 s, with a final extension step at 72 °C for 5 min. All experiments were performed at least three times.

The corrected potential variation measured with the EIS sensor is compared to that attained from a standard RT-PCR in Figure 5.15.

When compared to standard RT-PCR, it is clear that saturation for the EIS sensor is achieved earlier than for fluorescence based RT-PCR. It should also be noted that the inflexion point of the EIS curve seems to arise at an earlier stage of the reaction possibly indicating that, upon system optimization, the EIS sensor could provide for increased sensitivity.

The specificity of the amplified products of RT-PCR was confirmed by measuring the melting temperature profile, which consists of the thermal denaturation of amplified DNA. The shape of the melting curve indicates whether the amplified products are homogeneous and the melting temperature provides reassurance that the correct product has been amplified, as its value depends on the DNA fragment composition (Sambrook 2001). The melting curve of the RT-PCR amplification sample is depicted in Figure 5.16, and as can be seen it shows a unique product, indicating the specific amplification of c-MYC gene sequence.

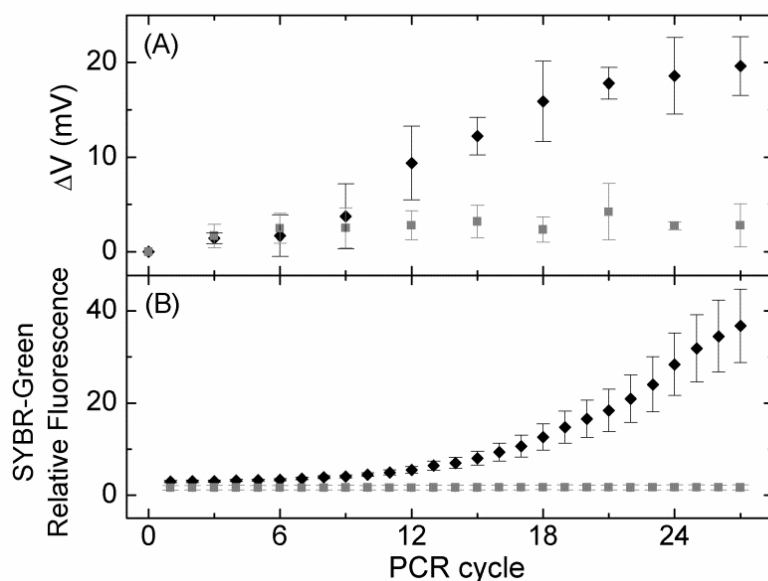


Figure 5.15. Monitoring DNA amplification in real-time. Comparison between A) corrected Ta_2O_5 EIS sensor amplification curve and B) standard RT-PCR: \blacklozenge) c-MYC gene sequence amplification, \blacksquare) RT-PCR negative control.

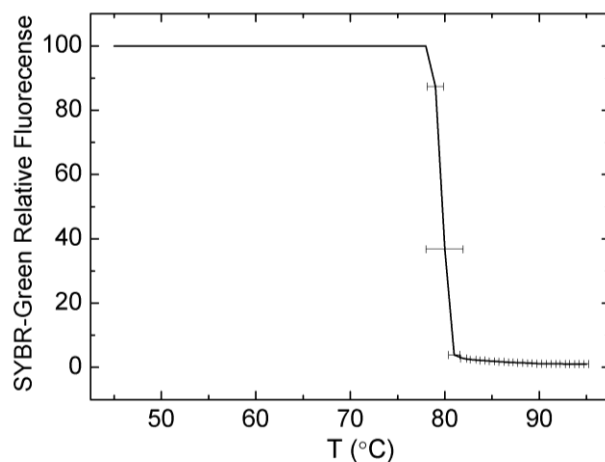


Figure 5.16. Melting temperature profile of the amplified products.

The Ta_2O_5 EIS sensor showed comparable capability to detect DNA amplification to that of standard real-time PCR using SYBR-green fluorescence without the need of expensive and cumbersome apparatus. Further optimization and miniaturization of the sensor towards its integration into the RT-PCR process could perhaps allow for an alternative non fluorescence-based DNA detection method that is direct and label-free (Branquinho 2011).

5.3.3. *Loop-mediated isothermal DNA amplification (LAMP)*

Loop-mediated isothermal DNA amplification (LAMP) is a recent but powerful gene amplification technique that is emerging as a simple and rapid diagnostics tool. It has applications in a wide range of fields including clinical diagnostics, single nucleotide polymorphism (SNP) typing, and quantification of template DNA, being considered as an effective gene amplification method for point-of-care testing devices (Parida 2008). LAMP employs a specific DNA polymerase and a set of four specially designed primers that recognise a total of six distinct sequences on the target DNA sequence that allow for a highly specific and rapid DNA amplification under isothermal conditions (Notomi 2000).

LAMP relies on auto-cycling strand displacement DNA synthesis that is performed by a DNA polymerase with high strand displacement activity (*Bst* DNA polymerase), with optimal temperature of 65 °C, and a set of two inner and two outer primers, each containing two distinct sequences corresponding to the sense and anti-sense sequences of the target DNA. In the initial steps of the LAMP reaction all primers are involved but only the inner primers are used for strand displacement, during the cycling reaction (Notomi 2000). Two additional primers, named loop primers, can also be used to accelerate the amplification reaction and thereby reduce the amplification time to as little as 30 minutes (Parida 2008).

LAMP amplification possesses several advantages over other amplification strategies: i) DNA can be amplified with high efficiency under isothermal conditions, in the range of 65 °C, after about one hour of reaction time; ii) LAMP is highly specific for the target DNA due to the recognition of the target sequence by six independent sequences accomplished by the use of the specifically designed set of four primers; which also contributes to the diminishing of the back-ground usually associated with nucleic acid amplification; iii) Amplification can be performed in a single step by incubating the mixture of samples, primers, DNA polymerase and substrates; only requiring a regular laboratory water bath or heating block for the reaction (Notomi 2000; Parida 2008).

5.3.4. *Field effect real-time monitoring of LAMP DNA amplification*

The monitoring of LAMP amplified products is commonly performed by agarose gel electrophoresis stained with a fluorescent intercalator, e.g. ethidium bromide, SYBR Green, etc. (Notomi 2000; Parida 2008), which can also be performed in real-time. It can be achieved through spectrophotometric measurements of turbidity, since the

LAMP reaction leads to the precipitation of by-products and consequently to a turbidity increase that correlates with the amount of DNA synthesized (Parida 2008).

The increasing popularity and wide range of applications of LAMP DNA amplification makes the development of new techniques for the real-time monitoring of this method to be highly desirable. Considering the successful results obtained for the field effect monitoring of DNA amplification products, the optimized Ta₂O₅-based EIS sensors were applied for the field effect real-time monitoring of LAMP DNA amplification.

A specific measurement cell with the necessary requirements for the LAMP reaction to occur and that simultaneously allows the real-time monitoring of this process was designed and fabricated. The LAMP measurement cell and a schematic representation of its components are presented in Figure 5.17.

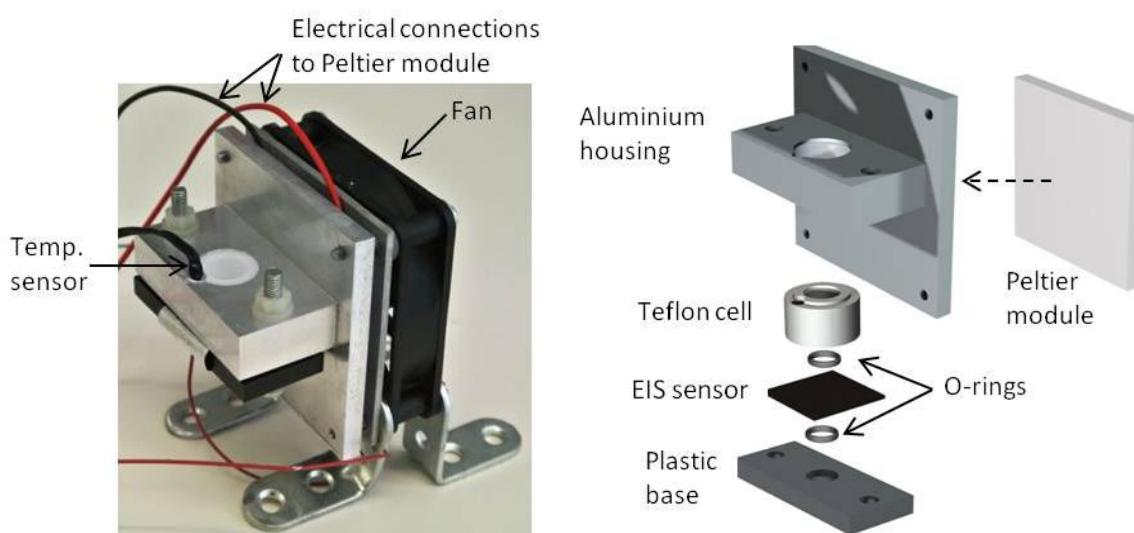


Figure 5.17. LAMP DNA amplification measurement cell: real image (left) and schematic assembly representation (right).

The measurement cell is basically a miniaturized version of the previous cell (Fig. 4.1 in *Section 4.1.1.*), with an identical sensitive area, that is inserted into an aluminium housing to allow for uniform heating and temperature control. A temperature sensor is connected to the cell and a thermoelectric power generation Peltier module (200 °C, 6.4 V, 3.1 W, Thermovoltak) is glued to the back of the aluminium housing with thermal paste and assembled to a small fan; these are then combined to a temperature controller (TC-XX-PR-59, Supercool AB) to allow for computer management of heating/cooling of the cell and temperature monitoring.

The applicability of the optimized Ta₂O₅ EIS sensor to monitor LAMP DNA amplification was assessed by measuring its response during the amplification process of a specific nucleic acid sequence of cMYC proto-oncogene. The presented results are only preliminary as these were obtained towards the end of the thesis writing process; nevertheless the successful LAMP DNA amplification in the specifically designed cell and the field effect based real-time monitoring of LAMP cMYC amplification was demonstrated.

The amplification of a 229 base pair (bp) fragment of the human MYC proto-oncogene (GenBank accession no. NM_002467) requires four specific primers; forward outer primer (FP), backward outer primer (BP), forward inner primer (FIP), backward inner primer (BIP); which sequences are:

FP TCTGAAGAGGACTTGTTC

BP TTCAGTCTCAAGACTCAGC

FIP CTTTTCCTTACGCACAAGAGTTCC-GGAAACGACGAGAACAGT

BIP ACGATTCCTTCTAACAGAAATGTCC-CAAGGTTGTGAGGTTGCA

LAMP primers for cMYC gene were designed according to the published sequences (GenBank accession no. NM_002467) using Primer Explorer version 4 (<http://primerexplorer.jp/elamp4.0.0/index.html>) and all primers were synthesized by StabVida, Portugal. The reaction mixture contained 1 µM of each inner primer FIP and BIP, 0.1 µM of each outer primer FP and BP, 0.3 mM of dNTP mix, 0.5 M betaine (Sigma–Aldrich, St. Louis, MO, USA), 2 mM MgCl₂, 1× of the supplied buffer, and 0.1 µg of DNA in a final volume of 100 µl.

LAMP reaction was performed by subjecting the reaction mixture to an initial 10 min denaturation step at 95 °C on a Bio-Rad MyCycler Thermocycler (BioRad, CA, USA); after which it was cooled down to 4 °C for one minute. The addition of 8U of *Bst* DNA polymerase (large fragment; New England Biolabs Inc., Beverly, MA, USA) followed, and then the final reaction mixture was transferred to the LAMP measurement cell, covered with mineral oil to prevent evaporation, and allowed to react for 90 min at 65 °C. As a control, a sample solution submitted to the same reaction procedure without any template DNA was used, i.e. negative control where no amplification is expected. Capacitance-voltage curves were recorded every 10 min and measurements were performed by applying a variable dc potential, with a superimposed ac voltage of 10 mV

at a 500 Hz frequency, to the sensor back-contact with respect to the Ag/AgCl reference electrode in solution; as described in *Section 4.1*.

Similarly to what was performed in field effect PCR amplification monitoring, a differential calculation of the potential variation was applied to diminish the contribution of the buffer solution composition to the overall sensor signal. Figure 5.18 represents the EIS sensor signal variation obtained for both positive and negative amplification samples.

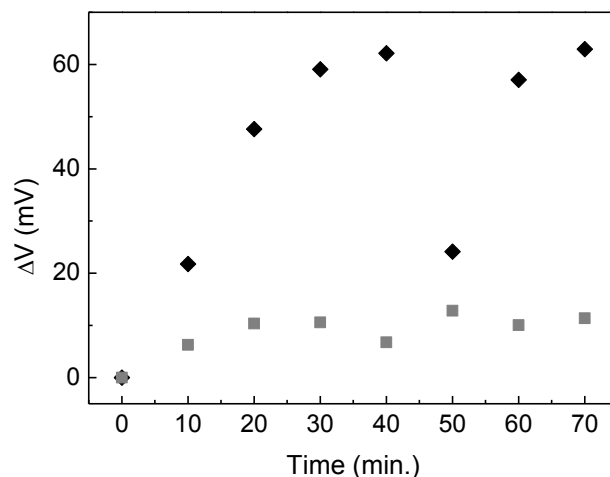


Figure 5.18. Field effect-based detection with optimized Ta₂O₅ sensitive layer of DNA accumulation during LAMP DNA amplification. ♦) c-MYC gene sequence amplification, ■) LAMP negative control.

As can be seen, a clear discrimination between positive and negative amplification was obtained. For positive amplification samples and with increasing reaction time, the observed potential shifts occur towards more positive potentials which is consistent with an increase of positive charge (counter ions) near the sensor's surface upon DNA concentration increase. The obtained results are in agreement with the previously explained detection mechanism based on the redistribution of ionic concentration near the sensor's surface.

The LAMP cMYC amplification was confirmed via gel electrophoresis analysis of the amplification product samples (positive and negative) on a 1% agarose gel electrophoresis stained with 1× GelRed™.

Sensor drifting assessment was made by collecting C(V) data for LAMP buffer containing 0.5 M betaine, 2 mM MgCl₂ and 1× of the supplied buffer in a final volume of 100 μl, in an identical manner as for the samples (Figure 5.19).

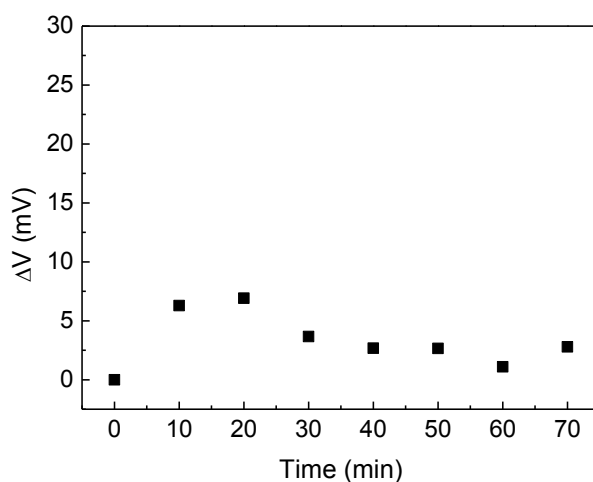


Figure 5.19. EIS sensor drift analysis: $C(V)$ measurements performed on a LAMP buffer solution following the same procedure as for the amplified DNA samples.

Results show a higher initial variation followed by stabilization of the system, which is similar to negative amplification control samples. However, a lower maximum variation, ~ 7 mV, was obtained for the buffer solution.

Summarising, the successful LAMP cMYC amplification was achieved in the specifically developed LAMP cell with a homemade temperature control setup. Moreover, the amplification reaction was monitored in real-time with the optimized Ta_2O_5 -based EIS sensor which allowed a clear distinction between positive and negative amplification samples. Although a statistical analysis of sensor behaviour is still needed, the obtained results are very promising and testify to the applicability of field effect based sensors to the real-time monitoring of LAMP DNA amplification.

Chapter 6. Semiconductor oxides based ISFETs

6.1. Introduction.....	141
6.2. Extended gate oxide semiconductor-based ISFETs.....	142
6.2.1. Sensor structure	142
6.2.2. Sensor fabrication	143
6.2.3. Structural and compositional characterization	144
6.2.4. Electrical characterization	146
6.3. pH sensitivity of oxide ISFETs	148

Some of the results presented in this chapter are currently in press in J.V. Pinto, R. Branquinho, P. Barquinha, E. Alves, R. Martins, E. Fortunato, '*Extended-gate ISFETs based on Sputtered Amorphous Oxides*', IEEE/OSA Journal of Display Technology.

Chapter 6. Oxide semiconductor–based ISFETs

This chapter is devoted to the presentation and discussion of the low temperature production of oxide semiconductor-based ISFETs comprising the optimized Ta₂O₅ sensitive layer and their application as field effect based sensors.

6.1. Introduction

In the 40 years since the introduction of the ISFET (Bergveld 1970 and 1972) research on these devices has grown significantly. A diversity of ISFETs with variations in the device structure and semiconductor material has been developed. Although most of reported devices are based on crystalline silicon (Poghossian 2004; Schoning 2006; Uslu 2004), where high processing temperatures and hazardous gases are required, alternative semiconductors are also being pursued as active layers for ISFET applications in a similar way as their electronic counterpart, the field effect transistor. As such, ISFETs comprising polycrystalline Si (Estrela 2007b; Yan 2005), amorphous Si (Gonçalves 2008; Gotoh 1989), diamond (Sasaki 2010; Song 2006) and organic semiconductors (Caboni 2009; Scarpa 2010) have been reported.

A promising class of materials for application in field effect transistors are transparent metal oxides due to the ability of achieving a wide range of electronic properties from conductive, to semiconductive and insulating oxides. The application of transparent semiconductor oxides as channel layer for thin film transistors (TFTs) emerged almost ten years ago with reports on fully transparent TFTs based on ZnO (Masuda 2003; Hoffman 2003; Carcia 2003), which demonstrated comparable performance to the typically exhibited by a-Si:H and organic TFTs. Besides ZnO other oxides, such as In₂O₃ and SnO₂, as well as multicomponent oxides, such as indium-zinc oxide (IZO) (Fortunato 2008), zinc-tin oxide (ZTO) (Nayak 2011) and gallium-indium-zinc oxide (GIZO), have been explored. In particular, GIZO presents improved tunability of electrical properties and is amorphous in a broader range of conditions and GIZO based TFTs have demonstrated remarkable electrical properties (Barquinha 2009 and 2010a; Fortunato 2012; Hsieh 2010; Kim 2007; Nomura 2004).

The room-temperature production of amorphous semiconductor oxides by rf magnetron sputtering allows control over the electric properties (Barquinha 2008; Carcia 2003) and simultaneously permits the use of low-cost and flexible substrates such as plastic and even paper (Fortunato 2008a). In fact, sputtered amorphous oxides

based TFTs comprising GIZO semiconductor and multicomponent dielectrics have demonstrated high electronic performance (Barquinha 2009a).

The remarkable characteristics of amorphous oxide based TFTs makes their application as sensors, such as ISFETs, not only advantageous but also highly desirable. As such, and taking into account the expertise of CENIMAT and CEMOP in the development of these devices (Barquinha 2012; Fortunato 2012), amorphous oxide semiconductor TFTs produced by rf sputtering at room-temperature were thus combined with the optimal Ta₂O₅ sensitive layer and applied as ISFET sensors. The fabrication of amorphous GIZO based ISFETs was performed following the deposition conditions previously optimized for amorphous GIZO based TFTs within the group (Barquinha 2009a, 2010 and 2010a; Pereira 2008).

6.2. Extended gate oxide semiconductor-based ISFETs

6.2.1. Sensor structure

Typically, an ISFET device is obtained by substituting the transistor's gate contact with an electrolyte solution and a reference electrode. In this configuration the gate dielectric is in direct contact with the electrolyte solution and threshold voltage modulation arises from oxide/electrolyte interfacial potential variations; however this device structure can lead to problems due to poor isolation between the device and the solution. On that account, another device structure; the extended gate field effect transistor (EGFET), has been frequently used revealing several advantages over the conventional ISFET structure (Estrela 2007b; Kamahori 2007; Kim 2006).

The EGFET was introduced by van der Spiegel in 1983 and its configuration allows the isolation of the electrically connected FET device from the liquid electrolyte (Kim 2006). Amorphous oxide semiconductors can thus be used in pH based sensors by depositing a sensitive layer on the end of a signal line extended from the TFTs gate electrode, as shown in Figure 6.1. Moreover, the EGFET structure has the added advantages of: i) allowing the use of bottom gate TFTs, which is a preferable configuration especially for sputtered amorphous oxides based TFTs because the dielectric layer is deposited prior to the semiconductor layer providing improved interfacial properties that are crucial for device stability and performance (Barquinha 2010a); and ii) providing facilitated device passivation in order to minimize threshold voltage variations due to environmental conditions that might affect the semiconductor

active layer such as oxygen adsorption, temperature and humidity (Olziersky 2010; Seo 2009).

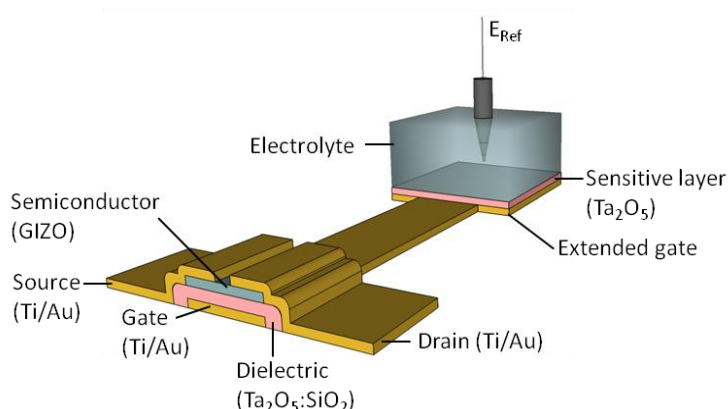


Figure 6.1. Schematic representation of an extended gate amorphous oxide based ISFET.

6.2.2. Sensor fabrication

Amorphous GIZO based ISFET devices comprising the optimal Ta_2O_5 sensitive layer were fabricated with an extended bottom gate configuration (Figure 6.1). The devices production was performed following the optimized deposition conditions for amorphous GIZO based TFTs (Barquinha 2009a, 2010 and 2010a; Pereira 2008).

The ISFETs were fabricated on Corning 1737 glass substrates and all layers were patterned by lift-off techniques with specifically designed photolithographic masks. The source, drain and gate contacts consisted of Ti/Au films with 10/65 nm thickness deposited by electron beam evaporation. The semiconductor and dielectric layers were produced by rf magnetron sputtering with an $\text{Ar}:\text{O}_2$ (14:1 sccm) reactive atmosphere and a deposition pressure of 0.3 Pa, without intentional substrate heating, in a AJA ATC-1300 sputtering system. The 350 nm thick dielectric film was deposited by co-sputtering of Ta_2O_5 and SiO_2 targets (99.99% purity from SCM) and the semiconductor layer (~26 nm thick) was sputtered using a GIZO 1:2:1 (Ga:In:Zn atomic ratio) multicomponent ceramic target (99.99% purity from LTS). The optimized Ta_2O_5 sensitive layer was deposited on top of the 1 mm² gold pad of the extended gate.

The fabricated ISFET sensors and an optical microscope image of a TFT device are shown in Figure 6.2.

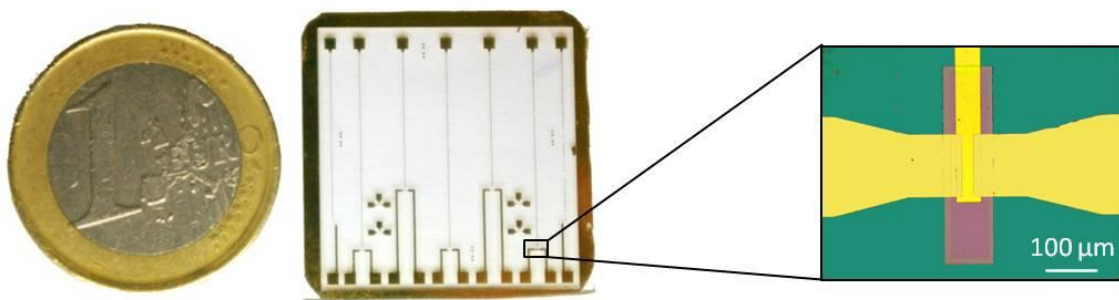


Figure 6.2. Amorphous oxides based extended gate ISFET sensors and detail of a TFT device.

Amorphous GIZO ISFETs were also produced on glass/ITO/ATO and highly doped Si/SiO₂ commercial substrates. These already possess a common gate electrode; ITO and Si; and dielectric layer; ATO and SiO₂; only requiring the deposition of the GIZO active layer and source and drain contacts. The optimized Ta₂O₅ sensitive layer was deposited on top of the dielectric layer. Passivation of the devices and sensing area delimitation was performed by spin-coating a thick layer of SU-8 (25 μm) and annealing the samples at 200 °C for 1 hour in air, in a Barnstead Thermolyne F21130 tubular furnace.

The devices fabrication steps (Figure 3.2) and techniques are described in more detail in *Chapter 3*.

6.2.3. Structural and compositional characterization

The sputtered semiconductor and dielectric thin films were analyzed by XRD and RBS in order to determine their structure, stoichiometry and the depth profile of their constituents.

Structural characterization was performed by XRD analysis of GIZO and Ta₂O₅:SiO₂ thin films deposited on silicon substrates simultaneously with ISFET devices production. A one degree offset in 2θ was applied to eliminate the intense diffraction peaks of crystalline silicon. The diffractograms of both materials are presented in Figure 6.3. The absence of diffraction peaks confirms the amorphous nature of the sputtered oxides.

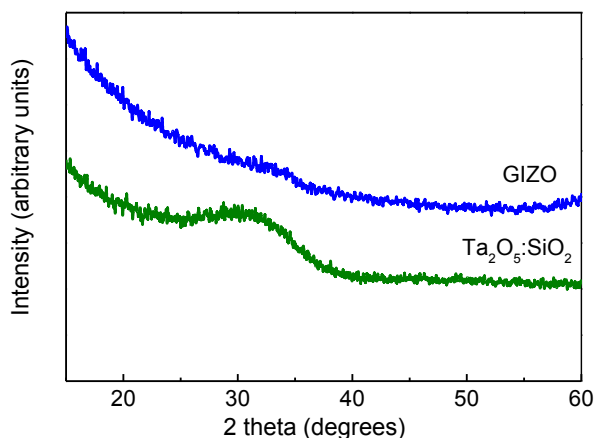


Figure 6.3. XRD diffractograms of semiconductor (GIZO) and multicomponent dielectric (Ta₂O₅:SiO₂) thin films.

Compositional characterization was performed by RBS analysis of GIZO and Ta₂O₅:SiO₂ thin films deposited on silicon substrates simultaneously with ISFET devices production. The obtained spectra are presented in Figure 6.4 where the arrows indicate the energy barrier for each element, which correspond to the energy of particles that have been backscattered by the surface atoms of the films.

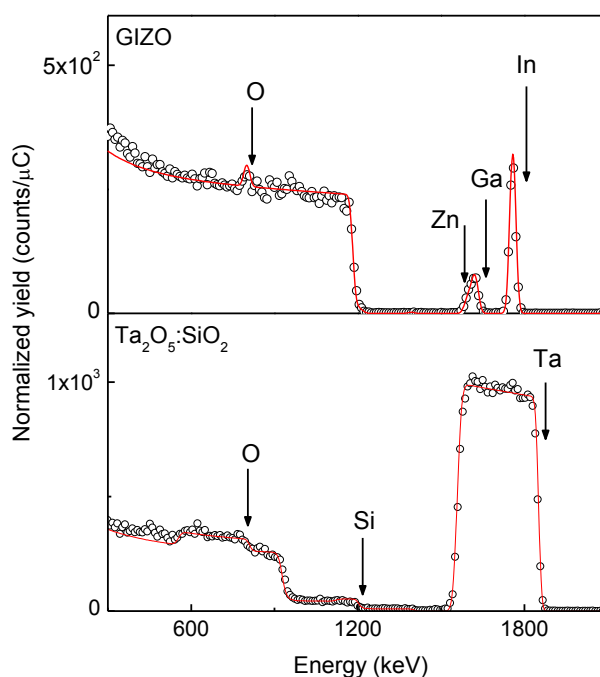


Figure 6.4. RBS spectra of GIZO semiconductor (top) and multicomponent Ta₂O₅:SiO₂ dielectric (bottom) thin films and corresponding fit lines.

RBS data fitting through specific software (Barradas 1997) allowed the calculation of the atomic composition for each film. The results are summarized in Table 6.1.

Table 6.1. Elemental composition of the deposited oxides obtained from RBS data fitting.

Elemental composition in atomic percentage (at.%)					
GIZO	Galium	Indium	Zinc	Oxygen	Argon
(Ga:In:Zn 1:2:1)	7.3	12.9	4.6	74.5	0.7
Ta₂O₅:SiO₂	Tantalum	Silicon	Oxygen	Argon	
	14.7	17.0	65.6	2.3	

The composition obtained for the GIZO semiconductor layer is very close to the expected target composition however the results indicate a Zn deficiency (~8%) in the deposited film. This phenomenon has been reported for sputtered GIZO films and might be related to a lower growth rate of ZnO when compared to In and Ga oxides (Kim 2007). For the co-sputtered multicomponent Ta₂O₅:SiO₂ dielectric the obtained Ta and Si atomic compositions were very similar, yielding approximately a 1:1 mixture. Similarly to what was observed for Ta₂O₅ sensitive layer, a small percentage of argon was also detected in both semiconductor and dielectric films although it is not visible in the presented spectra. The incorporation of argon into the films is a consequence of the deposition process and, as can be seen in Table 6.1, a larger percentage of argon is incorporated into the dielectric film due to the use of a higher power density which is required to deposit insulator materials.

6.2.4. Electrical characterization

The extended gate ISFET sensors are based on GIZO TFTs, as such these devices were characterized by determining their current-voltage ($I(V)$) curves. The TFTs properties were assessed by measuring the transfer characteristics, defined as the drain current (I_D) dependence on gate voltage (V_G) when applying a fixed drain-source voltage (V_D), and the output characteristics, defined as the I_D dependence on V_D when applying a fixed V_G . The transfer characteristics allow the determination of several electrical parameters that characterize TFT devices: turn-on voltage (V_{on}), threshold voltage (V_T); carries mobility (μ); On/Off current ratio ($I_{D\text{ On}}/I_{D\text{ Off}}$) and subthreshold swing (S), which is the necessary V_G to increase I_D by one decade.

The electrical characteristics of an extended gate amorphous oxides based TFT, comprising a GIZO semiconductor layer, a Ta₂O₅:SiO₂ multicomponent dielectric layer, Ti/Au source, and drain and gate electrodes, are represented in Figure 6.5.

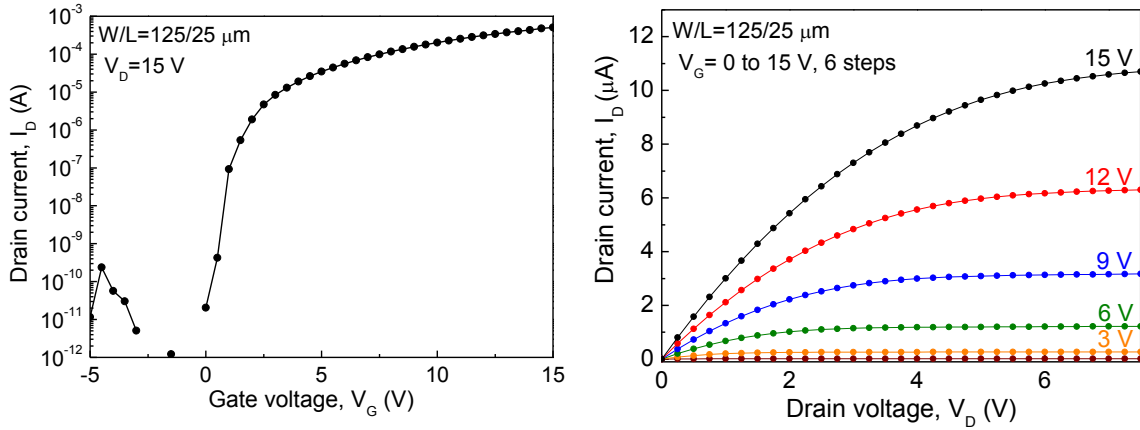


Figure 6.5. Transfer (left) and output (right) characteristics of an amorphous oxides based TFT.

The device shows the following electrical properties: close to zero turn-on voltage; ON/OFF ratio of 2×10^7 ; subthreshold swing of 0.23 V/dec and field effect mobility of $\sim 30 \text{ cm}^2 \cdot \text{V}^{-1} \cdot \text{s}^{-1}$. These results are in agreement with previously obtained for the same experimental deposition conditions and traditional device structure (Barquinha 2010 and 2010a).

The extended gate structure did not significantly alter the expected devices characteristics however passivation was a critical step in assuring device and measurement stability. The importance of passivation is clearly demonstrated in Figure 6.6, which shows ten sequential transfer characteristics measurements for a GIZO TFT fabricated on a glass/ITO/ATO commercial substrate prior to (Figure 6.6 - left) and after (Figure 6.6 - right) passivation with a PDMS layer.

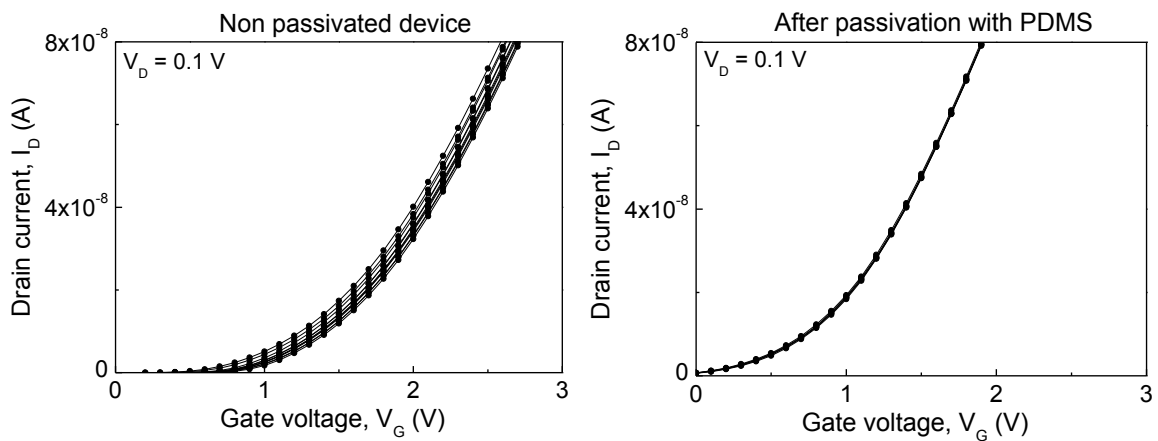


Figure 6.6. Influence of passivation on device stability and measurement reproducibility (GIZO TFT on glass/ITO/ATO substrate).

The PDMS layer is easily fabricated by casting a thin film of PDMS with the desired features; it is then applied to the TFT substrate and annealed at 200 °C for one hour to promote adhesion. Although PDMS demonstrated good passivation properties its adhesion to the substrate diminished with time, and consequently the devices stability was not maintained. As such, SU-8 was preferred as passivation material which although requiring a more elaborate experimental procedure guaranteed device passivation and stability, as already demonstrated for GIZO TFTs (Olziersky 2010).

The electrical properties of the ISFET devices were evaluated in a similar way to TFTs by assessing the $I(V)$ transfer and output characteristics of the devices however, the gate potential was applied through a commercial Ag/AgCl reference microelectrode (Unisense). These measurements required a special experimental setup as such, a specific measurement cell (Figure 6.7) was designed and fabricated to define an electrolyte container and allow $I(V)$ measurements in the micro-probe station; with the added advantage that the sensors are not dipped in the electrolyte.

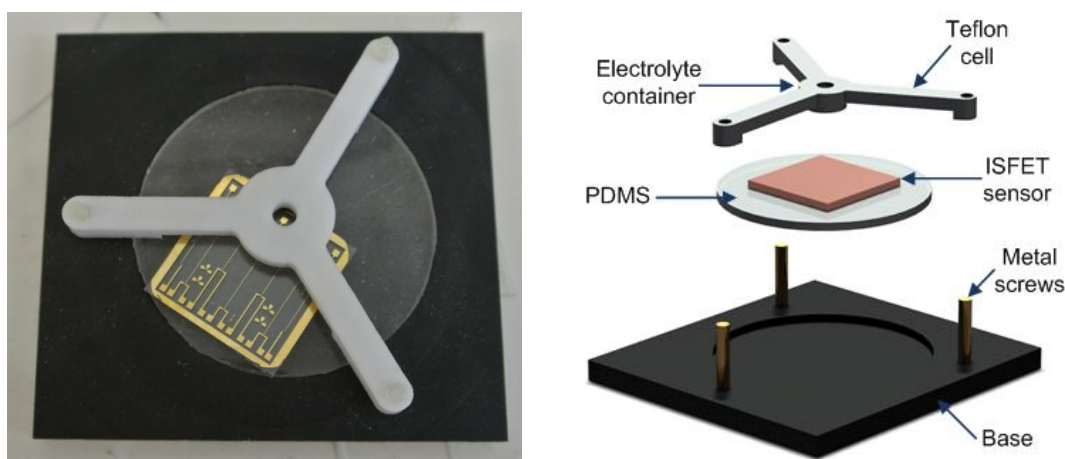


Figure 6.7. ISFET sensors measurement cell: real image (left) and schematic assembly representation (right).

6.3. pH sensitivity of oxide ISFETs

The devices pH sensing performance was evaluated by exposing the sensitive area to constant ionic strength buffer solutions of different pH. Three consecutive measurements were performed at each pH solution; upon changing solutions the sensitive surface was thoroughly rinsed with the following solution and it was allowed

to stabilize for 15 min prior to the first I(V) measurement. All measurements were performed using an Agilent 4155C semiconductor parameter analyzer connected to a Cascade Microtech M150 probe station inside a dark box, to minimize external noise.

The transfer curves obtained (at $V_D = 0.1$ V) by exposing the Ta_2O_5 sensitive layer of extended gate GIZO ISFETs with a multicomponent $\text{Ta}_2\text{O}_5:\text{SiO}_2$ dielectric layer to electrolyte solutions of varied pH, are presented in Figure 6.8 (top). The pH measurements were performed first with increasing proton concentration (decreasing pH) and then in the reverse order in two measurement cycles; namely Cycle 1: pH 10 \rightarrow pH 7 \rightarrow pH 4 and Cycle 2: pH 4 \rightarrow pH 7 \rightarrow and pH 10.

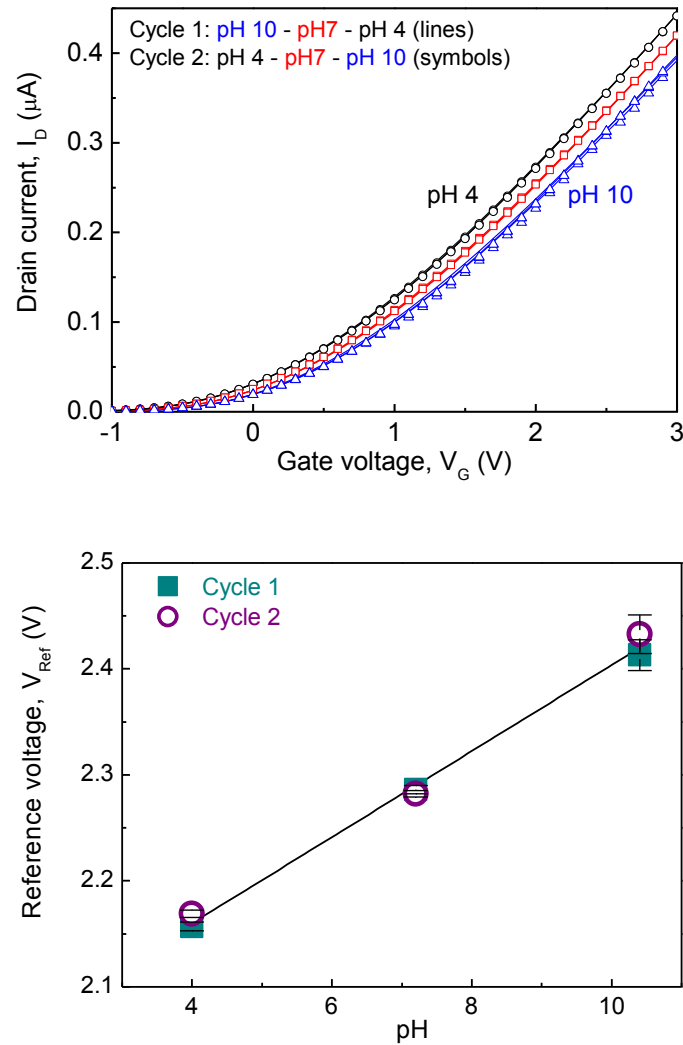


Figure 6.8. Transfer characteristics obtained with $V_D = 0.1$ V for two pH cycles (top) and pH sensitivity expressed as variation of the reference voltages with buffer solution pH (bottom).

The obtained device's response was coherent in both measurement cycles, which confirms a pH induced response. Similarly to EIS sensors, the reference voltage (V_{Ref})

can be obtained by considering a fixed drain current value ($I_D = 0.3 \mu\text{A}$) and determining the voltage for each electrolyte solution. The detected voltage shift was found to be linearly proportional to the pH change and graphical representation of the reference voltages variation with electrolyte pH allows the pH sensitivity determination (Yan 2005). A sensitivity of $40 \pm 1 \text{ mV/pH}$ was obtained either considering the two cycles separately or averaging the global data (Figure 6.8 - bottom).

The device's response was also evaluated through transfer characteristics measurements with $V_D = 0.5 \text{ V}$ and $V_D = 1.0 \text{ V}$, and determining the reference voltage values considering $I_D = 1.5 \mu\text{A}$ and $I_D = 2.5 \mu\text{A}$, respectively. Regardless of the applied drain-source voltage, the obtained sensitivity was very similar; $40 \pm 2 \text{ mV/pH}$.

The drift effect in ISFET devices is well known and can be due to the electrolyte/sensitive layer interaction and also to the device itself (Jamaspb 1998). Upon consecutive measurements with the same electrolyte solution, a slight drift effect was detected as the experimental data revealed a positive reference voltage shift. The higher variability between measurements was observed for curves obtained at pH 10 ($\sim 25 \text{ mV}$) whereas for pH 7 and pH 4 electrolyte solutions variability was lower ($\sim 6 \text{ mV}$). The higher variability for pH 10 solutions is consistent with the fact that sensitivity and stability of a sensitive layer is dependent on the pH of the point of zero charge (pH_{pzc}) of the sensitive material, being higher for solutions with pH within two units of the pH_{pzc} of the sensitive material which for Ta_2O_5 is within the range $4 < \text{pH}_{\text{pzc}} < 5$. The temporal response is presented in Figure 6.9 and illustrates these effects. The positive drift can also be attributed to electrical bias-stress as measurements were performed with a slower sweeping rate than the corresponding oxide TFTs.

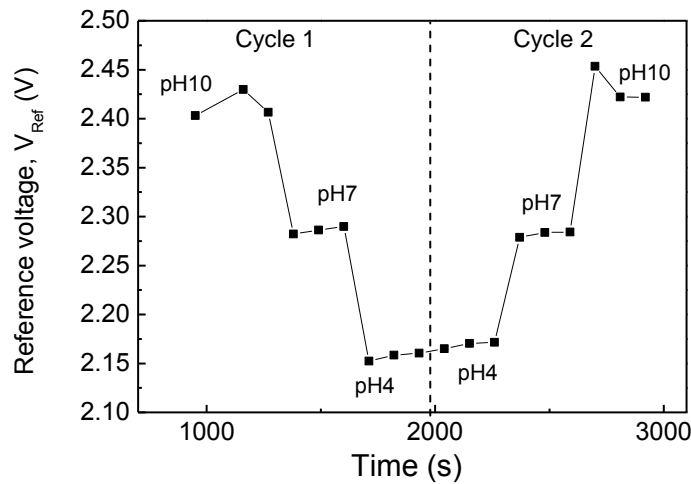


Figure 6.9. Temporal response variation of the reference voltages obtained at $0.3 \mu\text{A}$ for both cycles of pH measurements.

The hysteresis considering the reference voltage variations for measurements obtained with buffer solutions of the same pH but performed in different cycles (decreasing and increasing solutions pH, respectively) was ~ 6 mV for the pH 7 buffer solution, which is in agreement with reported results for these devices (Sasaki 2010).

The output characteristics of the device were measured for each pH buffer solution and are presented in Figure 6.10. An increase of the drain current (I_D), represented by the vertical shift in the $I(V)$ curves, induced by the pH solution can be observed.

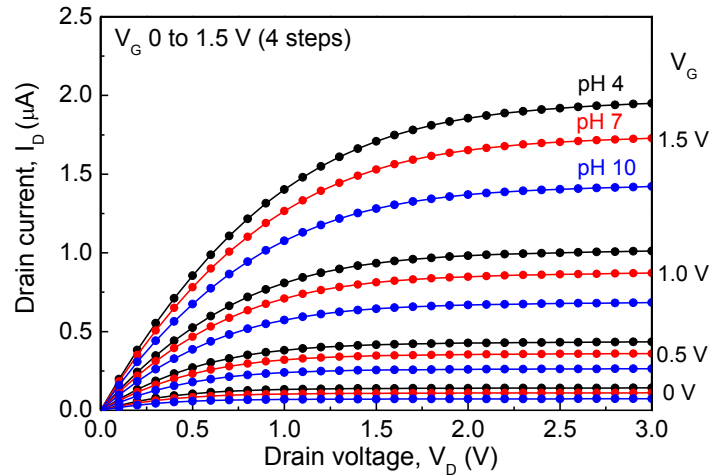


Figure 6.10. ISFET output characteristics at fixed gate voltage ($V_G = 0, 0.5, 1.0, 1.5$ V) with different pH solutions.

The increase in proton concentration (lower pH) leads to a variation of the Ta_2O_5 sensitive layer surface potential and consequently to the channel current increase. This effect is dependent on the applied gate voltage being larger for higher V_G values; for instance, considering the output curves obtained with $V_G = 1.5$ V and $V_D = 2.0$ V, the channel current increases approximately $0.5 \mu A$ when changing from pH 10 to pH 4 buffer solution. Nevertheless, even when no potential is applied to the electrolyte solutions ($V_G = 0$ V) a vertical I_D curves shift entirely due to pH variation can be observed.

The ISFET device performance was also evaluated with commercial buffer solutions of pH ranging from 2 to 12, in order to assess its response in a broader pH range. Transfer characteristics were obtained applying the same protocol; three consecutive measurements with $V_D = 0.1$ V after an initial 15 min stabilization in the dark; and results are presented in Figure 6.11 (top). A positive voltage shift of ~ 200 mV was detected when comparing transfer curves obtained with buffer solutions of similar pH. The shift in the reference voltages can be a consequence of temperature/humidity

variations as measurements were performed in different days. Nevertheless, the device presents a linear response between pH 4 and pH 10 maintaining pH sensitivity in the range of 40 to 41 mV/pH; as can be seen in Figure 6.11 (bottom).

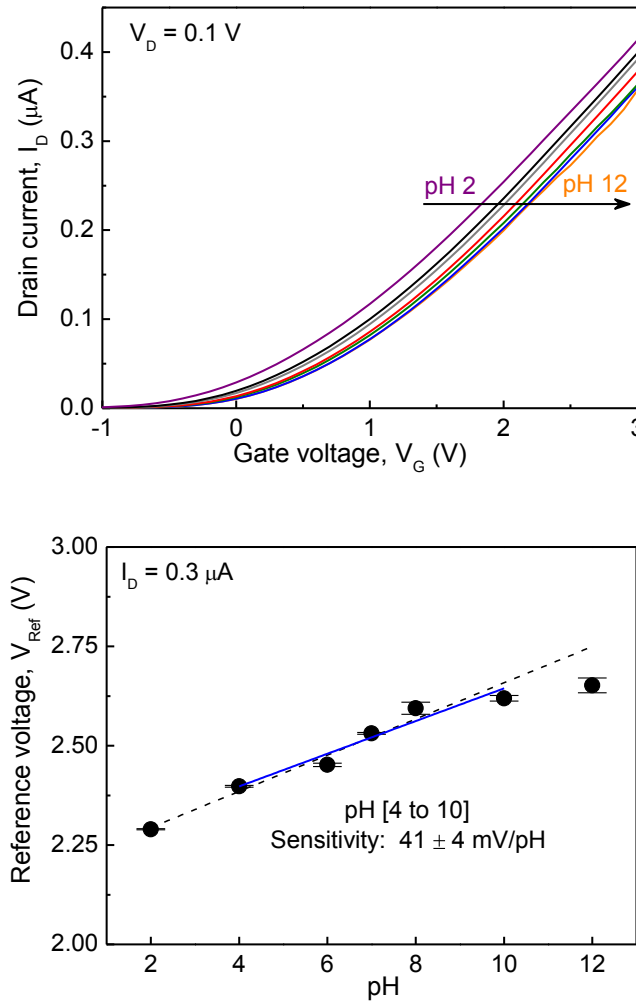


Figure 6.11. Device response to varied buffer solutions in a pH range between pH 2 and pH 12: (top) transfer characteristics obtained at $V_D = 0.1$ V and (bottom) pH sensitivity expressed as variation of the reference voltages with buffer solution pH.

The pH sensitivity obtained with the ISFET device is lower than that achieved with EIS sensors and also than the values reported (57–59 mV/pH) for Ta_2O_5 sensitive layer based ISFETs of different configurations (Chiang 2001; Know 1996; Poghosian 2004). The electrical bias-stress induced to during the measurements combined with short term drifts in the device itself may influence the ISFETs performance and prevent the determination of a stable response with good accuracy. In fact the stress induced instabilities and variations of temperature and humidity are still critical issues when considering oxide-based TFTs. On the other hand, both sensitivity and time response of the ISFETs are highly dependent on the measurement protocol used and currently a

consensual methodology is still lacking. Nevertheless, fully amorphous oxide based ISFETs were successfully produced and the sensitivity of the device was coherent throughout all the measurements (Pinto 2012). Further device optimization, in terms of layers deposition conditions and geometric structure of the device, while maintaining the optimized Ta_2O_5 sensitive layer has led to an increase in pH sensitivity to ~ 50 mV/pH. These results clearly indicate that the development and optimization of device fabrication specifically for ISFET applications is paramount and that there is still room for improvement in the future of amorphous oxides based ISFET sensors.

GIZO based ISFET devices comprising the optimized were also produced on commercial substrates (ITO/ATO and Si/SiO₂) which already possess common gate and dielectric layers. As such, these devices only require the deposition of the GIZO semiconductor layer and of the source and drain Ti/Au electrodes; which were performed following the same procedure and deposition conditions as before.

In ITO/ATO ISFET devices the conductive indium tin oxide (ITO) acts as the gate electrode and the Al_2O_3 – TiO_2 multi-layer (ATO) as the dielectric layer. ISFET devices were successfully produced and the transfer characteristics obtained by exposing the Ta_2O_5 sensitive layer to electrolyte buffer solutions of different pH are presented in Figure 6.12.

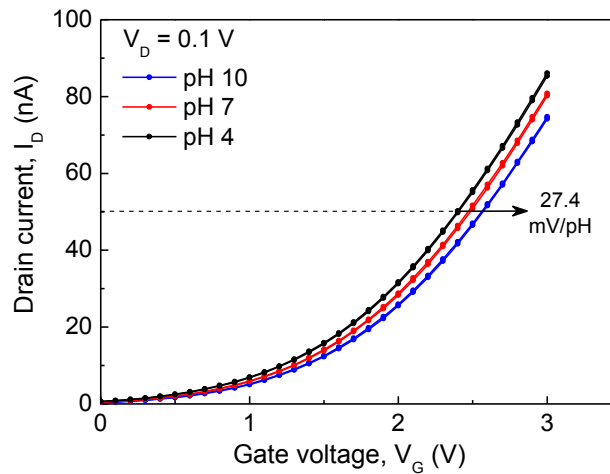


Figure 6.12. Variation of the transfer characteristics of a GIZO based ITO/ATO ISFET device with buffer solution's pH ($V_D = 0.1$ V).

The GIZO based ITO/ATO ISFET devices showed a pH induced response similarly to the extended gate GIZO ISFETs with a sputtered multicomponent Ta_2O_5 : SiO_2 dielectric layer. However lower pH sensitivity was determined for these sensors; 27.4 mV/pH. As the sensitive layer was produced with identical deposition conditions the pH sensitivity

difference can possibly be a consequence of the device structure. In ITO/ATO substrates both the gate and dielectric layers are deposited on all the substrate area and are not individualized, which can influence the measurements and lead to signal loss.

In Si/SiO₂ ISFET devices the highly doped Si substrate acts as the gate electrode and the SiO₂ as the dielectric layer. Electrolyte gated devices were successfully obtained and transfer characteristics could be measured by applying the gate voltage through the reference electrode in solution. However, the device's response was not coherent with pH variations so consequently pH sensitivity could not be determined for these devices. Similarly to the ITO/ATO ISFETs the fact that both the gate and dielectric layers are not individualized might be the most probable cause for this problem. Moreover, although the Si substrate is highly doped it is not a conductive material which can possibly contribute even further to signal dispersion.

Summarizing

Amorphous GIZO based ISFETs comprising the optimized Ta₂O₅ sensitive layer were successfully produced with an extended bottom gate structure, in three distinct configurations: i) ISFETs comprising a sputtered multicomponent Ta₂O₅:SiO₂ dielectric layer and Ti/Au gate electrode; ii) ISFETs based on commercial ITO/ATO substrates; and iii) ISFETs based on commercial Si/SiO₂ substrates. Similarly to EIS sensors, the pH sensitivity assessment of ISFET devices can be performed by determining the reference voltage for each electrolyte solution at a fixed drain current value and plotting the reference voltages variation with electrolyte pH.

For ISFETs based on commercial Si/SiO₂ substrates, although electrolyte gated I(V) measurements were successfully obtained, the reference voltage variation was not coherent with the solution's pH; and ISFETs based on commercial ITO/ATO substrates revealed a pH sensitivity of only ~27 mV/pH. The results are far from those obtained with EIS sensors and can probably be a consequence of the fact that, in these devices, neither the gate electrode nor the dielectric layer are individualized which might lead to signal loss. For ISFETs comprising a sputtered multicomponent Ta₂O₅:SiO₂ dielectric layer and Ti/Au gate electrode a 40±2 mV/pH sensitivity was obtained and further device fabrication optimization led to pH sensitivity improvement to ~50 mV/pH. Consequently, it can be concluded that configuration has a determinant role in the device's performance and that specific optimization of devices towards sensing applications is needed. Nevertheless, the obtained results clearly show that amorphous metal oxide transistors are promising candidates for biosensing applications.

Chapter 7. Conclusions and future perspectives

7.1. Conclusions.....	157
7.1.1. Optimization of sputtered Ta ₂ O ₅ thin films for sensing applications....	157
7.1.2. Enzyme-functionalized FEDs for penicillin detection	160
7.1.3. Label-free detection of DNA.....	161
7.1.4. Oxide semiconductor–based ISFETs	163
7.2. Future perspectives	164

Chapter 7. Conclusions and future perspectives

The research work presented in this dissertation was divided into three main areas: optimization of sputtered tantalum oxide thin films for sensing applications through the study of different processing and post-processing conditions and how these influence pH sensitivity; production of BioFEDs for penicillin detection via enzyme-modified devices and for label-free DNA detection and amplification monitoring; and finally, the production of ISFETs based on semiconductor oxides comprising the optimized Ta₂O₅ sensitive layer for pH and biosensing.

In this chapter general conclusions about these topics and future perspectives for further development of this research area, are presented.

7.1. Conclusions

The main conclusion that can be drawn from the work developed in this dissertation is that high quality and highly sensitive Ta₂O₅ thin films for application as sensitive layer in field effect sensors can be produced at low temperature by rf magnetron sputtering.

Succinctly, EIS field effect based sensors comprising Ta₂O₅ films produced with optimized conditions demonstrated near Nernstian pH sensitivity, 58 ± 0.3 mV/pH. These sensors were successfully applied to the development of BioFEDs for the label-free detection of penicillin and DNA. Enzyme functionalized sensors (EnFEDs) showed a 29 ± 7 mV/mM sensitivity towards penicillin detection up to 4 mM penicillin concentration. DNA detection was achieved with 30 mV/ μ M sensitivity and DNA amplification monitoring with optimized Ta₂O₅-based EIS sensors showed comparable results to those obtained with standard fluorescence based methods. ISFETs based on semiconductor oxides comprising the optimized Ta₂O₅ sensitive layer for pH and biosensing were also successfully fabricated.

7.1.1. Optimization of sputtered Ta₂O₅ thin films for sensing applications

The influence of the deposition parameters on pH sensitivity was studied by varying deposition pressure, deposition gases ratio (Ar:O₂) and rf power density. The Ta₂O₅-EIS sensors were all subjected to a post-deposition annealing at 200 °C for one hour in an air atmosphere. Structural, compositional, morphological and optical characterization

of the deposited films was performed and results showed that generally Ta₂O₅ properties do not significantly vary with the deposition parameters. Regardless of the deposition parameters, amorphous and stoichiometric Ta₂O₅ films were obtained. The obtained films are uniform with a smooth surface, revealing a surface roughness below 0.3 nm; as typically observed for amorphous films. Slightly higher values of surface roughness were obtained with ellipsometry modulation data, nevertheless no significant variation is observed and values are in agreement with reported data for amorphous Ta₂O₅. The average visible transparency was above 85% and optical band gap between 3.5 – 4.2 eV which is in agreement with ellipsometry modulation data for *E_g*; between 4.0 – 4.2 eV and reported values for amorphous Ta₂O₅ (Pereira 2008).

A closer analysis of spectroscopic ellipsometry modulation data revealed slight variations related to film density and in band gap energy. These could be correlated with pH sensitivity variation and allowed the determination of the optimized deposition parameters of the pH sensitive Ta₂O₅ layer. It was observed that with a deposition rf power of 150 W and by increasing the oxygen content from 0.5 sccm to 1 sccm a slight increase in band gap energy and film density improvement are attained. This tendency was observed for every deposition pressure studied and further increase in oxygen content did not lead to significant properties variation.

The pH sensitivity of EIS sensors was assessed by capacitance-voltage characteristics (C(V)) of EIS sensors exposed to buffer solutions of different pH. Sensitivity to pH varied between 45 – 58 mV/pH depending on film production parameters. This was an improvement to bare SiO₂ pH sensitivity; 32±3mV/pH which is in agreement with reported values for thermal SiO₂; 37 mV/pH (Abouzar 2011) and 35-40 mV/pH (Poghossian 2007a).

Typically high sensitivity, expected for Ta₂O₅ (above 55 mV/pH), was attained with selected deposition conditions and some relations between production parameters and pH sensitivity could be drawn. A clear pH sensitivity improvement was achieved for films produced with a rf power of 150 W and also with 1 sccm oxygen content, for intermediate deposition pressures 0.3 and 0.5 Pa. At 0.3 Pa deposition pressure not only an almost Nernstian pH response was obtained but also measurement variability was minimized. The pH sensitivity increase can be correlated with the slight improvements in films properties observed in the parameters obtained by spectroscopic ellipsometry modulation, as previously mentioned.

Near Nernstian pH sensitivity, 58±0.3 mV/pH, was achieved for the optimized Ta₂O₅ sensing layer, which was obtained with the following deposition conditions: 150 W rf

power; 0.3 Pa pressure and 14:1 Ar:O₂ ratio and a post-deposition annealing at 200 °C for one hour in an air atmosphere.

The influence of post-deposition annealing temperature was studied by annealing EIS sensors with the optimized Ta₂O₅ sensitive layer up to 800 °C in an air atmosphere for one hour. Structural characterization reveals that the Ta₂O₅ films remain amorphous up to 600 °C and no significant changes in film's properties were obtained, similarly to the previously discussed film deposition conditions study. Stoichiometric, uniform and smooth films with surface roughness below 0.3 nm and band gap energy of ~4.2 eV were obtained. At 700 °C the Ta₂O₅ film starts to crystallize in an orthorhombic phase, surface morphology changes and an increase in surface roughness is observed; 0.8 nm and 5.4 nm (800 °C). Ellipsometry modulation data indicate that densification of the films occurs with increasing annealing temperature. EIS sensors with an amorphous Ta₂O₅ sensing layer (up to 600 °C) showed pH sensitivity above 50 mV/pH, nevertheless maximum sensitivity and measurement stability improvement were obtained for a low annealing temperature of 200 °C.

The influence of post-production room temperature surface plasma treatments on the Ta₂O₅ sensing characteristics was assessed by exposing the samples to either argon plasma, in an attempt to increase surface roughness and consequently sensitive area, or oxygen plasma, in an attempt to increase the number of active surface sites.

In general, the argon plasma treatment had a negative influence on the pH sensitivity of Ta₂O₅. Surface roughness remained unchanged and $R_{rms} < 0.3$ nm was obtained even for the harshest argon plasma treatment. However, C(V) characteristics of treated films were shifted towards positive potentials which indicates an increase of positive charges at the sensor's surface. Such positive charge might arise from the accumulation of argon ions at the oxide's surface, leading to the conclusion that the decrease in sensitivity with increase time and power of argon plasma treatment might be a consequence of the blocking of surface active sites by argon ions.

Oxygen plasma treatment effectively increased pH sensitivity a maximum of 3.5 times the untreated sensor; however treated sensors suffered from instability and reproducibility issues. C(V) characteristics of treated films were shifted towards more negative potentials which indicates an increase of negative charge at the oxide's surface probably due to accumulation of oxygen ions. The higher concentration of oxygen ions at the oxide surface can justify the pH sensitivity increase; however obtained values are higher than the maximum theoretically predicted by the Nernst equation (59.2 mV/pH). This clearly indicates that additional sensing mechanisms that are not being

accounted for must therefore exist. Nevertheless, the most effective oxygen surface plasma treatment appears to be the one obtained for a 5 min. exposure with 30 W applied rf power since it yielded the best compromise between sensitivity enhancement and measurement variability; 121 ± 10 mV/pH (a ~ 2 times increase) and this sensor was used to successfully fabricate an enzyme-based penicillin sensor.

In conclusion, the deposition of Ta_2O_5 by rf sputtering yielded uniform, amorphous and stoichiometric films, with the tested deposition conditions. Ta_2O_5 EIS-based sensors demonstrated good pH sensitivity regardless of deposition conditions. The pH sensitivity of sputtered Ta_2O_5 sensitive layers can be related to the deposition parameters and an optimized near Nernstian sensitivity, 58 ± 0.3 mV/pH, was obtained for Ta_2O_5 films produced with; 150 W rf power; 0.3 Pa pressure and 14:1 Ar: O_2 ratio, and a post-deposition annealing at 200 °C for one hour in an air atmosphere.

Post-deposition surface treatments with O_2 plasma significantly enhanced pH sensitivity of the sensors; however these suffered from reproducibility and measurement variability issues. Moreover, pH sensitivity was beyond the theoretically expected maximum which indicates that unaccounted for mechanisms of detection must be taking place and a clearer understanding of these is necessary.

7.1.2. Enzyme-functionalized FEDs for penicillin detection

Penicillinase-modified EIS sensors comprising the optimized Ta_2O_5 sensitive layer, before and after oxygen plasma surface treatment (5 min.; 30 W), were constructed by coating the sensitive membrane with a penicillinase layer. The sensing principle of penicillin with penicillinase-modified FEDs is based on the detection of a pH variation that arises from proton production due to the penicillinase–penicillin reaction.

For both sensors, untreated and O_2 plasma treated, similar results were obtained. The C(V) curves shift to higher potentials upon penicillin concentration increase which is in agreement with a pH decrease and results reveal a typical enzymatic reaction curve; signal variation with analyte concentration is linear until saturation is reached.

Sensitivity is higher for low penicillin concentrations with a tendency to decrease for more concentrated solutions. A linear variation of reference voltage was found for penicillin concentrations below 4 mM. Considering the pH sensitivity of untreated and O_2 plasma treated sensors; 58.2 ± 0.3 mV/pH and 121 ± 10 mV/pH, respectively; a local pH variation of two pH units (pH ~ 5 near sensor surface) was found to be induced by a

4 mM penicillin solution, for both sensors. The decrease in sensitivity observed above 4 mM penicillin can be a consequence of enzyme inhibition due to the local pH decrease.

Nearly twice the sensitivity of the untreated sensor, 29 ± 7 mV/mM, was obtained for the O₂ plasma treated sensor, 62 ± 18 mV/mM; which is related to the pH sensitivity difference (also twice as high). However the results variability increased accordingly, and plasma treatment reproducibility issues must be taken into account when considering the application of this method for FEDs sensitivity increase.

In conclusion, penicillinase functionalized Ta₂O₅-based EIS sensors were successfully produced for penicillin detection. A linear variation of sensor signal with penicillin concentration increase was found up to 4 mM and sensitivity of 29 ± 7 mV/mM and 62 ± 18 mV/mM was obtained for untreated and O₂ plasma treated sensor, respectively. Although a significant sensor signal increase was obtained with oxygen plasma treated sensors, these suffered from measurement variability and reproducibility issues.

7.1.3. Label-free detection of DNA

The optimized Ta₂O₅ EIS sensors were also successfully applied to the label free detection of DNA and the monitoring of its amplification via polymerase chain reaction (PCR), real time PCR (RT-PCR) and loop mediated isothermal amplification (LAMP). The obtained results were comparable to conventional fluorescence based DNA detection methods.

The detection of DNA concentration variations with the optimized Ta₂O₅ EIS sensor was achieved with 30 mV/ μ M maximum sensitivity. The C(V) characteristics shift occur towards more positive potentials which is consistent with an increase of positive charge (counter ions) near the sensor's surface upon DNA concentration increase. The obtained results suggest that the detection mechanism is based on the redistribution of ionic concentration, namely attracting positive counter-ions and repelling negative ions, near the sensor's surface. A sensor signal variation of ~ 25 mV was obtained for a hybridization event or a twofold increase in DNA concentration, which is in good agreement with estimated values of 28-35 mV with a device that exhibits Nernstian sensitivity (Poghossian 2005). This allows the application of the optimized Ta₂O₅ EIS sensors to DNA amplification monitoring.

The applicability of the optimized Ta₂O₅ EIS sensor to monitor DNA amplification was assessed by measuring its response to samples collected during the PCR amplification

process of a specific nucleic acid sequence of cMYC proto-oncogene, which is related to a wide variety of human cancers. The obtained results were compared to conventional fluorescence based methods of PCR and RT-PCR cMYC amplification.

The PCR amplification process leads to a DNA concentration increase with each cycle. The DNA concentration increase was translated as a C(V) characteristics shift towards more positive potentials, which is consistent with the described detection mechanism. Although some drifting effects affected the sensor signal due to the complexity of PCR samples, corrected results show a typical PCR exponential curve. A clear discrimination between positive and negative samples was obtained at cycle 12 and the plateau stage is achieved at cycle 21. The obtained results are in agreement with and comparable to fluorescence-based analysis of PCR and RT-PCR amplification samples.

Considering the successful results obtained for the field effect monitoring of DNA amplification products, the optimized Ta₂O₅-based EIS sensors were also applied for the field effect real-time monitoring of LAMP DNA amplification. For that a specific measurement cell with the necessary requirements for the LAMP reaction to occur and that simultaneously allows the real-time monitoring of this process was designed and fabricated. The successful LAMP cMYC amplification was achieved in the specifically developed cell with a homemade temperature control setup; being confirmed by conventional fluorescence based methods. The amplification reaction was monitored in real-time and a clear distinction between positive and negative amplification samples was obtained. Although being only preliminary, these results are very promising and testify to the applicability of field effect sensors to the real-time monitoring of LAMP DNA amplification.

In conclusion, Ta₂O₅ EIS sensors were successfully applied to the label-free field effect detection of DNA, with 30 mV/ μ M sensitivity. Also these sensors showed comparable capability to detect DNA amplification via PCR to that of standard fluorescence based methods without the need of expensive and cumbersome apparatus. In LAMP DNA amplification real-time monitoring, a clear distinction between positive and negative amplification samples was achieved; which, despite being preliminary, are very promising results. Further optimization and miniaturization of the sensor could perhaps allow for an alternative non fluorescence-based DNA detection method that is direct and label-free.

7.1.4. Oxide semiconductor–based ISFETs

The optimized Ta₂O₅ sensitive layer was combined with amorphous GIZO based TFTs and oxide based ISFETs with an extended bottom gate structure were successfully produced, in three distinct configurations: i) ISFETs comprising a sputtered multicomponent Ta₂O₅:SiO₂ dielectric layer and Ti/Au gate electrode; ii) ISFETs based on commercial ITO/ATO substrates; and iii) ISFETs based on commercial Si/SiO₂ substrates. Similarly to EIS sensors, the pH sensitivity of ISFET devices was assessed by determining the reference voltages for each electrolyte solution at a fixed drain current value and plotting the reference voltages variation with electrolyte pH.

It was found that configuration has a determinant role in the device's performance and pH sensitivity measurement as results are far from those obtained with EIS sensors. For ISFETs based on commercial Si/SiO₂ substrates, although electrolyte gated I(V) measurements were successfully obtained, the reference voltage variation was not coherent with the solution's pH; and ISFETs based on commercial ITO/ATO substrates revealed a pH sensitivity of only 27 mV/pH. This can probably be a consequence of the fact that, in these devices, neither the gate electrode nor the dielectric layer are individualized which might lead to signal loss. For ISFETs comprising a sputtered multicomponent Ta₂O₅:SiO₂ dielectric layer and Ti/Au gate electrode a 40±2 mV/pH sensitivity was obtained and further device fabrication optimization led to pH sensitivity improvement to ~50 mV/pH. Consequently, it can be concluded that specific optimization of devices towards sensing applications is needed nevertheless; the obtained results clearly show that amorphous metal oxide transistors are promising candidates for biosensing applications.

7.2. Future perspectives

As with any kind of research work, a large number of questions and paths remain unanswered and unexplored. Based on the results presented herein and in recent literature regarding field effect based sensors, some recommendations for future work are suggested in this section.

Sensitive layer production and characterization improvement

The study on the effect of the deposition conditions on pH sensitivity presented in this dissertation allowed some conclusions to be drawn; however it can be extended and improved to better understand the relation between material's production and pH sensitivity.

Milder deposition conditions can be explored such as lower rf power density which, although requiring longer deposition time, can improve interface properties due to less ion bombardment and also lead to denser films. This would allow deposition directly on Si and eliminate the need for the intermediate SiO₂ layer, which is useful for application with other semiconductors where the deposition of thermal SiO₂ is not possible.

Characterization of metal-insulator-semiconductor (MIS) devices comprising the insulating sensitive layer can be performed to infer on films properties and defects. This is also important to the enlightenment of the effect of O₂ plasma surface treatment on the oxide surface and consequential pH sensitivity improvement above the theoretical maximum.

Transparent sensors development

The development of transparent EIS devices, on glass and paper, based on the rf sputtering of all the layers; transparent conductive oxide (TCOs), semiconductor (TSOs) and dielectric sensitive layer; is highly desirable. This opens the advantageous possibility to combine electrical and optical measurements simultaneously. Also the fabrication of disposable sensors can be envisioned; especially with paper substrates which are ideal in biodetection due to strict cleaning requirements, such as sterilization and other harsh processes that can damage the sensor. In fact, colorimetric paper based biosensors are currently being developed within the group (Veigas 2012).

Considering the excellent results obtained with transparent TFTs (Barquinha 2012) and paper transistors (Fortunato 2008), attempts to produce transparent EIS sensor both on glass and paper substrates were performed on the course of this work; however several difficulties arose when the devices were exposed to electrolyte solutions.

EIS devices on glass suffered from film peeling (Figure 7.1) due to the combination of exposure to liquid under voltage bias. Several variations were made to obtain working devices: back-contact material (aluminium, different TCOs – commercial ITO and FTO, sputtered IZO, FTO by spray pyrolysis), in semiconductor thickness (40 and 80 nm) and in Ta_2O_5 thickness (250 and 400 nm); however these were all unsuccessful. This is probably related to the deposition of the dielectric layer over the semiconductor layer which results in poor interface properties due to ion bombardment. The exploration of milder deposition conditions can provide improvement.

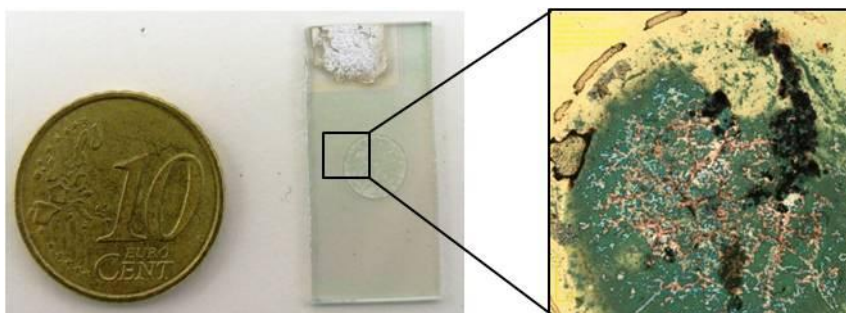


Figure 7.1. Image of a transparent EIS based sensor depicting the peeling of the layers.

EIS devices on hydrophobic papers were produced with two distinct structures, using paper only as a substrate (similar to glass devices) and simultaneously as substrate and an integrated part of the device, as the dielectric layer (Figure 7.2). However, in both structures, after the deposition of the Ta_2O_5 film the hydrophobic properties of paper are lost and water is absorbed into the device to some extent, consequently the devices are unusable. The degradation of the papers hydrophobic polymeric layer is probably due to the harsher deposition conditions required for dielectric materials as hydrofobicity is maintained after the deposition of the back-contact and semiconductor oxide layers. Again milder deposition conditions could provide an improvement; however the longer deposition time required can lead to excessive substrate heating and damage the paper itself. Another option could be the use of new paper substrates that are completely based on mineral materials, such as calcium carbonate, that might withstand the deposition conditions without affecting their properties.

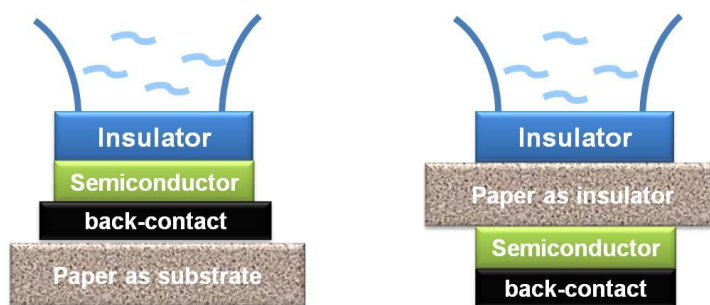


Figure 7.2. Schematic representation of both paper device structures.

Other materials and combination of different materials as sensitive layer

Although Ta_2O_5 has demonstrated excellent sensing properties, many other materials and materials combination can be explored for this purpose. HfO_2 is an example of an alternative material that can be deposited by rf sputtering. It has been explored for sensitive layer applications within our group and demonstrated good properties and high pH sensitivity (~ 55 mV/pH).

Combining materials with complementary properties such as combining high k /low E_g with low k /high E_g can result in improved film properties. Exploring either a co-sputtering deposition (results obtained within our group with co-sputtered $\text{Ta}_2\text{O}_5:\text{ZrO}_2$ mixture are very promising) or a multi-layer approach that has demonstrated excellent results in TFTs applications (Barquinha 2010); in this case the final layer would be composed of the material that demonstrated higher pH sensitivity. This approach is also promising for semiconductor oxides based EIS devices.

EnFEDs development

Optimization of the enzymatic layer in order to stabilize the sensors and increase enzyme loading, which can lead to an increase in the analyte concentration range and sensitivity and to a decrease of the limit of detection. The use of more elaborate immobilization methods such as polymeric entrapment or alternate layers of enzyme and charged macromolecules or dendrimer/carbon nanotubes (Siqueira 2009) have been reported with good results. Within our group the use of a layer of electrospun nitrocellulose fibres as a matrix for penicillinase immobilization improvement has demonstrated good results. Functionalization with various enzymes can provide new sensors for the detection of analytes of biological interest such as urea, glucose, lactate

among others and the fabrication of a sensor array for multi-analyte detection can be envisioned.

DNA detection

The results obtained in the label-free monitorization of PCR DNA amplification allow for the application of these devices to the monitoring of quantitative PCR DNA amplification which implies performing the PCR process with different template DNA concentrations to obtain a calibration curve and thus expand the obtain results from mere qualitative to quantitative.

The LAMP DNA amplification uses quite complex chemistry to allow for the isothermal DNA amplification consequently the process can be optimized. As the results obtained in this dissertation although preliminary are very promising further development of this study should be pursued. A more detailed study of the sensor device's behaviour at the process temperature and its dependence on temperature should be performed. Moreover the measurement cell and setup can be improved to minimize interferences (differential measurement setup) and to reduce reaction volumes. A sealed cell that mimics the eppendorf reaction vessel typically used in LAMP equipments can be employed to eliminate the need of mineral oil to prevent evaporation thus simplifying the setup and minimizing possible contaminations.

Methods to increase the biological signal such as the use of Au NPs as signal enhancers (Abouzar 2012) which, although not being totally label-free, might provide an advantageous signal gain and would still be a direct electrical measurement system without the need for other detection methods such as fluorescence.

Device optimization

Differential measurements have proven to be effective for the minimization of sensor drift issues and temperature related variations; in biological measurements, even more so, as these could serve as a semi-reference electrode. The development of a differential sensor setup is thus advantageous and desirable.

ISFETs device optimization towards biosensing can be performed as the devices used herein were optimized for microelectronic applications (Barquinha 2010a). For sensor applications the device's stability requirements are much more demanding while device

performance is not as critical; it is stability over performance since in biosensing the signal variation is in the order of hundreds or even only tenths of mV. Such small variations are within accepted variability of TFTs performance for microelectronic applications, so there is still room for device's improvement.

Other device structures can also be explored. Although the extended gate device structure has some advantages such as separating the electronic components from solution and allowing for a bottom gate device configuration; the direct modelling of the channel can provide better results, nonetheless a top gate structure usually yields poorer device performance due to the 'damaged' semiconductor/dielectric interface as the insulator layer is deposited over the semiconductor layer. Also dual gate devices have demonstrated super-Nernst sensitivity because of signal amplification that arises from the device structure (Spijkman 2010 and 2011) so this device structure can also be an appealing alternative.

Alternative deposition techniques

Other deposition techniques that avoid the need for high vacuum can be developed such as ink-jet printing; which has the added advantage of direct patterning. This would also require the development of solution processed materials that can be printed with this technique. Ink-jet printed electronics have demonstrated excellent results (Singh 2010) so the application of this technology for biosensor development seems only natural.

Miniaturization

An important step towards field effect based miniaturization is the elimination or substitution of bulky reference electrodes, with the use of differential measurements with quasi-reference electrodes or an on-chip reference electrode.

ISFETs are more suitable for miniaturization as these require only I(V) stimuli however the fabrication process is complex, requiring several process steps. EIS based sensor on the other hand are much easier to fabricate and have demonstrated higher stability and reproducibility, nevertheless these require ac signals an impedance measurement which increases the complexity of miniaturization.

Field effect based devices are becoming a basic structural element in a new generation of micro biosensors. Their numerous advantages such as small size, label-free response and versatility, together with the possibility of on-chip integration of biosensor arrays with a future prospect of low-cost mass production, can make the development of a pocket sized multi-parameter analyzer for applications in point-of-care medicine; environmental monitoring; food and drug industries, to name just a few; a reality.

As a final note, it is relevant to point out that the work developed in the course of this dissertation makes a bridge between materials science and life sciences thus contributing, in an interdisciplinary way, to the development of Science.

References

- Abouzar 2008 Abouzar, M.H., Poghossian, A., Razavi, A., Besmehn, A., Bijmens, N., Williams, O.A., Haenen, K., Wagner, P., Schöning, M.J., 2008. Penicillin detection with nanocrystalline-diamond field-effect sensor. *physica status solidi (a)* 205(9), 2141-2145.
- Abouzar 2011 Abouzar, M.H., 2011. Detection of molecular interactions using field-effect-based capacitive devices. PhD thesis, Humboldt University Berlin (Germany).
- Abouzar 2012 Abouzar, M.H., Poghossian, A., Cherstvy, A.G., Pedraza, A.M., Ingebrandt, S., Schöning, M.J., 2012. Label-free electrical detection of DNA by means of field-effect nanoplate capacitors: Experiments and modeling. *physica status solidi (a)* 209(5), 925-934.
- Abramova 2009 Abramova, N., Bratov, A., 2009. Photocurable Polymers for Ion Selective Field Effect Transistors. 20 Years of Applications. *Sensors* 9(9), 7097-7110.
- Abramova 2009a Abramova, N., Ipatov, A., Levichev, S., Bratov, A., 2009. Integrated multi-sensor chip with photocured polymer membranes containing copolymerised plasticizer for direct pH, potassium, sodium and chloride ions determination in blood serum. *Talanta* 79(4), 984-989.
- Aguas 2003 Aguas, H., Goncalves, A., Pereira, L., Silva, R., Fortunato, E., Martins, R., 2003. Spectroscopic ellipsometry study of amorphous silicon anodically oxidised. *Thin Solid Films* 427(1), 345-349.
- Assuncao 2003 Assuncao, V., Fortunato, E., Marques, A., Aguas, H., Ferreira, I., Costa, M.E.V., Martins, R., 2003. Influence of the deposition pressure on the properties of transparent and conductive ZnO:Ga thin-film produced by r.f. sputtering at room temperature. *Thin Solid Films* 427(1-2), 401-405.
- Atanassova 2010 Atanassova, E., Georgieva, M., Spassov, D., Paskaleva, A., 2010. High-k HfO₂-Ta₂O₅ mixed layers: Electrical characteristics and mechanisms of conductivity. *Microelectronic Engineering* 87(4), 668-676.
- Atkins 1998 Atkins, P.W., 1998. Physical chemistry. 6th ed., Oxford University Press, USA
- Backer 2009 Backer, M., Beging, S., Biselli, M., Poghossian, A., Wang, J., Zang, W., Wagner, P., Schoning, M.J., 2009. Concept for a solid-state multi-parameter sensor system for cell-culture monitoring. *Electrochimica Acta* 54(25), 6107-6112.

- Bandiera 2007 Bandiera, L., Cellere, G., Cagnin, S., De Toni, A., Zanoni, E., Lanfranchi, G., Lorenzelli, L., 2007. A fully electronic sensor for the measurement of cDNA hybridization kinetics. *Biosens. Bioelectron.* 22(9-10), 2108-2114.
- Barabash 1987 Barabash, P.R., Cobbold, R.S.C., Wlodarski, W.B., 1987. Analysis of the Threshold Voltage and Its Temperature-Dependence in Electrolyte-Insulator-Semiconductor Field-Effect Transistors (Eisfets). *Ieee Transactions on Electron Devices* 34(6), 1271-1282.
- Barhoumi 2010 Barhoumi, H., Maaref, A., Jaffrezic-Renault, N., 2010. Experimental Study of Thermodynamic Surface Characteristics and pH Sensitivity of Silicon Dioxide and Silicon Nitride. *Langmuir* 26(10), 7165-7173.
- Barquinha 2008 Barquinha, P., Pereira, L., Goncalves, G., Martins, R., Fortunato, E., 2008. The Effect of Deposition Conditions and Annealing on the Performance of High-Mobility GIZO TFTs. *Electrochemical and Solid-State Letters* 11(9), H248-H251.
- Barquinha 2009 Barquinha, P., Pereira, L., Goncalves, G., Martins, R., Fortunato, E., 2009. Toward High-Performance Amorphous GIZO TFTs. *Journal of The Electrochemical Society* 156(3), H161-H168.
- Barquinha 2009a Barquinha, P., Pereira, L., Goncalves, G., Martins, R., Kuscer, D., Kosec, M., Fortunato, E., 2009. Performance and Stability of Low Temperature Transparent Thin-Film Transistors Using Amorphous Multicomponent Dielectrics. *Journal of The Electrochemical Society* 156(11), H824-H831.
- Barquinha 2010 Barquinha, P., Pereira, L., Gonçalves, G., Martins, R., Fortunato, E., Kuscer, D., Kosec, M., Vilà, A., Olziersky, A., Morante, J.R., 2010. Low-temperature sputtered mixtures of high- κ and high bandgap dielectrics for GIZO TFTs. *Journal of the Society for Information Display* 18(10), 762-772.
- Barquinha 2010a Barquinha, P., 2010. Transparent Oxide Thin-Film Transistors: production, characterization and integration. PhD thesis, Faculdade de Ciência e Tecnologia, Universidade Nova de Lisboa (Portugal)
- Barquinha 2012 Barquinha, P., Pereira, L., Fortunato, E., and Martins, R., 2012. *Transparent Electronics: From Materials to Devices*. John Wiley & Sons Ltd.
- Barradas 1997 Barradas, N.P., Jaynes, C., Webb, R.P., 1997. *Appl. Phys. Lett.* 71, 291.
- Barsoukov 2005 Barsoukov, E., Macdonald, J.R., 2005. *Impedance Spectroscopy: Theory, Experiment, and Applications*, Second ed. John Wiley & Sons.
- Batista 2005 Batista, P.D., Mulato, M., 2005. ZnO extended-gate field-effect transistors as pH sensors. *Appl. Phys. Lett.* 87(14).

- Baumann 1999 Baumann, W.H., Lehmann, M., Schwinde, A., Ehret, R., Brischwein, M., Wolf, B., 1999. Microelectronic sensor system for microphysiological application on living cells. *Sensors and Actuators B: Chemical* 55(1), 77-89.
- Becker 2009 Becker, W.M.; Kleinsmith, L.J.; Hardin, J.; Bertoni, G.P., 2009. *The World of the Cell* (7th ed.). Pearson/Benjamin Cummings, San Francisco.
- Beging 2010 Beging, S., Mlynek, D., Hatahimakul, S., Poghossian, A., Baldsiefen, G., Busch, H., Laube, N., Kleinen, L., Schöning, M.J., 2010. Field-effect calcium sensor for the determination of the risk of urinary stone formation. *Sensors and Actuators B: Chemical* 144(2), 374-379.
- Bergveld 1970 Bergveld, P., 1970. Development of an ion-sensitive solid-state device for neurophysiological measurements. *IEEE Trans. Biomed. Eng.* BME-17, 70-71.
- Bergveld 1972 Bergveld, P., 1972. Development, operation and application of the ion sensitive field effect transistor as a tool for electrophysiology, *IEEE Trans. Biomed. Eng.* BME-19, 342-351.
- Bergveld 1991 Bergveld, P., 1991. A Critical-Evaluation of Direct Electrical Protein-Detection Methods. *Biosens. Bioelectron.* 6(1), 55-72.
- Bergveld 2003 Bergveld, P., 2003. Thirty years of ISFETOLOGY: What happened in the past 30 years and what may happen in the next 30 years. *Sensors and Actuators B: Chemical* 88(1), 1-20.
- Berney 1997 Berney, H., Alderman, J., Lane, W., Collins, J.K., 1997. A differential capacitive biosensor using polyethylene glycol to overlay the biolayer. *Sensors and Actuators B: Chemical* 44(1-3), 578-584.
- Blanchard 1996 Blanchard, C.R., 1996. Atomic Force Microscopy. *The Chemical Educator* 1(5), 1-8.
- Bousse 1982 Bousse, L., 1982. Single Electrode-Potentials Related to Flat-Band Voltage Measurements on Eos and Mos Structures. *Journal of Chemical Physics* 76(10), 5128-5133.
- Bousse 1983 Bousse, L., Derooij, N.F., Bergveld, P., 1983. Operation of Chemically Sensitive Field-Effect Sensors as a Function of the Insulator-Electrolyte Interface. *Ieee Transactions on Electron Devices* 30(10), 1263-1270.
- Branquinho 2011 Branquinho, R., Veigas, B., Pinto, J.V., Martins, R., Fortunato, E., Baptista, P.V., 2011. Real-time monitoring of PCR amplification of proto-oncogene c-MYC using a Ta₂O₅ electrolyte-insulator-semiconductor sensor. *Biosensors and Bioelectronics* 28(1), 44-49.

- Branquinho 2012 Branquinho, R., Pinto, J.V., Busani, T., Barquinha, P., Pereira, L., Baptista, P.V., Martins, R., Fortunato, E., 2012. Biosensors based on Sputtered Ta₂O₅ with Low Thermal Annealing. IEEE/OSA Journal of Display Technology, in press.
- Bratov 2000 Bratov, A., Abramova, N., Domínguez, C., Baldi, A., 2000. Ion-selective field effect transistor (ISFET)-based calcium ion sensor with photocured polyurethane membrane suitable for ionised calcium determination in milk. *Analytica Chimica Acta* 408(1-2), 57-64.
- Bratov 2004 Bratov, A., Abramova, N., Domínguez, C., 2004. Investigation of chloride sensitive ISFETs with different membrane compositions suitable for medical applications. *Analytica Chimica Acta* 514(1), 99-106.
- Brett 1993 Brett, C.M.A., Brett, A.M.O., 1993. *Electrochemistry: Principles, Methods, and Applications*. Oxford University Press, USA.
- Briand 2005 Briand, D., Mondin, G., Jenny, S., van der Wal, P.D., Jeanneret, S., de Rooij, N.F., Banakh, O., Keppner, H., 2005. Metallo-organic low-pressure chemical vapor deposition of Ta₂O₅ using TaC₁₂H₃₀O₅N as precursor for batch fabrication of microsystems. *Thin Solid Films* 493(1-2), 6-12.
- Bryce 1998 Bryce, C.F.A. and Pacini, D., 1998. *The Structure and Function of Nucleic Acids*. (reviewed ed.). The Biochemical Society.
- Buchholz 2009 Buchholz, D.B., Liu, J., Marks, T.J., Zhang, M., Chang, R.P.H., 2009. Control and Characterization of the Structural, Electrical, and Optical Properties of Amorphous Zinc-Indium-Tin Oxide Thin Films. *ACS Applied Materials & Interfaces* 1(10), 2147-2153. (paper and supplementary information)
- Butt 2003 Butt, H.J., Graf, K., Kappl, M., 2003. *Physics and Chemistry of Interfaces*. John Wiley & Sons, Wiley.
- Caboni 2009 Caboni, A., Orgiu, E., Scavetta, E., Barbaro, M., Bonfiglio, A., 2009. Organic-based sensor for chemical detection in aqueous solution. *Appl. Phys. Lett.* 95(12), 123304.
- Cappellani 1999 Cappellani, A., Keddie, J.L., Barradas, N.P., Jackson, S.M., 1999. Processing and characterisation of sol-gel deposited Ta₂O₅ and TiO₂-Ta₂O₅ dielectric thin films. *Solid-State Electronics* 43(6), 1095-1099.
- Caras 1980 Caras, S., Janata, J., 1980. Field effect transistor sensitive to penicillin. *Analytical Chemistry* 52(12), 1935-1937.

-
- Carcia 2003 Carcia, P.F., McLean, R.S., Reilly, M.H., G. Nunes, Jr., 2003. Transparent ZnO thin-film transistor fabricated by rf magnetron sputtering. *Appl. Phys. Lett.* 82(7), 1117-1119.
- Casal 2012 Casal, P., Wen, X., Gupta, S., Nicholson III, T., Wang, Y., Theiss, A., Bhushan, B., Brillson, L., Lu, W., Lee, S.C., 2012. ImmunoFET feasibility in physiological salt environments. *Phil. Trans. R. Soc. A* 370(1667), 2474-2488.
- Chaneliere 1998 Chaneliere, C., Autran, J.L., Devine, R.A.B., Balland, B., 1998. Tantalum pentoxide (Ta₂O₅) thin films for advanced dielectric applications. *Materials Science and Engineering: R: Reports* 22(6), 269-322.
- Chi 2000 Chi, L.-L., Yin, L.-T., Chou, J.-C., Chung, W.-Y., Sun, T.-P., Hsiung, K.-P., Hsiung, S.-K., 2000. Study on separative structure of EnFET to detect acetylcholine. *Sensors and Actuators B: Chemical* 71(1-2), 68-72.
- Chi 2000a Chi, L.L., Chou, J.C., Chung, W.Y., Sun, T.P., Hsiung, S.K., 2000. Study on extended gate field effect transistor with tin oxide sensing membrane. *Materials Chemistry and Physics* 63(1), 19-23.
- Chiang 2001 Chiang, J.-L., Jan, S.-S., Chou, J.-C., Chen, Y.-C., 2001. Study on the temperature effect, hysteresis and drift of pH-ISFET devices based on amorphous tungsten oxide. *Sensors and Actuators B: Chemical* 76(1-3), 624-628.
- Chou 2005 Chou, J.-C., Liao, L.P., 2005. Study on pH at the point of zero charge of TiO₂ pH ion-sensitive field effect transistor made by the sputtering method. *Thin Solid Films* 476(1), 157-161.
- Clark 1962 Clark, L.C. and Lyons, C., 1962. *Ann. N.Y. Acad. Sci.* Electrode systems for continuous monitoring in cardiovascular surgery. 102, 29-45.
- Colapicchioni 1991 Colapicchioni, C., Barbaro, A., Porcelli, F., Giannini, I., 1991. Immunoenzymatic Assay Using Chemfet Devices. *Sensors and Actuators B-Chemical* 4(3-4), 245-250.
- Connolly 1983 Connolly, A.K., Waley, S.G., 1983. Characterization of the membrane beta-lactamase in *Bacillus cereus* 569/H/9. *Biochemistry* 22(20), 4647-4651.
- Dang 2006 Dang, C.V., O'Donnell, K.A., Zeller, K.I., Nguyen, T., Osthus, R.C., Li, F., 2006. The c-Myc target gene network. *Seminars in Cancer Biology*. 16(4), 253-264.
- Demoz 1995 Demoz, A., Verpoorte, E.M.J., Harrison, D.J., 1995. An equivalent circuit model of ion-selective membrane|insulator|semiconductor interfaces used for chemical sensors. *Journal of Electroanalytical Chemistry* 389(1-2), 71-78.

- Dimitrova 1998 Dimitrova, T., Atanassova, E., 1998. Interface and oxide properties of rf sputtered Ta₂O₅- Si structures. *Vacuum* 51(2), 151-152.
- Diot 1985 Diot, J.L., Joseph, J., Martin, J.R., Clechet, P., 1985. pH dependence of the Si/SiO₂ interface state density for EOS systems : Quasi-static and AC conductance methods. *Journal of Electroanalytical Chemistry* 193(1-2), 75-88.
- Drummond 2003 Drummond, T.G., Hill, M.G., Barton, J.K., 2003. Electrochemical DNA sensors. *Nat Biotech* 21(10), 1192-1199.
- Dzyadevych 2006 Dzyadevych, S.V., Soldatkin, A.P., El'skaya, A.V., Martelet, C., Jaffrezic-Renault, N., 2006. Enzyme biosensors based on ion-selective field-effect transistors. *Analytica Chimica Acta* 568(1-2), 248-258.
- Ellmer 2000 Ellmer, K., 2000. Magnetron sputtering of transparent conductive zinc oxide: relation between the sputtering parameters and the electronic properties. *J. Phys. D: Appl. Phys.* 33, R17.
- Estrela 2005 Estrela, P., Stewart, A.G., Yan, F., Migliorato, P., 2005. Field effect detection of biomolecular interactions. *Electrochimica Acta* 50(25-26), 4995-5000.
- Estrela 2007a Estrela, P., Keighley, S.D., Migliorato, P., 2007. Field Effect Potentiometric Biosensors. In: Ozoemena, K.I. (Ed.), *Recent Advances in Analytical Electrochemistry*, pp. 199 - 230. Transworld Research Network, Kerala, India.
- Estrela 2007b Estrela, P., Migliorato, P., 2007. Chemical and biological sensors using polycrystalline silicon TFTs. *Journal of Materials Chemistry* 17, 219-224.
- Eteshola 2008 Eteshola, E., Keener, M.T., Elias, M., Shapiro, J., Brillson, L.J., Bhushan, B., Lee, S.C., 2008. Engineering functional protein interfaces for immunologically modified field effect transistor (ImmunoFET) by molecular genetic means. *Journal of the Royal Society Interface* 5(18), 123-127.
- Fabry 1990 Fabry, P., Laurent-Yvonnou, L., 1990. The C-V method for characterizing ISFET or EOS devices with ion-sensitive membranes. *Journal of Electroanalytical Chemistry and Interfacial Electrochemistry* 286(1-2), 23-40.
- Fanigliulo 1996 Fanigliulo, A., Accossato, P., Adami, M., Lanzi, M., Martinoia, S., Paddeu, S., Parodi, M.T., Rossi, A., Sartore, M., Grattarola, M., Nicolini, C., 1996. Comparison between a LAPS and an FET-based sensor for cell-metabolism detection. *Sensors and Actuators B: Chemical* 32(1), 41-48.
- Felici 1993 Felici, A., Amicosante, G., Oratore, A., Strom, R., Ledent, P., Joris, B., Fanuel, L., Frere, J.M., 1993. An overview of the kinetic parameters of class B beta-lactamases. *Biochem. J.* 291(1), 151-155.

- Fenollar-Ferrer 2002 Fenollar-Ferrer, C., Frau, J., Vilanova, B., Donoso, J., Munoz, F., 2002. Molecular modelling studies on Henry-Michaelis complexes of a class-C β -lactamase and β -lactam compounds. *Journal of Molecular Structure: THEOCHEM* 578(-3), 19-28.
- Flores 2003 Flores, F., Artigas, J., Marty, J.-L., Valdes, F., 2003. Development of an EnFET for the detection of organophosphorous and carbamate insecticides. *Analytical and Bioanalytical Chemistry* 376(4), 476-480.
- Fortunato 2008 Fortunato, E., Barquinha, P., Gonçalves, G., Pereira, L., Martins, R., 2008. High mobility and low threshold voltage transparent thin film transistors based on amorphous indium zinc oxide semiconductors. *Solid-State Electronics* 52(3), 443-448.
- Fortunato 2008a Fortunato, E., Correia, N., Barquinha, P., Pereira, L., Goncalves, G., Martins, R., 2008. High-Performance Flexible Hybrid Field-Effect Transistors Based on Cellulose Fiber Paper. *Electron Device Letters, IEEE* 29(9), 988-990.
- Fortunato 2012 Fortunato, E., Barquinha, P., Martins, R., 2012. Oxide Semiconductor Thin-Film Transistors: A Review of Recent Advances. *Adv. Mater.* 24(22), 2945-2986.
- Franke 2001 Franke, E., Schubert, M., Trimble, C.L., DeVries, M.J., Woollam, J.A., 2001. Optical properties of amorphous and polycrystalline tantalum oxide thin films measured by spectroscopic ellipsometry from 0.03 to 8.5 eV. *Thin Solid Films* 388(1-2), 283-289.
- Gamry 2010 Gamry Instruments, 2010. Application Notes: Basics of Electrochemical Impedance Spectroscopy. Also available at <http://www.gamry.com/>
- Gaudin 2001 Gaudin, V.r., Fontaine, J.h., Maris, P., 2001. Screening of penicillin residues in milk by a surface plasmon resonance-based biosensor assay: comparison of chemical and enzymatic sample pre-treatment. *Analytica Chimica Acta* 436(2), 191-198.
- Ghosh 2006 Ghosh, I., Stains, C.I., Ooi, A.T., Segal, D.J., 2006. Direct detection of double-stranded DNA: molecular methods and applications for DNA diagnostics. *Molecular BioSystems* 2(11), 551-560.
- Gonçalves 2008 Gonçalves, D., Prazeres, D.M.F., Chu, V., Conde, J.P., 2008. Detection of DNA and proteins using amorphous silicon ion-sensitive thin-film field effect transistors. *Biosensors and Bioelectronics* 24(4), 545-551.
- Gonçalves 2008a Goncalves, D., Prazeres, D.M.F., Chu, V., Conde, J.P., 2008. Amorphous Silicon Thin-Film Transistors Gated Through an Electrolyte Solution. *Electron Device Letters, IEEE* 29(9), 1030-1033.
- Gotoh 1989 Gotoh, M., Oda, S., Shimizu, I., Seki, A., Tamiya, E., Karube, I., 1989. Construction of amorphous silicon ISFET. *Sensors and Actuators* 16(1-2), 55-65.

-
- Gustavsson 2008 Gustavsson, J., Altankov, G., Errachid, A., Samitier, J., Planell, J.A., Engel, E., 2008. Surface modifications of silicon nitride for cellular biosensor applications. *Journal of Materials Science-Materials in Medicine* 19(4), 1839-1850.
- Hamlaoui 2002 Hamlaoui, M.L., Reybier, K., Marrakchi, M., Jaffrezic-Renault, N., Martelet, C., Kherrat, R., Walcarius, A., 2002. Development of a urea biosensor based on a polymeric membrane including zeolite. *Analytica Chimica Acta* 466(1), 39-45.
- Han 2006 Han, Y., Mayer, D., Offenhausser, A., Ingebrandt, S., 2006. Surface activation of thin silicon oxides by wet cleaning and silanization. *Thin Solid Films* 510(1-2), 175-180.
- Hartnagel 1995 Hartnagel, H., Dawar, A., Jain, A. and Jagadish, C., 1995. *Semiconducting Transparent Thin Films*. Bristol: IOP Publishing.
- Heller 2002 Heller, M.J., 2002. DNA MICROARRAY TECHNOLOGY: Devices, Systems, and Applications. *Annual Review of Biomedical Engineering* 4(1), 129-153.
- Hermeking 2003 Hermeking H., 2003. The MYC oncogene as a cancer drug target. *Curr Cancer Drug Targets* 3(3), 163-75.
- Hoffman 2003 Hoffman, R.L., Norris, B.J., Wager, J.F., 2003. ZnO-based transparent thin-film transistors. *Appl. Phys. Lett.* 82(5), 733-735.
- Hsieh 2010 Hsieh, H.-H., Wu, C.-H., Chien, C.-W., Chen, C.-K., Yang, C.-S., Wu, C.-C., Influence of channel-deposition conditions and gate insulators on performance and stability of top-gate IGZO transparent thin-film transistors. *Journal of the Society for Information Display* 18(10), 796-801.
- Ingebrandt 2007 Ingebrandt, S., Han, Y., Nakamura, F., Poghossian, A., Schoning, M.J., Offenhausser, A., 2007. Label-free detection of single nucleotide polymorphisms utilizing the differential transfer function of field-effect transistors. *Biosensors and Bioelectronics* 22(12), 2834-2840.
- Ipatov 2008 Ipatov, A., Abramova, N., Bratov, A., Domínguez, C., 2008. Integrated multisensor chip with sequential injection technique as a base for "electronic tongue" devices. *Sensors and Actuators B: Chemical* 131(1), 48-52.
- Jagadeesh 2010 Jagadeesh Chandra, S.V., Choi, C.-J., Uthanna, S., Mohan Rao, G., 2010. Structural and electrical properties of radio frequency magnetron sputtered tantalum oxide films: Influence of post-deposition annealing. *Materials Science in Semiconductor Processing* 13(4), 245-251.
- Jamasb 1998 Jamasb, S., Collins, S., Smith, R.L., 1998. A physical model for drift in pH ISFETs. *Sensors and Actuators B: Chemical* 49(1-2), 146-155.

-
- Janata 1976 Janata, J., Moss, S., 1976. Chemically sensitive field effect transistors. *Biomed. Eng.* 6, 241–245.
- Jimenez-Jorquera 2010 Jimenez-Jorquera, C., Orozco, J., Baldi, A., 2009. ISFET Based Microsensors for Environmental Monitoring. *Sensors* 10(1), 61-83.
- Kadurina 2004 Kadurina, M., Bocheva, G., Tonev, S., 2004. Penicillin and semisynthetic penicillins in dermatology. *Disease-a-Month* 50(6), 291-314.
- Kamahori 2007 Kamahori, M., Ishige, Y., Shimoda, M., 2007. A novel enzyme immunoassay based on potentiometric measurement of molecular adsorption events by an extended-gate field-effect transistor sensor. *Biosens. Bioelectron.* 22(12), 3080-3085.
- Keighley 2008 Keighley, S.D., Li, P., Estrela, P., Migliorato, P., 2008. Optimization of DNA immobilization on gold electrodes for label-free detection by electrochemical impedance spectroscopy. *Biosensors and Bioelectronics* 23(8), 1291-1297.
- Khanna 2006 Khanna, V.K., Kumar, A., Jain, Y.K., Ahmad, S., 2006. Design and development of a novel high-transconductance pH-ISFET (ion-sensitive field-effect transistor)-based glucose biosensor. *International Journal of Electronics* 93(2), 81-96.
- Kharitonov 2000 Kharitonov, A.B., Zayats, M., Lichtenstein, A., Katz, E., Willner, I., 2000. Enzyme monolayer-functionalized field-effect transistors for biosensor applications. *Sensors and Actuators B-Chemical* 70(1-3), 222-231.
- Kharitonov 2001 Kharitonov, A.B., Zayats, M., Alfonta, L., Katz, E., Willner, I., 2001. A novel ISFET-based NAD⁺-dependent enzyme sensor for lactate. *Sensors and Actuators B: Chemical* 76(1-3), 203-210.
- Kim 1998 Kim, J.S., Granstrom, M., Friend, R.H., Johansson, N., Salaneck, W.R., Daik, R., Feast, W.J., Cacialli, F., 1998. Indium-tin oxide treatments for single- and double-layer polymeric light-emitting diodes: The relation between the anode physical, chemical, and morphological properties and the device performance. *Journal of Applied Physics* 84(12), 6859-6870.
- Kim 2006 Kim, D.S., Park, J.E., Shin, J.K., Kim, P.K., Lim, G., Shoji, S., 2006. An extended gate FET-based biosensor integrated with a Si microfluidic channel for detection of protein complexes. *Sensors and Actuators B-Chemical*. 117(2), 488-494
- Kim 2007 Kim, M., Jeong, J.H., Lee, H.J., Ahn, T.K., Shin, H.S., Park, J.-S., Jeong, J.K., Mo, Y.-G., Kim, H.D., 2007. High mobility bottom gate InGaZnO thin film transistors with SiO_x etch stopper. *Appl. Phys. Lett.* 90(21), 212114.

-
- Kim 2009 Kim, J.C., Heo, J.S., Cho, Y.S., Moon, S.H., 2009. Atomic layer deposition of an HfO₂ thin film using Hf(O-iPr)₄. *Thin Solid Films* 517(19), 5695-5699.
- Kim 2012 Kim, S.-J., Yoon, E., Label-Free CMOS Bio Sensor With On-Chip Noise Reduction Scheme for Real-Time Quantitative Monitoring of Biomolecules. *Biomedical Circuits and Systems, IEEE Transactions on* 6(3), 189-196.
- Know 1996 Kwon, D.-H., Cho, B.-W., Kim, C.-S., Sohn, B.-K., 1996. Effects of heat treatment on Ta₂O₅ sensing membrane for low drift and high sensitivity pH-ISFET. *Sensors and Actuators B: Chemical* 34(1-3), 441-445.
- Kukli 2000 Kukli, K., Ritala, M., Matero, R., Leskelä, M., 2000. Influence of atomic layer deposition parameters on the phase content of Ta₂O₅ films. *Journal of Crystal Growth* 212(3-4), 459-468.
- Kukli 2002 Kukli, K., Ritala, M., Leskelä, M., Sajavaara, T., Keinonen, J., Gilmer, D., Bagchi, S., Prabhu, L., 2002. Atomic layer deposition of Al₂O₃, ZrO₂, Ta₂O₅, and Nb₂O₅ based nanolayered dielectrics. *Journal of Non-Crystalline Solids* 303(1), 35-39.
- Lai 2008 Lai, C.S., Lue, C.E., Yang, C.M., Jao, J.H., Tai, C.C., 2008. New pH-sensitive TaO_xNy membranes prepared by NH₃ plasma surface treatment and nitrogen incorporated reactive sputtering. *Sensors and Actuators B-Chemical* 130(1), 77-81.
- Landheer 2005 Landheer, D., Aers, G., McKinnon, W.R., Deen, M.J., Ranuarez, J.C., 2005. Model for the field effect from layers of biological macromolecules on the gates of metal-oxide-semiconductor transistors. *Journal of Applied Physics* 98(4).
- Landheer 2008 Landheer, D., McKinnon, W.R., Jiang, W.H., Aers, G., 2008. Effect of screening on the sensitivity of field-effect devices used to detect oligonucleotides. *Appl. Phys. Lett.* 92(25), 253901.
- Lee 2005 Lee, C.-C., Jan, D.-J., 2005. Optical properties and deposition rate of sputtered Ta₂O₅ films deposited by ion-beam oxidation. *Thin Solid Films* 483(1-2), 130-135.
- Lee 2009 Lee, C.-S., Kim, S., Kim, M., 2009. Ion-Sensitive Field-Effect Transistor for Biological Sensing. *Sensors* 9(9), 7111-7131.
- Lehmann 2000 Lehmann, M., Baumann, W., Brischwein, M., Ehret, R., Kraus, M., Schwinde, A., Bitzenhofer, M., Freund, I., Wolf, B., 2000. Non-invasive measurement of cell membrane associated proton gradients by ion-sensitive field effect transistor arrays for microphysiological and bioelectronic applications. *Biosensors and Bioelectronics* 15(3-4), 117-124.

- Lillis 2007 Lillis, B., Manning, M., Hurley, E., Berney, H., Duane, R., Mathewson, A., Sheehan, M.M., 2007. Investigation into the effect that probe immobilisation method type has on the analytical signal of an EIS DNA biosensor. *Biosensors and Bioelectronics* 22(7), 1289-1295.
- Lin 2010 Lin, T.-W., Kekuda, D., Chu, C.-W., 2010. Label-free detection of DNA using novel organic-based electrolyte-insulator-semiconductor. *Biosensors and Bioelectronics* 25(12), 2706-2710.
- Li-Te 2001 Li-Te, Y., Jung-Chuan, C., Wen-Yaw, C., Tai-Ping, S., Shen-Ken, H., 2001. Characteristics of silicon nitride after O₂ plasma surface treatment for pH-ISFET applications. *Biomedical Engineering, IEEE Transactions on* 48(3), 340-344.
- Lorenzelli 2003 Lorenzelli, L., Margesin, B., Martinoia, S., Tedesco, M.T., Valle, M., 2003. Bioelectrochemical signal monitoring of in-vitro cultured cells by means of an automated microsystem based on solid state sensor-array. *Biosensors and Bioelectronics* 18(5-6), 621-626.
- Lu 2010 Lu, T.-F., Wang, J.-C., Yang, C.-M., Chang, C.-P., Ho, K.-I., Ai, C.-F., Lai, C.-S., 2010. Non-ideal effects improvement of SF₆ plasma treated hafnium oxide film based on electrolyte-insulator-semiconductor structure for pH-sensor application. *Microelectronics Reliability* 50(5), 742-746.
- Lue 2011 Lue, C.-E., Yu, T.-C., Yang, C.-M., Pijanowska, D.G., Lai, C.-S., 2011. Optimization of Urea-EnFET Based on Ta₂O₅ Layer with Post Annealing. *Sensors* 11(5), 4562-4571.
- Luo 2004 Luo, X.-L., Xu, J.-J., Zhao, W., Chen, H.-Y., 2004. A novel glucose ENFET based on the special reactivity of MnO₂ nanoparticles. *Biosensors and Bioelectronics* 19(10), 1295-1300.
- Madou 1989 Madou, M.J., Morrison, S.R., 1989. *Chemical Sensing with Solid State Devices*. Academic Press.
- Madou 2002 Madou, M.J., 2002. *Fundamentals of Microfabrication: The Science of Miniaturization*, Second Edition. CRC Press.
- Martinoia 2001 Martinoia, S., Rosso, N., Grattarola, M., Lorenzelli, L., Margesin, B., Zen, M., 2001. Development of ISFET array-based microsystems for bioelectrochemical measurements of cell populations. *Biosensors and Bioelectronics* 16(9-12), 1043-1050.
- Martinoia 2004 Martinoia, S., Massobrio, P., 2004. ISFET-neuron junction: circuit models and extracellular signal simulations. *Biosensors and Bioelectronics* 19(11), 1487-1496.

-
- Masuda 2003 Masuda, S., Kitamura, K., Okumura, Y., Miyatake, S., Tabata, H., Kawai, T., 2003. Transparent thin film transistors using ZnO as an active channel layer and their electrical properties. *Journal of Applied Physics* 93(3), 1624-1630.
- Mayer 2003 Mayer, M., 2003. Rutherford Backscattering Spectrometry (RBS). Workshop on Nuclear Data for Science and Technology: Materials Analysis, LNS0822003.
- Melo 2003 Melo, J.V., Soldatkin, A.P., Martelet, C., Jaffrezic-Renault, N., Cosnier, S., 2003. Use of competitive inhibition for driving sensitivity and dynamic range of urea ENFETs. *Biosensors and Bioelectronics* 18(4), 345-351.
- Meyer 1992 Meyer, E., 1992. Atomic force microscopy. *Progress in Surface Science* 41(1), 3-49.
- Mohri 2006 Mohri, S., Shimizu, J., Goda, N., Miyasaka, T., Fujita, A., Nakamura, M., Kajiya, F., 2006. Measurements of CO₂, lactic acid and sodium bicarbonate secreted by cultured cells using a flow-through type pH/CO₂ sensor system based on ISFET. *Sensors and Actuators B: Chemical* 115(1), 519-525.
- Moreno 2006 Moreno, L., Merlos, A., Abramova, N., Jiménez, C., Bratov, A., 2006. Multi-sensor array used as an "electronic tongue" for mineral water analysis. *Sensors and Actuators B: Chemical* 116(1-2), 130-134.
- Mourzina 2003 Mourzina, Y., Mai, T., Poghossian, A., Ermolenko, Y., Yoshinobu, T., Vlasov, Y., Iwasaki, H., J. Schoning, M., 2003. K⁺-selective field-effect sensors as transducers for bioelectronic applications. *Electrochimica Acta* 48(20-22), 3333-3339.
- Nayak 2011 Nayak, P.K., Pinto, J.V., Gonçalves, G., Martins, R., Fortunato, E., 2011. Environmental, Optical, and Electrical Stability Study of Solution-Processed Zinc-Tin-Oxide Thin-Film Transistors. *J. Display Technol.* 7(12), 640-643.
- Ngaruiya 2003 Ngaruiya, J.M., Venkataraj, S., Drese, R., Kappertz, O., Leervad Pedersen, T.P., Wuttig, M., 2003. Preparation and characterization of tantalum oxide films produced by reactive DC magnetron sputtering. *physica status solidi (a)* 198(1), 99-110.
- Nomura 2004 Nomura, K., Ohta, H., Takagi, A., Kamiya, T., Hirano, M., Hosono, H., 2004. Room-temperature fabrication of transparent flexible thin-film transistors using amorphous oxide semiconductors. *Nature* 432(7016), 488-492.
- Notomi 2000 Notomi, T., Okayama, H., Masubuchi, H., Yonekawa, T., Watanabe, K., Amino, N., Hase, T., 2000. Loop-mediated isothermal amplification of DNA. *Nucleic Acids Research* 28(12), e63.

-
- Olziersky 2010 Olziersky, A., Barquinha, P., Vila, A., Pereira, L., Goncalves, G., Fortunato, E., Martins, R., Morante, J.R., 2010. Insight on the SU-8 resist as passivation layer for transparent Ga₂O₃-In₂O₃-ZnO thin-film transistors. *Journal of Applied Physics* 108(6), 064505.
- Ozer 1997 Ozer, N., Lampert, C., 1997. Structural and optical properties of sol-gel deposited proton conducting Ta₂O₅ films. *Journal of Sol-Gel Science and Technology* 8(1), 703-709.
- Pai 2008 Pai, Y.-H., Chou, C.-C., Shieu, F.-S., 2008. Preparation and optical properties of Ta₂O₅-x thin films. *Materials Chemistry and Physics* 107(2-3), 524-527.
- Pan 2007 Pan, T.-M., Liao, K.-M., 2007. Structural properties and sensing characteristics of Y₂O₃ sensing membrane for pH-ISFET. *Sensors and Actuators B: Chemical* 127(2), 480-485.
- Pan 2008 Pan, T.M., Liao, K.M., 2008. Comparison of structural and sensing characteristics of Pr₂O₃ and PrTiO₃ sensing membrane for pH-ISFET application. *Sensors and Actuators B-Chemical* 133(1), 97-104.
- Pan 2009 Pan, T.M., Lin, J.C., 2009. A TiO₂/Er₂O₃ stacked electrolyte/insulator /semiconductor film pH-sensor for the detection of urea. *Sensors and Actuators B-Chemical* 138(2), 474-479.
- Pan 2009a Pan, T.M., Lin, J.C., Wu, M.H., Lai, C.S., 2009. Study of high-k Er₂O₃ thin layers as ISFET sensitive insulator surface for pH detection. *Sensors and Actuators B-Chemical* 138(2), 619-624.
- Pan 2009b Pan, T.-M., Huang, M.-D., Lin, C.-W., Wu, M.-H., 2010. Development of high-k HoTiO₃ sensing membrane for pH detection and glucose biosensing. *Sensors and Actuators B-Chemical* 144(1), 139-145.
- Pan 2009c Pan, T.-M., Lin, J.-C., Wu, M.-H., Lai, C.-S., 2009. Structural properties and sensing performance of high-k Nd₂TiO₅ thin layer-based electrolyte-insulator-semiconductor for pH detection and urea biosensing. *Biosensors and Bioelectronics* 24(9), 2864-2870.
- Pan 2011 Pan, T.-M., Chang, K.-Y., Lin, C.-W., Tsai, S.-W., Wu, M.-H., 2011. Label-free detection of uric acid using a disposable poly-N-isopropylacrylamide as an encapsulating enzyme material based on high-k Eu₂Ti₂O₇ electrolyte-insulator-semiconductor devices. *Sensors and Actuators B: Chemical* 160(1), 850-857.
- Parida 2008 Parida, M., Sannarangaiah, S., Dash, P.K., Rao, P.V.L., Morita, K., 2008. Loop mediated isothermal amplification (LAMP): a new generation of innovative gene amplification technique; perspectives in clinical diagnosis of infectious diseases. *Reviews in Medical Virology* 18(6), 407-421.

-
- Park 2002 Park, K.-Y., Choi, S.-B., Lee, M., Sohn, B.-K., Choi, S.-Y., 2002. ISFET glucose sensor system with fast recovery characteristics by employing electrolysis. *Sensors and Actuators B: Chemical* 83(1-3), 90-97.
- Paskaleva 2000 Paskaleva, A., Atanassova, E., Dimitrova, T., 2000. Leakage currents and conduction mechanisms of Ta₂O₅ layers on Si obtained by RF sputtering. *Vacuum* 58(2-3), 470-477.
- PenG 2011 Penicillin G Product data sheet version 2.0. 2011, TOKU-E
- Pereira 2006 Pereira, L., Águas, H., Fortunato, E., Martins, R., 2006. Nanostructure characterization of high k materials by spectroscopic ellipsometry. *Applied Surface Science* 253(1), 339-343.
- Pereira 2008 Pereira, L., Barquinha, P., Fortunato, E., Martins, R., Kang, D., Kim, C.J., Lim, H., Song, I., Park, Y., 2008. High k dielectrics for low temperature electronics. *Thin Solid Films* 516(7), 1544-1548.
- Pereira 2008a Pereira, L., 2008. Produção e caracterização de silício policristalino e sua aplicação a TFTs. PhD thesis, Faculdade de Ciência e Tecnologia, Universidade Nova de Lisboa (Portugal)
- Pignolet 1995 Pignolet, A., Rao, G.M., Krupanidhi, S.B., 1995. Rapid thermal processed thin films of reactively sputtered Ta₂O₅. *Thin Solid Films* 258(1-2), 230-235.
- Pinto 2012 Pinto, J.V., Branquinho, R., Barquinha, P., Alves, E., Martins, R., Fortunato, E., 2012. Extended-gate ISFETs based on Sputtered Amorphous Oxides. *IEEE/OSA Journal of Display Technology*, in press.
- Poghossian 2000 Poghossian, A., Thust, M., Schoning, M.J., Muller-Veggian, M., Kordos, P., Luth, H., 2000. Cross-sensitivity of a capacitive penicillin sensor combined with a diffusion barrier. *Sensors and Actuators B: Chemical* 68(1-3), 260-265.
- Poghossian 2001 Poghossian, A., Schoning, M.J., Schroth, P., Simonis, A., Luth, H., 2001. An ISFET-based penicillin sensor with high sensitivity, low detection limit and long lifetime. *Sensors and Actuators B: Chemical* 76(1-3), 519-526.
- Poghossian 2001a Poghossian, A., Luth, H., Schultze, J.W., Schoning, M.J., 2001. (Bio-)chemical and physical microsensor arrays using an identical transducer principle. *Electrochimica Acta* 47(1-2), 243-249.
- Poghossian 2004 Poghossian, A., Schöning, M.J., 2004. Detecting Both Physical and (Bio-)Chemical Parameters by Means of ISFET Devices. *Electroanalysis* 16(22), 1863-1872.

- Poghossian 2006 Poghossian, A., Abouzar, M.H., Sakkari, M., Kassab, T., Han, Y., Ingebrandt, S., Offenhausser, A., Schoning, M.J., 2006. Field-effect sensors for monitoring the layer-by-layer adsorption of charged macromolecules. *Sensors and Actuators B-Chemical* 118(1-2), 163-170.
- Poghossian 2007 Poghossian, A., Ingebrandt, S., Abouzar, M.H., Schoning, M.J., 2007. Label-free detection of charged macromolecules by using a field-effect-based sensor platform: Experiments and possible mechanisms of signal generation. *Applied Physics A* 87(3), 517-524.
- Poghossian 2007a Poghossian, A., Abouzar, M.H., Amberger, F., Mayer, D., Han, Y., Ingebrandt, S., Offenhäusser, A., Schöning, M.J., 2007. Field-effect sensors with charged macromolecules: Characterisation by capacitance-voltage, constant-capacitance, impedance spectroscopy and atomic-force microscopy methods. *Biosensors and Bioelectronics* 22(9-10), 2100-2107.
- Poghossian 2009 Poghossian, A., Ingebrandt, S., Offenhausser, A., Schoning, M.J., 2009. Field-effect devices for detecting cellular signals. *Seminars in Cell & Developmental Biology* 20(1), 41-48.
- Porporati 2003 Porporati, A., Roitti, S., Sbaizero, O., 2003. Metallorganic chemical vapor deposition of Ta₂O₅ films. *Journal of the European Ceramic Society* 23(2), 247-251.
- Riekkinen 2003 Riekkinen, T., Molarius, J., 2003. Reactively sputtered tantalum pentoxide thin films for integrated capacitors. *Microelectronic Engineering* 70(2-4), 392-397.
- Rothberg 2011 Rothberg, J.M., Hinz, W., Rearick, T.M., Schultz, J., Mileski, W., Davey, M., Leamon, J.H., Johnson, K., Milgrew, M.J., Edwards, M., Hoon, J., Simons, J.F., Marran, D., Myers, J.W., Davidson, J.F., Branting, A., Nobile, J.R., Puc, B.P., Light, D., Clark, T.A., Huber, M., Branciforte, J.T., Stoner, I.B., Cawley, S.E., Lyons, M., Fu, Y., Homer, N., Sedova, M., Miao, X., Reed, B., Sabina, J., Feierstein, E., Schorn, M., Alanjary, M., Dimalanta, E., Dressman, D., Kasinskas, R., Sokolsky, T., Fidanza, J.A., Namsaraev, E., McKernan, K.J., Williams, A., Roth, G.T., Bustillo, J., 2011. An integrated semiconductor device enabling non-optical genome sequencing. *Nature* 475(7356), 348-352.
- Sambrook 2001 Sambrook, J., Russell, D.W., 2001. *Molecular Cloning: A Laboratory Manual*, 3rd ed. Cold Spring Harbor Laboratory Press.
- Sant 2011 Sant, W., Temple-Boyer, P., E.Chanie, Launay, J., Martinez, A., On-line monitoring of urea using enzymatic field effect transistors. *Sensors and Actuators B: Chemical* 160(1), 59-64.
- Sasaki 2010 Sasaki, Y., Kawarada, H., 2010. Low drift and small hysteresis characteristics of diamond electrolyte-solution-gate FET. *Journal of Physics D: Applied Physics* 43(37), 374020.

- Scarpa 2010 Scarpa, G., Idzko, A.-L., Yadav, A., Thalhammer, S., 2010. Organic ISFET Based on Poly (3-hexylthiophene). *Sensors* 10(3), 2262-2273.
- Schneider 2010 Schneider, M.J., Mastovska, K., Solomon, M.B. 2010. Distribution of Penicillin G Residues in Culled Dairy Cow Muscles: Implications for Residue Monitoring. *Journal of Agricultural Food & Chemistry*. 58(12):5408-5413.
- Schoning 2002 Schoning, M.J., Poghossian, A., 2002. Recent advances in biologically sensitive field-effect transistors (BioFETs). *The Analyst* 127(9), 1137-1151.
- Schoning 2002a Schoning, M., Simonis, A., Ruge, C., Ecken, H., Muller-Veggian, M., Luth, H., 2002. A (Bio-)Chemical Field-Effect Sensor with Macroporous Si as Substrate Material and a SiO₂ / LPCVD-Si₃N₄ Double Layer as pH Transducer. *Sensors* 2(1), 11-22.
- Schoning 2003 Schoning, M.J., Arzdorf, M., Mulchandani, P., Chen, W., Mulchandani, A., 2003. Towards a capacitive enzyme sensor for direct determination of organophosphorus pesticides: Fundamental studies and aspects of development. *Sensors* 3(6), 119-127.
- Schoning 2006 Schoning, M.J., Poghossian, A., 2006. Bio FEDs (Field-Effect devices): State-of-the-art and new directions. *Electroanalysis* 18(19-20), 1893-1900.
- Schroder 2006 Schroder, D.K., 2006. *Semiconductor Material and Device Characterization*, 3rd ed. John Wiley & Sons, Wiley.
- Seo 2009 Seo, H.-S., Bae, J.-U., Kim, D.-H., Park, Y., Kim, C.-D., Kang, I.B., Chung, I.-J., Choi, J.-H., Myoung, J.-M., 2009. Reliable Bottom Gate Amorphous Indium-Gallium-Zinc Oxide Thin-Film Transistors with TiO_x Passivation Layer. *Electrochemical and Solid-State Letters* 12(9), H348-H351.
- Shinwari 2007 Shinwari, M.W., Deen, M.J., Landheer, D., 2007. Study of the electrolyte-insulator-semiconductor field-effect transistor (EISFET) with applications in biosensor design. *Microelectronics Reliability* 47(12), 2025-2057.
- Singh 2010 Singh, M., Haverinen, H.M., Dhagat, P., Jabbour, G.E., 2010. Inkjet Printing—Process and Its Applications. *Adv. Mater.* 22(6), 673-685.
- Siqueira 2009 Siqueira Jr, J.R., Abouzar, M.H., Poghossian, A., Zucolotto, V., Oliveira Jr, O.N., Schöning, M.J., 2009. Penicillin biosensor based on a capacitive field-effect structure functionalized with a dendrimer/carbon nanotube multilayer. *Biosensors and Bioelectronics* 25(2), 497-501.

- Song 2006 Song, K.-S., Nakamura, Y., Sasaki, Y., Degawa, M., Yang, J.-H., Kawarada, H., 2006. pH-sensitive diamond field-effect transistors (FETs) with directly aminated channel surface. *Analytica Chimica Acta* 573-574, 3-8.
- Song 2009 Song, Q.M., Wu, B.J., Xie, B., Huang, F., Li, M., Wang, H., Jiang, Y., Song, Y., 2009. Resputtering of zinc oxide films prepared by radical assisted sputtering. *Journal of Applied Physics* 105(4), 044509.
- Souteyrand 1997 Souteyrand, E., Cloarec, J.P., Martin, J.R., Wilson, C., Lawrence, I., Mikkelsen, S., Lawrence, M.F., 1997. Direct Detection of the Hybridization of Synthetic Homo-Oligomer DNA Sequences by Field Effect. *J. Phys. Chem. B* 101(15), 2980-2985.
- Spijkman 2010 Spijkman, M.-J., Brondijk, J.J., Geuns, T.C.T., Smits, E.C.P., Cramer, T., Zerbetto, F., Stoliar, P., Biscarini, F., Blom, P.W.M., de Leeuw, D.M., 2010. Dual-Gate Organic Field-Effect Transistors as Potentiometric Sensors in Aqueous Solution. *Advanced Functional Materials* 20(6), 898-905.
- Spijkman 2011 Spijkman, M., Smits, E.C.P., Cillessen, J.F.M., Biscarini, F., Blom, P.W.M., de Leeuw, D.M., 2011. Beyond the Nernst-limit with dual-gate ZnO ion-sensitive field-effect transistors. *Appl. Phys. Lett.* 98(4), 043502-043503.
- Subramanian 1999 Subramanian, A., Kennel, S.J., Oden, P.I., Jacobson, K.B., Woodward, J., Doktycz, M.J., 1999. Comparison of techniques for enzyme immobilization on silicon supports. *Enzyme and Microbial Technology* 24(1-2), 26-34.
- Sze 2007 Sze, S.M., Ng, K.K., 2006. *Physics of Semiconductor Devices*, 3rd ed. John Wiley & Sons, Wiley.
- Thevenot 1999 Thevenot, D. R., Toth, K., Durst, R. A. and Wilson, G. S., 1999. Electrochemical biosensors: recommended definitions and classification. *IUPAC, Pure Appl. Chem.*, 71, 2333-2348
- Thevenot 2001 Thevenot, D.R., Toth, K., Durst, R.A., Wilson, G.S., 2001. Electrochemical biosensors: recommended definitions and classification. *Biosensors and Bioelectronics* 16(1-2), 121-131.
- Tickle 1969 Tickle, A.C., 1969. *Thin-Film Transistors: a new approach to microelectronics*. John Wiley & Sons, Inc.
- Tlili 2005 Tlili, A., Jarboui, M.A., Abdelghani, A., Fathallah, D.M., Maaref, M.A., 2005. A novel silicon nitride biosensor for specific antibody-antigen interaction. *Materials Science and Engineering: C* 25(4), 490-495.

-
- Tomaszewski 2002 Tomaszewski, H., Poelman, H., Depla, D., Poelman, D., De Gryse, R., Fiermans, L., Reyniers, M.-F.o., Heynderickx, G., Marin, G.B., 2002. TiO₂ films prepared by DC magnetron sputtering from ceramic targets. *Vacuum* 68(1), 31-38.
- Turek 2007 Turek, M., Ketterer, L., Classen, M., Berndt, H.K., Elbers, G., Kruger, P., Keusgen, M., Schoning, M.J., 2007. Development and electrochemical investigations of an EIS(electrolyte-insulator-semiconductor) based biosensor for cyanide detection. *Sensors* 7(8), 1415-1426.
- Turek 2008 Turek, M., Keusgen, M., Poghossian, A., Mulchandani, A., Wang, J., Schoning, M.J., 2008. Enzyme-Modified Electrolyte-Insulator-Semiconductor Sensors. *J Contemp Phys-Arme+* 43(2), 82-85.
- Turner 1987 Turner, A.P.F., Karube, I. and Wilson, G.S., 1987. *Biosensors: Fundamentals and Applications*. Oxford University Press, Oxford. 770p.
- Uslu 2004 Uslu, F., Ingebrandt, S., Mayer, D., Bocker-Meffert, S., Odenthal, M., Offenhausser, A., 2004. Labelfree fully electronic nucleic acid detection system based on a field-effect transistor device. *Biosensors and Bioelectronics* 19(12), 1723-1731.
- van der Spiegel 1983 Van der Spiegel, J., Lauks, I., Chan, P., Babic, D., 1983. *Sensors and Actuators B*. 4, 291-298.
- vanHal 1995 van Hal, R.E.G., Eijkel, J.C.T., Bergveld, P., 1995. A novel description of ISFET sensitivity with the buffer capacity and double-layer capacitance as key parameters. *Sensors and Actuators B: Chemical* 24(1-3), 201-205.
- vanHal 1996 van Hal, R.E.G., Eijkel, J.C.T., Bergveld, P., 1996. A general model to describe the electrostatic potential at electrolyte oxide interfaces. *Advances in Colloid and Interface Science* 69(1-3), 31-62.
- Veigas 2012 Veigas, B., Jacob, J.M., Costa, M.N., Santos, D.S., Viveiros, M., Inacio, J., Martins, R., Barquinha, P., Fortunato, E., Baptista, P.V., 2012. Gold on paper-paper platform for Au-nanoprobe TB detection. *Lab on a Chip* 12(22), 4802-4808.
- Vijayalakshmi 2008 Vijayalakshmi, A., Tarunashree, Y., Baruwati, B., Manorama, S.V., Narayana, B.L., Johnson, R.E.C., Rao, N.M., 2008. Enzyme field effect transistor (ENFET) for estimation of triglycerides using magnetic nanoparticles. *Biosensors and Bioelectronics* 23(11), 1708-1714.
- Waley 1975 Waley, S. G., 1975. The pH-dependence and group modification of β -Lactamase I. *Biochem. J.* 149, 547-551.
- Wasa 2004 Wasa, K., Kitabatake, M., Adachi, H., 2004. *Thin Film Materials Technology: Sputtering of Compound Materials*. William Andrew, Inc. and Springer-Verlag GmbH & Co. KG.

-
- Watson 1953 Watson J.D. and Crick F.H.C., 1953. A Structure for Deoxyribose Nucleic Acid. *Nature* 171 (4356), 737–738.
- Web01 <http://www.sensorsmag.com/specialty-markets/medical/strong-growth-predicted-biosensors-market-7640>
- Web02 http://www.engineerlive.com/Design-Engineer/Materials_Processes/Magnetron_sputtering_cathodes/18921/
- Web03 <http://www.foodsafetywatch.com/public/1050.cfm>
- Web04 <http://www.mycancergene.org>
- Wu 2009 Wu, M.H., Cheng, C.H., Lai, C.S., Pan, T.M., 2009. Structural properties and sensing performance of high-k Sm₂O₃ membrane-based electrolyte-insulator-semiconductor for pH and urea detection. *Sensors and Actuators B-Chemical* 138(1), 221-227.
- Wunderlich 2007 Wunderlich, B.K., Neff, P.A., Bausch, A.R., 2007. Mechanism and sensitivity of the intrinsic charge detection of biomolecular interactions by field effect devices. *Appl. Phys. Lett.* 91(8), 083904.
- Yan 2005 Yan, F., Estrela, P., Mo, Y., Migliorato, P., Maeda, H., 2005. Polycrystalline silicon ISFETs on glass substrate. *Sensors* 5(4-5), 293-301.
- Yates 1974 Yates, D.E., Levine, S., Healy, T.W., 1974. Site-binding model of the electrical double layer at the oxide/water interface. *Journal of the Chemical Society, Faraday Transactions 1: Physical Chemistry in Condensed Phases* 70, 1807-1818.
- Yildirim 2005 Yildirim, S., Ulutas, K., Deger, D., Zayim, E.O., Turhan, I., 2005. Dielectric properties of sol-gel derived Ta₂O₅ thin films. *Vacuum* 77(3), 329-335.
- Zayats 2000 Zayats, M., Kharitonov, A.B., Katz, E., Buckmann, A.F., Willner, I., 2000. An integrated NAD⁺-dependent enzyme-functionalized field-effect transistor (ENFET) system: development of a lactate biosensor. *Biosensors and Bioelectronics* 15(11-12), 671-680.

